Raman Microscopy Studies of Carbon Particles from Diesel Particulate Matter (DPM) and Coal Dust

Paul Whelan

A thesis submitted in partial fulfilment of the requirements of Sheffield Hallam University for the degree of Doctor of Philosophy

November 2001

Declaration

The work described in this thesis was carried out by the author in the Materials Research Institute, Sheffield Hallam University, between October 1998 and September 2001. The author declares that this work has not been submitted for any other degree. The work is original except where acknowledged by reference

Author: Paul Whelan

Paul Whelan

Supervisor: _____

Prof. Jack Yarwood

Acknowledgements

I would like to thank my supervisors Prof. Jack Yarwood and Mr. Barry Tylee for their supervision and support over the three years of my PhD research. I would also like to thank the staff at the Health and Safety Laboratories, especially Peter Stacey, for their help and making me feel welcome whenever I used their facilities. The service staff at the MRI deserves a mention. This includes Mike and Bob who preformed the XPS and XRF analysis of my samples. Also, I would like to thank the members of the Vibrational Spectroscopy group for contributing to the pleasant working environment at the MRI. It was an enjoyable experience working with Delphine, JP, Pierre, Jane, Sandry, Lena, Andy, Paul, Nigel and Christophe. However, Chris and Jeff deserve a special mention. We had some great times together in Sheffield and in these two guys I believe I have found some true friends.
Finally, I would like to thank my parents for their support throughout my academic career. It has been seven long years and I would never have made it this far without their support and encouragement. Their backing has been the major contribution to my success so far.

Abstract

Diesel Particulate Matter (DPM) and coal dust samples were characterised using Raman microscopy, X-ray Photoelectron Spectroscopy (XPS), Diffuse Reflectance Infrared Fourier Transform Spectroscopy (DRIFTS), Thermo-Gravimetric Analysis (TGA), X-ray Fluorescence (XRF) spectrometry and Scanning electron Microscopy. The sp2/sp3 carbon bonding ratios for DPM and coal dust were determined as 6.1 and 0.7, respectively, from XPS. Principal Component Analysis (PCA) was successfully implemented as a tool for distinguishing between the very similar DPM and coal dust Raman spectra, with over 99% of the variance contained in the first principal component.

DPM and coal dust mixtures with known compositions were produced. Raman instrumental parameters were systematically optimised by varying the objective lenses, acquisition times and laser powers, to improve spectral and obtain the most reproducible integrated spectral areas. A rotation stage was developed and employed to spin the specimens during analysis, resulting in a larger sampling area. This resulted in a more representative sampling regime for the heterogeneous specimens and a considerable improvement in the reproducibility of integrated spectral areas. The error in the integrated spectral areas of 10 replicate spectra of different mixtures ranged from 5-22% before implementation of the rotating stage and was notably reduced to 2-6% due to the action of spinning.

Raman spectra of mixtures were used to construct a Partial Least Squares (PLS) model. The R^2 values for the DPM and coal dust were 0.865 and 0.763, respectively. The differential burn-off of volatile organics during the Raman analysis due to localised heating from the laser hindered the ability to gain highly reproducible spectra and thus markedly affected the PLS model. A method development stage aimed at improving the R^2 values was applied to the samples. This involved heat-treating the specimens to 625°C in an inert nitrogen atmosphere, before the Raman analysis. The resultant PLS model, after heat-treatment, dramatically improved the R^2 values such that the DPM and coal dust were 0.974 and 0.907, respectively. This model was used to predict the composition of a test sample with known amounts of DPM and coal dust. The concentrations predicted by the model were 166 ± 3.9μg for the DPM and 68 ± 7.8μg for the coal dust. The model slightly overestimated the amount of DPM present in the sample but gave a large underestimation of the coal dust content. The diagnostics of the model were investigated and recommendations for the improvement of future models were given.

Introduction

Diesel emissions are classified as a potential occupational carcinogen and have a number of other negative health effects associated with their exposure.[1] Small nanoparticles are present in the emissions. These are called diesel particular matter (DPM) and are of particular concern because they are readily respirable and more easily retained in the deep recesses of the lungs, causing adverse health effects. Due to the risks associated with exposure to DPM, occupational exposure limits have been established in some countries. The coal mining industry is one particular area where the use of diesel-powered machinery is on the increase, due to the development of new more efficient technologies. It is believed that elemental carbon (EC) is the most reliable overall measure of exposure to diesel exhaust.[2] However, current analytical methods can not effectively distinguish between the EC from coal dust and EC from DPM. This makes it virtually impossible to monitor occupational exposure levels to DPM in a coal mine. Diesel engine emissions, control and detection are discussed more thoroughly in chapter 1.

The carbon from DPM and the carbon from coal dust are expected to have different structures due to their different modes of formation. Raman spectroscopy has previously been used to determine the particle size and structure of a wide variety of different carbonaceous materials.[3-7] So, this method may have the potential to distinguish between EC from coal dust and EC from DPM, in mixtures. The principal aim of the present work was to develop a Raman spectroscopy-based method to analyse carbon-based particulates in mixtures produced from DPM and coal dust in coal mines. Spectra of particulates from the different sources are very similar and it is non-trivial to characterise quantitatively each separate carbon type, let alone separate them in a mixture. It is therefore necessary to follow carefully designed and controlled experiments in order to achieve the objectives. These experiments will include:

1) Exploration of the detailed spectral characteristics of each particulate type and the sensitivity of the Raman spectra to such variables as laser power, exposure time and microscope objective.

2) Performing a feasibility study on the Raman spectra of the individual materials. A comparison of Raman spectra of carbon particles from coal dust and DPM, using a qualitative principal component analysis (PCA) model, will be employed. The results form this model

can be utilised to determine if there is a significant difference between the coal dust and the DPM spectra for it to be a potential method for distinguishing between coal dust and DPM in mixture samples

3) Calibration of each source separately against known (gravimetrically determined) standards, collected under known conditions.

4) Production of a set of mixture standards with know amounts of coal dust and DPM. These standards can then be analysed by Raman microscopy and the resultant spectra incorporated into a multivariate chemomectric model such as partial least squares (PLS).

5) Once a satisfactory model has been developed it can be used to determine the amounts of DPM and coal dust in field samples (unknowns) from a coal mine.

The DPM and coal dust samples are also be studied by XPS, FTIR, TGA, XRF, and SEM, to give complementary information and a more thorough characterisation of the samples being analysed by Raman microscopy. XPS is used to determine the elemental composition and get an estimation of the carbon bonding hybridisation of the surface layer of the samples, both of which are unavailable from a Raman spectroscopy analysis. FTIR is used to give complementary and additional information on the organic functional groups of molecules present in the samples. TGA is used to estimate the different amounts of volatile organic compounds present in the DPM and coal dust. XRF is used to determine the elemental composition of the coal dust sample bulk and is compared to the surface elemental composition, from the XPS analysis. Finally, SEM images are collected to get an idea of the distribution of the samples on the quartz fibre filters, the substrate on which they were collected. The principles of Raman spectroscopy and the alternative experimental techniques are explained in chapter 2. The results from the alternative techniques are discussed in chapter 4. Raman spectroscopy of graphitic and diamond like carbon (DCL) materials is discussed in chapter 3. The results of the Raman analysis of the carbonaceous samples, analysed in the present work, are presented in chapter 5.

References

1) B. Rudell, U. Wass, P. Horstedt, J. Levin, R. Lindahl, A. Sunesson, U. Rannung, Y. Ostberg, Occupational Environmental Medicine, **56**, 1999, 222
2) B. Cantrell and W. Watts, Applied Occupational Environmental Hygiene, **12**, 1997, 1019
3) H. Scheibe, D. Drescher, P. Alers, Fresenius' Journal of Analytical Chemistry, **353**, 1995, 695
4) G. Compagnini, O. Puglisi, G. Foti, Carbon, **35**, 1997, 1793
5) A. Ramirez, R. Sinclair, Surface and Coatings Technology, **94**, 1997, 549
6) Y. Wang, D. Alsmeyer, R. McCreery , Chemistry of Materials, **2**, 1990, 557-563
7) N. Everall, J. Lumsdon, Journal of Materials Science, **26**, 1991, 5269

Chapter 1

Diesel Engine Emissions Control and Detection

1. Diesel engine emissions, controls and detection

1.1. Introduction

In 1892 the German engineer Rudolph Diesel developed an alternative engine type from the standard petrol engine, which had been introduced 30 years previously. This became known as the diesel engine and was capable of spontaneous combustion of liquid fuel without requiring spark ignition. This engine had low efficiency and was not widely used until it was redeveloped in the 1920's. The engine's use rapidly increased due to its high reliability, robustness and fuel economy. In the 1950's diesel engines became the conventional power unit used in the U.S. railway, heavy construction, mining and farming industries. An increase in global popularity of diesel engines soon followed. Although diesel engines are efficient and reliable they are not as popular for use in commercial vehicles due to being generally noisier and their emissions being more odorous than their petrol counterparts. However, diesel fuel and engine technology are constantly being improved resulting in ongoing reductions in emissions and noise. Therefore a continued growth in their use is expected.[1-3]

Gas phases such as CO_2, hydrocarbons (HC), NO & NO_2 (NO_X) are the main emissions for petrol engines. However, particulate matter (PM) is the main constituent of the emissions from diesel engines being 20-100 times greater than petrol. There are also higher levels of NO_X emitted from diesel engines. A recent American study[4] concluded that in California diesel engines were responsible for 30% of NO_X and 65% of PM in the air, but only account for 2% of the on-road population. A significant proportion of diesel particulate matter (DPM) has an aerodynamic diameter of less than 1μm, making them readily respirable.[5] Hence, an increase in the use of diesel powered equipment causes concern due to the potential health risk and environmental damage, which can occur as a result of exposure to diesel emissions. This has prompted numerous studies involving the characterisation of diesel emissions and investigations into the possible health effects from exposure to them. Characterising diesel emissions has involved studies on the composition of diesel emission products and estimation of diesel particulate matter

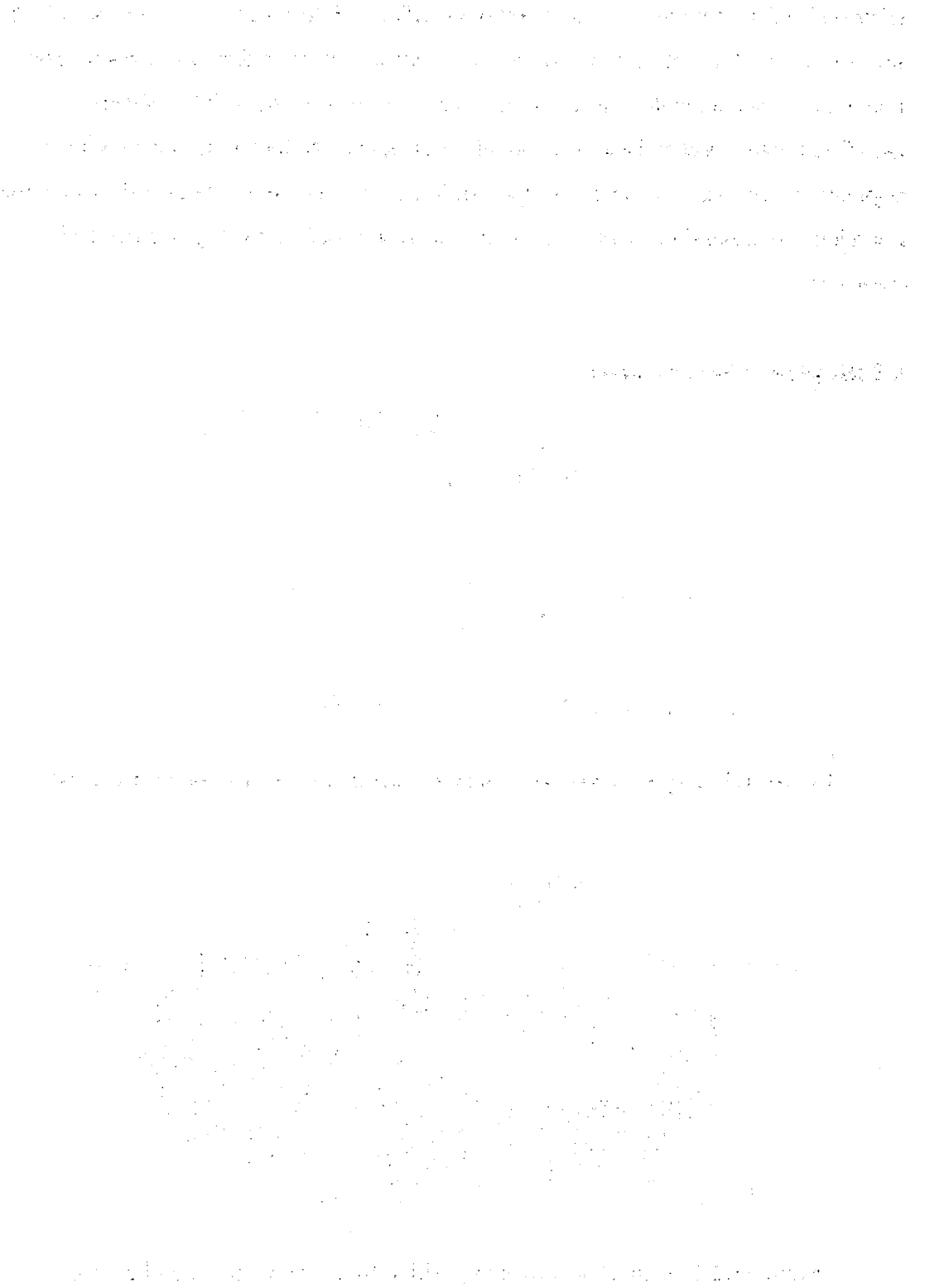

(DPM) size distributions, in an attempt to identify possible harmful compounds and the levels of respirable particles. Investigations of adverse health effects include studies on both humans and animals. These compare the prevalence of the health problems, associated with diesel emissions, in populations exposed to high levels of emissions to populations who are considered unexposed. In this chapter we will discuss diesel engine emissions, their possible health effects and the methods of controlling and detecting exposure.

1.2 Diesel emission products:

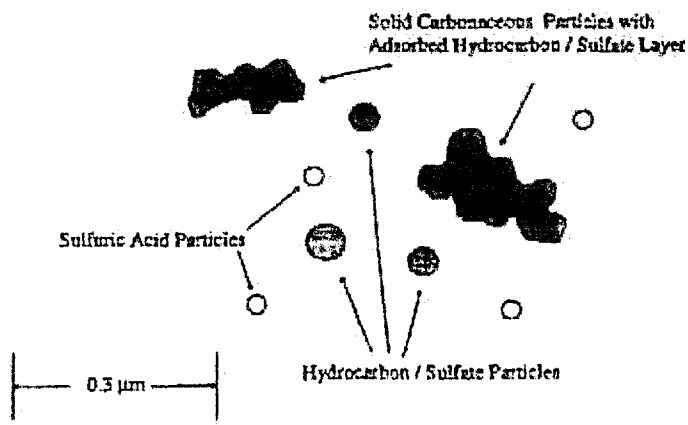

Figure 1.2.1: Typical composition and structure of engine exhaust particles[2]

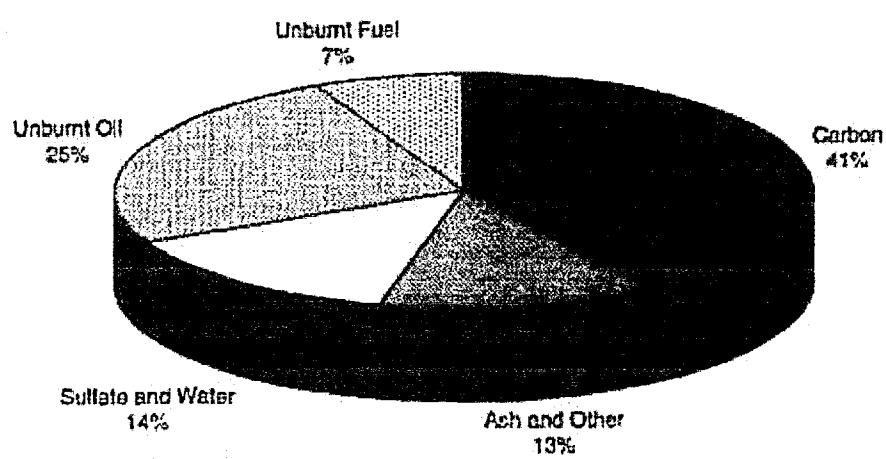

Figure 1.2.2: Typical particle composition for a heavy-duty diesel engine[2]

Diesel exhaust contains products of complete air and carbon combustion, CO_2, N, H_2O, and products of incomplete combustion CO, NO, NO_2, hydrocarbons (HC); partially oxidised HCs such as aldehydes, ketones, phenols, PAH's such as fluroene, fluoranthene, pyrene, naphthalene, phenanthrene and anthracene.[5-8] Unburned fuel and evaporated lube oil are major contributors to the hydrocarbon content of diesel emissions. Sulphur present in the fuel is mostly oxidised to SO_2 but some is oxidised to SO_3 which in turn leads sulphuric acid and sulphates.[9-11] DPM is mainly sub-micrometer agglomerates of spherical particles. They principally consist of carbonaceous material with two components; elemental carbon (EC) (typically 40-60%) and organic carbon (OC) in the form of hydrocarbons and hydrocarbon derivatives adsorbed or condensed on the surface of the EC particles.[1,12-14] Trace metals and metal ash, such as aluminium, iron, titanium and barium, have been observed. Water-soluble ionic species that have been detected include sulphate, nitrate, chloride, ammonium, sodium, potassium, magnesium and calcium. These originate from organometallic additives to the lubricating oil, trace elements in fuel and wear and corrosion of engine and exhaust systems.[10-12] Typical particle compositions and structures are shown in figures 1.2.1 and 1.2.2

1.3 Particle size distribution

Several methods have been used to estimate the size distributions and numbers of DPM. These include differential mobility particle sizers (DMPS), aerodynamic particle sizers (APS), optical particle counter (OPC) and micro-orifice uniform deposit impactors (MOUDIs).[10,15,16] A typical engine exhaust size distribution showing both mass and number weightings is shown in fig. 3. It has been observed that over 80% of particle mass is in the 0.05 to 1μm aerodynamic diameter range with the peak of mass size distribution at approximately 0.1μm. This is known as the accumulation mode. Combustion generated particles are typically agglomerates of primary particles that have diameters of 0.015 to 0.04μm. The accumulation mode consists of carbonaceous agglomerates and adsorbed organic material. The agglomeration is due to the relative movement and resulting coagulation of the spherules and their small clusters. The dominating mechanism producing agglomerates in diesel exhaust is thought to be Brownian movement.

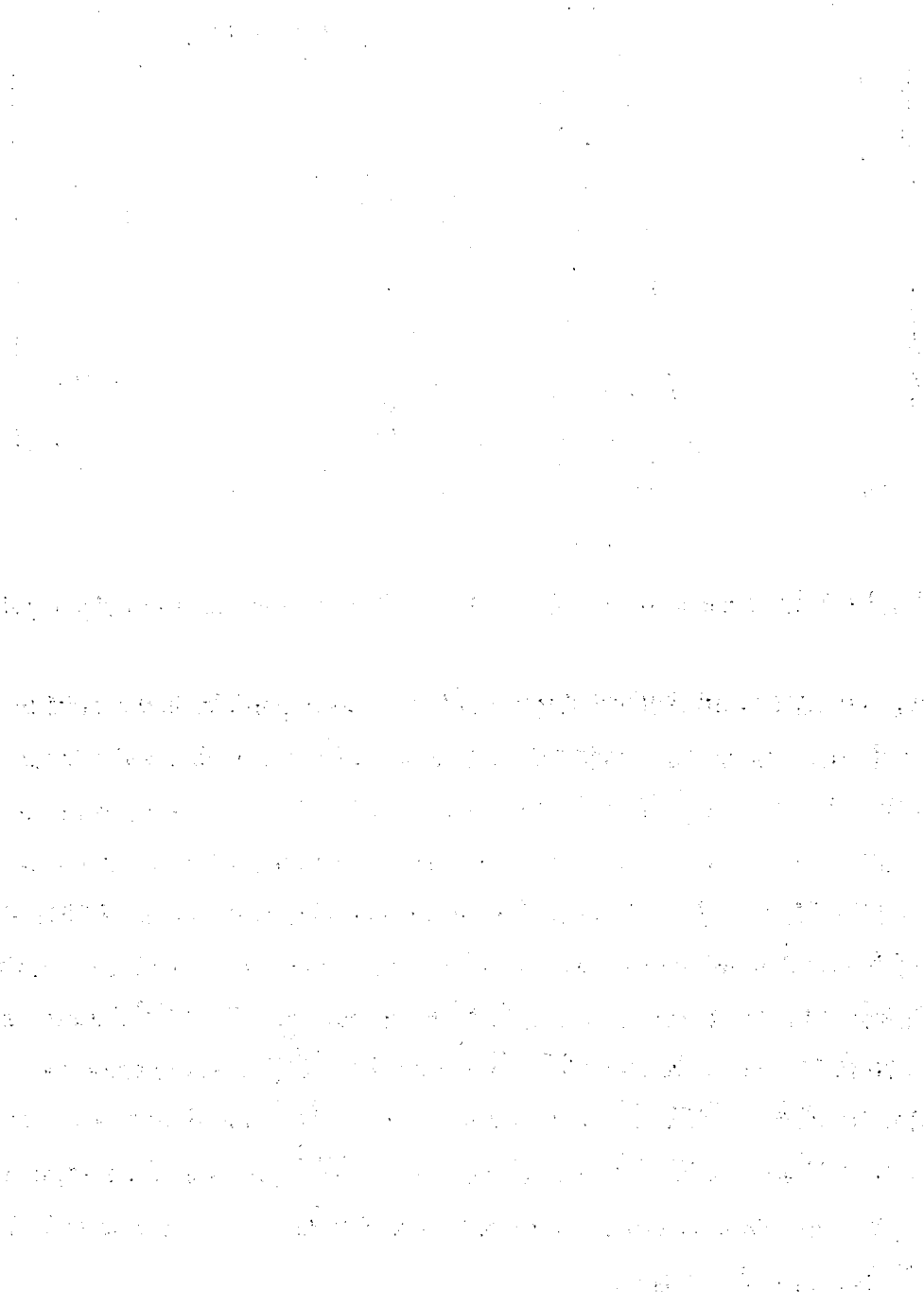

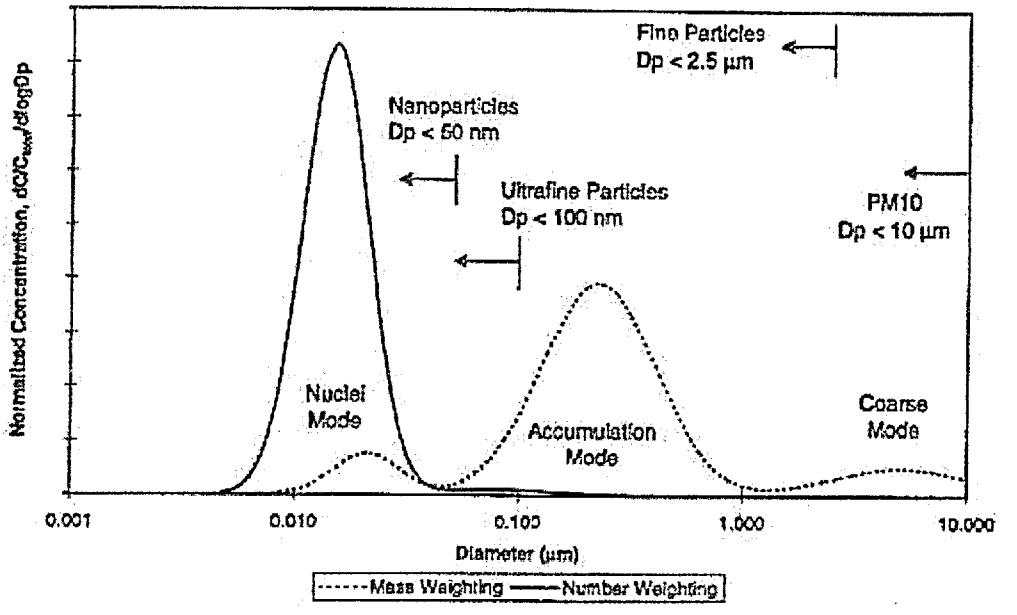

Figure 1.3.1: Typical engine exhaust size distribution, both mass and number weighting shown[25]

The nuclei mode (shown in figure 1.3) typically consists of particles in the 0.005 to 0.05µm diameter range. This mode usually consists of volatile organic and sulphur compounds that form during exhaust dilution and cooling, and may also contain solid carbon and metal compounds. It can contain from1-20% of the particulate mass but up to 90% of the particle number. The coarse mode with particles over 1µm has 5-20% of the particle mass and originate from accumulation mode particles that have been deposited on cylinder and exhaust system surfaces and later re-entrained.[10-13,17,18,19] Further studies have been carried out on the metallic and ionic species of DPM.[4] Aluminium, for example, has been observed to have two modes the 1st with a mass distribution peak at 0.1µm and a 2nd smaller one between 0.3 and 0.4µm. Ionic species; sodium, ammonium and sulphate also show a bimodal mass size distribution the first at approximately 0.1µm and a 2nd between 0.3 and 1µm.

1.4 Factors affecting diesel exhaust emission products and size distributions

Driving conditions, inspection and maintenance of the vehicle, fuel, engine type, after treatment devices such as catalytic converters and particle traps, operator habits, duty cycle, lube oil consumption, ambient air temperature and humidity all affect diesel emission products.[4,19-24]

NO_X occurs at high temperatures where the air/fuel mixture is about 1:1. HC, CO and PM increase under conditions of incomplete combustion such as lower combustion temperatures or poor fuel and air mixing. An inverse correlation between NO_X and PM emissions is the major challenge to lowering diesel emissions. Addition of oxygenates to the fuel can decrease PM but increases NO_X. Different altitudes and humidity can affect engine efficiency and emissions products. Higher altitudes and humidity result in less oxygen in the air intake for mixing with the fuel in the combustion chamber. This results in an increase in PM, CO and HC but a decrease in NO_X. Lower aromatic content can lead to a decrease in both NO_X and PM.[11,4] A reduction in sulphur content in the fuel can also reduce the amount of particulate matter. The use of alternative fuels such as biodiesel, a fuel that can be made from renewable biological sources such as vegetable oils or animal fats, has been reported to result in a reduction of PM emissions, compared to petroleum diesel.[25] VOC and sulphur compounds in the gas phase at exhaust temperatures are transformed to PM by nucleation and adsorption as the exhaust dilutes and cools. The majority of these particles are adsorbed onto EC agglomerates but they can also form their own particulates, with nanopartical diameters, by homogenous nucleation. The reduction of carbon emissions without reducing VOC can result in an increase in nanoparticle emissions because they have less carbonaceous agglomerates to adsorb onto.[18] Catalytic converters can reduce total particulate emissions by up to 50% however DPM collected after catalytic conversion has a narrower size distribution and a higher percentage of particles smaller than 0.1μm.[12,15]
In one study OC: EC was 0.43 without catalytic conversion and 0.33 with. This suggested that catalytic conversion removes OC in some preference to EC.[13] Two possible reasons for this are as follows:

1) Smaller particles having lower OC to EC ratios penetrate the converter more easily
2) The converter removes condensable organic gases from the exhaust, hence reducing the amount of organics transported to the particulate phase after the converter.

PM emissions from heavy-duty engines are greater than light duty engines but have no significant difference in their size distributions. Newer more efficient engines use turbocharged fuel injection, which helps reduce total emissions. However, this type of engine has been found to produce emissions with a higher percentage of fine particles than an engine with naturally aspirated air inhalation. In some instances these more efficient engines emit around 4 times more particles than the older engines.[11,15]
In summary, the use of catalytic converters, particle traps, high-pressure injection systems or turbo-charging systems and fuel additives has resulted in the gradual reduction of total PM but increased the number of smaller particles.

1.5 Health effects associated with diesel emission exposure

Diesel emissions have been classified as 'a potential occupational carcinogen' by NIOSH since 1988 and as 'a probable occupational' carcinogen by the IRAC and the EPA since 1989 and 1990 respectively.[20,26] Numerous studies have been carried out which suggest that long-term exposure to high levels of diesel emissions can promote lung cancer.[2,19,21,27,28] The risk is estimated by comparing the occurrence of lung cancer in an exposed population with that of a population considered to be unexposed. In most cases the risk has been estimated to be 1.2 to 1.5 times greater for the exposed population. However, many of the studies are considered to be unreliable because the risks have been estimated by inadequate methods, poor experimental design and risk figures possess considerable uncertainties. A number of studies failed to account for contributions from confounding factors such as smoking habits, age, non-diesel particulate exposure, socioeconomic and dietary effects. In certain cases vital information about the subjects such as full employment records and medical histories were not taken into account.

Experiments have been carried out on rats, which resulted in an increase in the development of lung tumours. Due to the short life of animals it was necessary to give high exposures over a short period of time to the rats. It has been argued that the development of lung tumours occurred due to overwhelming the defence mechanisms of the rats with such high doses, rather than a mutagenic effect caused by the emissions. Similar tests were carried out on mice and guinea pigs with negative results. Also, it is generally accepted that such studies on animals can only be used as an indication of cancer risk in humans because many animal species have an increased incidence of certain malignant tumours that do not occur in man.[2,22,26,29] Although there is no conclusive evidence to prove that DPM causes lung cancer it has received its classification as a probable carcinogen due to the presence of some organic compounds and in particular PAHs and nitro-PAHs which have been unquestionably proven to be genotoxic carcinogens. Phenanthrene, metylphenanthrene, fluroanthrene and benzo[α]pyrene are all effective mutagens. Benzene, formaldehyde and butadiene are strong carcinogens, while nitroarenes promote mutagenicity. [19,20,26]

The high number of submicron particles present in diesel emissions also causes concern as the size of a respirable particle determines where it is deposited in the respiratory tract. Submicron particles have a high probability of deposition deeper in the respiratory tract, are not cleared as efficiently from the lungs and may penetrate into the surface tissue more easily. Smaller particles have a larger surface area resulting in them having a larger proportion of adsorbed organic material that may contain mutagens and carcinogens. Therefore exposure to these particles is likely to trigger or exacerbate respiratory diseases.[1,15,10] It has been suggested that the small particles themselves are responsible for tumour response rather than the adsorbed organic material.[10] Further work has been carried out to compare the results of exposing rats to DPM and carbon black which was almost pure carbon with similar particle sizes. Similar results were observed for both the DPM and carbon black, which suggests that cancer may be due to an overwhelming of the rats' clearance system or lung overload. The effects due to the adsorbed hydrocarbons still cannot be ruled out as the overwhelming effects of the particulate may have masked

their effect. Cancer may be due to nongenotoxic mechanisms (no direct interaction with the DNA) at high exposure and perhaps a genotoxic effect at low exposure.[29]
Exposure to diesel emissions can also cause many non-malignant health effects. These may include increased prevalence of cough, phlegm, laboured breathing, wheezing and headache. DPM can exacerbate asthma, bronchitis and other chronic pulmonary diseases. An increase in cardiac and respiratory deaths has been associated with an increase in PM. The gas phase of the emissions can contain CO, NOX, aldehydes and HC, which also contribute to eye, nose and throat irritation.[1,2,23]

1.6 Diesel emission Standards[1,30,,31,32]

1.6.1 Introduction

The countries across the world have different emission standards for different types of diesel engines. These include heavy-duty engines, light dusty engines, off-road engines, locomotives, marine engines and public transport vehicles.
In 1996 the Swedish government even introduced "Environmental Zones" which prohibited the use of old and highly polluting heavy-duty vehicles in town centres, hence improving ambient air quality. However, the only countries to introduce specific occupational health regulations are the USA and Germany. Other countries, including the UK, use these standards as guide when developing methods for estimating occupational exposures. The main points of these regulations are laid out below.

1.6.2 USA Occupational Health Regulations

1.6.2.1 Authorities

Occupational health and safety regulations are set in the USA by two agencies within the Department of Labour:
- Occupational Safety and Health Administration (OSHA) for general occupational environments.

- Mine Safety and Health Administration (MSHA) is responsible for mining.
They make their laws based on recommendations/guidelines from the American Conference of Governmental Industrial Hygienists (ACGIH), which establish the maximum ambient concentration of toxic chemical substances.

1.6.2.2 Exposure Limits for Gases

Exposure limits for some of the gaseous pollutants present in diesel exhaust are listed in Table 1.2.1 The exposure limits set by the different organisations are as follows:
OSHA = Permissible Exposure Limits (PEL) (legally enforceable)
MSHA = TVL (legally enforceable)
ACGIH = TVL (recommendations)
All limits are 8 hour time weighted averages (TWA), unless marked as ceiling values.

Substance	OSHA PEL	MSHA TVL	ACGIH TVL
CO	50	50	25
CO_2	5000	5000	5000
NO	25	25	25
NO_2	(c) 5	5	3
HCHO	0.75	-	(c) 0.3
SO_2	5	5*/2**	2

Table 1.6.1: Exposure limits for gaseous (ppm, TWA, 8 hours)
*- non-coal mine
**- coal mine
(c)- ceiling value

1.6.2.3 Exposure Limits for Particulates

Legal exposure limits for DPM have been adopted by MSHA for underground non-coal mines. Currently, there are no legal limits for DPM in general occupational settings in the USA. DPM exposure limits have been proposed by ACGIH but not yet been adopted.

1.6.2.4 Non-Mining Environments

In a 2001 report on intended changes the ACGIH recommended a TLV of 0.02mg/m^3 for diesel exhaust particulates measured as EC. The ACGIH first recommended a TLV of 0.15mg/m^3 for DPM in 1995 since then DPM has remained on the list of intended changes but the TLV has never been finalised.

1.6.2.5 Underground Mining

Jan 19th MSHA published final regulations for metal/non-metal underground mines and coal mines.
The metal/non-metal mine rule adopts exposure limits for DPM. No limits have been introduced for coal mines because of no suitable method for measuring DPM in the presence of coal dust.
The limit for metal/non-metal mines is to phase in over 5 yrs starting July 19th 2002 they must have DPM levels lower than 400μg/m^3. Effective from Jan 19th 2006 that level must be reduced to 160μg/m^3.
DPM is defined as total carbon (TC) EC + OC but excludes metal ash or sulphates.
DPM is measured as total carbon.

1.6.2.6 Mining Diesel Engine Regulations

MSHA have set other levels in order to protect workers from diesel emissions.
All diesel engines used in underground mines require a formal MSHA approval.

1.6.2.7 Coal Mining Regulations

In January 2001 a specific engine emission limit of 2.5g/hr of DPM was set for both permissible and non-permissible equipment, to be phased in over the next 48 months. There is an interim limit of 5g/hr for non-permissible machines but not for permissible machines. This necessitates the use of particulate traps in older equipment because old engines with no after-treatment can't meet this requirement.

1.6.2.8 Diesel Fuel Requirements

Coal mining regulations adopted in 1997 introduced the following diesel fuel requirements:
Maximum sulphur content of 500ppm wt., flashpoint above 100°F, fuel additives have to be EPA registered.

1.6.3 German Occupational Health Regulations

1.6.3.1 Regulatory Authorities

Occupational health and safety (OHS) standards are based on the federal "Chemicals Act" (getsetzliche Grundlage "Chemikaliengesetz") and on a federal government rule, which addresses various issues related to dangerous substances.
Exposure limits in the workplace are proposed by a special scientific board of DFG (Deutsche Forschungsgemeinschaft). Then discussed with all stakeholders within the MAK-Kommission. Final limits are established by the German Ministry of Labour (Bundesministerium fur Arbeit – BMA) through TRGS regulations (technische Regeln fur Gefahrstoffe).

OHS standards are enforced by occupational insurance organisations called Berufsgenossenschafen. There are 35 Berufsgenossenschafen for different areas of industry. These insurance organisations perform various functions, such as air quality measurements at the site, to ensure compliance with the regulations.
All Berufsgenossenschafen have a common institution BIA (Berufsgenossenschaftliches Intitut fur Arbeitssicherheit) which performs many functions, including regular publication of all OHS limits and rules. The above organisation extends to all occupational health environments with the exception of coal mining. Until the year 2002 the OHS matters in the coal mining are the responsibility of state (Land) mining authorities called Oberbergbehorde.

1.6.3.2 Exposure limits

There are 2 types of exposure limit and once established they are both legally binding:
-MAK (Maximale Arbeitsplatzkonzentration) max conc of a substance in the ambient air in the workplace, which has no adverse effect on workers health.
-TRK (Technishe Richtkonzentration) max conc of a substance in the ambient air in the workplace that can be achieved using technically available measures.
Table 1.6.2: summarises the exposure limits for the major diesel exhaust pollutants

Substance	ppmv	mg/m^3	Category*
CO	30	33	4
CO_2	5000	9000	4
NO	25	30	-
NO_2	5	9	1
HCHO	0.5	0.6	1
SO_2	2	5	1
Diesel Particulates (EC) tunnelling and non-coal mining	-	0.3^+	4
Diesel Particulates (EC) other applications	-	0.1^+	-

Table 1.6.2: MAK exposure limits for diesel exhaust pollutants.
* - All values in the table have to be met as work-shift time weighted averages. The following short-term exposure categories apply: 1-ceiling value, not to be exceeded at any point in time; 4- ceiling value = 4x the limit value
+ - TRK limit

The diesel particulate emissions (DME – Dieselmotorenemissionen) are defined as elemental carbon (EC). Diesel particulates are defined as "probably carcinogenic for humans". This classification requires that the "best available technology" (BAT) is used for emission reduction.

1.6.3.3 Diesel Engine Regulations

Specific rules in regards to the use of diesel engines in occupational health environments were first introduced on 30/04/1993.
These introduced a general TRK of $0.2mg/m^3$ for diesel particulates and a limit of 0.6mg/m3 for underground non-coalmines. The particulates were defined as total carbon (EC + OC) and determined by a coulometric analysis.

The regulations were modified in 1996 with the limits reduced to 0.1mg/m3 and 0.3mg/m3 respectively. The definition for diesel particulate was changed to elemental carbon. The measurement involves a two stage thermal analysis with coulometric identification. Coal mines are exempted from the limits due to difficulties in differentiating between diesel particulate and coal dust. The TRGS also set several different requirements for engines used in buildings, underground or other enclosed areas. These additional provisions have to be also observed in coal mines. The following are some of the requirements:

- Diesel engines that are entirely or partly operated in enclosed spaces or underground must be equipped with particulate traps, provided such traps are technically feasible.
- The particulate traps must achieve at least 70% total gravimetric filtration rate, as measured on the UBA (Umwelt Bundesamt) engine cycle.
- Diesel engines must undergo periodic measurements of smoke number and CO level.
-Diesel traps are required in addition to the TRK exposure limit and the efficiency of most traps used is better than the required 70%. Resulting in the average particulate exposure in tunnels being well below 0.1mg/m^3 which is lower than the TRK of 0.3.

1.6.3.4 Future Directions

The general trend of a reduction in the total mass of particular matter emissions but an increase in the number of fine particles and the health risk associated with these particles causes concern. Therefore it is expected that future regulations will include limits for the number of diesel particulates, in addition, or in place, of the mass concentrations that are used today.

1.7 Methods for determining DPM levels in mines

With the emergence of regulations pertaining to the occupational exposure limits of DPM it is necessary to develop methods for determining its levels in the workplace. It is believed that elemental carbon (EC) is the most reliable overall measure of exposure to diesel exhaust. This is not only because it is a large proportion of DPM, usually 40-60%,

but also because it is difficult to select an extractable organic compound or class of compounds, as a reliable indicator of exposure.[33] The organic component may be chemically complex and highly variable in composition. It may also be present in low concentrations and be subject to interference from similar compounds. A method has been developed in Germany where the organic carbon is firstly desorbed by heating the sample in a nitrogen atmosphere. This step is followed by heating the sample again in an oxygen atmosphere that converts the carbon present into CO_2, which is analysed by applying coulometry, giving an estimation of the amount of DPM present. Unfortunately, this method cannot be used in coal mines because of interference from the high levels of carbon present in coal dust.[32]

Mechanically generated aerosols generally contain particles greater than 1μm in diameter with only a small fraction less than 1μm in size. However, the vast majority of diesel particulates are less than 1μm in size. Attempts have been made to use size-selective sampling, which separates the larger coal dust particles from the DPM. The sub-micron particulate matter is then determined gravimetrically or analysed by a thermal technique similar to the one described above. The accuracy of this procedure is limited by the fact that there are some diesel particulates and coal dust particles with similar sizes which may result in one component being confused for the other. Aerosols from other sources can also be mistaken for DPM.[33]

Some of the factors which can contribute to the levels of DPM that coal mine workers are exposed to include; fuel quality, maintenance of vehicles, number of vehicles, enclosed cabs on the vehicles to prevent exposure, fleet management/working practices, length of work shift, quantity of ventilating air being used and efficiency of applied control technology. The MSHA has recently developed two different models, for estimating DPM levels in mines, which incorporate all these factors. The major difference between the models is the use of different methods for determining the amount of DPM emitted in the mine. There is a poor agreement between each method, with differences of up to 40% reported. These models can be useful for determining the effects of applying different control technologies but are too inaccurate for determining real DPM exposures in mines.

[22] There is still no sufficiently reliable method at present for determining DPM in coal mines.

References

1) B. Rudell, U. Wass, P. Horstedt, J. Levin, R. Lindahl, A. Sunesson, U. Rannung, Y. Ostberg, Occupational Environmental Medicine, **56**, 1999, 222
2) W. Morgan, R. Reger and D. Tucker, Annals of Occupational Hygiene, **41**,1997, 643
3) Pioneers of Science and Discovery: Rudolf Diesel and the Diesel Engine J. MoonPriory Press Limited, 1974, 1-94
4) J. Yanowitz, R. McCormick, M. Graboski, Environmental Science & Technology, **34**, 2000, 729
5) L. Morawska, N. Bofinger, L. Kockis, A. Nwankwoala, Environmental Science & Technology, **32**, 1998, 432
6) D. Kittelson, M. Arnold, W. Watts, Research report for the University of Minnesota, Department of Mechanical Engineering, Centre for Diesel Research, 1999, 1-64
7) M. Baum, E. Kiyomiya, S. Kumar, A. Lappas, H. Lord, Environmental Science & Technology, **34**, 2000, 2851
8) A. Miguel, T. Kirchstetter, R. Harley, S. Hering, Environmental Science & Technology, **32**, 1998, 450
9) J. Lyyranen, J. Jokiniemi, E. Kauppinen, J. Joutsensaari, Journal of Aerosol Science 1999, **30**, 771
10) M. Kleeman, J. Schauer, G. Cass, Environmental Science & Technology, **34**, 2000, 1132
11) D. Kittelson, Journal of Aerosol Science, 29, 1998, 575
12) V. Kerminen, T. Makela, C. Ojanen, R. Hillamo, J. Vilhunen, L. Rantanen, N. Harvers, A. Von Bohlen, D. Klockow, Environmental Science & Technology, **31**, 1997, 1883
13) S. Bagley, L. Gratz, J. Johnson, J. McDonald, Environmental Science & Technology, **32**, 1998, 1183
14) H. Moosmuller, W. Arnott, C. Rogers, J. Bowen, J. Gillies, W. Pierson, J. Collins, T. Durbin, J. Norbeck, Environmental Science & Technology (in press)
14) W. Kim, S. Kim, D. Lee, S. Lee, C. Lim, J. Ryu, Environmental Science & Technology, **35**, 2001,1005
16) U. Panne, A. Petzold and R. Niessner , Journal of Aerosol Science, **26**, 1995, 659
17) H. Tobias, D. Beving, P. Ziemann, H. Sakurai, M. Zuk, P. McMurry, D. Zarling, R. Waytulonis, D. Kittelson, Environmental Science & Technology (in press)
18) D. Kittelson, I. Abdul-Khalek, EFI Members Conference: "Fuels, Lubricants, Engines, & Emissions" January 18-20, 1999, 1-13
19) R. Westerholm, A. Christensen, M. Tornqvist, L. Ehrenberg, U. Rannug, M. Sjogern, J Rafter, C. Soontjens, J. Almen, K. Gragg, Environmental Science & Technology, **35**, 8, 2001, 1748
20) B. Cantrell and W. Watts, Applied Occupational Environmental Hygiene, **12**, 1997, 1019
21) F. Nyberg, P. Gustavsson, L. Jarup, T. Bellander, N. Berglind, R. Jakobsson, G. Pershagen, Epidemiology, **11**, 2000, 487
22) Diesel Exhaust: A Critical Analysis of Emissions, Exposure, and Health Effects K. Nauss, Summary of a Health Effects Institute (HEI) Special Report, HEI Diesel Working Group, 1997, 1-8

23) R. Haney, G. Saseen, Mining Engineering, **April**, 2000, 60
24) F. Brear, The Science of the Total Environment **235**,1999, 421
25) W. Wang, D. Lyons, N. Clark, M. Gautam, P. Norton, Environmental Science and Technology , **34**, 2000, 933
26) S. Qu, J. Leigh, H. Koelmeyer, N. Stacey, Biomarkers, **2**, 1997, 95
27) J. Weeks, American Journal of Industrial Medicine 34, 1998, 203
28) T. Coburn, Inhalation Toxicology, **12(S2)**, 2000, 23
29) Shun-Hua Ye, Wei Zhou, Jian Song, Bao-Cheng Peng, Dong Yuan, Yuan-Ming Lu, Ping-Ping Qi, Athmospheric Environment, **34**,1999, 419
30) USA Occupational Health Regulations, www.dieselnet.com/standards/usa/ohs.html, 2001, 1-3
31) Germany Occupational Health Regulations, A. Mayer, www.dieselnet.com/standards/de/ohs.html, 2001, 1-4
32) D. Dahmann, H, Bauer, Applied Occupational and Environmental Hygiene, **12**, 1997, 1028

Chapter 2

Experimental Techniques

2 Experimental techniques

2.1 Raman Spectroscopy

2.1.1 Introduction and History

Brillouin in 1922[1] and Smekal in 1923[2] initially predicted the Raman effect. However, Raman and Krishnan made the first experimental observation in 1928[3]. They discovered that the wavelength of a small fraction of the radiation scattered by certain molecules differed from that of the incident beam and furthermore that the shifts in wavelength depended on the chemical structure of the molecule responsible for the scattering. The level of scattered light is very weak, being much less intense than the incident radiation. The sources used in early experiments were sunlight and mercury lamps, which required very long collection times to get an appreciable signal. This reduced interest in the technique and it didn't become widely used until the development of lasers in the late 50's and early 60's. They emitted an intense monochromatic light source, which was ideal for Raman analysis. Further technological advances since then have improved the technique's sensitivity (and hence popularity), and a similar trend is expected in the future.

2.1.2 The Raman Effect

When a substance is irradiated with a monochromatic beam of laser light most of the light is transmitted or adsorbed, 1 to 5% is reflected and a very small quantity is scattered. The majority of the scattered photons (>99%) are elastically scattered, with no change in the frequency. This is called Rayleigh scattering. A very small proportion (<0.1%) of the incident photons are inelastically scattered with a gain or loss in energy. This is called Raman scattering. The scattered photons that are higher in frequency than the incident radiation are called anti-stokes Raman scattered photons and the photons lower in frequency are called stokes Raman scattered phonons.

2.1.3 Classical Theory of Raman Scattering[4]

When a molecule is placed in an electric field, its electrons are displaced in relation to its nuclei. This results in an induced dipole moment, μ, which is proportional to the electric field strength, ε, and the polarisability, α, of the molecule.

$$\mu = \alpha\ \varepsilon \tag{2.1.1}$$

The magnitude of μ is dependent on the ease to which the electron cloud is displaced relative to its nucleus. An alternating applied electric field produces a fluctuating dipole moment at the same frequency. The oscillating electric field may be expressed as:

$$\varepsilon' = \varepsilon \cos 2\pi t \nu_0 \tag{2.1.2}$$

where ε = amplitude

and ν_0 = angular frequency of the radiation

The induced dipole scatters radiation of frequency υ_o i.e. Rayleigh scattering.

If we consider a diatomic molecule that vibrates with a frequency of, υ_{vib}, performing simple harmonic vibrations, then a coordinate q_{vib} along the axis of vibration at time, t, is given by:

$$q'_{vib} = q_0 \cos 2\pi \upsilon_{vib} t \tag{2.1.3}$$

If the vibration leads to a change in polarisability, the polarisability may be written as:

$$\alpha' = \alpha^0 + \left(\frac{\partial \alpha}{\partial q_{vib}}\right)_0 q'_{vib} \tag{2.1.4}$$

Substitution of Equation **(2.1.3)** in Equation **(2.1.4)** yields:

$$\alpha' = \alpha^0 + \left(\frac{\partial \alpha}{\partial q_{vib}}\right)_0 q_0 \cos 2\pi \upsilon_{vib} t \qquad \textbf{(2.1.5)}$$

If the incident radiation of frequency υ_0 interacts with the molecule then from Equation 1 and 2:

$$\mu' = \alpha E = \alpha \varepsilon^0 cos 2\pi \upsilon_0 t \qquad \textbf{(2.1.6)}$$

Substitution of Equation **(2.1.5)** in Equation **(2.1.6)** yields:

$$\mu' = \alpha^0 \varepsilon^0 \cos 2\pi \upsilon_0 t + \left(\frac{\partial \alpha}{\partial q_{vib}}\right)_0 \varepsilon^0 q_0 cos 2\pi \upsilon_{vib} t \cos 2\pi \upsilon_0 t \qquad \textbf{(2.1.7)}$$

Equation **(2.1.7)** may also be written as:

$$\mu' = \alpha^0 \varepsilon^0 \cos 2\pi \upsilon_0 t + \left(\frac{\partial \alpha}{\partial q_{vib}}\right)_0 \frac{\varepsilon^0 q_0}{2} \left[cos 2\pi (\upsilon_0 - \upsilon_{vib}) t + cos 2\pi (\upsilon_0 - \upsilon_{vib}) t \right] \qquad \textbf{(2.1.8)}$$

The first term describes Rayleigh scattering and the remaining terms describe Raman scattering. Therefore for Raman scattering to occur there must be a change in the polarisability during any given vibration i.e.

$$\left(\frac{\partial \alpha}{\partial q_{vib}}\right)_0 \neq 0 \qquad \textbf{(2.1.9)}$$

2.1.4 Quantum Mechanical Theory[4]

This theory considers that the vibration energy of a molecule can be quantised. Photons of light of frequency, υ, can be scattered inelastically or elastically, by a molecule. Each vibration has a characteristic energy of E_{vib}.

$$E_{vib} = h\nu(\mathrm{v} + 1/2) \text{ (For a Simple Harmonic Oscillator)} \qquad \textbf{(2.1.10)}$$

Where v is the vibrational quantum number that can take values 0, 1, 2...etc.
When Raman scattering occurs, a molecule can lose or gain energy. When a molecule loses energy, ΔE, the photon is scattered with energy $h\nu + \Delta E$ and when a molecule gains energy the photon will be scattered with energy $h\nu - \Delta E$.
The quantum mechanic diagram for Raman and Rayleigh scattering is shown in fig. 2.1.1

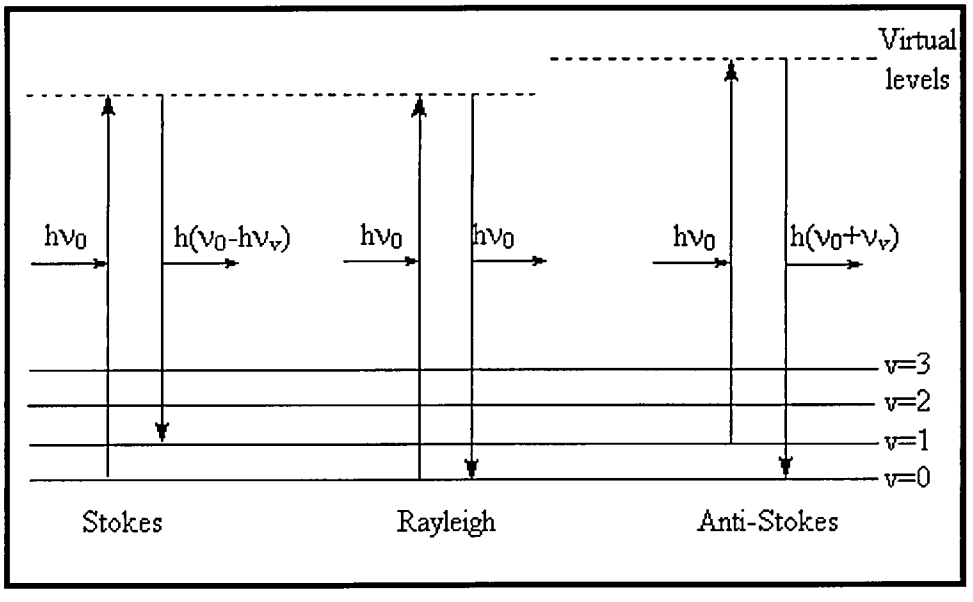

Figure 2.1.1: Energy level diagram for Raman and Rayleigh scattering effects by quantum theory

According to the Boltzmann distribution law, the ratio of the number of molecules (N_i) in state i, having energy E_i, to the number of molecules (N_j) in state j, having energy E_j, at thermal equilibrium, is given by:

$$\frac{N_j}{N_i} = \frac{g_j}{g_i} e^{-\left(\frac{Ej-Ei}{k_B T}\right)} \qquad \textbf{(2.1.11)}$$

g_i and g_j are the degeneracies of the two states i and j.

At ambient temperature (from equation 2.1.11) the number of molecules in the ground state N_i will be greater than that of the excited state N_j. Since the intensity of a transition depends on the population of molecules in the state corresponding to the starting point of the transition, the Stokes line intensity of a molecule will be greater than that of the anti-Stokes line, at ambient temperature. As a result of this, Raman spectroscopy is mainly carried out using Stokes scattering.

2.1.5 Raman Selection Rules and Intensities

There are 3N-5 normal modes of vibration for linear molecules and 3N-6 for non-linear molecules. However, not all these vibrations will be Raman active. For a vibration to be active there must be a change in the polarisability during the vibration.
The number of allowable vibrations for a molecule can be predicted theoretically by applying group theory.[5,6]

The intensity of scattered light is proportional to the fourth power of frequency of the incident radiation (ν_0):

$$I_{(scat)} \propto (\nu_0 - \nu_{vib})^4 \qquad \textbf{(2.1.11)}$$

Raman line intensities are proportional to:

$$\frac{(\nu_o - \nu_{vib})4}{(1 - e - Ei / KT)} \sigma(\lambda) I \qquad \textbf{(2.1.12)}$$

Where λ is the wavelength of the incident radiation, $\sigma(\lambda)$ is the Raman cross section, I is the radiation intensity, $\exp(-E_i/kT)$ is the Boltzmann factor for state I, and C is the analyte concentration

Generally, when a molecular vibration has a large IR dipole moment $\left(\frac{\delta\mu}{\delta q} \right)$ the Raman polarisability $\left(\frac{\delta\alpha}{\delta q} \right)$ is small and vice versa. Many vibrations are either strong in the infrared or Raman, but not both. Although this is not always the case due to some exceptions it is still a good "rule of thumb". Due to these differences in the selection rules between Raman and IR it is important to acquire both an IR and Raman spectrum (where possible) to have complete vibrational information on the target species. Because of this Raman and IR are said to be complementary, not competitive, techniques.

2.1.6 Challenges to collecting a Raman spectrum

2.1.6.1 Fluorescence

Fluorescence occurs when the incident light excites the species beyond the vibrational energy levels to actual excited electronic states. The species then returns to the ground state by the emission of photons in the visible region. These photons are detected in the same manner as the Raman scattered photons and generate a signal on the detector that is observed as a high background in the Raman spectrum. An energy level diagram for fluorescence is given in figure 2.1.2.

Fluorescence is a major problem that has limited the applications of Raman spectroscopy. As a phenomenon, fluorescence is approximately 10^6 to 10^8 stronger than Raman. Trace impurities, additives, etc may fluoresce so strongly that it is impossible to observe the Raman spectrum of a major component. Also, the sample itself may be inherently fluorescent, dyes for example.[7]

For certain samples, it is not possible to avoid the problem of fluorescence but for others several methods have been developed that have successfully reduced or eliminated this problem. These include heating off the fluorescent causing impurities by leaving the sample under the laser for a period of time, which can be up to several hours, before performing a scan. Also, using different excitation wavelengths, which do not have sufficient energy to excite the species beyond the vibrational energy levels. In the present work the differential burn off of fluorescence causing organic impurities affected the reproducibility of the Raman spectra (chapter 5 section 5.3). This problem was overcome by heat-treating the samples before analysis. So, the heat from the laser had no effect on the fluorescence levels. These are some of the more popular methods for overcoming fluorescence, additional methods are discussed elswhere.[8]

2.1.6.2 Sensitivity

As stated earlier the Raman effect is very weak and when first developed it was impractical to use as a routine analytical technique until the development of intense light sources and detectors with adequate sensitivity. In a Raman instrument the function of the optics and components includes filtering of laser plasma lines, keeping the laser collimated throughout the instrument and preventing the Rayleigh scattered light from being detected. Even with the use of recent technological advances, such as sensitive CCD detectors and more efficient filters, the combined effect of these components still reduces the throughput to 5-10%. This has the effect of dramatically reducing the overall S/N.

The sensitivity of Raman studies is ordinarily limited to concentrations greater than 0.1M. However, enhancement techniques are available. These include Surface Enhanced Raman Spectroscopy (SERS) and Resonant Raman Spectroscopy.

SERS involves obtaining the Raman spectra of samples that are adsorbed on the surface of colloidal metal particles or on roughened surfaces of metals. For reasons that are still

not fully understood, the Raman line intensities are often enhanced by a factor of 10^3 to 10^6. The metals usually used are silver, gold or copper.

Resonance Raman occurs when the exciting frequency approaches that of electronic transitions and the observed spectrum changes dramatically showing an enhancement of intensity of certain vibrational modes. This effect can result in the Raman signal being enhanced by a factor of 10^2 to 10^6. As a consequence, resonance Raman spectra have been obtained at analyte concentrations as low as 10^{-8} M.[9] An energy level diagram comparing resonance Raman and fluorescence is shown in figure 2.1.2.

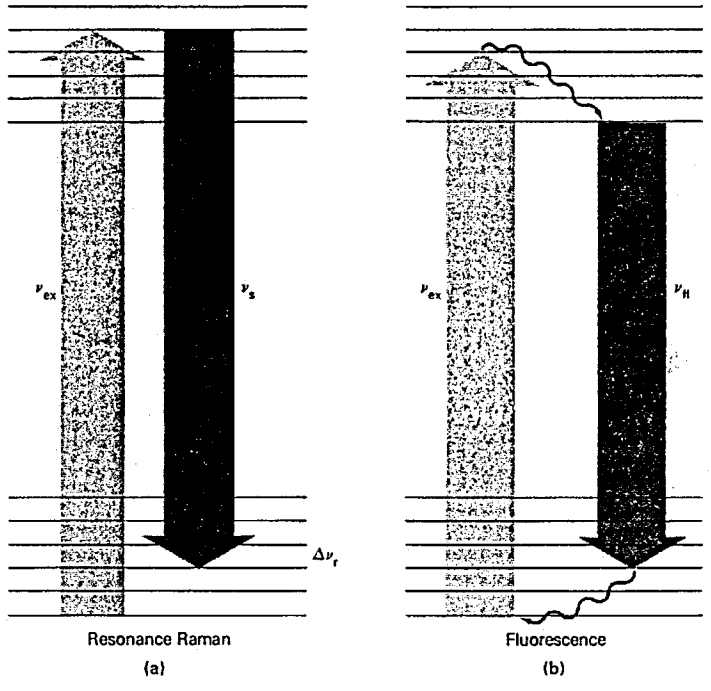

Figure 2.1.2: Energy level diagram for (a) resonance Raman scattering and (b) fluorescent emission. (Radiationless relaxation shown as wavy arrows)[9]

Increasing the strength of the electric field, which is increasing the laser power in this case, will increase the number of Raman scattered photons. Therefore using a high-powered laser should increase the intensity of a Raman spectrum. However, this approach can create problems of its own which are discussed in the next section.

In certain set-ups a laser can be focused onto a 1-2μm spot on a sample. The confinement of laser power to such a small area can result in high laser power density at the sample, which can cause localised heating. This heating may result in the structure of the sample at the analysis area being altered or even burned and converted to a carbonaceous material. It is possible to detect such an occurrence by observing the sample area change to a darker colour compared to the surrounding area. The presence of the amorphous carbon bands in the resulting spectrum is also an indication of the occurrence of sample degradation. Reducing the laser power or defocusing the laser, so the sample is exposed to less power per unit area, are the most common methods for preventing/reducing sample degradation. However, this makes it necessary to scan for longer. Another approach for combating this problem is to rotate the sample during analysis, this prevents the laser from being focused on the same spot for long enough to cause heating. According to equation 2.1.12 the intensity of a Raman spectrum increases with the intensity of the incident radiation. However, in a lot of cases the possibility of sample degradation prevents the use of high power lasers to improve the sensitivity of a Raman instrument.

2.1.7 Raman Microscopy

The first results of practical Raman microscopy were presented at the IVth International Conference on Raman Spectroscopy in 1974.[10] The most common sources used for Raman spectroscopy are 514nm Argon ion laser and the 633nm HeNe laser. These produce light in the visible range, which make coupling a Raman spectrometer to a microscope relatively easy, as a standard optical microscope can be used. Raman microscopy is a very powerful tool for the characterisation, study and mapping of materials, using high spatial resolution. Using a 100x objective the laser spot can be focused down to 1-2μm, making it possible to study individual particles or fibres in a sample. An example of this is the use of Raman microscopy to identify microscopic asbestos fibres in a building material matrix without the need for sample treatment.[11]

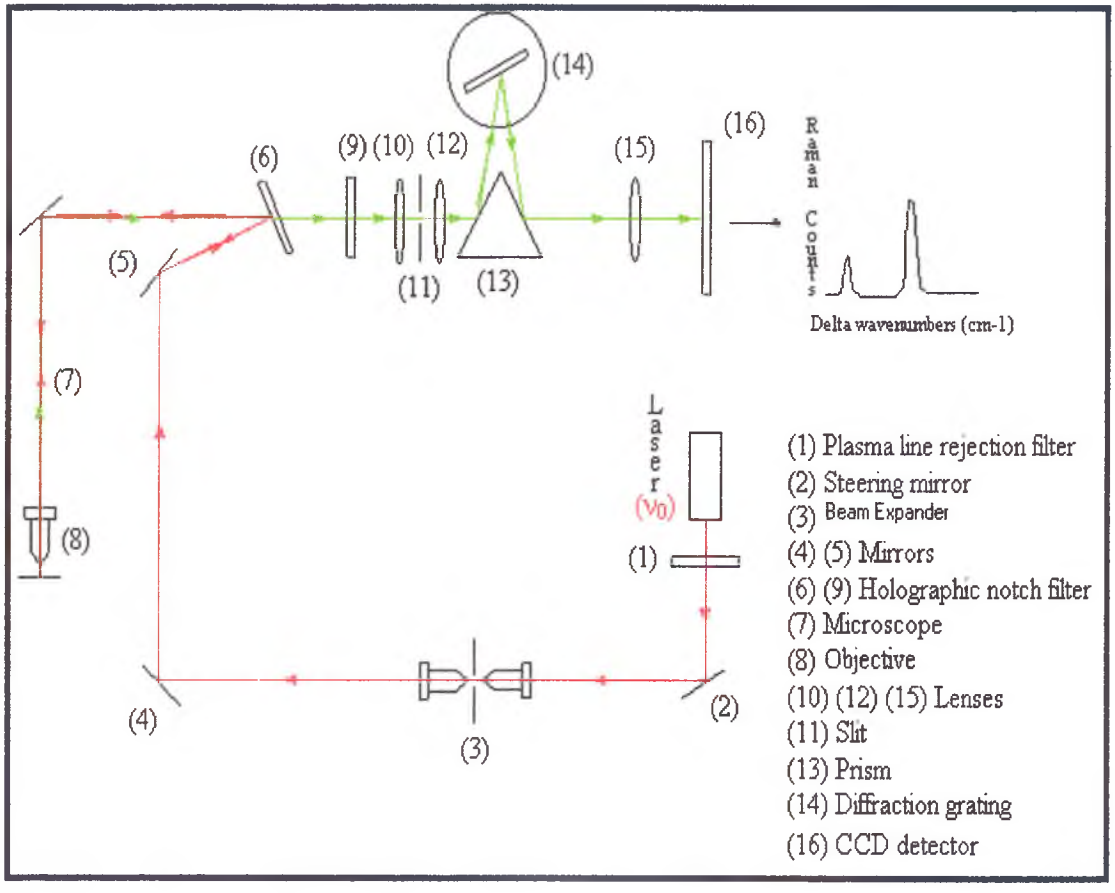

Figure 2.1.3: Schematic diagram of the Renishaw Raman Microscope

A schematic diagram of the Renishaw Raman System 2000, used for the work in this project, is shown in figure 2.1.3. The source used was a 25mW helium-neon laser emitting at 632.8nm. It is necessary to pass the laser light through a plasma line rejection filter (PLRF)(1). The PLFR prohibits the unwanted plasma lines from entering the instrument but transmits the main laser line. The steering mirror (2) directs the laser beam through the beam expander (3), which recollimates any stray laser light and also expands the beam to the size required for use in the microscope objective. The expanded and collimated beam is then deflected by mirrors (4 and 5) onto the first holographic notch filter (HNF) (6). This first HNF reflects the laser beam down the microscope (7) and the light is focused onto the sample using a microscope objective (8). The microscope lenses used in this project were the x5, x10, x20, x50 and x100. The light scattered from the sample (both Rayleigh and Raman) is collected back up through the objective and the

microscope, at 180° scattering geometry, until it reaches the first HNF. This first filter reflects the strong unwanted Rayleigh light back through the instrument and away from the detection path but transmits the Raman scattered light. The second HNF (9) filters out almost all the remaining Rayleigh scattered light but still transmits the Raman scattered light. The remaining Raman light then passes through a pre-slit lens (10), which focuses the light through an adjustable entrance slit (11). A second lens (12) recollimates the scattered light before a mirrored prism (13) directs it onto a diffraction grating (14), which separates the beam into its component wavelengths. The prism deflects the dispersed light through a lens (15) on to a CCD (charge coupled device) detector (16).

2.2 X-Ray Photoelectron Spectroscopy (XPS)

In principle, Raman studies should allow the identification and estimation of sp^2 and sp^3 sites in carbonaceous materials, owing to the fact that the zone-centred optical phonons in graphite and diamond occur at well separated frequencies of $1580cm^{-1}$ and $1332cm^{-1}$, respectively.[12] However, when using visible sources of excitation a resonance enhancement of the Raman cross-section of sp^2 bonds occurs.[13] This phenomenon can result in sp^2 bonds having scattering efficiencies 50 to 100 times greater than sp^3 bonds, which leads to the contribution of sp^2 sites dominating the spectra. The use of visible Raman to characterise the hybridisation of carbonaceous material has been based on empirical relationships between bonding and shifts or broadening of the G band. A more thorough examination of the relationship between Raman spectra of carbonaceous materials in relation to the resonance effects and sp^2/sp^3 hybridisation is discussed in chapter 3 (sections 3.4.5 and 3.4.6).

In electron spectroscopy the kinetic energy of emitted electrons is recorded.
A photon from a monochromatic X-ray beam of known energy, $h\nu$, displaces an electron, e^-, from a K orbital E_b.

$$A + h\nu = A^{+*} + e^- \qquad \textbf{(2.2.1)}$$

A can be an atom, a molecule or an ion and A^{+*} is an electronically excited ion with a positive charge one greater than that of A. The kinetic energy of the emitted electron, E_k, is measured in an electron spectrometer. Binding energy of the electron, E_b, can be calculated as follows:

$$E_b = h\nu - E_k - w \qquad \textbf{(2.2.2)}$$

W is the so-called work function of the spectrometer, a factor that corrects for the electrostatic environment in which the electron is formed and measured. The binding energy of an electron is characteristic of the atom and orbital from which the electron was emitted.

A recent study[14] observed the C1s band for purely sp^3-bonded diamond at 285.5eV with a FWHM of 2.2eV and purely sp^2 bonded graphite at 284.15eV with a FWHM of 1eV. The separation between each band is around 0.8eV. So, when analysing a material that has a mixture of sp^3 and sp^2 sites there is strong overlapping of their C1s bands. This necessitates the use of high resolution (<0.5eV) instrumentation and a curve fitting procedure, to resolve the contribution of both components to the C1s band. The number of carbon atoms in each hybridisation is proportional to the area under each peak divided by its sensitivity factor. The sensitivity factor for XPS core-level spectra depends only on the atomic factors and is independent of the chemical state of the atoms; the sensitivity factor for the two peaks is the same in this case. Therefore, XPS can give a direct estimation of sp^2/sp^3 hybridisation. Lung et al[15] and Merel et al[16] have performed similar studies on thin amorphous hydrogenated carbon (a-C:H) and diamond-like carbon films respectively.

A low-resolution wide-scan/survey spectrum can be used to determine the elemental composition of samples. All elements except hydrogen and helium emit core electrons having characteristic binding energies. Typical wide-scans use a range of 0 to 1250eV in binding energy. XPS has previously been used to determine the elemental composition of coal[17-19] and DPM[20]. XPS not only provides qualitative information but can also estimate

the relative number of each atom if it present in concentrations greater than 0.1%. This technique has also been used to identify different oxidation states of elements contained in inorganic materials. It must be emphasised that XPS is a surface technique with a penetration depth of only 10-50Å and the results obtained may not reflect the composition and/or structure of the bulk material. However, XPS has the potential to provide some useful additional information about the coal dust and DPM samples to be analysed by Raman.

2.3 Diffuse Reflectance Infrared Fourier Transform Spectroscopy (DRIFTS)

Coal and DPM are known to have a significant organic content. However, no Raman bands characteristic of organic material were observed when analysing the DPM and coal dust samples used in this project. The Raman resonance effect of the C=C elemental carbon can result in the Raman signal being enhanced by a factor of 10^2 to 10^6. Therefore, it is possible that the intense signal from the elemental carbon can mask any signal from other materials present in the samples. Infrared is a technique regularly used for the identification of organic functional groups in a variety of samples and has previously been used to analyse coal[21-23] and DPM[24].

The samples to be analysed were already in powder form, so, it was decided to analyse them using DRIFTS. This is an infrared sampling technique, which is particularly useful for the analysis of powered samples, being sensitive, and needing minimal sample preparation. Diffuse reflection is a complex process that occurs when a beam of radiation strikes the surface of a finely divided powder. Specular reflection occurs at each plane surface and the radiation is reflected in all directions.[9] The relative reflectance intensity for a powder $f(R'_\infty)$ is given by:

$$f(R'_\infty) = \frac{(1-R'_\infty)^2}{2R'_\infty} = \frac{K}{S} \qquad \textbf{(2.3.1)}$$

Where R'_∞ is the ratio of the reflected intensity of the sample to that of a nonadsorbing standard, such as finely ground KBr. K is the molar absorption coefficient of the analyte

and S is a scattering coefficient. Reflectance spectra consist of a plot of $f(R'_\infty)$ versus wavenumber.

2.4 Thermogravimetric Analysis (TGA)

From the Raman analysis of the samples during this project it became apparent that the reproducibility of the spectra was affected by differential burn-off of the organic component. (see chapter 5 section 5.3.10) It was decided to investigate the effect of heat-treating the samples in an inert atmosphere, to heat off the organic material, before analysing the samples by Raman. A TGA analysis was performed on some DPM and coal dust to study the effects of heating and to help decide on the appropriate temperature to heat the samples used for the Raman analysis. The TGA studies of DPM[25] and coal[26-28] have been reported previously.

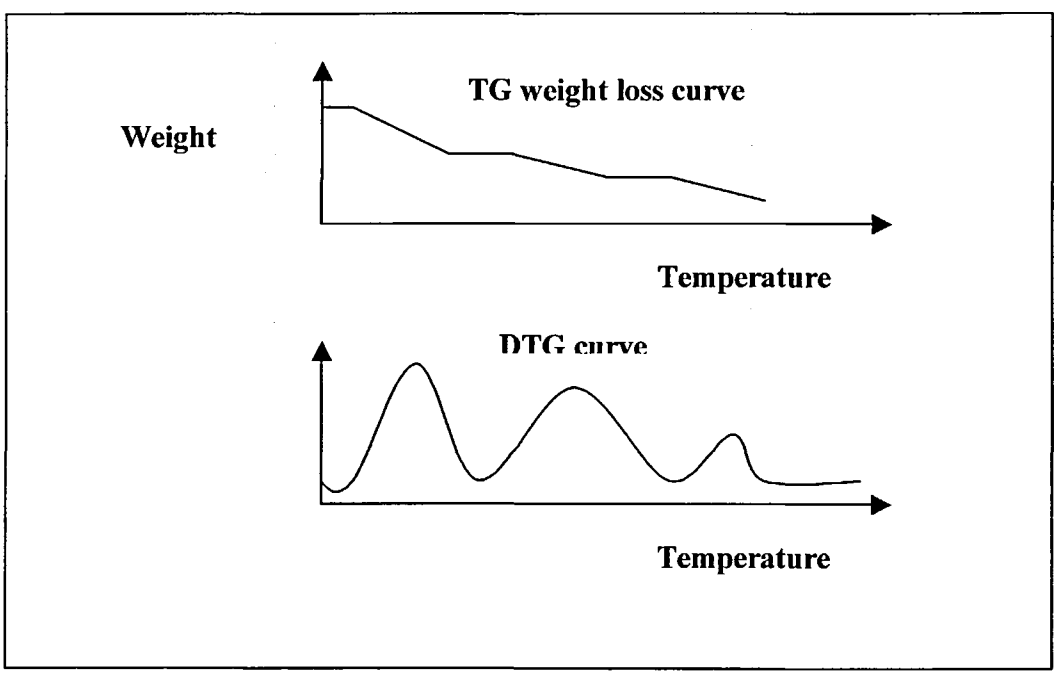

Figure 2.3: TGA data output curves

TGA involves the continual recording of sample weight when subjected to a precise temperature program.[29] Samples may be heated from room temperature to 1500°C. The TG curve plots weight decreasing downwards on the y-axis and temperature increasing to

the right on the x-axis (fig. 2.3). This is known as a TG weight loss curve. However, in this format, subtle weight changes can be difficult to determine. Alternatively, the negative derivative curve (-dw/dt-DTG) of the TG weight loss curve can be utilised, which shows the rate of change in mass in relation to the rate of change in temperature.[30]

2.5 X-Ray Fluorescence (XRF) Spectrometry

Raman spectra give structural information about coal dust and DPM but it is not possible to determine the elemental composition of the sample using this technique. XRF has previously been used to estimate the carbon content[31] and other major, minor and trace elements[32,33] in coal samples.

XRF is a non-destructive technique used to determine the quantity of elements present in a sample. Excitation is brought about by irradiation of the sample with a beam of X-rays from an X-ray tube or a radioactive source. The elements in the sample are excited by absorption of the primary beam and emit their own characteristic fluorescence radiation at specific wavelengths, which is related to the concentration of the element in the sample.[9] Irradiation area is of the order of $5cm^2$ with a penetration depth of an average wavelength about 20μm and a volume of analysis in the order of 50mg.[34] XRF was utilised in this study to estimate the chemical composition of coal dust. The composition of DPM was not estimated due to the large amount of sample required.

2.6 Scanning Electron Microscopy (SEM)

DPM and coal dust samples were collected on quartz fibre filters as described in chapter 5 (see sections 5.3.1 and 5.3.4). Optical micrographs of the samples were taken using the video camera coupled to the microscope of Raman instrument. However, the quartz filters are a woven mesh of fibres, which are by no means flat (see figure 2.6.1) As a consequence of this, it was not possible to keep the whole optical image in focus when using an objective with greater magnification than X5.

This was due to insufficient resolution and poor depth of field, when using an optical microscope. Figure 2.6.2 illustrates the inadequate depth of field of an optical micrograph for a DPM sample on a quartz fibre filter, with a X20 objective.

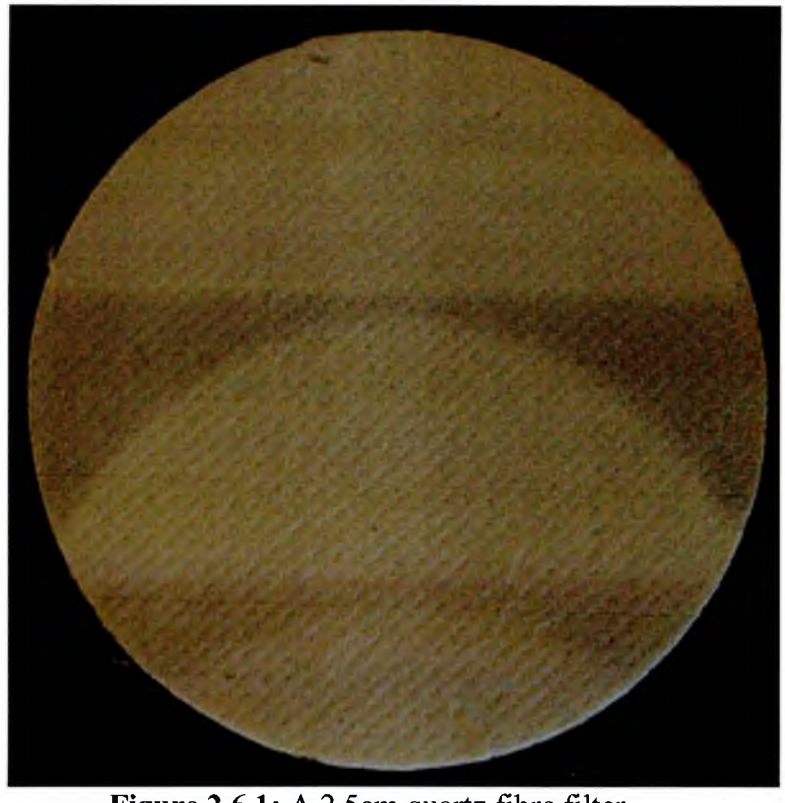

Figure 2.6.1: A 2.5cm quartz fibre filter

SEM has a considerably higher resolution and far better depth of field than optical microscopy. SEM has previously been used to obtain images of coal[35-36] and DPM samples.[37-38] Such images are necessary to get an idea of the distribution of the samples on quartz fibre filters, which gives information on their homogeneity/heterogeneity. The size distribution of the coal dust particles can also be determined because of their narrow size distribution. However, SEM is not very useful for size estimation of DPM as it can range in size from less than 0.01μm to over 10μm. Also, adequate information is available in the literature on size distributions of DPM, so, it is not necessary to make such estimations here

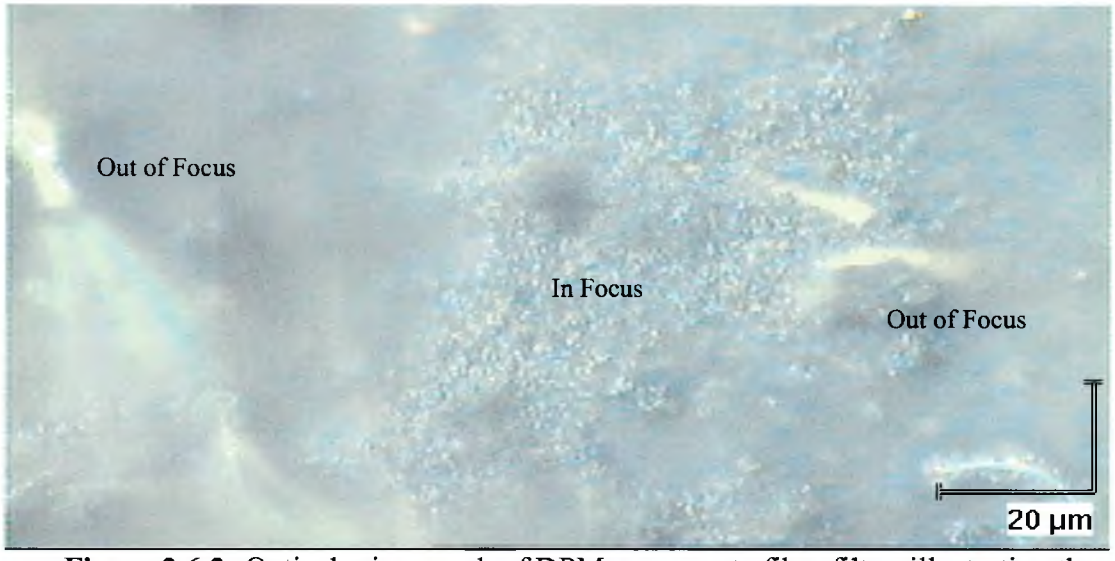

Figure 2.6.2: Optical micrograph of DPM on a quartz fibre filter, illustrating the inadequate depth of field of an optical micrograph for the samples analysed here

In obtaining an image by SEM the surface of the sample is swept in a raster pattern by a finely focused beam of electrons (5-200nm spot size), until a desired area of the surface has been scanned. During the scanning process, a signal is detected above the surface. Several types of signals are produced from the surface. These include backscattered, secondary and Auger electrons; X-ray fluorescence photons; and other photons of various energy. Backscattered and secondary electrons are usually detected in an SEM instrument.[9]

References

1) L. Brillouin, Ann . Phys., **88**, 1922,17
2) A. Smekal, Naturwissenshaften, **11**, 1923, 873
3) C. Raman, K. Krishnam, Nature, **121**, 1928, 50
4) D. Gardiner in, Practical Raman Spectroscopy, Springer-Verlag, Berlin, 1989
5) G. Davidson in, Group Theory for Chemist, McMillan Physical Science Series, Macmillan Education, London, 1991.
6) P. Dorain in, Symmetry In Inorganic Chemistry, Addison-Wesley, Massachusetts, 1965
7) J. Grasselli, B. Bulkin in, Analytical Raman Spectroscopy, John Wiley & Sons, New York, 1991
8) C. Constable, Raman Microscopic Studies of PVD Deposited Hard Ceramic Coatings, Sheffield-Hallam University PhD Thesis, 2001
9) Skoog, Holler and Nieman in, Principles of Instrumental Analysis (5^{th} Ed.), Saunders College Publishing, London, 1999
10) G. Rosasco, E. Etz, W. Cassatt, IV^{th} International Conference on Raman Spectroscopy, Brunswick, Me., USA, 1974
11) D. Bard, Raman Spectroscopic Characterisation of Inorganic Fibres and Particles and their Coverage by Wetting Agents, Sheffield-Hallam University PhD Thesis, 1998
12) K. Gilkes, H. Sands, D. Bachelder, W. Milne, J. Robertson, Journal of Non-Crystalline Solids, **227-230**, 1998, 612
13) T. Leung, W. Man, P. Lim, W. Chan, F. Gaspari, S. Zukotynski, Journal of Non-Crystalline Solids, **254**, 1999, 156
14) C. Mossner, P. Grant, H. Tran, G. Clarke, D. Lockwood, H. Labbe, B. Mason, I. Sproule, Thin Solid Films, **317**, 1998, 397
15) Y. Taki, O. Takai, Thin Solid Films, **316**, 1998, 45
16) P. Merel, M. Tabbal, M. Chaker, S. Moisa, J. Margot, Applied Surface Science, **136**, 1998, 105
17) B. Gong, P. Pigram, R. Lamb, C. Ward, Fuel Processing Technology, **50**, 1997, 69
18) C. Weitzsacker, J. Gardella, Energy & Fuels, **10**, 1996, 141
19) A. Buckley, M. Kelly, P. Nelson, K. Riley, Fuel Processing Technology, **43**, 1995, 47
20) H. Klein, E. Lox, K. Seibold, G. Prescher, Physical Chemistry Chemical Physics, **2**, 2000, 1051
21) M. Cloke, A. Gilfillan, E. Lester, Fuel, **76**, 1997, 1289
22) J. Thomasson, C. Coin, H. Kahraman, P. Fredericks, Fuel, **79**, 2000, 685
23) C. Alciaturi, M. Escobar, R. Vallejo, Fuel, **75**, 1996, 491
24) A. Clague, J. Donnet, T. Wang, J. Peng, Carbon, **37**, 1999, 1553
25) H. Schulz, G. De Mello, F. Ousmanov, Combustion and Flame, **118**, 1999, 118
26) J. Podder, T. Hossain, K. Mannan, Thermochemica Acta, **225**, 1995, 221
27) J. Jaber, S. Probert, Fuel Processing Technology, **63**, 2000, 57
28) A. Bjorkman, Fuel, **80**, 2001, 155
29) Dodd J.W, Tonge K.H in, Thermal Methods, John Wiley & Sons, London, 1987
30) F. Fifield, P. Haines in, Environmental Analytical Chemistry, Blakie Academic & Professional, Glasgow, 1995
31) J. Parus, J. Kierzek, B. Malozewska-Buko, X-Ray Spectrometry, **29**, 2000, 192

32) G. Suarez-Fernandez, J. Vega, A. Fuertes, A. Garcia, M. Martinez-Tarazona, Fuel, **80**. 2001, 255
33) D. Spears, L. Manzanares-Papayanopoulos, C. Booth, Fuel, **78**, 1999, 161
34) Ron Jenkins in, X-Ray Fluorescence Spectrometry, John Wiley & Sons, 1988
35) H. Wang, J. West, J. Harb, Energy & Fuels, **13**, 1999, 570
36) J. Shi, D. Mark, R. Harrison, Environmental Science & Technology, 1999, **34**, 748
37) L. Rainey, A. Palotas, P. Bolsaitis, J. Vander Sande, A. Sarofin, Applied Occupational Environmental Hygiene, **11**, 1996, 777
38) A. Watson, P. Valberg, AIHAJ, **62**, 2001, 218

Chapter 3

Raman Spectroscopy of Carbon Materials

3. Raman spectroscopy of carbon materials

3.1 Crystals

The regular arrangement of atoms in a molecule results in a regular shape. A crystal is defined as a substance which has solidified in a definite geometrical form.[1] The orderly arrangement of the crystalline state is a consequence of attractive binding forces, which form permanent attachments between the constituent atoms; the development of perfect regularity corresponds to a minimisation of the energy of the solid at the change of state in which it is formed.[2] A crystal is characterised by a primitive cell or unit cell, which is the smallest unit, repeated in three dimensions. The crystal is constructed by stacking identical unit cells face to face in perfect alignment in three dimensions. The position of the planes, directions, and point sites, in a lattice is described by reference to the unit cell and the three principal axes x, y and z.

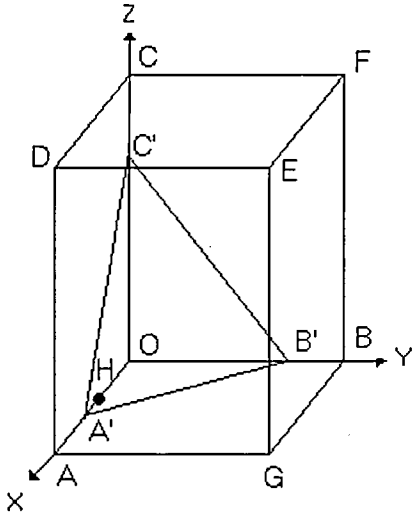

Cell Dimensions

OA = a
OB = b
OC = c
Lattice parameters

$\langle BOC = \alpha$
$\langle COA = \beta$
$\langle AOB = \gamma$
Defines size/shape

Any plane A'B'C' is defined by the intercepts OA', OB' and OC' with the three principal axes

Figure 3.1.1: Crystal unit cell and its dimensions

The usual notation (Miller indices) defining crystal planes is to take the reciprocals of the ratios of the intercepts to the corresponding unit cell dimensions. Thus, A'B'C' is given by

$$\left(\frac{OA}{OA'},\frac{OB}{OB'},\frac{OC}{OC'}\right)$$

the planes ABC, ABE, CEA and CEB are (111), (11 $\bar{1}$), (1 $\bar{1}$ 1), and ($\bar{1}$ 11) respectively and are all planes of the same group/type {111}. Square brackets are used for direction vectors i.e. the directions CG, AF, DB and EO being [11 $\bar{1}$], [$\bar{1}$ 11], [$\bar{1}$ 1 $\bar{1}$] and [$\bar{1}$ $\bar{1}$ $\bar{1}$] respectively. Any point in a crystal is described by the fractional displacements of the point from the principal axes relative to the dimensions of the unit cell. Therefore the centre of the cell (Figure 3.1) is $\frac{1}{2},\frac{1}{2},\frac{1}{2}$, points F, E and H are 0,1,1; 1,1,1; $\frac{1}{2}$,0,0 respectively.[3]

3.2 Crystal Imperfections[2]

The chemical and physical properties of crystals depend on the structure of the atoms and the nature of the atomic binding. Perfect crystals, in which every atom site is filled and there are no disturbances in the regular arrangement of atoms, do not exist. All real crystals contain imperfections that may be point, line, surface or volume defects, which occur during the nucleation process. Knowledge of the structure of defects and their properties is essential to fully understand all aspects of properties of materials.

3.2.1 Point Imperfections

In compounds an exact identity of all unit cells is achievable only within the restriction of stoichiometric combination in which elements of the appropriate valencies are present in fixed proportions according to the chemical formulae. But in many crystalline compounds the chemical combination is non-stoichiometric. This may be due to the parent structure being able to take in foreign atoms (or ions) without its structural pattern being significantly changed. A more realistic conception of the crystal atomic structure is a three-dimensional pattern of sites available for occupation by atoms of the crystal. Chemically different atoms may be found in crystallographically equivalent sites in

different parts of the structural continuum, and, sometimes, some sites may be unoccupied.

Impurity atoms, which define some of the point defects, can be accommodated in two different ways: substitutional impurity atoms and interstitial impurity atoms. Substitutional impurity atoms replace atoms of an ideal perfect structure on certain kinds of sites. The particular impurity atoms which are acceptable on given sites are dependent on a wide variety of factors, including relative sizes, the physicochemical conditions of formation, etc. Interstitial impurity atoms are incorporated into the crystal structure by fitting into cavities between atoms of the parent structure and are in positions that are not sites of the original structural pattern. This may only occur if the atoms are small enough to fit into the cavities and their presence does not cause too much distortion. Interstitial impurities are particularly important in metallic systems where small atoms, like H, B, C and N, are introduced to fill the interstices of a parent metal framework and can cause substantial changes in properties. Another type of point defect is caused by the absence of atoms from some available sites. These are called lattice vacancies, which are possible even in strictly stoichiometric combinations. Various kinds of vacancy defects have been hypothesized. The simplest are the Frenkel and Schottky imperfections. In the former the lattice vacancy is created when a small cation leaves its structural site but is retained in an interstitial position in the structure, whilst in the latter a vacant cation site is accompanied by a vacancy on a neighbouring anion site. In most structures Frenkel defects are less probable than Schottky defects due to the lack of sufficient empty space to accommodate a displaced cation.

3.2.2 Surface imperfections and grain boundaries.

Surface imperfections have the effect of separating blocks of structure within the solid into grains separated by grain boundaries. Each grain is a single crystal and contains defects. The existence of grain boundaries is implicit in the occurrence of polycrystalline solids whose crystallites can be in a random array or have some sort of preferred orientation. Boundary regions can be non-structural but only those that relate to structural

changes across the surface are considered here. Such boundaries can be divided according to the misorentation of the blocks of structure that they separate. The greater any misorentation between the blocks, the more easily they are distinguished due to the more severe atomic distortions within the boundary regions. In a polycrystalline aggregate there is large misorentation between adjacent grains and although only a few cells thick the boundary regions are highly distorted with little or no coherency with the structures of the regions on either side of them. With small misorentation, the atomic arrangement in the boundary is to some extent coherent with that of the adjacent crystalline blocks. Low angle boundaries are often formed by local concentrations of dislocations to relieve the strain of the crystal.

3.3 Raman scattering in crystals

The Raman effect stems from vibration-induced changes in the electronic polarisability of a molecular system. Vibrations involving the crystal lattice may not be ascribed to an individual molecule. In a crystalline solid the lattice-vibrational excitations are plane waves characterised by wave vector k as well as frequency ω.[4] The wave vector is a vector which points in the direction of propagation of the wave. It is measured in cm^{-1} and defines the vector in reciprocal space. In contrast to electromagnetic waves the wave vector, k, of lattice vibrations has a discrete spectrum within defined limits.[5]
Each mode of excitation is termed a phonon mode. Phonon modes are properties of the crystal lattice, often referred to as being delocalised, which may be visualised as collective states of the entire solid that lie lower in energy than the individual molecular internal vibration states. When energy is deposited into the phonon modes of the crystal, the transfer of energy from the phonon modes to the internal vibrational modes maintains equilibrium. [6] Phonons are the smallest possible vibrations a solid can make[7]. The energy of each phonon is given by $h.\ \omega$, where h is Planck's constant.[8] The $\omega(\mathbf{k})$ phonon dispersion relations (dispersion curve) provide an energy versus momentum representation of the vibrational modes.

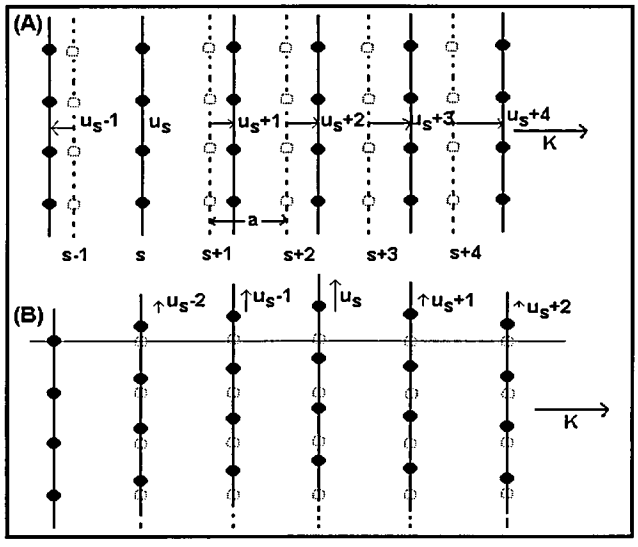

Fig 3.2.1: (A) Dashed lines planes of atoms when in equilibrium and solid lines are planes of atoms when displaced as for a longitudinal wave. The coordinate u measures the displacement of the planes (B) Planes of atoms as displaced during a passage of a transverse wave[9]

With crystals having more than one atom per primitive cell the vibrational spectrum shows new features. If we consider two atoms per primitive cell for each polarisation mode in a given propagation direction, the dispersion relation ω(k) develops two branches, known as acoustical and optical branches. There are longitudinal (LA) and transverse (TA) acoustical modes, and longitudinal (LO) and transverse (TO) optical modes. In the case longitudinal modes the displacement of atoms from their equilibrium position coincides with the propagation direction of the wave, whereas for transverse mode, atoms move perpendicular to the propagation of the wave

3.3.1 Acoustical phonon modes[5]

Consider a chain of identical atoms of mass M spaced at a distance α, the lattice constant, connected by invisible Hooke's law springs. For simplicity longitudinal deformations (displacements of atoms are parallel to the chain) are considered.

U_n = displacement of atom n from it's equilibrium position

U_{n-1} = displacement of atom n-1 from it's equilibrium position

U_{n+1} = displacement of atom n-1 from it's equilibrium position

The force on an atom is given by its displacement and the displacement of its nearest neighbours:

$$F_n = \beta(U_{n+1} - 2U_n + U_{n-1}) \qquad \textbf{(3.3.1)}$$

The equation of motion is:

$$M\frac{\partial^2 U_n}{\partial.t^2} = \beta(U_{n+1} - 2U_n + U_{n-1}) \qquad \textbf{(3.3.2)}$$

where β is a spring constant. Equation 3.3.2 is not obviously a wave equation, but assuming a travelling wave solution, namely

$$U_n = U_{no} \exp[i(kn\alpha \pm \omega t)] \qquad \textbf{(3.3.3)}$$

Let $U_{n0} = U_0$ since if it is a wave, it has to have a definite amplitude.
If the wave solution is substituted into the equation of motion, the phonon's dispersion relation for linear monatomic chain is as follows:

$$\omega = \pm\sqrt{\frac{4\beta}{M}}\sin\frac{k\alpha}{2} \qquad \textbf{(3.3.4)}$$

The dispersion curve for a monatomic molecule is shown in fig 3.3.1.

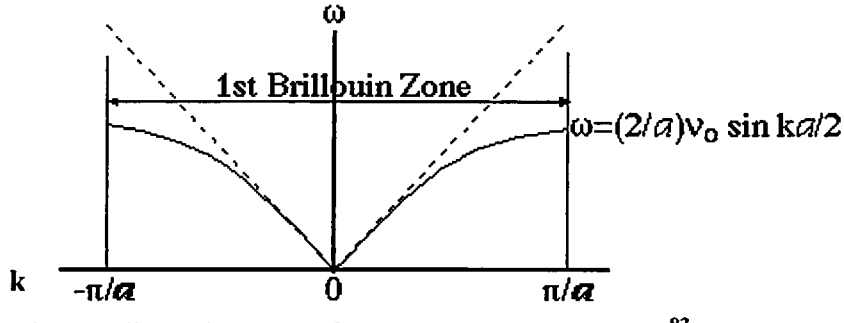

Fig 3.3.1 Phonon dispersion curve for a monoatomic molecule[83]

An important feature of the dispersion curve is the periodicity of the function. For unit cell length α, the repeat period is $2\pi/\alpha$, which is equal to the unit cell length in the reciprocal lattice. Therefore the useful information is contained in the waves with wave vectors lying between the limits:

$$-\frac{\pi}{\alpha} < k < \frac{\pi}{\alpha}$$

This range of wave vectors is called the first Brillouin zone. At the Brillouin zone boundaries, the nearest atoms of the chains vibrate in the opposite directions and the wave becomes a standing wave.

As k approaches zero (the long-wavelength limit) $\sin x \rightarrow x$ and we have

$$\omega = \sqrt{\frac{4\beta}{M}}\frac{k\alpha}{2} = v_0 k \qquad \textbf{(3.3.5)}$$

where v_0 is a phase velocity, which is equivalent to the velocity of a sound in the crystal. Phonons with frequency which goes to zero in the limit of small k are known as acoustical phonons.

3.3.2 Optical Phonon Modes[5]

Considering a lattice with two atoms in the primitive cell it is necessary to write solutions for the deplacement corresponding to the masses M and M_1. The equations of motion are:

$$M\frac{\partial^2 U_{2n}}{\partial^2 t} = \beta(U_{2n+1} - 2U_{2n} + U_{2n-1}) \qquad \textbf{(3.3.6)}$$

$$M\frac{\partial^2 U_{2n+1}}{\partial^2 t} = \beta(U_{2n+2} - 2U_{2n+1} + U_{2n}) \qquad \textbf{(3.3.7)}$$

and assuming solutions:

$$U_{2n} = A\exp[i(2nk\alpha \pm \omega * t] \quad \textbf{(3.3.8)}$$

$$U_{2n+1} = B\exp[i((2n+1)k\alpha \pm \omega * t)] \quad \textbf{(3.3.9)}$$

where A and B are the amplitudes of vibration of atoms M and M_1 respectively.
The diatomic case has two solutions of the dispersion relation:

$$\omega^2 = \beta\left(\frac{1}{M}+\frac{1}{M_1}\right)^2 \pm \beta\sqrt{\left(\frac{1}{M}+\frac{1}{M_1}\right) - \frac{4\sin^2 k\alpha}{MM_1}} \quad \textbf{(3.3.10)}$$

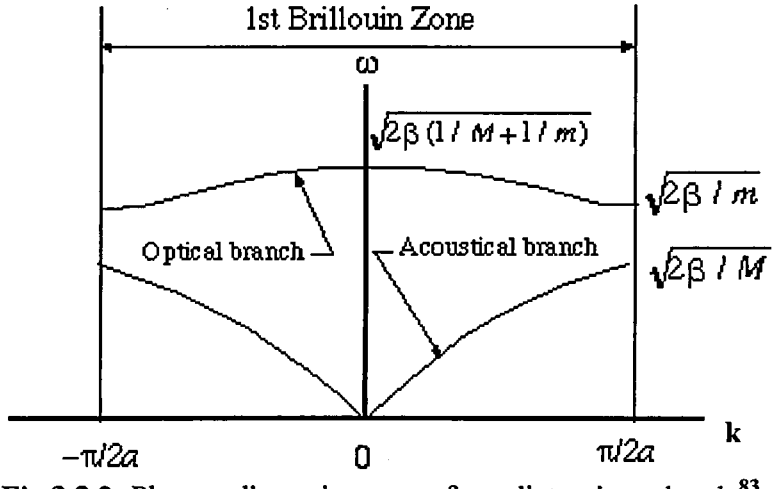

Fig 3.3.2: Phonon dispersion curve for a diatomic molecule[83]

The allowed frequencies of propagation wave are split into an upper branch, known as the optical branch, and a lower branch called the acoustical branch. There is a band of frequencies between the two branches that cannot propagate. The width of this forbidden band depends on the difference of the masses (M and M_1). If the two masses are equal, the two branches join (become degenerate) at $\pi/2\alpha$. The first Briillouin zone goes from $k= -\pi/\alpha_0$ to $k = \pi/\alpha_0$ just as in the monatomic case if the lattice constant α_0 is used instead of the interatomic distance α. The acoustical branch is qualitatively similar to the dispersion relation for a monatomic lattice, but the optical branch represents a completely

different form of wave. The major difference between the acoustical and optical branches is that for the optical branch (LO) the two atoms in the unit cell move opposite each other and the light mass amplitude is greater. For the acoustical branch (LA) the displacement of both atoms has the same amplitude, direction and phase. This relationship can be visualised from figure 3.3.3.

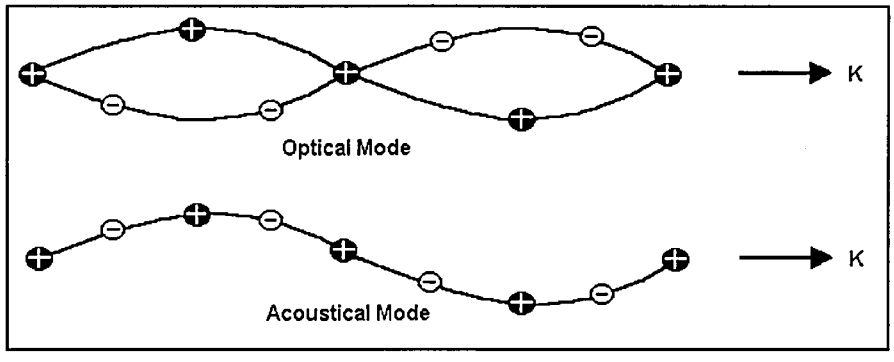

Fig 3.3.3: Transverse optical and transverse acoustical waves in a diatomic linear lattice (particle displacements for the two modes at the same wavelength)

If there are n atoms in the primitive cell, there will be 3n branches to the dispersion relation: 3 acoustical branches and 3n-3 optical branches. Thus NaCl will have six branches: one LA, one LO, two TA and two TO. The number of the branches follows from the number of degrees of freedom of the atoms. With n atoms in the primitive cell and N primitive cells, there are nN atoms. Each atom has three degrees of freedom, one for each of the x, y and z directions, making a total of 3nN degrees of freedom for the crystal. The number of allowed K values in a single branch is just N for one Brillouin zone. Thus the LA and the two TA branches have a total of 3N modes, thereby accounting for 3N of the total; degrees of freedom. The remaining (3n – 3)N degrees of freedom are accommodated by the optical branches.

In amorphous solids the vibrations are no longer plane waves and k has no meaning. The $\omega(\mathbf{k})$ relationship is not valid in an amorphous solid. However, the concept of vibrational density of states $g(\omega)$ retains its validity. Here $g(\omega)d\omega$ is the number of eigenvectors per unit volume, with frequencies between ω and $\omega + d\omega$. The k conservation rule is very

strict for phonons. There can be up to 10^{24} possible vibrations in a typical macroscopic crystal but only an small number (the order of 10^{1}) interact with light in the first order optical experiments.[4] Crystal vibrations come from zone-centre (k=0) phonons of the right symmetry to interact with the light used. Only zone-centred modes can produce first-order (one photon annihilated, one phonon created) infrared absorption in a crystal. Crystal modes with k values away from the centre of the Brillouin zone are optically inactive. The k=0, conservation rule is overthrown for amorphous solid and all phonons may participate in first-order interactions with light. In first-order-Raman scattering, an incident photon is annihilated and a phonon and scattered photon are created. The phonon-energy shift of the scattered light, with respect to the incident light, locates the frequency of the phonon involved. Broad bands for an amorphous material is an image of the density of states $g(\omega)$. In an amorphous solid, contributions from the entire phonon density of states appear in the first-order Raman spectra.

3.4 Raman spectroscopy of carbonaceous materials

3.4.1 Introduction

Carbonaceous materials are substances of which carbon is the major element.[10]
The most common crystalline forms of carbon are graphite and diamond.[11]
Graphite has a hexagonal, layered structure with weak interlayer bonding forces.[12] Its crystal may be visualised as infinite parallel layers of hexagon, benzene-like structures, stacked 3.57Å apart with an interatomic distance of 1.42Å in the basal plane. The basal plane atoms are trigonally coordinated and closely packed with strong σ (covalent) bonds to three neighbouring carbon atoms via sp^2-hybridised orbitals (sp^2-bonding). The fourth electron lies in a p_z orbital lying normal to the σ bonding plane and forms a weak π bond by overlapping side to side with a p_z orbital of an adjacent atom to which carbon is attached by a σ bond. The layers are relatively far apart and are weakly bonded by van der Waals forces.

The diamond crystal is arranged in a modified face-centred cubic (fcc) structure with an interatomic distance of 1.54Å. Its cubic lattice comprises of two interpenetrating fcc lattices displaced by one-quarter of the cubic diagonal. Each atom is tetrahedrally coordinated with strong σ bonds to its four neighbouring atoms via sp^3-hybridised orbitals (sp^3-bonding).

The graphite and diamond structures are shown in figure 3.4.1(a) and 3.4.1(a) respectively.

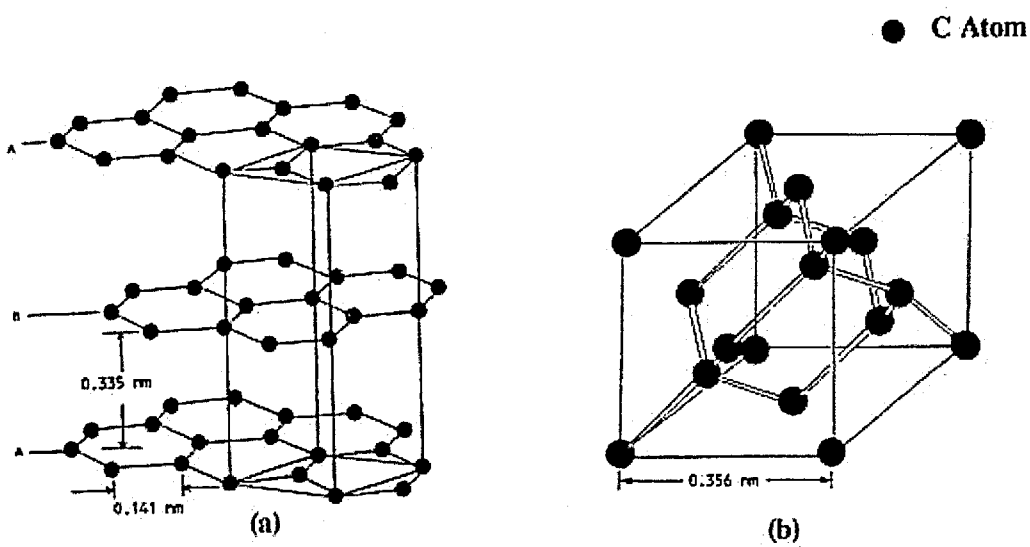

Figure 3.4.1: The structure of **(a)** graphite and **(b)** diamond from Bushan[12]

The carbon from DPM and coal dust studied here is expected to be similar to disordered graphite with limited long-range order and sp^3-bonded diamond-like carbon inclusions. The most probable arrangement being sp^2-bonded graphitic regions distributed in a random network of sp^2 and sp^3 bonded carbons. The graphitic-like regions have three basic structures; crystallite, turbostratal and amorphous.[13] Graphite crystallites are three-dimensionally ordered regions with a substantial number of defects in the crystal lattice. Turbostratal carbons are planar polyaromatic basic structural units (BSU), solitary or in clustres, in which the BSUs are parallel but the order of the packing layers along the c-axis perpendicular to the layers, which is typical for crystalline graphite, is altered. This phase can include small clusters of 2-D hexagonal graphite layers (graphene). However,

the position of the carbon atoms in the BSUs may deviate markedly from an ideal hexagonal network. Amorphous carbon (a-C) exhibits a complete lack of translational order associated with crystalline (even nanocrystalline) materials. The simplest form of a-C is graphitic amorphous carbon (g-C), which is a 2-D continuous random network (CRN) with sp^2 bonding being dominant.[11] Some models[14,15] of a-C incorporate graphitic rafts formed from rapped layers of 3-coordinated (sp^2-bonded) atoms arranged in quasi-2-D CRNs with planar dimensions of 5-20A. Bond lengths stay much the same as graphite (1.42A) but bond-angle distributions with 10-25° widths allow for the formation of a significant number of 5,7 and perhaps even 4,8,9 membered rings. These models suggest that the quasi-planar rafts are linked together with varying concentrations of sp^3-bonded atoms (1-10% in g-C) which allow for changes in orientations of the raft planes without the necessity of dangling bonds or voids that would result from unconnected, randomly orientated plane. This results in mesoscopic isotropicity in g-C. The edge carbon atoms at the crystal boundary may also be attached to chemical groups, such as a carbonyl groups, hydroxyl groups, carboxyl groups or hydrogen atoms.[16] Amorphous materials generally exhibit broad Raman peaks caused by structural distributions and breakdown of the k=0 Raman selection rule. The degree of order is characterised by the in-plane coherence length or mean basal plane diameter (L_a) of hexagonal order and the range of planar stacking (L_c). Polycrystalline graphite exhibits varying degrees of crystalline order from high ordered pyrolytic graphite (HOPG) (L_a ~ 1μm and L_c ~ 4μm) to glassy, turbostatic, or nanocrystalline graphite and graphite fibres (L_a> 1.5nm and L_c ~ 1nm).[11,17] The Raman spectra of carbon materials are known to very sensitively reflect their atomic structure.[18]

3.4.2 Raman spectroscopy of graphitic carbon materials

3.4.2.1 The Raman D and G bands of graphite

Before the advent of the laser as a Raman source, Raman spectra of completely black materials like graphite was not possible. Tuinstra and Koenig obtained the first reported Raman spectrum of graphite in 1970.[19] They observed a single peak at 1575cm^{-1} for a single crystal of graphite (see figure 3.4.2). Raman selection rules dictate that Raman

activity for a crystal can only be observed in the limit where the wave vector (k) is equal to zero. The single crystal graphite belongs to the D^4_{6h} symmetry group and its optical zone-centre phonon modes (Γ) are calculated as follows:

$$\Gamma = 2B_{2g} + 2E_{2g} + A_{2u} + E_{1u}$$

Only the 4 E_{2g} modes are Raman active. These correspond to a very strong in-plane stretching band (E_{2g}^2) at1581 ± 1cm^{-1} and a weaker low-frequency band (E_{2g}^1) at 47 ± 2cm^{-1}. The E_{1u} and A_{2u} modes are infrared active with calculated frequencies of 1588cm^{-1} and 863cm^{-1} respectively. All other modes are optically inactive.[20]

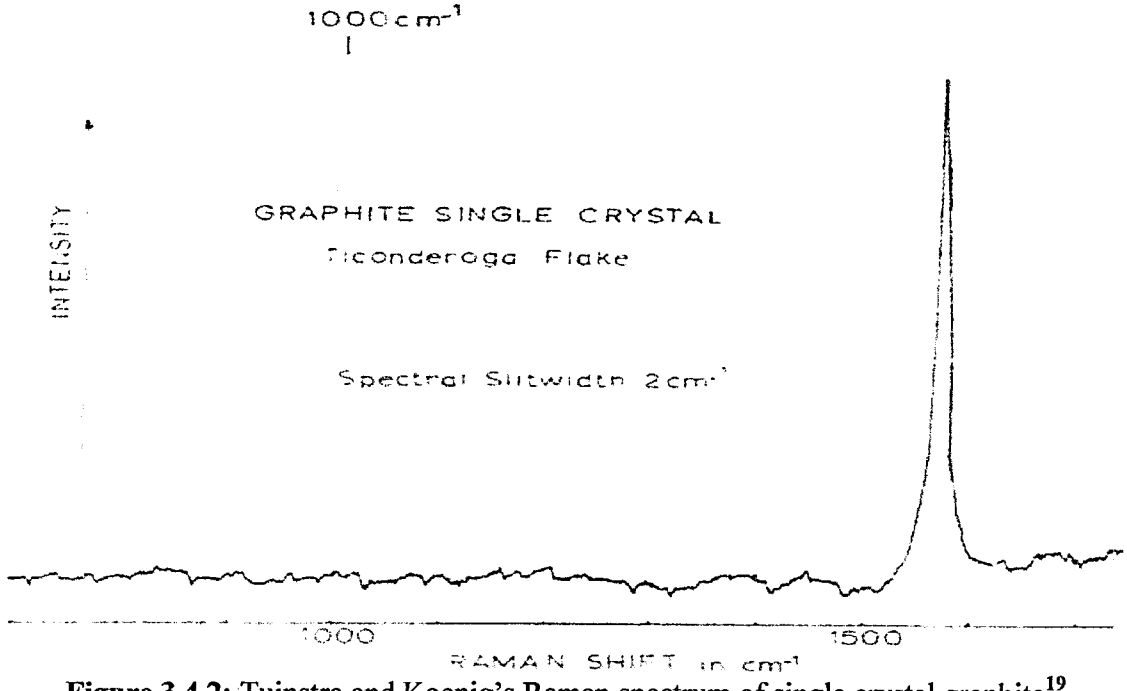

Figure 3.4.2: Tuinstra and Koenig's Raman spectrum of single crystal graphite[19]

When studying other graphitic materials Tuinstra and Koenig also observed a second band near 1355cm^{-1} (see figure 3.4.3). The relative intensity of this band increased with an increase in the amount of disordered carbon in the sample and a decrease in the graphite crystal size. Diamond gives a strong Raman line at 1332cm^{-1} [12] and it was possible that this new feature at 1355cm^{-1} was just a shifted diamond band. However, this was ruled out because the diamond band would be expected to shift to lower frequencies

because of tensile stress associated with bond distortions and from a heating effect due to the laser radiation. So, they attributed the 1355cm^{-1} line to a breakdown in the k = 0 selection rule for Raman activity of certain phonons, in small crystallites or boundaries of larger crystals, which were inactive in the infinite lattice. Looking at these small crystallites as large molecules with different sizes and shapes, the only new Raman active modes are of the A_{1g} type with D_{3h} symmetry. This mode is inactive in infinite crystals because changes in polarisability cancel over the infinite crystal. This is not true for small crystals and activity can be observed. The more disordered the structure the broader the bands become. The complete separation of the 1580cm^{-1} and 1360cm^{-1} bands has been observed in samples where the microcrystallite size is greater than 5nm.[10] Overlapped features are observed from samples containing smaller crystallites.[21]

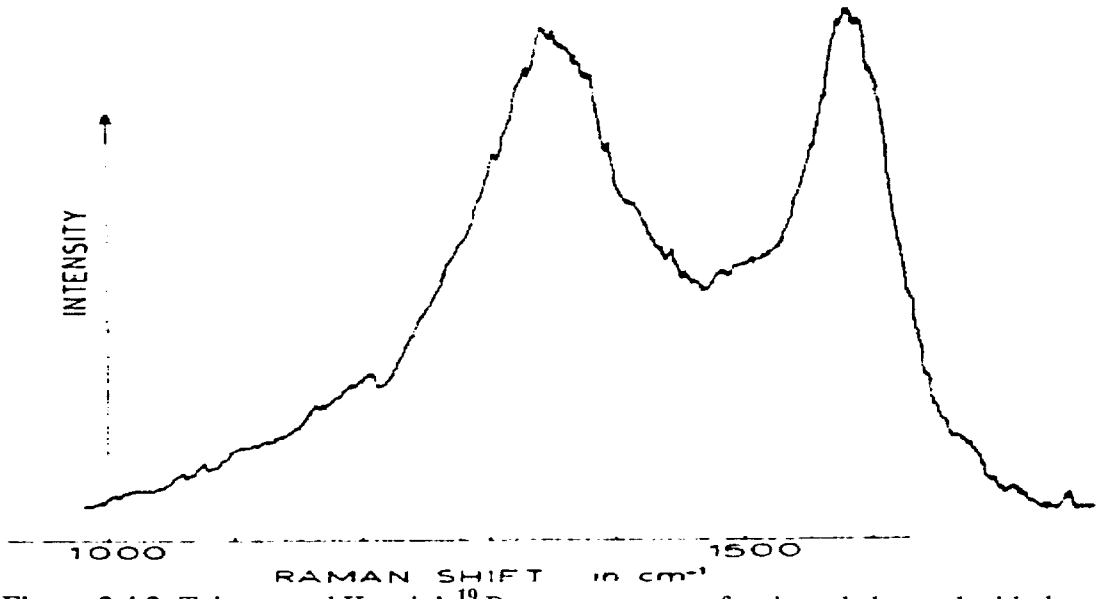

Figure 3.4.3: Tuinstra and Koenig's[19] Raman spectrum of activated charcoal with the graphitic band at ~1580cm^{-1} and the disorder induced band at ~1360cm^{-1}

Since Tuinstra and Koenig's work several different explanations have been given for the band at ~1355cm^{-1} but all agree that it is related to structural disorder in the graphite lattice. Hereafter, the line at ~1575cm^{-1} will be referred to as the G (for graphitic) band and the line at ~1355cm^{-1} will be referred to as the D (for disorder) band. However, in certain cases disorder is considered an inappropriate term to apply to the D band. Finite-size effect, the influence of the boundary phonons; (nothing to do with disorder in the

sense that the term "disordered carbon") often implies only short-range order in all directions whereas in some cases the sample can have long coherence lengths within the plane, but disorder in the third direction. [22] First- and second-order Raman spectra are sensitive to the degree of graphitisation. The first-order is especially sensitive to the extent of the 2-D graphitic order, while the second-order is most sensitive to the graphitisation process which gives rise to the 3-D ordering of hexagonal graphite stacking.[23] Wang et al[20] discussed three possible origins of the D band. The first explanation being a decrease in symmetry near microcrystallite edges, reducing the space group from D_{6h} to C_{3v} or even C_s. New modes, such as the A_{1g} mode, can then become active. The second explanation, which is related to the first, is the breakdown of the k=0 selection rule for optical phonons near crystallite edges, permitting phonons other than the 1588cm^{-1} and 47cm^{-1} bands to become active, and the spectra reflect the density of phonon states in the disordered lattice. These explanations are closely related to Tuinstra and Koenig's theory and have been used to explain the D band in numerous publications.[16,18,24-30] However, a third explanation proposed by Mernagh et al[31] is very different. They postulate that the D band originates from specific vibrations at crystallite edges, e.g., oxides or C=C groups which are present only at the edges and not directly related to the hexagonal graphite lattice but are analogous to functional groups. Recently Pocsik et al[32] proposed yet another theory. They argue that the previous explanations fail to account for different in the D band positions with different excitation sources and propose that Resonance causes this dispersion. This is as a result of coupling of the k-vector of the electronic states involved in the light absorption with the k-vector of phonons contributing to the Raman spectrum. The dependence of the Raman spectra of carbon on the excitation wavelength is explained in section 3.4.5 of this chapter. This includes a more detailed explanation of Pocsik et al's theory on the D band.

3.4.2.2 The D' band

A line at ~1620cm^{-1} was observed by Nakamizo et al in 1974.[33] Vinado and Fischbach[24] assigned it to the splitting of the degenerate E_{2g} mode and a breakdown of the selection rules allowing the contribution from non-zero-centre phonons. This band has been

calculated to be a peak in the density of states in graphite.[18, 34,35] Dresselhaus and Dresselhaus[36] assigned this line to an E_{2g} mode for a graphite boundary layer adjacent to an intercalant layer and not located between two other graphite planes. They attribute the upward frequency shift to differences in the electronic environment for the boundary layer compared to an inner layer. The mode for the 1620cm^{-1} band, which has been denoted as the E'_{2g} mode[20], is dependent on structural disorder and, like the D band, its intensity increases when crystallite size decreases. Hereafter the 1620cm^{-1} band will be referred to as the D' band. Sze et al[27] also assign the D' band to the E'_{2g} mode for the graphite layers located at the boundaries of the crystals. The D' band is sensitive to the composition of the material in contact with the surface layers of the graphite, which modifies their electronic environment. Like Dresselhaus they attribute the upward shift to an altered electronic state of a boundary plane or by its reduced symmetry. In disordered carbons the G band shifts from ~1580cm^{-1} to ~1600cm^{-1} this shift has been attributed to the presence of a D' band and in highly amorphous carbons. In this case, the D' band dominates the G band.[29]

3.4.2.3 Crystallite size estimations using D/G band ratios

Tuinstra and Koenig[19] observed that the ratio of the intensities for G and D band was inversely proportional to the crystallite size L_a as determined by XRD.

$$R = I_D/I_G \qquad \textbf{(3.4.1)}$$

Using equation 3.3 they could calculate the size of graphite crystallites:

$$L_a(nm) = 4.4/R \qquad \textbf{(3.4.2)}$$

These equations have since been used to determine crystallite sizes in a wide variety of graphitic materials.[11,16,21,22,26,29,35,37-39] Some studies use just the R value to identify changes in carbon materials with different treatments,[38] stating that the crystallite size had become smaller if the R value increased and the size had increased if the value decreased. Other work used equation 3.4.2[16, 28, 35] and discussed the results without taking

into account the possibility of high errors. However, the majority of researchers incorporating this formula in their work are aware that it is a strictly empirical measure.[22] Custa et al[26] observed that it is only valid for a first approximation of L_a and can have very large errors. Green et al[29] observed that sizes of graphite microcrystallites in coal could be measured reasonably accurately if aromatic structures predominate; otherwise the results were highly erroneous. It has also been observed that the formula works best for crystallite sizes in the range of 2.5–100nm.[11,37]

The equation was originally formulated using spectra obtained using a 488nm Kr^+ excitation source. The Raman spectra of carbon materials is highly dependent on the excitation source used (discussed later in this chapter), making it necessary to modify the original equation if a different source than 488nm is used. Recently Endo et al[35] studied carbon fibres using a HeNe 633nm source, similar to the source used in the present study. They adapted Tuinstra and Koenig's equation into equation 3.4 to account for the use of this different source.

$$L_a = 12\left(\frac{I_G}{I_D}\right) \qquad \textbf{(3.4.1)}$$

Sze et al[27] used a simplified model comparing the graphite crystal structure to a cylinder. The intensity of the G band is a measure of the average volume of the ordered graphite crystals in the sample. The intensity of the D band is inversely proportional to the average crystal size (within a range). The D band should only be observed for crystals smaller than a few tens of nanometers and its precise origin is still in doubt. The D band intensity is a measure of the total area of the crystal edges and the ratio of D to G would be inversely proportional to the radius of the crystal. The D' band originates in the surface modes and is characteristic of layers which have a graphite layer on one side and something else on the other. The D' band intensity reflects the surface area of the average crystal (if the influence of the something else is ignored). In the cylindrical approximation, the ratio of the D' peak to the G peak is inversely proportional to the average thickness of the crystals. If the ratio of D' to G is large the surface to volume

ratio of the graphitic crystallites is large. This approximation is subject to other influences and can not be applied quantitatively.

3.4.2.4 Bands in addition to the G, D and D' bands

A fourth band occurring between 1500-1550cm^{-1} has also been observed.[25, 40-43] This band has been generally attributed to defects/imperfection in the graphite structure[40,42,43] More specifically Zou et al[25] assigned a band at about 1500cm^{-1} to impurities in an amorphous carbon; in this case it was due to the incorporation of nitrogen into an amorphous carbon film. Kraft et al[41] attributed a band at 1530cm^{-1} to sp^2-bonded carbon clusters in a sp^3-network of amorphous carbon. This band has been denoted the D" band.[43]

Wang et al[44] observed a saddle shaped feature at 200-900cm^{-1}, which may be related to the phonon density of states of graphite (see figure 3.4.4). They found this feature to be sensitive to changes in the short-range order in amorphous carbon. The main peaks for carbon are found in the 1000-2000cm^{-1} region but that region is complicated by the presence of Raman scattering from both fully amorphous carbon and partially ordered regions. The lower frequency region is about one quarter in intensity compared to the 1000-2000 cm^{-1} region but it is more intense than the 2900cm^{-1} band (discussed in the next section) and is not contributed to by the scattering from totally graphitic carbon. As the sample becomes more ordered the two bands at 400cm^{-1} and 800cm^{-1} progressively decrease in intensity and shift to higher wavenumbers. They suggest that changes in this low frequency feature with changes in order are easier to quantify than the changes in the main peaks and this feature may give more accurate information on the short-range order of amorphous carbon materials.

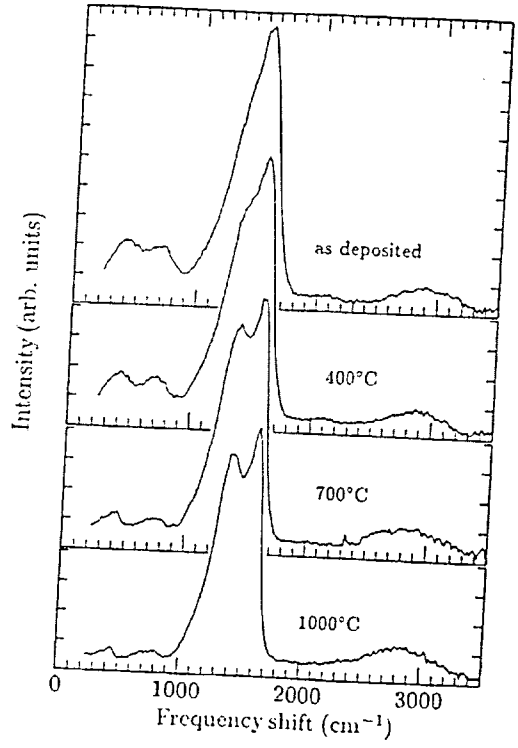

Figure 3.4.4: Raman spectra of amorphous carbon films showing the low-order saddle-shaped feature between 400-800cm^{-1} as observed by Wang et al[44]

A summary of the bands observed in the first-order Raman spectra of graphitic carbon materials is given in table 3.4.1

Position (cm^{-1})	Assignment
1575 (G band)	E_{2g} mode of natural single crystal graphite
1581	E_{2g} mode of HOPG
1582-1610	E_{2g} mode of amorphous/disordered carbon
1320-1360 (D band)	A_{1g} disorder induced mode
~1620 (D' band)	Due to disordered graphitic layers located at crystal boundaries
1500-1500 (D" band)	Due to defects in the graphite structure induced by impurities
400 & 800 Saddle shaped feature	Disorder induced feature for highly amorphous graphitic materials

Table 3.4.1: bands observed in the first-order Raman spectra of graphitic carbon materials

3.4.2.5 Second-order Raman bands of graphitic carbon materials

Vidano and Fischbach[24] refer to a weak band at ~2270cm^{-1} which they attributed to a surface impurity mode in single crystal graphite. They also found a new band at 2720cm^{-1} ± 5cm^{-1} in ordered carbons. This band was denoted the G' band as it had similar intensity to the G band. In highly ordered graphite G' split into two bands called the G'_1 and G'_2 bands both having a full width at half maximum (FWHM) of 40-60cm^{-1}. G' is characteristic of graphitic carbon, consists of two bands at least in graphitic carbon but is one broad band in disordered carbon, it can be intense despite small crystallite size and random layer stacking disorder. In very disordered materials it's FWHM was almost 150cm^{-1} and was approximately 40cm^{-1} in imperfect graphites. This G' band was attributed to the first overtone of the D band (1360cm^{-1} x 2 = 2720cm^{-1}). Wright et al[45] reported weak bands at 2440cm^{-1} and 3245cm^{-1} as well as a strong band at 2735cm^{-1}, in single crystal graphite; and, in imperfect synthetic graphite, an additional band at 2950cm^{-1} whose intensity correlated with that of the D band. Wang et al[20] reported second-order lines at 2450cm^{-1}, 2722cm^{-1}, 2950cm^{-1}, 3240cm^{-1}, 3654cm^{-1} and 4300cm^{-1}. These bands were assigned to various overtones and combinations as follows; 2950cm^{-1} from a combination of the G band (1580cm^{-1}) or the D' band (1620cm^{-1}) with the D band (1360cm^{-1}); 3242cm^{-1} could be the 1st overtone of the D' band, 4300cm^{-1} could possibly be a combination of the 1st overtone of D and G, that is 2D + G; the weak peak at 3654cm^{-1} could be 3 x 1220cm^{-1}, 1220cm^{-1} being a peak from the calculated phonon density of states; the band at 2244cm^{-1} could be 2x1220cm^{-1}. In fact, all the bands at 2444cm^{-1}, 2722cm^{-1}, 3242cm^{-1} and 3654cm^{-1} could be overtones for forbidden fundamentals. Wilhelm et al[22] reported a sharp peak at 3248cm^{-1} which was interpreted as being a direct indication that the maximum phonon energy of graphite occurred at some finite value of the wave vector and not the zone-centre point. They observed three broad bands in the spectra of single crystal graphite and HOPG; a strong feature near 2710cm^{-1} and two weaker ones at 2450cm^{-1} and 3250cm^{-1}. They discovered that the spectra of these materials were uniformly and strongly polarised in the region between 2300 – 3300cm^{-1} and concluded that the second-order spectra of highly ordered carbon was thus due to overtones and not due to combinations. The 3250cm^{-1} was associated with an overtone of

the D' band and it was suggested that the 2950cm^{-1} band was a combination of D and D'. They also observed a splitting of the G' (2710cm^{-1}) and attribute this to a sharpening of the features in the phonon density of states upon establishing good 3-D stacking and the observation of the doublet means there is sufficient long-range order. As the stacking becomes more turbostratic the G' band coalesces into a single broad peak. Green et al[29] observed that the degree of splitting of the two bands making up the G' band is proportional to the perfectness of the 3D lattice. Kelemen and Fang[28] observed a band at 3050cm^{-1} and assigned it to a disorder induced Raman feature. Popvitcheva et al[39] suggest weak bands they observed at 2965cm^{-1} and 3041cm^{-1} could be due to symmetric and anti-symmetric stretching of methyl groups and other bands at 3411cm^{-1} and 2500cm^{-1} could be due to ν(OH) and ν(CO) vibrations respectively. This hypothesis was possible for their samples as they analysed carbon from soot produced by an aircraft, which would be expected to have a high organic content.

A summary of the bands observed in the second-order Raman spectra of graphitic carbon materials is given in table 3.4.2.

Position (cm^{-1})	**Assignment**
2270	Surface impurity mode in single crystal graphite
~2450	2 x 1225 (perhaps)
2720 (G' band)	2 x D
~2745 & ~2710 (G'$_1$ and G'$_2$ bands)	Splitting of the G' band for highly ordered graphite
2970	D' + D
3250	2 x D'
4300	2970 + D

Table 3.4.1: reported bands in the second-order Raman spectra of graphitic carbon materials

Figure 3.4.5 for Wilhelm et al[22] shows the Raman spectrum of imperfect graphite in the 1000cm^{-1} to 3500cm-1 region. This sample's spectrum included the disordered induced D and D' bands but it was also significantly ordered to show the G' band starting to split into the G'$_1$ and G$_2$' bands. The bands at 2450cm^{-1} and 3245cm^{-1} are also shown.

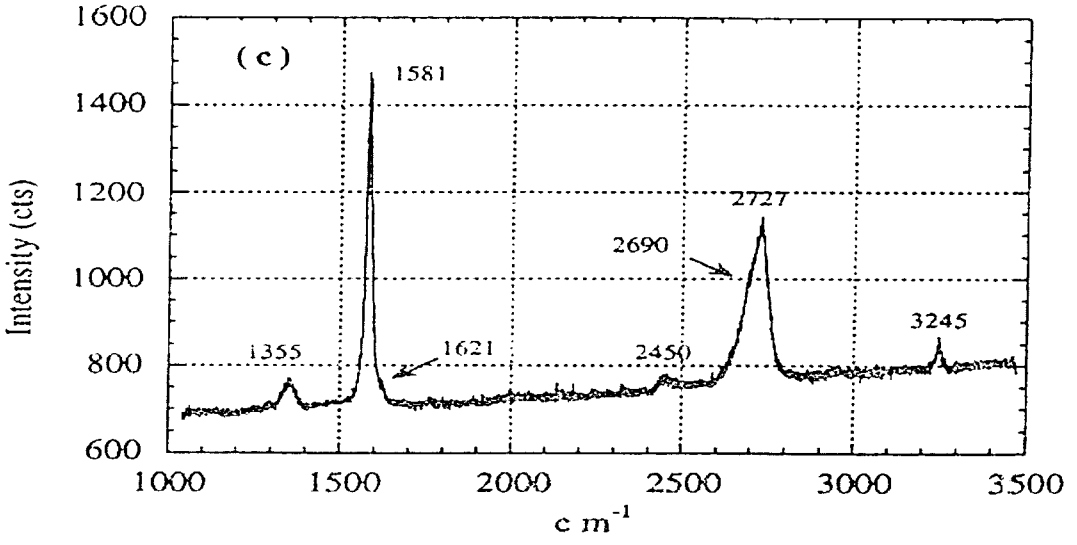

Figure 3.4.5: The Raman spectrum of imperfect graphite from Wilhelm et al[22]

3.4.3 The affect of different treatments on the Raman spectra of graphitic materials

3.4.3.1 Heat-treatment

There have been several Raman studies on the effects of heat treatment on carbon materials.[11, 24, 35, 29] Generally the pyrolysis of organic materials evolves volatile species during carbonisation at temperatures between 400-700°C. The formation of 2-D graphene sheets of pyrolytic carbon (polymerisation) typically occurs between 600-1200°C. Annealing of pyrolytic carbon at 1200-3000°C produces gradual ordering of the sheets (graphitisation), eventually reaching a 3-D lattice of crystalline graphite.[11] During graphitisation the G' band at 2720cm^{-1} appears. It is not seen in samples heated to less than 1000°C but its intensity increases with increased heat treatment temperature (HTT) and it is well developed by 2000°C and eventually splits into two bands at temperatures approaching 3000°C.[24] This splitting is indicative of the development of well-ordered graphite. The G' band shifts to higher wavenumbers with increasing temperature. The D line narrows and the I_D/I_G value decreases. Endo et al[35] reported that with an increase in HTT from 700°C to 3000°C an increase in the intensity and a narrowing of the G band with a decrease in intensity and width of D. With a HTT between 2000-3000°C a strong

peak at 2660cm^{-1}(G') and a weak peak 1620cm^{-1}(D') appear, which they attributed to the development of an ordered graphite structure. Upon reaching a HTT of 3000°C the D' band decreases in intensity and the G' band increases. 2000°C was recognised as a transition temperature from turbostratic to graphitic carbon. At this temperature d_{002} (calculated from XRD traces) becomes <3.44Å indicating the 3-D graphite structure starting to grow. The G band generally downshifts with increasing HTT. For HTT ≤2000°C the change in position is relatively fast and the frequency becomes relatively stable between 2000-3000°C. The change below 2000°C corresponds to the development of in-plane ordering due to carbonisation and between 2000-3000°C the change occurs due to the development of a 3-D graphite structure. Above 2000°C the decrease in the FWHM of D band is very small but the G band still decreases and approaches the value of crystalline graphite (~30cm^{-1}) as the contributions from the zone-centre phonons becomes more dominant. In glassy carbon the relative peak height and bandwidth decreases with increasing HTT. When heated to 3000°C the G band FWHM in glassy carbon decreases from 80cm^{-1} to 50cm^{-1} compared to a decrease from 140cm^{-1} to 25cm^{-1} for pyrolytic carbon.[29] The $I_{D'}/I_G$ value is 0.3 to 0.4 in disordered carbons and decreases with increasing HTT and is zero for well ordered graphite. The D' FWHM is typically 30-55cm^{-1} and decreases with increasing HTT. The D bandwidth is much more sensitive to changes in temperature than the D' band even though they both originate from disorder. The D band's FWHM is typically 200cm^{-1} in a disordered carbon but decreases to about 50cm^{-1} when heated to 2000°C. I_D/I_G decreases with increasing HTT until it is about 0.9 at 2000°C. The D' band becomes a shoulder on the G at this temperature.

3.2.3.2 Treatment by grinding

The effects of grinding on highly ordered crystalline graphite samples has also been studied.[16,43] Wakayama et al[16] observed that grinding causes a rapid reduction in the range of planar stacking (L_c) but only a slight reduction in the basal plane diameter (L_a). The width of the D band decreased with the reduction of L_a. Ground graphite yielded a smaller value of FWHM than heat-treated carbon for a given L_a. This indicated that the crystallites of the ground graphite have more uniform boundaries and less-defective

hexagonal graphite lattice than the heat-treated carbon. Salver-Disma et al[43] performed shock and shear grinding on graphite samples. They observed a broadening of the G band and the formation of a D band at 1350cm^{-1} and a D' band at 1610cm^{-1}. A fourth band at 1510cm^{-1} (D") was also observed. The D width and the I_D/I_G ratio increased with increasing grinding time. They attributed this to a decrease of L_a as an increase in the I_D/I_G (R) value corresponds to a decrease in L_a, according to equation 3.4.2.

3.4.4 Raman spectroscopy of diamond/diamond-like carbon materials

Pure crystalline diamond has a single Raman line for a triply degenerated F_{2g} optical phonon belonging to O^7_h symmetry of fourfould coordinated sp^3 bonding.[46] This line occurs at 1332.5 ± 1cm^{-1} and is extremely narrow with a width of 2cm^{-1}.[11] (see figure 3.4.6) The position and width of this line has frequently been used to determine the quality of diamond materials. It shifts to higher wavenumbers with increased isotropic pressure but little broadening occurs. However, strain can reduce the cubic symmetry splitting the zone-centre phonon degeneracy and cause broadening. The diamond band usually occurs between 1325-1330cm^{-1} for nanocrystalline diamond but can be downshifted as far as 1320cm^{-1} owing to size effects.[41] Nistor et al[47] deposited nanocrystalline diamond films in a mixture of CH_4 and air. As the CH_4 increased from 3 to 100% the diamond band shifted from 1334cm^{-1} to 1337cm^{-1}. They attributed the shift to compressive stress in the film. Prawer et al[48] used changes in position from 1333cm^{-1} as an indication of stress in diamond films, with ± 0.3cm^{-1} accuracy. Anisotropic (axial or biaxial) stress can lift partially or completely the degeneracy of the F_{2g} diamond mode and the zone-centred optical phonon peak at 1333cm^{-1} can split into two or three components. The magnitude of the splitting is linearly dependent on stress with a positive shift for compressive stress and a negative shift for tensile stress.

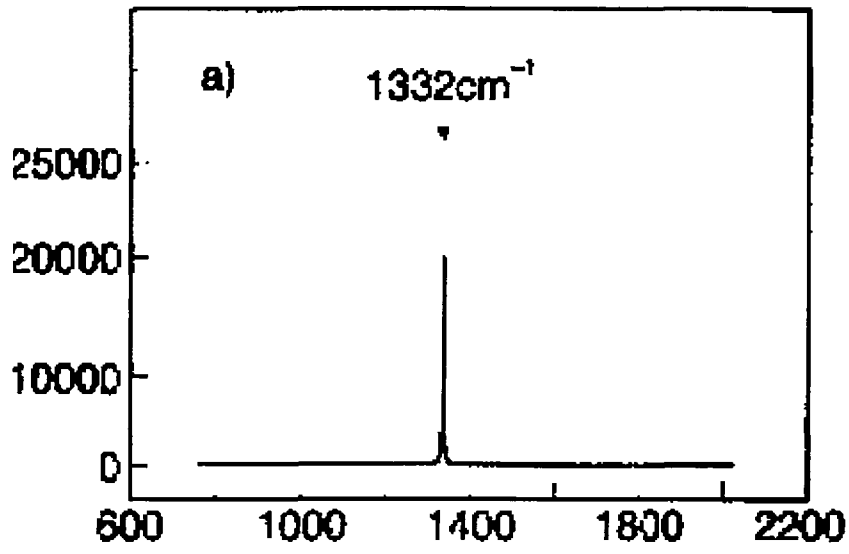

Figure 3.4.6: Raman spectrum of crystalline diamond from Salzer et al[82]

Raman bandwidth contains information about the phonon's lifetime, which can be correlated with the concentration of point defects.[49] In diamond there are complications since the band at 1333cm^{-1} is triply degenerated and often splits for diamond materials due to in-plane stresses that develop as the grains grow laterally. This phenomenon causes a broadening due to the overlapping of the bands with their central positions slightly shifted, which can be confused with deterioration in the crystalline quality. Zou et al[25] observed a broad diamond band with a width of 25cm^{-1}. They attributed this broadening to a diamond phase with a high density of defects resulting in a significant reduction in phonon lifetimes. Arora et al[50] also reported broadening and a blueshift of the 1333cm^{-1} peak and attributed it to scattering from defects and compressive strain.

Defects in the diamond structure and reduction in crystallite size leads to a relaxing of the k=0 selection rule for Raman scattering, allowing other modes besides the one at 1333cm^{-1} in crystalline diamond.[51] These new modes are responsible for lines at ~1470cm^{-1}, ~1240cm^{-1}, ~1190cm^{-1} and ~1100cm^{-1}. Due to the wide variety of possible amorphous structures and the different types of materials being studied large differences for the positions of these bands have been reported. All these bands have been associated with sp^3-bonded carbon phases.[41, 47, 52-56] The 1240cm^{-1}, 1190cm^{-1} and 1100cm^{-1} lines have been denoted as diamond prebands due to small sp^3-bonded clusters and are usually present in nanocrystalline diamond.[41,51] These lines are representative of the DOS of amorphous diamond. A band at 1248cm^{-1} has been observed in nitrogen doped carbon films [25] and it was estimated that the stretching frequency of tetrahedral covalent N-C

single bonds is in the range of 1212-1265cm^{-1}. So, it is possible that the presence of nitrogen as an impurity can contribute to the 1240cm^{-1} band. A band at 1133cm^{-1} has been assigned to small or defective nanocrystals of diamond or a wurtzite-like precursor structure.[50] This band may also be due to disordered tetrahedrally bonded carbon at grain boundaries.[48] A band at 1120cm^{-1} has been attributed to surface phonon modes arising from the cluster size of 1-2nm.[46,57] Another band at 1170cm^{-1} has been assigned to hexagonal diamond[58] Nemanich et al[59] agreed with this assignment but also suggested it was due to a sp^3 rich phase or nanocrystalline diamond. The assignment of the 1470cm^{-1} band to sp^3-bonded carbon is controversial because the diamond-like structure does not allow first order Raman modes higher than 1332cm^{-1}, even in the presence of disorder.[60] Two results that were noted from the calculated VDOS of crystalline diamond.[48] These were a large peak at around 1200cm^{-1} and that there was no vibrational modes for sp^3-bonded carbon at energies exceeding 1400cm^{-1}. Marcus et al[60] suggested that a band at 1470cm^{-1} could be due to the presence of fullerenes as it is the dominant band for C_{60}. 1470cm^{-1} may also arise from tetrahedrally bonded diamond precursor phase and tetrahedrally bonded atoms linking small domains comprising of stacked aromatic planes. Yet another possibility for 1470cm^{-1} and 1140cm^{-1} is the presence of polymeric chains like polyenes or transpolyacetylene. In a recent study Ferrari and Robertson[61] argue that the band at ~1150cm^{-1} in nanocrystalline diamond films is not due to sp^3-bonded carbon but from a coexisting sp^2-phase and suggest that this sp^2-phase is transpolyacetylene. The theory behind their argument is discussed in more detail in the next section.

Approximate Position (cm^{-1})	Assignment
1333	F_{2g} mode of crystalline diamond
1470	Nanocrystalline/disordered diamond
1240	Nanocrystalline/disordered diamond
1190	Nanocrystalline/disordered diamond
1100	Nanocrystalline/disordered diamond

Table 3.4.3: bands observed in the Raman spectra of diamond/diamond-like carbon

3.4.5 Dependence of Raman Spectra of Carbon Materials on Excitation Wavelength

In principle Raman studies should allow the identification and estimation of sp^2 and sp^3 sites in carbonaceous materials, owing to the fact that the zone-centred optical phonons in graphite and diamond occur at well separated frequencies of $1580cm^{-1}$ and $1332cm^{-1}$, respectively.[62] However, the high frequency stretching modes of sp^2-bonded carbon are overemphasised due to the to the π-π^* transition resonance effect.[63] The sp^2-bonded carbon network exhibits resonance enhancement in the Raman cross-section since the local sp^2-bonded carbon energy gap of approximately 2eV is comparable with the energy of the incident photons. The visible 488nm, 514nm and the 633nm sources having photon energies of 2.54eV, 2.41eV and 1.96eV respectively.[64,65] The sp^3 atoms do not exhibit such a resonance effect because of the higher local bandgap of approximately 5.5eV. As a result the Raman scattering cross-section for sp^2-bonded carbon has been estimated to be 50-100 times greater than sp^3-bonded carbon, when using a visible Raman excitation source.[11, 62, 63] Even in carbon materials with less than 20% sp^2-bonded carbon the G and D bands dominate the spectra making it difficult to identify sp^3-bonded carbon. The use of visible Raman spectroscopy for the characterisation of sp^3 containing carbon materials such as DLC, tetrahedral amorphous carbon (ta-C) and hydrogenated tetrahedral amorphous carbon (ta-C:H) has been based on empirical relationships between bonding and shifts or broadening of the G band.[66] In the last decade there have been a number of investigations into the effects of using different excitation wavelengths for the Raman analysis of carbon materials.[46,60,64 - 69] Wagner et al[64] observed a large increase in intensities for G and D bands separately, depending on the excitation wavelength. They studied high, medium and low purity diamond films using different laser wavelengths. The use of different laser wavelengths resulted in different intensities, band shifts and spectral resolution. They suggested that it is best to study almost perfect diamond with a near- IR source (782nm) and disordered/nanocrystalline diamond with a UV (244nm) source. They proposed the reason for this behaviour was due to differences in resonance behaviour of Raman scattering from amorphous sp^2- and sp^3-bonded carbon or possibly clusters of sp^2-bonded carbon of various sizes contributing differently to the observed

Raman spectrum for different exciting photon energies. Sinha et al[65] studied HOPG and resonant profiles for the lines at 2700cm^{-1} (G'), 1580cm^{-1} (G) and 41cm^{-1} (low frequency E_{2g} mode) were investigated using excitation sources ranging in photon energy from 1.8-2.6eV. All three bands increased in resonance with increasing energy. With the 1580cm^{-1} mode being highly resonant followed by the 2700cm^{-1} mode and weak resonance for the 41cm^{-1} mode. There was no correlation between the first- and second- order resonance. Gilkes et al[66] avoided the resonance of the sp^2-bonded sites in ta-C and a-C by using a UV 244nm (5.1eV) excitation source as it provided a more equally weighted measure of the VDOS. This occurred due to a suppression of the dominant resonance Raman scattering from sp^2 sites and the possible increase in intensity from sp^3 sites, for which resonance is expected to be attained as the excitation photon energy approaches the band gap energy (~5.5eV) of diamond-like bonding. They first analysed various ta-C and a-C films using 514nm excitation. The a-C was dominated by a G band at 1570cm^{-1} and a small D band at 1350cm^{-1}. The ta-C was dominated by a broad G band at 1600cm^{-1} which was composed of a G band with a small shoulder around 1350cm^{-1} corresponding to a D band. They repeated the work using 244nm excitation. The ta-C had two bands centred around 1100cm^{-1} and 1650cm^{-1}. 1600cm^{-1} had moved to 1650cm^{-1} and was sharper with no shoulder from D. 1100cm^{-1} reduced in intensity and shifted upwards in films with smaller sp^3 content. A single band at 1600cm^{-1} (G band) and a small feature at 1300cm^{-1} (D band) were observed for a-C. The feature at ~1100cm^{-1} in ta-C was attributed to sp^3 bonding, due to the amplitude increasing with increasing sp^3 content. The feature had already been seen in EELS and the peak lies at the maximum of the calculated VDOS of a sp^3 bonded network. This band at 1100cm^{-1} has been referred to as the T (for tetrahedral) band.[68] In a more recent paper Gilkes et al[70] observed that even with UV excitation at 244nm there is strong resonance of sp^2-bonded carbon and use this as a possible explanation for why they observed positions as high as 1670cm^{-1} for the G band in DLC films. Although the photon energy of the UV source is far from the sp^2 bandgap energy, the π-π^* separation is highly dependent on cluster size, becoming large as cluster size decreases. The bond strength of the olfinic bonds is also affected by cluster size. The bond order changes from 1.33 for graphite to 1.5 for an isolated aromatic ring, to 2 for a simple olefinic bond, which may explain the ~1650cm^{-1} position being much

higher than graphite. The observed spectra were interpreted as being composed of contributions from overlapping spectra from isolated sp^2-bonded clusters with a range of different sizes. A G band observed at 1630cm^{-1} could be due to the diamond split interstitial defect or so-called dumbbell effect.[48] This occurs when one carbon is replaced with an sp^2-bonded pair of carbon atoms centred on the missing atom. Adamopoulos et al[71] also observed a T peak at 1100cm^{-1} and a G peak near 1650cm^{-1} when using 244nm excitation. The T peak was identified as a VDOS feature in ta-C resulting from C-C stretching vibrations at sp^3 sites.

Okada et al[46] studied microcrystalline diamond films using 514nm, 325nm and 244nm excitation sources. The D and G bands at 1355cm^{-1} and 1580cm^{-1} were observed for a film with a low fraction of sp^3-bonding, using the 514nm excitation source. New bands appeared at 1480cm^{-1} and 1150cm^{-1} as the fraction of sp^3-bonding increased. Using the 325nm (4.8eV) excitation source there was a clear diamond peak at 1332cm^{-1}, and a remarkable enhancement of the 1580cm^{-1} band with a shoulder at 1150cm^{-1}. With the 244nm excitation source the 1332cm^{-1} band was enhanced and the 1580cm^{-1} band was weakened. It appeared unusual that both the 1580cm^{-1} and 1332cm^{-1} bands were enhanced with the 325nm source. 4.8eV is close to the onset of the σ-σ^* transitions in both sp^2- and sp^3-bonded carbon. They suggest the enhancement of both peaks at 325nm is because resonance enhancement of Raman cross-section due to sp^2-bonded carbon still remains and that the σ-σ^* transition in both sp^2 and sp^3 bonded carbon is possibly induced. Wang et al[20] observed that the D band position changed with excitation wavelength, reporting a shift from 1360cm^{-1} to 1330cm^{-1} when the source energy decreased from 488nm to 647nm. They studied a variety of carbon materials and reported that the D band relative to the G band varies with carbon type because of varying edge density. One explanation they proposed for this dispersion in the D band position was a change in the sample depth, leading to variation in the spectrum if the structure varies with depth. Another possibility they proposed was that the D band was resonantly enhanced; so different subpopulations of crystallites may be sampled at different incident wavelengths. They were not certain of an exact mechanism but there was scattering of

different photons from phonons of different energy and they suggested that different laser wavelengths sampled different points along the phonon dispersion curve.
Pocsik et al[32] recently proposed that Raman resonance causes the dispersion for the D band for different excitation energies. This is as a result of coupling of the k-vector of the electronic states involved in the light absorption with the k-vector of phonons contributing to the Raman spectrum. Their hypothesis is that from all possible modes in the Brillouin zone, only those contribute to the Raman spectrum that are resonantly enhanced. To find the electronic transition energies for the respective exciting photon energies, electronic band structure need to be inspected. Low lying electronic transition excitations are restricted to the π-electron system because the lowest σ-gap amounts to more than 5eV in graphite. The π-π^* transitions cover a continuum of excitation energies from 15eV at Γ to 0eV at the edge of the Brillouin zone at K. The k-vectors of the excitation energies they used occurred at k-vectors in the neighbourhood of the K and M points, i.e., the edges of the Brillouin zone. So, by tuning the excitation energy the k-vector of the optical transition is effectively varied over a range. They assume that in the resonant increase of the Raman scattering process the k = 0 selection rule of ordinary Raman is replaced by a new selection rule such that the resonant scattering cross-section occurs for those phonons which have the same k-vector as that of the electronic transition responsible for the resonance. They studied a microcrystalline graphite sample using excitation energies in the range of 1.16 - 4.13eV and the dispersion of the D peak agreed well with their calculated phonon dispersion curves.

The dispersion in the position of the bands at 1150cm^{-1} and 1450cm^{-1} in nanocrystalline diamond films has also been attributed to Raman resonance.[61] Ferrari and Robertson[61] argue that the band at ~1150cm^{-1} is not due to sp^3-bonded carbon but from a coexisting sp^2-phase. They propose these bands cannot be a due to $k \neq 0$ phonons activated by disorder because the grains are too large to observe a zone boundary peak. Phonon confinement allows the participation of phonons with a wave vector $k \approx 2\pi/d$, where d is the grain size. Grains of 5-100nm would still favour modes quite close to Γ, rather than modes nearer the zone boundary at L, which contribute most to the VDOS maximum. In visible Raman, sp^2-bonded carbons have much larger cross section than sp^3-bonded

carbon but the intensity of the 1150cm^{-1} band is sometimes equivalent to or greater than, the amorphous carbon phase and the crystalline diamond phase. The 1150cm^{-1} and 1450cm^{-1} bands disperse by 50-100cm^{-1} with excitation energy. If these were DOS features, their positions should stay fixed. They both decrease in intensity, compared to diamond, as excitation energy is increased. If they were due to sp^3-bonded carbon, they should increase with increasing excitation energy due to resonance, as the energy gets closer to the band gap. However, the 1150cm^{-1} band disappears with UV 244nm excitation, which is the type of behaviour expected for sp^2-bonded carbon. They also rule out 1150cm^{-1} being due to hexagonal diamond, as suggested by other authors, because it is known to have a mode at 1323cm^{-1}, just below that of cubic diamond. In studies using 325-229nm excitation they observed a peak at 1050cm^{-1}, which was not present with visible excitation. This feature appears due to resonance of sp^3-bonded carbons, which is a true VDOS of diamond feature and has opposite dependence of excitation wavelength to the 1150cm^{-1} band so they cannot be related. The bands at 1150cm^{-1} and 1450cm^{-1} are roughly the sum and difference combinations of C=C chain stretching and CH wagging modes. Transpolyacetylene is an alternate chain of sp^2 carbon atoms, with a single hydrogen bonded to each C. The dispersion arises because of the conjugated π bonding along the PA chain is broken into segments of different conjugated lengths. The local band gap of each segment increases as the length decreases. Varying the excitation energy selectively tunes into a segment with that length and excites it. The vibrational frequency of the segments also varies with the conjugation length, so this mode wavenumber increases as the segment length decreases. They found a length of 6-15 C=C units, as the excitation changes from 325 to 633nm. So, they assigned these peaks to transpolyacetylene lying in grain boundaries. They also observed a band at around 1240cm^{-1}, which could also possibly arise from transpolyacetylene. But it is weaker than the other two bands and does not show significant dispersion.

3.4.6 Effects of carbon bonding hybridisation on Raman spectra

Raman spectroscopy probes the local environment of sp^2- and sp^3-bonded carbon.[72] In the last section the effect of different energy sources on the Raman spectra of carbon

materials was discussed. This involved a change in Raman spectra due to different Raman scattering cross-sections of each hybridised species. In this section the change in the spectra due to different ratios of sp^2:sp^3 hybridisation when using the same excitation source is discussed.

As mentioned in the previous section when using UV excitation there are two major peaks one at 1100cm^{-1} (T peak) and another at ~ 1650cm^{-1} (G peak). Gilkes et al[70] observed that the T peak became more symmetrical with increasing sp^3-bonded carbon. The T band intensity increases and the G band shifts upwards with increasing sp^3-bonded carbon. The ratio of $I_T/I_T + I_G$ increased with increasing sp^3-bonding. The T and G peak widths do not change significantly with increasing sp^3 content. The T band shifts downwards with increasing sp^3-bonded carbon because the sp^2-bonded carbons have the ability to form chains, which have higher frequencies. The G peak changes in intensity with sp^3 content because if the sp^3 content decreases the relative proportion of sp^2-bonded pairs increases and the number of larger clusters of sp^2-bonded carbon increases resulting in increased order and a decrease in the G band position. An increase in the sp^3-bonded carbon results in an increase in compressive stress and an increase in density. This results in a downward shift for the G band. As sp^2-bonding increases there will be more sp^3-sp^2 bonding. These bonds are shorter than sp^3-sp^3 bond hence shifting the G band to a higher a frequency with increasing sp^2-bonded carbon. Sp^3-bonding is under high levels of compressive strain. More sp^2 can break sp^3 bonds and relieve some of the local strain, reducing the mean separation of the sp^3 bonds and shifting the G band to a higher frequency. Prawer et al[73] studied diamond-like carbon films and monitored the changes in their Raman spectra with decreasing sp^2-bonded carbon. The films became more transparent, which was consistent with the increase in the optical bandgap as the films became more diamond-like. Spectra became more symmetrical and the G band position decreased as a function of sp^2 content but this was only a shift of 5cm^{-1} with a decrease from 40% to 20% sp^2-bonded carbon. Patterson et al[74] observed an upward shift for the G band and assigned it as a decrease in the sp^2 bond angle distortions. They also attributed an upward shift for the D band to a reduction in sp^3 or diamond-like bonding. Shi et al[68] studied ta-C using UV Raman. They reported that the G band position increases almost

linearly and the T band position decreases almost linearly as the sp^3 fraction increases. The T band position is almost exclusively related to the sp^3 sites. The nearest neighbour of sp^3-bonded carbon atoms can be an sp^3- or sp^2-bonded carbon. They assumed that the neighbouring atoms contain zero or one sp^2-bonded carbon atom for films with more than 80% sp^3-bonded carbon. As the sp^3-bonding decreases the amount of sp^2-bonded carbons near the sp^3-bonded sites increases, resulting in an upward movement of the T peak because of the high vibrational frequency of the sp^2-bonded atoms. They also observed that the I_T/I_G value increased almost linearly with increasing sp^3-bonding but the I_D/I_G value decreased with increasing sp^3-bonding. This was attributed to the fact that the size of sp^2-bonded clusters decreases as the sp^3-bonded fraction increases.

3.4.7 Raman Spectroscopy of Carbon from Coal and DPM

It is well know that in response to increasing temperatures and time, organic matter undergoes progressive maturation (coalification).[75] The end product of coalification is graphite and most major graphite deposits are considered to be organic in origin. Mechanisms of coalification from peat through anthracite are generally well understood. Coals can contain approximately 75-95% carbon and anthracite, the coal dust studied in this work, contains around 95% carbon. It is a naturally occurring hard coal, which shows some degree of graphitisation and a low content of impurities when compared to other hard coals but it still contains considerable amounts of H, N, O and S from its organic precursors.[13] The maturity level of sedimentary organic matter is an important geological parameter for coal.[28] Traditionally, optical microscopic methods such as the measurement of reflectance of vitranite in coals (vitranite reflectance, $\%R_0$), which is a function of the interaction of the electric field of incident polarised light and the electric field within the carbon lattice, is used as a measure of coal maturity.[29] The higher the R_0 the more mature the sample. Samples with low maturity are called low ranking soft coals and samples with high maturity are called high ranking hard coals. Since Tuingstra and Koenig first investigated black graphitic materials using Raman spectroscopy there have been a number of Raman studies on coal samples investigating their structure and maturity.[13,26,29,76-80] In 1971 Friedel and Carlson[76] performed the first Raman studies on

coals. They observed only D and G bands. In 1972 they studied a wide variety of coals ranging in carbon content from about 74% for a lignite sample to about 94% in an anthracite sample[77]. They observed the G', G and D bands. There was no general trend for band positions with increasing rank but the bandwidths appeared to decrease with increasing rank and the D band intensity and I_D/I_G ratio decreased. This was indicative of increasing order and larger crystallite sizes. Tsu et al[78] also observed the D and G bands for coal. They explained the occurrence of the D band at 1380cm^{-1} using the phonon dispersion of graphite and evaluated the size of the coal crystallites using Tuingstra and Koenig's equation. Zerda et al[79] studied a low ranking brown coal and anthracite. They found no correlation between the rank of coal and the position of the G and D bands but the separation between the two bands was greater in the anthracite with its G band having a width of 40cm^{-1} compared to 140cm^{-1} for the brown coal. The D bandwidth varied from 80cm^{-1} to 200cm^{-1}. This broadening was attributed to a crystallite size effect with the width increasing with decreasing size. They discussed two different effects in coal that influence the Raman band shape. The first effect being the limitation of microcrystallite sizes by the graphite plane boundary. The second effect being disorder induced in the local graphite-like crystallites by aliphatic components and various substituents linked to aromatic rings. The increase in the G bandwidth could have been associated with the first effect and the D band broadening may be related to both effects. The great number of possible disordered structures in coal can create a very broad D band. They also observed a broad shoulder at around 1270cm^{-1} in the anthracite sample. This was ascribed to a possible diamond-like atomic arrangement, which might be a downshifted 1332cm^{-1} diamond band due to defects. They ruled out the possibility of this band arising from a decrease of the scattering unit of symmetry because anthracite is a high-rank coal in which the translational symmetry is believed to be quite high. Green et al[29] performed Raman studies on different coals and cokes. They monitored the change in the Raman spectra of coal with different heat treatment temperatures. They also explained the origins of the G, D, D' and G' bands. Their results have already been incorporated into my explanation of these bands and the effects of HTT. From the Raman studies of coals Beny and Jehlicka[80] observed that higher maturity results in lower I_D/I_G ratios with a progressive narrowing of the bands and a slow disappearance of the D band. They

observed broad bands in anthracite with the D band having a width of 100cm^{-1} and the G band with a width of 65cm^{-1}. They also observed a very weak band at 2240cm^{-1} and a broad G' band centred at 2682cm^{-1} which did not split into G'_1 and G'_2, demonstrating low structural order. Kelemen and Fang[26] claimed that a difference in the appearance of the Raman bands for coals depends on the geologic history of the sample. They reported that the D band position shifts to lower energies with increasing R_0/maturity. This shift can exceed 50cm^{-1}. The G band shifts towards higher frequencies with increasing maturity but this shift does not exceed 10cm^{-1}. There is an increase in band separation with increasing maturity, which is a result of the narrowing of both the G and D bands leading to a decrease in the I_D/I_G value. However, even at high R_0 values the D bandwidth is much wider than the widths observed with imperfect graphites. During coalification the development of graphitic layered stacking is inhibited by defects and boundary structures including H, N, S and O.

There has been a limited number of Raman studies on DPM related carbon although Blaha et al[21] recognised its potential for studying carbonaceous material associated with urban airborne particulates as far back as 1978. They observed D and G bands at 1350cm^{-1} and 1600cm^{-1} respectively. From their studies they concluded that carbon in environmental samples is analogous to polycrystalline graphite. Zerda et al[81] studied combustion engine deposits and observed D and G bands at 1350cm^{-1} and 1590cm^{-1} respectively. They calculated the crystallite lateral size (L_a) for fuels with 22-44% aromatic content. The crystallite size increased with the aromatic content from 1.59nm to 1.82nm, which corresponded to 6 to 7 benzene rings across each graphene layer. Popvitcheva et al[39] performed Raman studies on aircraft combustor soot. They observed a D band at 1347cm^{-1} G band at 1595cm^{-1} and took the spectra to be a clear signature of disordered graphitic carbons. They assigned the D band to polyaromatic ring vibrations in small graphitic crystallites and the G band to carbon-carbon stretching vibrations. They also observed weak bands at 2965cm^{-1} and 3041cm^{-1}, which could be due to symmetric and anti-symmetric stretching of methyl groups from adsorbed hydrocarbons. Bands at 3411cm^{-1} and 2500cm^{-1} were assigned to -OH and CO- stretching vibrations respectively. Using Tuinstra and Koenig's equation they calculated the crystallite size to be in the 1.2-

3nm range. Size et al[27] studied diesel and urban particulates. They believed that the most important Raman features for the characterisation of the particles were the three graphitic G, D and D' bands. The DPM had a D band at 1395cm^{-1}. The D' line at about 1620cm^{-1} was the strongest feature and there was a very weak G band at approximately 1580cm^{-1}. The large $I_{D'}/I_G$ ratio suggested that the surface to volume ratio of the graphitic crystallites was large. The large shift in the maximum of the D line from the usual 1360cm^{-1} of disordered carbons suggested that the crystallite edges may have been chemically modified by the diesel combustion in a way that changes the electronic environment of the edge vibrations. In contrast to the diesel particles the three graphitic bands were located at frequencies more closely related to graphitic samples in the Raman spectra of the urban particles. This was attributed to a much lower fraction of diesel particles in the urban samples. The intensity of the D' band was still greater than the G band and they observed this for all their ambient air samples.

3.5 Qualitative Raman analysis of the coal dust and DPM samples used in the present Study

3.5.1 Introduction

The principle aim of this project is the development of a Raman spectroscopy-based method to analyse carbon-based particulates in mixtures produced from DPM and coal dust in coalmines. To achieve this aim it was necessary to determine a suitable combination of instrument parameters, which gave reproducible spectra for the coal and DPM samples. A number of experiments with various combinations of objective lenses, laser powers and scan times were carried out. These experiments are described in detail in chapter 5. In this section band positions, bandwidths and band intensity ratios of coal dust and DPM spectra will be used to give molecular/structural information about the samples.

3.5.2 Experimental

A Raman spectrum of a blank quartz fibre filter was taken in the 900-1900cm^{-1} range using x50 times objective, 250 seconds scan time and a 25mW 633nm HeNe laser at 10% power. Raman spectra were taken separately of coal dust and DPM, collected on quartz fibre filters, in the 200-4000cm^{-1} range using a x50 times objective, 250 seconds scan time and a 25mW 633nm HeNe laser at 10% power (2.5mW) to avoid heating the sample. The scans were repeated using the same instrument parameters but in the 900-1900cm^{-1} range, where the main first-order bands for carbon occur. 2nd derivative curves of the shorter range spectra were obtained. The 2nd derivative curves were used to estimate the number and position of the peaks present in the coal dust and DPM spectra. Aided by the information from the 2nd derivative curves, the peak fitting application in the Grams32 spectral processing software was used to peak fit the spectra. The peak positions, heights, widths and areas were also calculated using the fitting application.

3.5.3 Results and discussion

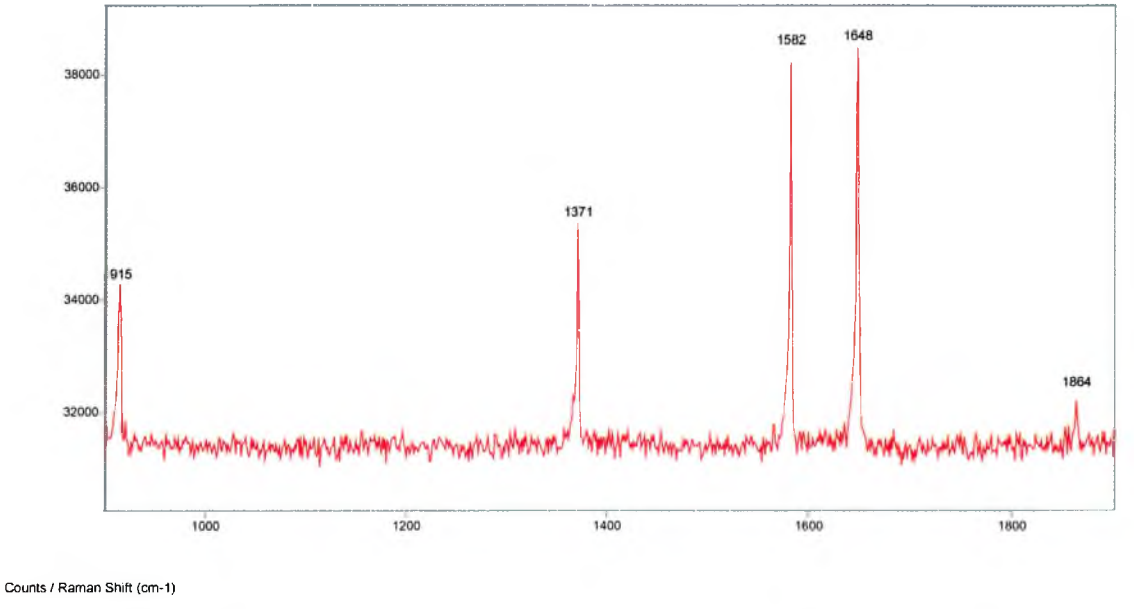

Spectrum 3.5.1: Blank quartz fibre filter, 250s, x50obj, 633nm Laser at 10%

From the Raman spectrum of the quartz fibre filter (spectrum 3.5.1) 5 bands at 915cm^{-1}, 1371cm^{-1}, 1582cm^{-1}, 1648cm^{-1} and 1864cm^{-1} were observed. These bands did not occur in the spectra of the DPM and coal dust shown here. It was originally presumed that these bands were due to the quartz fibre substrate. The assumption was supported by the fact that when there was a high concentration of sample on the filter there was little or no contribution of these bands to the spectrum. This suggested that at higher concentrations the filter was covered by the sample preventing a signal from the quartz. However, later in this work it was discovered that these bands were not due to the quartz fibre filters but they were actually unfiltered plasma lines from the 633nm HeNe laser. The true reason why these bands were more intense when there was less sample on the substrate was because the white substrate more effectively reflects the laser light when there is less of the black sample present to adsorb the light, resulting in more laser light being reflected into the instrument and an increase in the contribution due to the plasma lines. Also, when there is less sample there on the filter the signal due to the carbon particles is reduced and the laser plasma lines are not as significantly masked by the carbon spectrum.

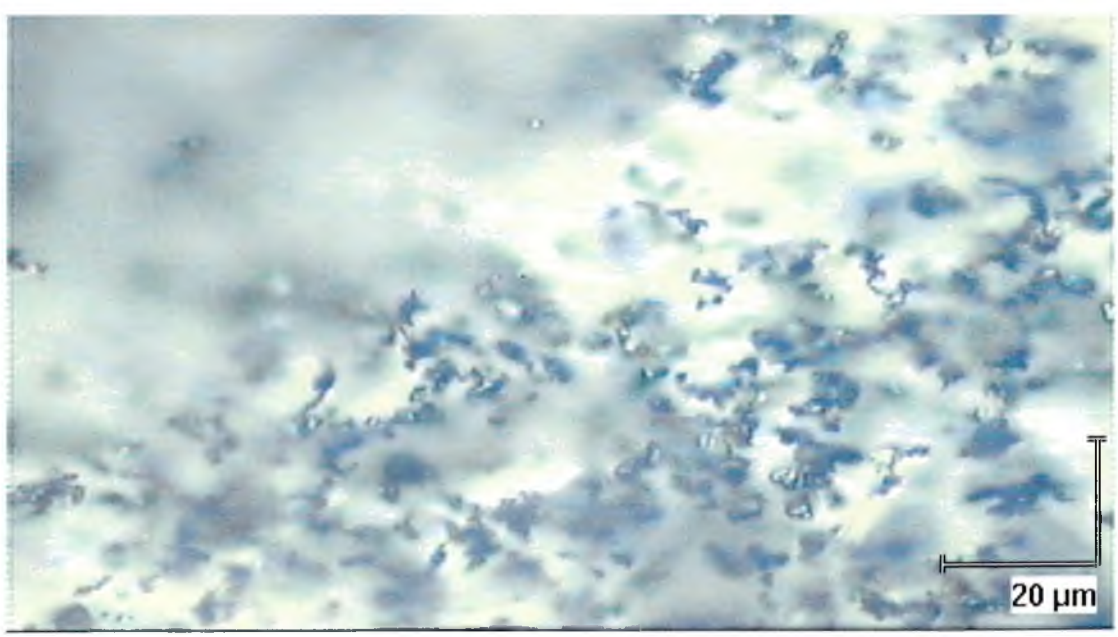

Fig 3.5.1: Coal dust on a quartz fibre filter (X20 magnification)

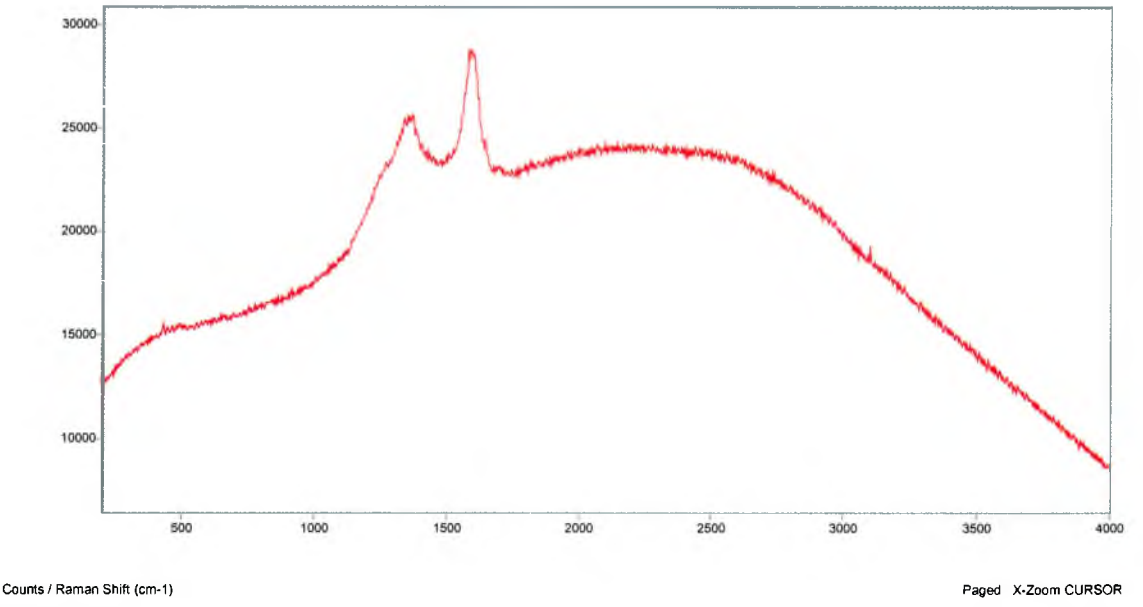

Spectrum 3.5.2: Coal dust on a quartz fibre filter, 250s, x50obj, 633nm Laser at 10%

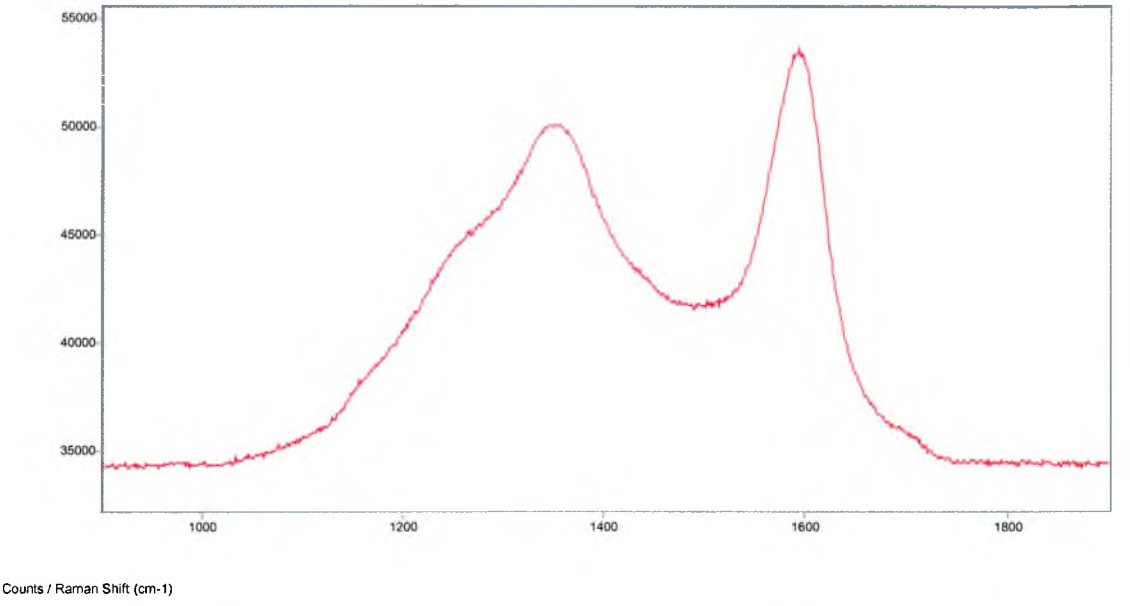

Spectrum 3.5.3: 271µg Coal dust, 250s, x50obj, 633nm Laser at 10%

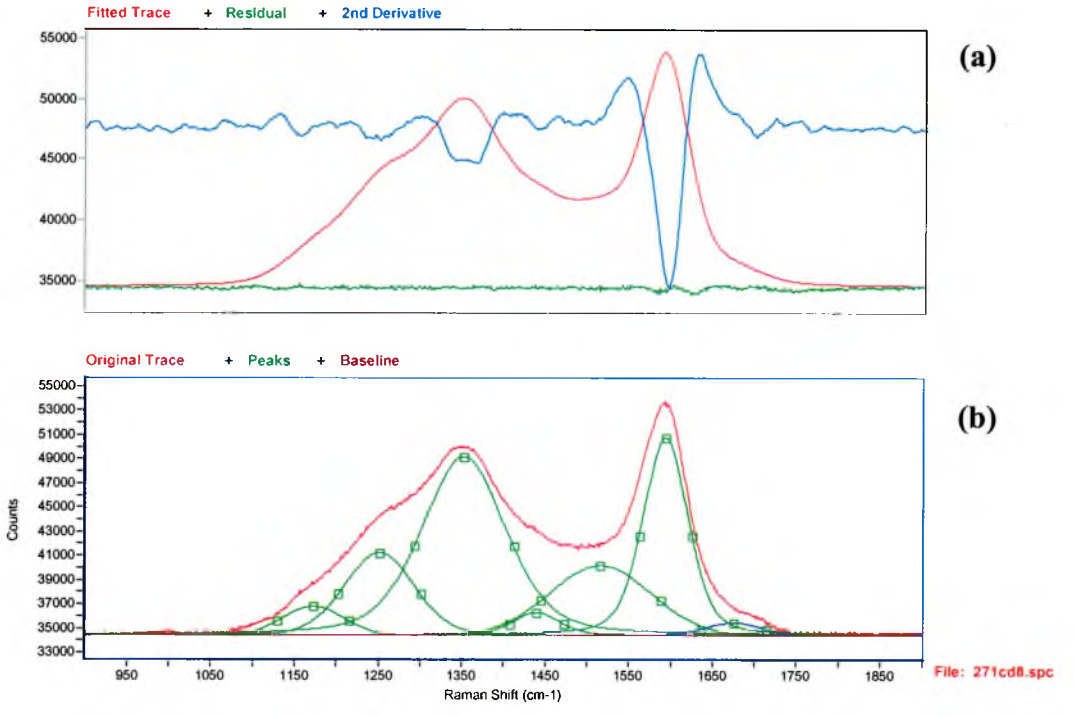

Fig 3.5.2: (a) Fitted trace, residual and second derivative of a coal spectrum

(b) Original coal dust spectrum and its fitted peaks

Peak Number	Position (cm^{-1})	Height	Width (cm^{-1})	Integrated spectral area
1	1173	2420	86	221565
2	1252	6858	98	760011
3	1353	14756	118	2119589
4	1440	1901	66	153089
5	1517	5776	142	880578
6	1595	16355	63	1256820
7	1676	1048	78	87354

Table 3.5.1: Peak positions, heights, widths and areas from a coal spectrum peak fit

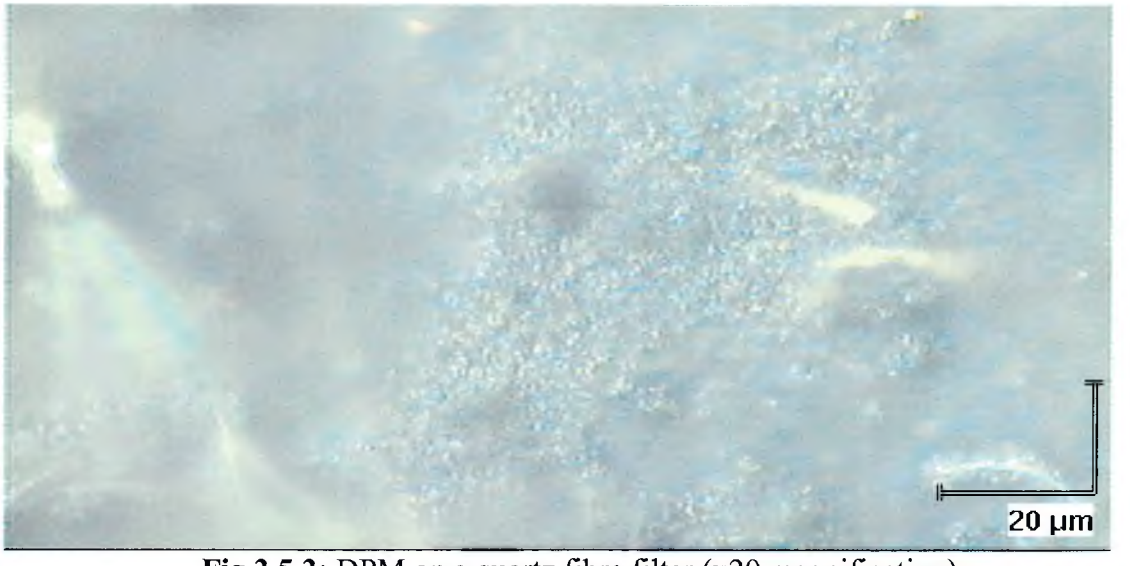

Fig 3.5.3: DPM on a quartz fibre filter (x20 magnification)

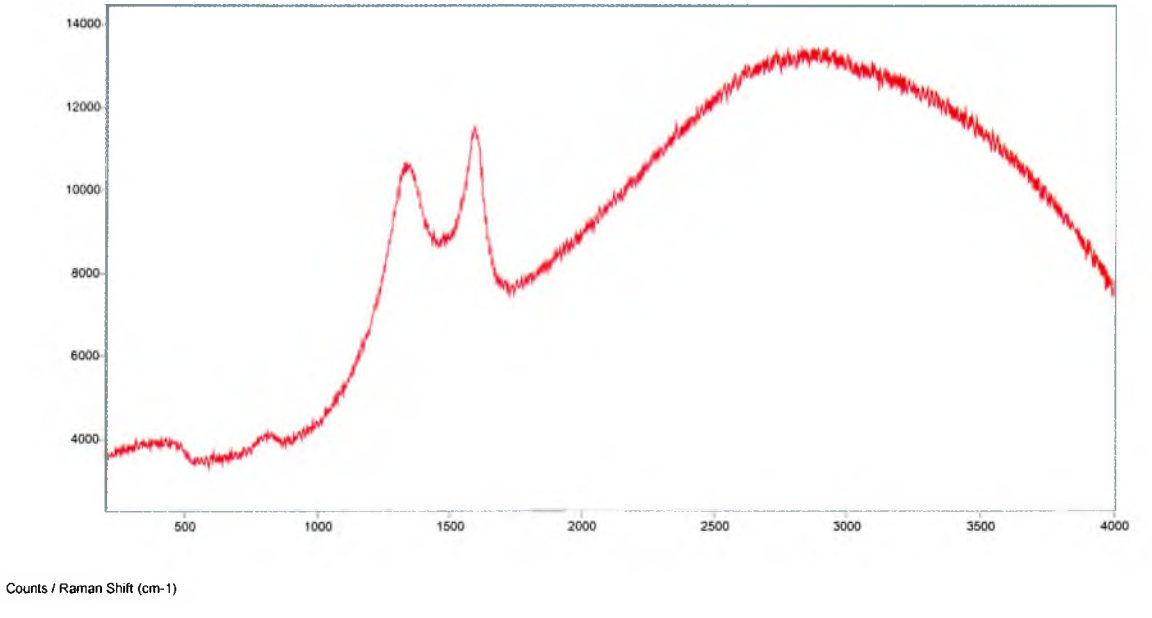

Spectrum 3.5.4: 328µg DPM on a quartz fibre filter, 250s, x50obj, 633nm Laser at 10%

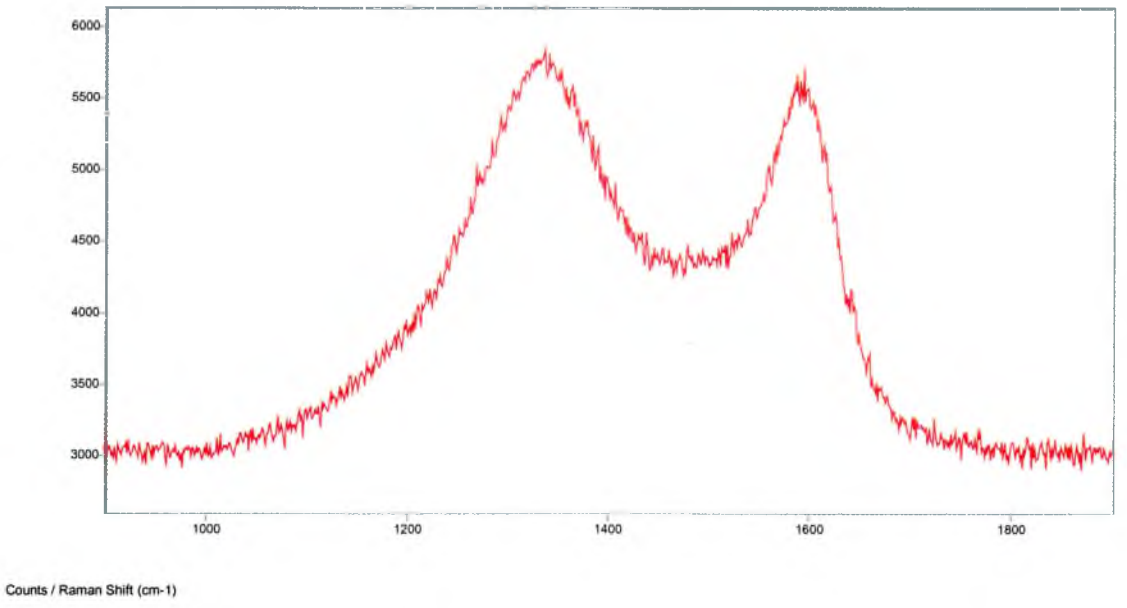

Spectrum 3.5.5: 328μg DPM, 250s, x50obj, 633nm Laser at 10%

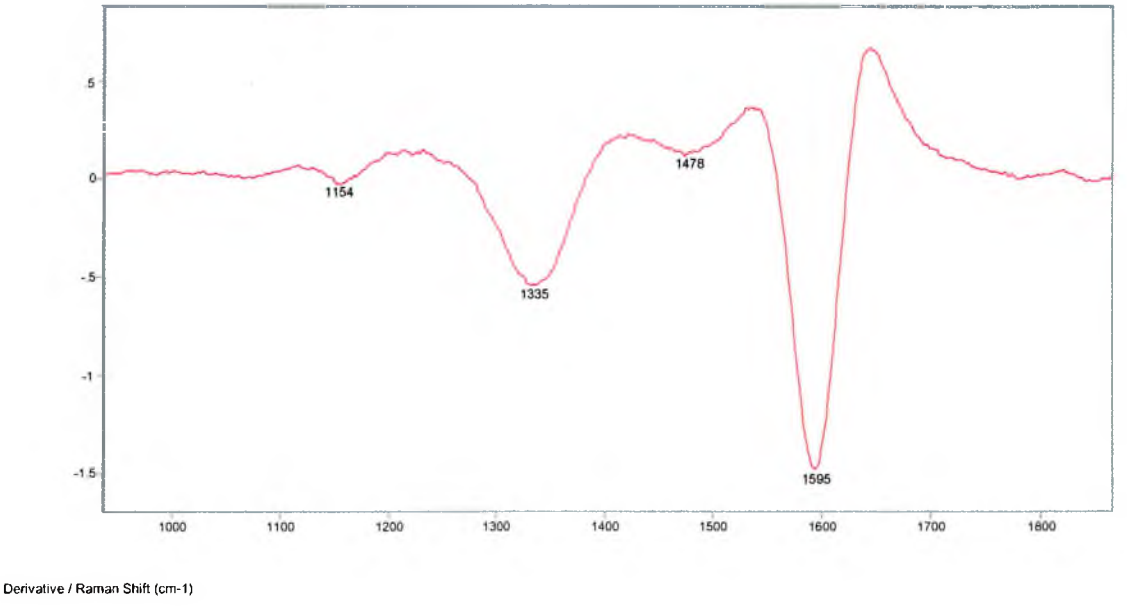

Fig 3.5.4: 2nd derivative of a DPM spectrum

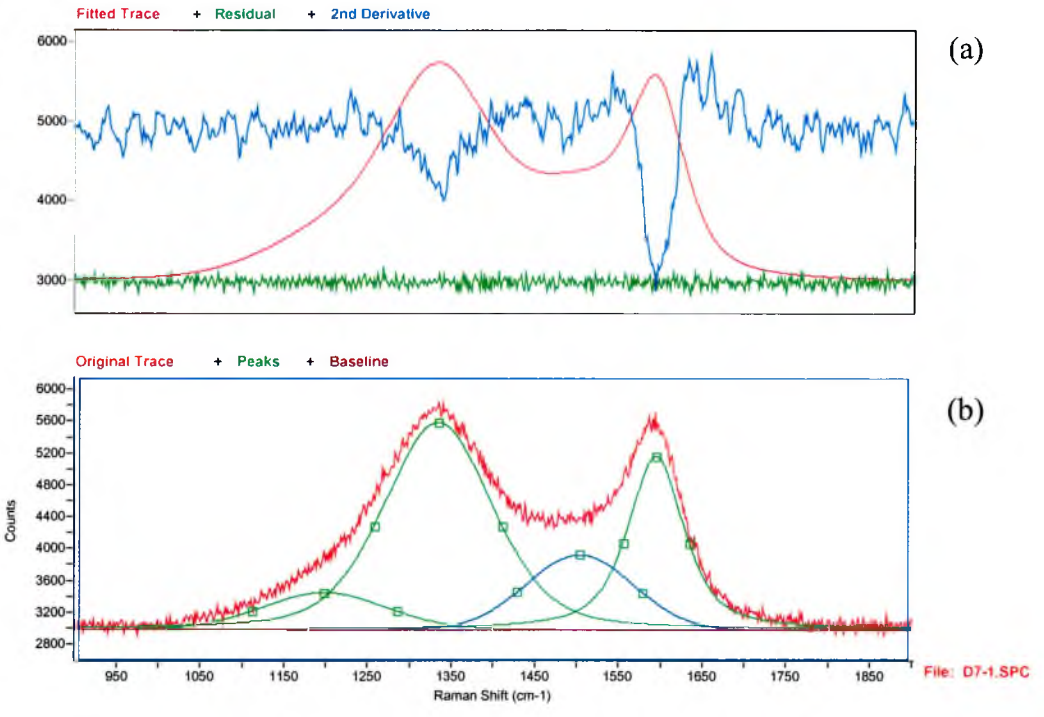

Fig 3.5.5: (a) Fitted trace, residual and second derivative of a DPM spectrum
(b) Original DPM spectrum and its fitted peaks

Peak Number	Position (cm^{-1})	Height	Width (cm^{-1})	Integrated spectral area
1	1199	457	174	89146
2	1335	2603	154	473252
3	1504	944	150	151132
4	1596	2182	79	233062

Table 3.5.2: Peak positions, heights, widths and areas from DPM spectrum peak fit

From spectrum 3.5.2 and 3.5.4 it can be seen that both the coal and DPM spectra have high fluorescence levels in the second-order region. If any second-order features were present in the spectra due to the carbon they have been masked by this fluorescence. There are no significant features in the low frequency region for the coal dust. However, there is a saddle shaped feature at 200-900cm^{-1} with two bands centred at ~400cm^{-1} and ~800cm^{-1}, for the DPM. According to Wang et al[44] this feature arises due to the short-range order in amorphous carbon. The band positions of 400cm^{-1} and 800cm^{-1} are similar to those observed for highly amorphous carbon. These bands would be less intense and

be centred at a higher frequency for carbon materials with a more ordered structure. The absence of this feature in the coal spectrum is one of the most obvious indicators, in this study, that it has a much more ordered carbon structure than the carbon from the DPM.

There were 7 bands fitted to the coal spectrum and their positions, heights, widths and areas are shown table 3.5.2. The D and G bands are located at 1353cm^{-1} and 1595cm^{-1} respectively. The band at 1173cm^{-1} could possibly be a VDOS feature for diamond-like sp^3-bonded carbon or hexagonal diamond. However, according to Ferrari and Robertson[61] this band and a band near 1450cm^{-1} cannot originate from sp^3-bonded carbon-carbon bonds and attribute these bands to sp^2-bonded carbon from transpolyacetylene chains lying in grain boundaries. The band at 1252cm^{-1} is almost certainly a feature in the VDOS of diamond-like carbon. There was no peak observed near 1440cm^{-1} in the 2nd derivative trace of the coal dust spectrum. However, a band was required in this position to get a good curve fit of the spectrum. Therefore, it is unclear if this is a real feature or if it is just required to satisfy the mathematics of the fitting program. If this band is a real feature and is not due to sp^2-bonded carbon from transpolyacetylene it could possibly arise from a tetrahedrally bonded diamond precursor phase or sp^3-bonded atoms linking small domains constituted of stacked aromatic planes. The band at 1517cm^{-1} is characteristic of imperfect graphite and may be due to the presence of impurities, such as nitrogen, in the amorphous carbon phase. It can also originate from isolated sp^2-bonded carbon clusters in an sp^3-network of amorphous carbon. The origin of the band at 1676cm^{-1} is unknown but the fact that it is shifted to higher wavenumbers than the G band suggest that it is similar to a D' band which is usually present around 1620cm^{-1}. The D' band is suspected to arise from graphite layers located at the boundaries of crystallites and is sensitive to the composition of the material in contact with the surface layers of the graphite, which modifies their electronic environment. The upward shift from the G band position may be due to an altered electronic state of a boundary plane or by its reduced symmetry. This band at 1679cm^{-1} could perhaps originate from a blue shifted G band due to dramatically changed electronic states of certain boundary planes due to the presence of impurities in the grain boundaries.

The positions, heights, widths and areas for the 4 bands fitted to the DPM spectrum are shown in table 3.5.2. The D and G bands are centred at 1335cm^{-1} and 1596cm^{-1} respectively. The 1199cm^{-1} and 1504cm^{-1} bands can be assigned to similar origins as the 1173cm^{-1} and 1517cm^{-1} bands in the coal spectrum respectively.

The G band for both the coal and the DPM spectra is located at around 1595cm^{-1}. This shift from the ~1580cm^{-1} peak for the E_{2g} mode of graphite is usually attributed to the presence of a D' band at about 1620cm^{-1}. However, no band at 1620cm^{-1} was detected for either the coal or DPM spectra. The fact that the G band occurs at such a high position suggests that there might possibly be a weak band about 1620cm^{-1} which is intense enough result in a shift but not intense enough for it to necessitate its inclusion for a good peak fit.

The additional bands around 1250cm^{-1} and 1440cm^{-1} present in the coal spectrum point towards the coal having a higher sp^3-bonded carbon content than the DPM.
The typical bandwidth for the E_{2g} mode of well-ordered graphite is around 30cm^{-1}. The G bandwidths for the coal and diesel spectra in the present study are 63cm^{-1} and 78cm^{-1} respectively and the D bandwidths for coal and DPM are 154cm^{-1} and 118cm^{-1} respectively. The bandwidth of the peak around 1180cm^{-1} is 86cm^{-1} for the coal and 174cm^{-1} for the DPM. However, the bandwidth of the line around 1510cm^{-1} is very similar for both samples being 142cm^{-1} for the coal and 150cm^{-1} for the DPM. Generally speaking the bandwidths for the peaks in the DPM spectra are much broader than the peaks in the coal spectrum. This is a further indication that the DPM sample has a much less ordered structure with smaller crystallites than the coal dust. The separation between the G and D peaks is 242cm^{-1} for the coal spectrum whereas the separation for the DPM spectrum is 261cm^{-1}. It is unusual that the DPM has a larger separation between the peaks because the bands are broader than for the coal spectrum and if the carbon from the DPM is more disordered than the carbon from the coal the separation between the peaks would be expected to be less for the DPM spectrum.

Using equation 3.4.3:

$$L_a = 12\left(\frac{I_G}{I_D}\right)$$

The value of L_a was calculated to be 7.1nm for coal dust and 5.9nm for DPM. Although these are strictly empirical values, the larger crystallite size for the coal dust agrees with the conjecture that the narrower bandwidths indicate the carbon in the coal is more ordered than the carbon from the DPM. However, the two crystallite sizes are very similar. If the calculation were an accurate estimation the small difference in crystallite size, that difference in itself would probably not be responsible for the large differences in the bandwidths and the presence of the saddle shaped feature between 200-900cm^{-1} in the DPM spectrum. It is likely that the carbon from the DPM is more amorphous with less short-range order than the carbon. This assumption is backed up by the spectra for the DPM being much less intense than the coal dust spectra. The coal dust appears to contain a higher fraction of sp^3-bonded carbon than the DPM. The spectra here were collected using a 633nm excitation source and sp^3-bonded carbon has a much lower Raman scattering cross-section than sp^2-bonded carbon for visible Raman.[63] Therefore, if the coal dust has a larger fraction of sp^3-bonded carbon than the DPM its spectra would be expected to be less intense than the DPM. However, the DPM spectra are less intense than the coal dust spectra here. This indicates that the carbon from the DPM is much less ordered than the carbon from the coal dust because Raman intensity is greatly reduced for amorphous materials compared to those in their crystalline form. Another factor which may influence the intensity difference is the fact that sp^3-bonded carbon has a larger optical bandgap than sp^2-bonded carbon. So, if the coal has a higher sp^3-bonded carbon content than the DPM it would be more transparent than the DPM. This would result in the DPM sample adsorbing more of the incident radiation and reduce the amount of scattered light compared to the coal sample.

The fact that the DPM spectrum has broader bands, reduced intensity and contains a low-frequency saddle shaped feature between 200-900cm^{-1}, due to amorphous carbon, indicates that the carbon from the DPM is much less ordered than the carbon from the

coal. The presence of bands at 1173cm^{-1}, 1252cm^{-1} and 1440cm^{-1} in the coal spectrum points towards the coal sample having a higher content of sp^3-bonded carbon than the DPM sample.

The large differences in bandwidths, the different separations between the D and G bands and the occurrence of additional peaks in the coal spectrum compared to the DPM spectrum suggests that Raman spectroscopy may have to potential to be used to distinguish between these two samples in a mixture.

References

1) K. Hutton in "Chemistry: The Conquest of Materials", Penguin Books Ltd, Middlesex, 1957
2) P. Gay in "The Crystalline State", Oliver and Boyd, Edinburgh, 1972
3) D. Hull in "Introduction to dislocations", Pergomon Press, London, 1965
4) R. Zallen in "The Physics of Amorphous Solids", John Wiley & Sons, New York, 1983
5) http://www.chembio.uoguelph.ca
6) C. Constable, "Raman Microscopic Studies of PVD Deposited Hard Ceramic Coatings", Sheffield-Hallam University PhD Thesis, 2001
7) http://www.kinsler.org
8) http://www.encarta.msn.com
9) C. Kittel, in "Introduction to Solid State Physics (5^{th} Ed.)", John Willey & Sons, New York, 1976
10) B. Wopenka, Earth and Planetary Science Letters, **88**, 1988, 221
11) J. Dennison, M. Holtz, G. Swain, Spectroscopy, **11**, 1996, 38
12) B. Bushan, Diamond and Related Materials, **8**, 1999, 1985
13) A. Abyzov, E. Ivanova, E. Smirnov, Neorganicheskie Materialy, **23**, 1664
14) J. Robertson, Surface Coating Technologies, **50**, 1986, 317
15) G. Galli, R. Martin, R. Car, M. Pairnelto, Physical Review Letters, **62**, 1989, 555
16) H. Wakayama, J. Mizuno, Y. Fukushima, K. Nagano, T. Fukunaga, U. Mizutani Carbon, **37**, 1999, 947
17) J. Pasteris, Brigitte Wopenka, Canadian Mineralogist, **29**, 1991, 1
18) G. Compagnini, O. Pluglisi, Foti. Carbon, **35**, 1999, 1793
19) F. Tuinstra, J. Koenig, The Journal of Chemical Physics, **33**, 1970, 1126
20) Y. Wang, D. Alsmeyer, R. McCreery, Chemical Materials, **2**, 1990, 557
21) J. Blaha, G. Rosasco, E. Etz , Applied Spectroscopy, **32**, 1978, 292
22) H. Wilhelm, M. Lelaurain, E. McRae, B. Humbert , Journal of Applied Physics, **84**, 1998, 6552
23) P. Lespade, R. Al-Jishi, M. Dresselhaus, Carbon, **20**, 1982, 427
24) R. Vidano, D. Fischbach, Journal of the American Ceramic Society, **61**, 1978, 13
25) X. Zou, H. Lu, J. Xie, J. Feng, Thin Solid films, **345**, 1999, 208
26) A. Cuesta, P. Damelincourt, R. Laureyns, A. Martinez-Alonzo, J. Tascon, J. Materials. Chemistry, **8**, 1998, 2875
27) S. Sze, N. Siddique, J. Sloan, R. Escribano, Atmospheric Environment, **35**, 2001, 561
28) S. Kelemen, H. Fang, Energy & Fuels, 2001, in press
29) P. Green, C. Johnson, K. Thomas, Fuel, **62**, 1983, 1013
30) Z. Zheng, X. Chen, Science in China B, **38**, 1995, 97
31) T. Mernagh, R. Cooney, R. Johnson, Carbon, **22**, 1984, 39
32) I. Pocsik, M. Hundhausen, M. Koos, L. Ley, Journal of Non-Crystalline Solids, **227-230**, 1998, 1083
33) M. Nakamizo, R. Kammereck, P. Walker, Carbon, **12**, 1974, 259
34) R. Nemanich, S. Solin, Physics Review B, **20**, 1979, 392
35) M. Endo, C. Kim, T. Karaki, T. Kasai, M. Matthews, S. Brown, Carbon, **36**, 1998, 1633

36) M. Dresselhaus, G. Dresselhaus, Advances in Physics, **30**, 1981, 290
37) M. Dubois, A. Naji, B. Humbert, E. Grivei, D. Billaud, Carbon, **38**, 2000, 1411
38) V. Kudoyarova, A. Chernyshov, T. Zvonareva, N. Dzhelepova, M. Tsolov Surface and Coating Technology, **100**, 1998, 192
39) O. Popvitcheva, N. Persiantseva, M. Trukhin, G. Rulev, N' Shonija, Y. Buriko, A. Starik, B. Demirdjian, D. Ferry, J. Suzanne, Physical Chemistry Chemical Physics, **2**, 2000, 4421
40) C. Beny-Bassez, J. Rouzaud, Scanning Electron Microscopy, **1985**, 1985, 119
41) T. Kraft, K. Nickle, Journal of Material Chemistry, **10**, 2000, 671
42) F. Haghseresht, G. Lu, A. Whittaker, Carbon, **37**, 1999, 1491
43) F. Salver-Disma, R. Fahri, G. Guery, J. Tarascon, J. Bruneel, J. Lassegues, Molecular Crystal Liquid Crystal, **310**, 1998, 219
44) Q. Wang, D. Allred, J. Gonzalez-Hernandez, Physical Review B, **47**, 1993, 47
45) R. Wright, R. Varma, D. Greun, Journal of Nuclear Matter, **63**, 1976, 415
46) K. Okada, H. Kanda, S. Komatsu, S. Matsumoto, Journal of Applied Physics, **88**, 2000, 1674
47) L. Nistor, V. Ralchenko, E. Obraztsova, A. Smolin, Diamond and Related Materials, **6**, 1997, 159
48) S. Prawer, K. Nugent, D. Jamieson, J. Owra, L. Bursill, J. Peng, Chemical Physics Letters, **332**, 2000, 93
49) G. Morell, O. Quinones, Y. Diaz, I. Vargas, B. Weiner, R. Katiyar, Diamond and Related Materials, **7**, 1998, 1029
50) A. Arora, T. Ravindran, G. Reddy, A. Skider, D. Mistra, Diamond and Related Materials, **10**, 2001, 1477
51) E. Rzepka, A. Lusson, C. Levy-Clement, M. Kumar, K. Mukhopadhyay, M. Sharon Diamond and Related Materials, **8**, 1999, 481
52) D. Schneider, B. Schultrich, P. Burck, H. Scheibe, G. Jorgensen, M. Lahres Diamond and Related Materials, **7**, 1998, 589
53) Z. Chen, J. Zaho, Y. Yano, T. Ooie, M. Yoneda, J. Sakakibara, Journal of Applied Physics, **88**, 2000, 2305
54) S. Amirhaghi, H. Reehal, R. Wood, D. Wheeler, Surface and Coatings Technology, **135**, 2001, 126
55) V. Vorlicek, J. Rosa, M. Vanecek., M. Nelsladek, M. Stals, Diamond and Related Materials **6**, 1997, 704
56) S. Buhlmann, E. Blank, R. Haubner, M. Lux, Diamond and Related Materials, **8**, 1999, 194
57) S. Prawer, K. Nugent, D. Jamieson, Diamond and Related Materials, **7**, 1998, 106
58) S. Silva, G. Amaratunga, E. Salje, K. Knowles, Journal of Materials Research, **29**, 1994, 4962
59) R. Nemanich, J. Glass, G. Lucovsky, R. Shroder, Journal of Vacuum Science Technology, **A6**, 1988, 1783
60) B. Marcus, L. Fayette, M. Mermoux, L. Abello, G. Lucazeau, Journal of Applied Physics, **76**, 1994, 3463
61) A. Ferrari, J. Robertson, Physical Review B, **63**, 2001, 121405
62) K. Gilkes, H. Sands, D. Bachelder, W. Milne, J. Robertson, Journal of Non-Crystalline Solids, **227-230**, 1998, 612

63) S. Matsunuma, Thin Solid Films, **306**, 1997, 17-22
64) J. Wagner, C. Wild, P. Koidl, Applied Physics Letters, 59, 1991, 779-781
65) K. Sinha, Menendez, Physical Review B, **41**, 1990, 41
66) K. Gilkes; S. Sands; D. Batchelder; W. Milne, J. Robertson , Journal of Non-Crystalline Solids, **227-230**, 1998, 612-616
67) Z. Sun, J. Shi, B. Tay, S. Lau, Diamond and Related Materials, 9, 2000, 1979
68) J. Shi, X. Shi, S. Lau, A. Tay, H. Tan, Diamond and Related Materials, **10**, 2001, 76
69) S. Leeds, J. Davis, P. May, C. Pickard, M. Ashfold, Diamond and Related Materials, **8**, 1998, 233
70) K. Gilkes, S. Prawer, K. Nugent, J. Robertson, H. Sands, Y. Lifshitz, X. Shi, Journal of Applied Physics, **87**, 2000, 7283
71) G. Adamopoulos, K. Gilkes, J. Robertson, N. Conway, B. Kleinsorge, A. Buckley, D. Batchelder, Diamond and Related Materials, **8**, 1999, 514
72) M. Gioti, D. Papadimitriou, S. Logothetidis, Diamond and Related Materials, **9**, 741
73) S. Prawer, K. Nugent, Y. Lifshitz, G. Lempert, E. Grossman, J. Kulik, I. Avigal, R. Kalish, Diamond and Related Materials, **5**, 1996, 433
74) M. Paterson, Diamond and Related Materials, **5**, 1996, 1407
75) R. Bustin, J. Rouzaud, J. Ross, Carbon, **33**, 1995, 679
76) R. Friedel, G. Carlson, Chemistry in Industry, **40**, 1971, 1128
77) R. Friedel, G. Carlson, Fuel, **51**, 1972, 194
78) R. Tsu, J. Gonzales, I. Hernandez, C. Luengo, Solid State Communications, **24**, 1977, 809
79) T. Zerda, A. John, K. Chmura, Fuel, **60**, 1981, 375
80) C. Beny, J. Jehlicka, Journal of Molecular Structure **480-481**, 1999, 541
81) T. Zerda., X. Yuan, S. Moore, C. Leon, Carbon, **37**, 1999, 1999
82) R. Salzer, U. Roland, H. Drummer, L. Summchen, Zeitschrift fur Physikalische Chemie, **191**, 1995, 1
83) http://www.chembio.uoguelph.ca/educmat/chm729/Phonons

Chapter 4

Characterisation of DPM and Coal Dust using Alternative Techniques

4. Characterisation of DPM and Coal dust using alternative techniques

4.1 X-ray photoelectron spectroscopy (XPS)

4.1.1 Introduction

When using visible sources of excitation, for the Raman study of carbonaceous materials, a resonance enhancement of the Raman cross-section of sp^2 bonds occurs. This phenomenon can result in sp^2 bonds having scattering efficiencies 50 to 100 times greater than sp^3 bonds, which leads to the contribution of sp^2 sites dominating the spectra.[1] Therefore, Raman studies alone do not allow for the direct identification and estimation of sp^2- and sp^3-bonded sites in carbonaceous materials. However, the sensitivity factor for XPS core-level spectra depends only on the atomic factors and is independent of the chemical state of the atoms. Therefore, XPS can give a direct estimation of the carbon sp^2/sp^3 hybridisation. In this section both DPM and coal dust samples are analysed using XPS and their C1s bands curvefitted to get an estimation of the carbon sp^2/sp^3 hybridisation. The elemental composition of each sample is also estimated.

4.1.2 Experimental

DPM and coal dust samples were mounted on indium foil. The analysis was performed using a Kratos Axis 165 XPS spectrometer with an Al Kα monochromatic source, having a spectral resolution of 0.1-0.2eV. A survey scan was taken of each sample. The survey scan was used to determine the elemental composition of each sample. A narrow scan for each element was performed to determine the amount present. A narrow scan of the C1s band was curvefitted to get an estimation of the carbon sp^2/sp^3 hybridisation of DPM and coal dust.

4.1.3 Results and discussion

The XPS survey scans of DPM and coal dust are shown in figures 4.1.1 and 4.1.3 respectively. Peak assignments for the XPS survey scan of DPM and coal dust are shown in figures 4.1.2 and 4.1.4.

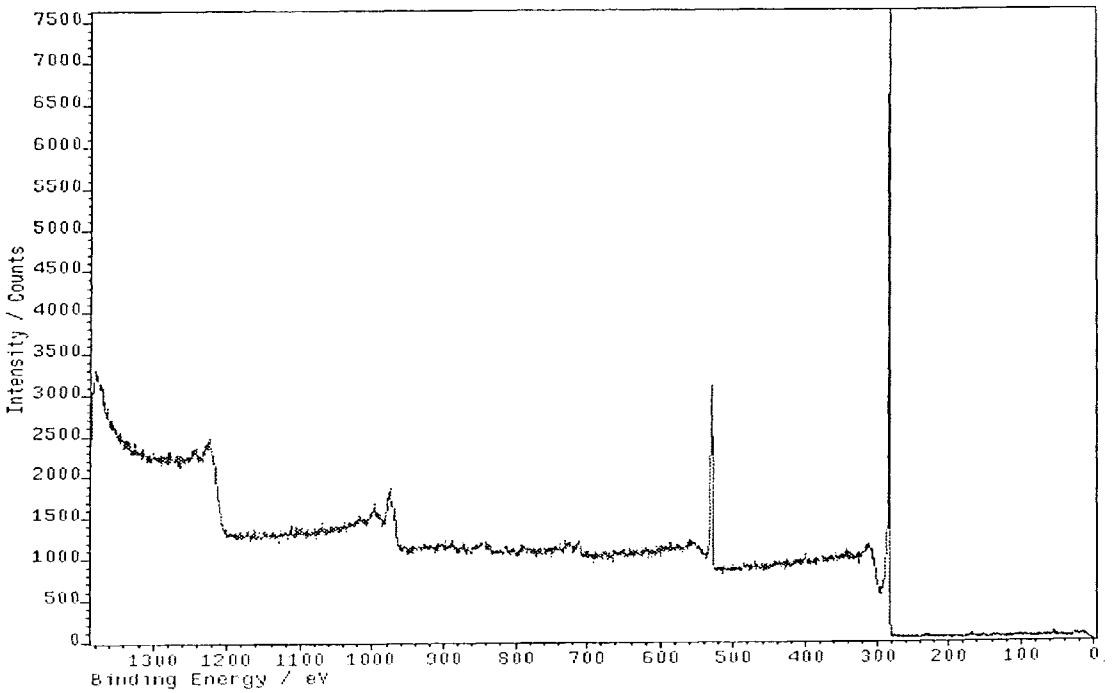

Figure 4.1.1: XPS survey scan of DPM

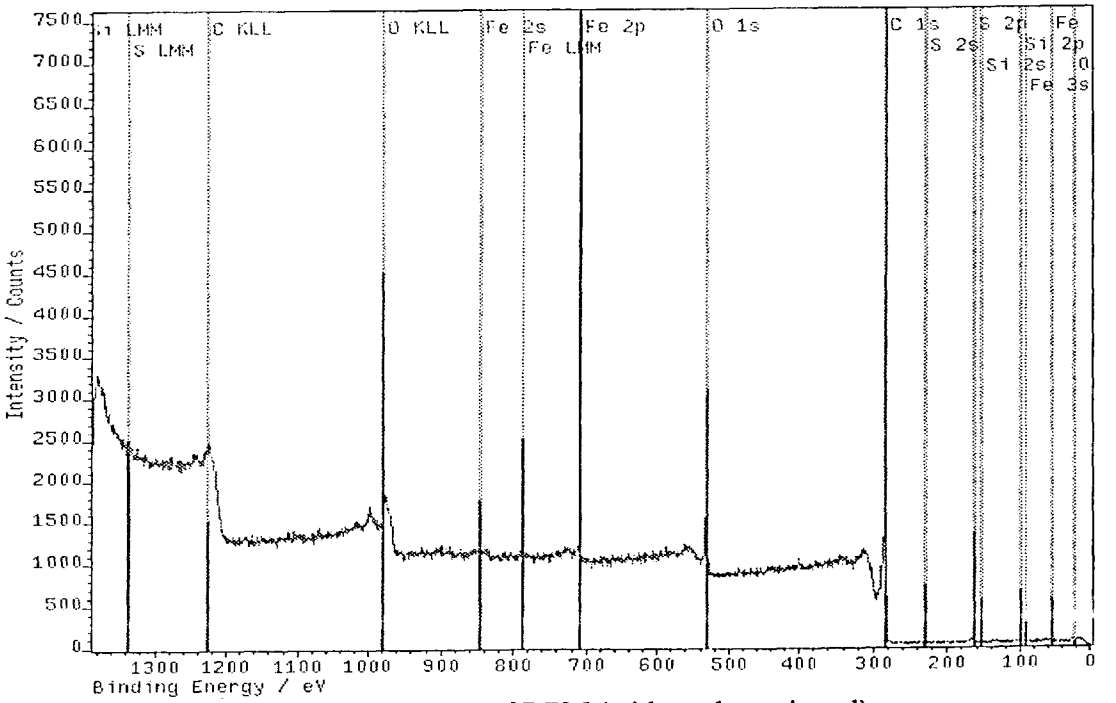

Figure 4.1.2: XPS survey scan of DPM (with peaks assigned)

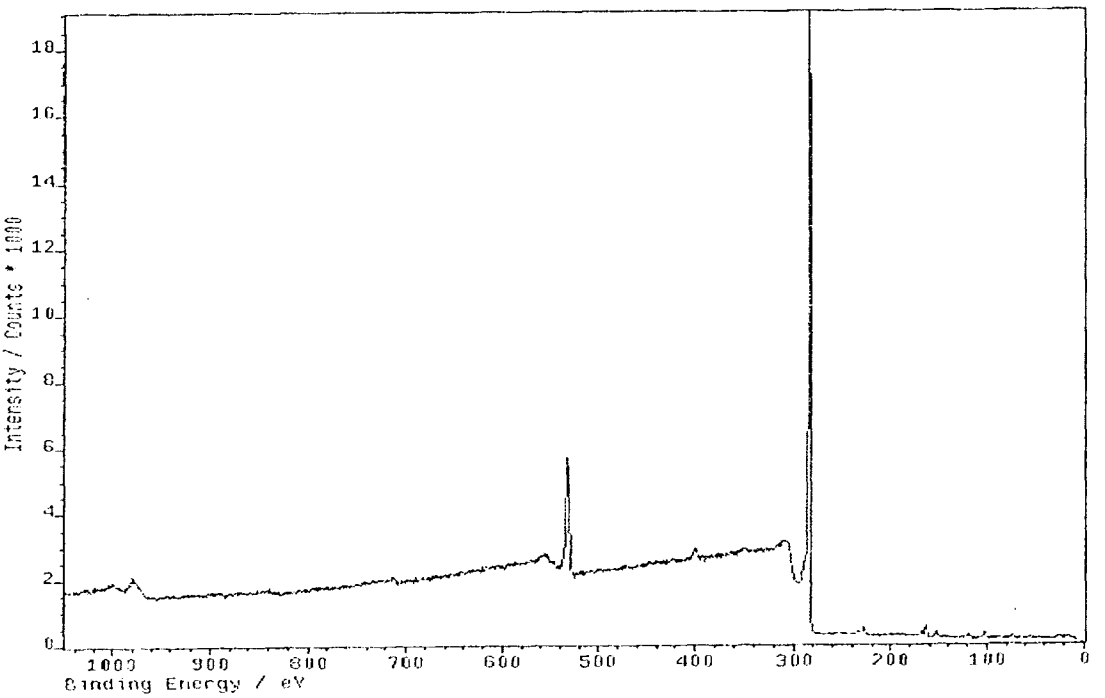

Figure 4.1.3: XPS survey scan of coal dust

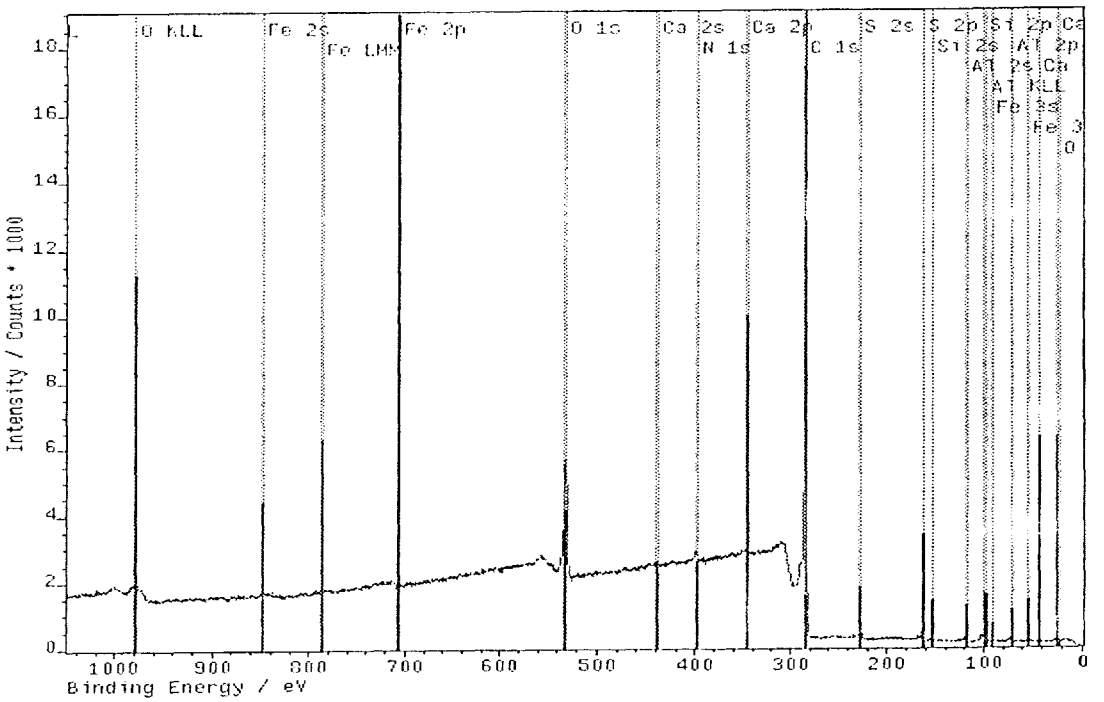

Figure 4.1.4: XPS survey scan of coal dust (with peaks assigned)

The atomic percentages, for the elements present in concentrations greater than 0.1%, of the DPM and coal dust are shown tables 4.1.1 and 4.1.2 respectively.

Element	Concentration (at.%)
C	68.82
O	28.78
Fe	0.75
S	0.32
Si	0.16

Table 4.1.1: Elemental composition of DPM from XPS analysis

Element	Concentration (at.%)
C	87.03
O	11.51
Fe	0.22
S	0.79
Si	0.31
Al	0.13

Table 4.1.2: Elemental composition of coal dust from XPS analysis

C, O, Fe, S and Si were detected in the DPM sample. These elements have previously been detected in XPS studies on vehicle exhaust emissions.[2,3] Like the previous work the major elements in the DPM were C and O. The Fe is likely to originate from wear and corrosion of the engine and exhaust systems. The S is probably from S in the fuel, which has been oxidised to SO_2. The Si could come from organometallic additives in the lubricating oil.[4-6]

The major elements in the coal dust were also C and O, as observed in previous work.[7-11] The Fe and S are expected to be mainly present from pyrite (FeS_2). The Si and aluminium are likely to mainly originate from clay minerals such as kaolinite, illite and smectite. Quartz can also contribute to the Si content. The carbon content for the DPM was 68.8%, which is less than the 87% carbon content of the coal dust. This indicates that the DPM has a higher organic content than the coal dust.

Curve fits of the C1s peak of DPM and coal dust are shown in figures 4.1.5 and 4.1.6 respectively. The composition (at. %) of the C1s peak is given in table 4.1.3.

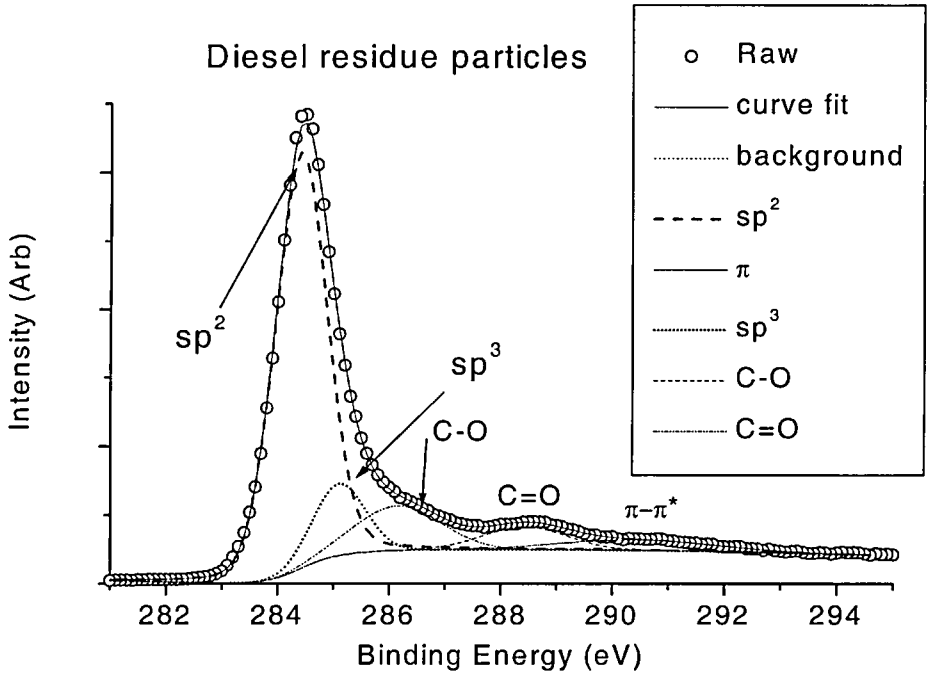

Figure 4.1.5: Curvefit of an the XPS C1s peak of DPM

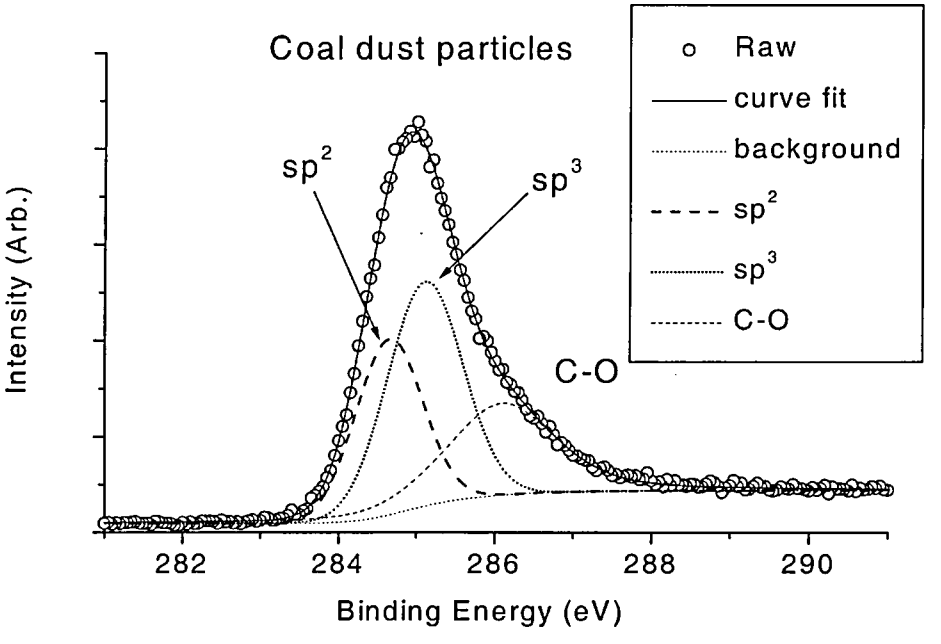

Figure 4.1.6: Curvefit of the XPS C1s peak of coal dust

Carbon Bonding	DPM (at.%)	Coal Dust (at.%)
C=C/C-C (sp^2)	70.7	28.9
C=C/C-C (sp^3)	11.6	41.4
C-O	11.8	29.7
C=O	5.8	0

Table 4.1.3: Bonding composition (at.%) of the C1s peak of DPM and coal dust

From the curvefit of the C1s peak of the DPM and coal dust it is evident that the coal dust has a much larger proportion of sp^3-bonded carbon at 41.4% than the DPM at 11.6%. The respective sp^2/sp^3 ratios for the DPM and coal dust were 6.1 and 0.7. The coal particles appear to have a much larger proportion of their surface carbons bonded to oxygen than the DPM. This may be influenced by contamination from the air. The presence of a band above 291eV indicated the presence of uncovered polyaromatic or graphite-like basic structural units in the surface regions of DPM.[3]

4.2. Diffuse Reflectance Infrared Fourier Transform Spectroscopy (DRIFTS)

4.2.1 Introduction

In this section DRIFTS is used for the identification of organic functional groups and possible minerals in the coal dust and DPM samples.

4.2.2 Experimental

The KBr dilutent readily takes up water and organics from the air. Therefore, to minimise these effects, the KBr was dried overnight at 400°C, then stored in an airtight dessicator. The instrument was sealed and constantly purged with dry air to minimise carbon dioxide and water vapour contributions. DPM and coal dust samples were diluted to 5% (by weight) in KBr and mixed for 40 seconds, using an agate pestle and mortar. The sample being analysed was placed in the sample holder. A DRIFTS study was performed using a Mattson Polaris FTIR spectrometer equipped with a Graseby Specac "Selector™" DRIFT accessory.

4.2.3 Results and discussion

A DRIFTS spectrum of coal dust is shown in figure 4.2.1. The attempt to obtain a spectrum of DPM using the same technique was unsuccessful due to the IR light being strongly adsorbed by the black sample. Carbonaceous materials are known to strongly disperse IR radiation, thus reducing the signal reaching the detector.[12] So, 5% DPM in KBr may have been too concentrated. Therefore, the experiment was repeated with the DPM diluted further to 2.5% in KBr. However, a spectrum was still not obtained of this sample. From the XPS analysis of DPM and coal dust the carbon from the DPM was estimated to be 71% sp^2-bonded, whereas the coal dust carbon was estimated to be 29% sp^2-bonded. It is known that sp^2-bonded carbon materials absorb radiation more readily than sp^3-bonded carbon materials.[13] This may explain why it was possible to obtain a spectrum for the coal dust and not the DPM.

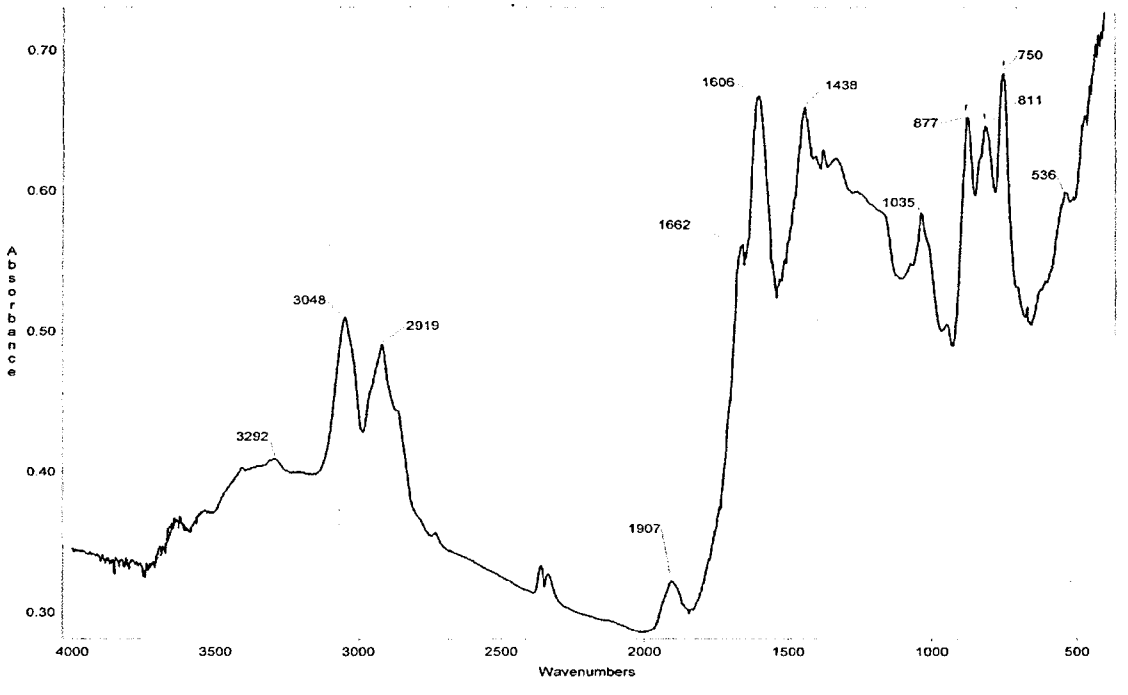

Figure 4.2.1: DRIFTS spectrum of 5% coal dust in KBr

Similar spectra to figure 4.2.1 have been previously obtained from the FTIR analysis of coal.[12, 14-17] The assignments for the bands in the spectrum are given in table 4.2.1.

Band Position (cm^{-1})	Assignment
3100-3000	Aromatic C-H stretching mode
3000-2750	Aliphatic C-H stretching
1600	Aromatic C=C
1450-1410, 880-860, 720-680	Carbonates or C-H bending
1100-800, 600-400	Silicate minerals or C-H bending
900-700	Aromatic bending modes

Table 4.2.1: Assignment of the bands from the DRIFTS analysis of coal dust

The DRIFTS spectrum of coal in figure 4.2.1 clearly shows that there are aromatic, aliphatic and mineral compound present in the coal dust, which were not detected by the Raman analysis. There are a number of possible reasons for this. The first reason being that IR is more sensitive to organic materials than Raman. It is also possible that the intense (resonance enhanced) D and G bands, due to the elemental carbon, may mask peaks present from organic matter or minerals. Another possibility is that, in the Raman analysis, the heat from the laser may have burned off organic material during the analysis, resulting in no peaks being observed for these compounds.

4.3 Thermogravimetric Analysis (TGA)

4.3.1 Introduction

From the Raman analysis of coal and DPM samples (chapter 5) it became apparent that the sample would need to be heat-treated before Raman analysis, to avoid modification by localised heating due to the laser power. In this section a TG analysis of both the DPM and coal dust samples are performed to determine the possible sample weight losses that would occur due to heat-treatments.

4.3.2 Experimental

TGA was performed on 7.03mg DPM and 7.16mg coal dust samples using a Mettler-Telodo TA8000 thermoanalyser. A nitrogen carrier gas flow of $20cm^3$/min was maintained throughout. Samples were firstly conditioned at 35°C min^{-1} for 15 minutes in order to remove physisorbed components and obtain a stable weight reading. Heating of the sample was then initialised at a rate of 10°C min^{-1} up to 800°C.

4.3.3 Results and discussion

The TGA and differentiated thermogravimetic (DTG) traces are shown for DPM and coal dust in figures 4.3.1 and 4.3.2 respectively.

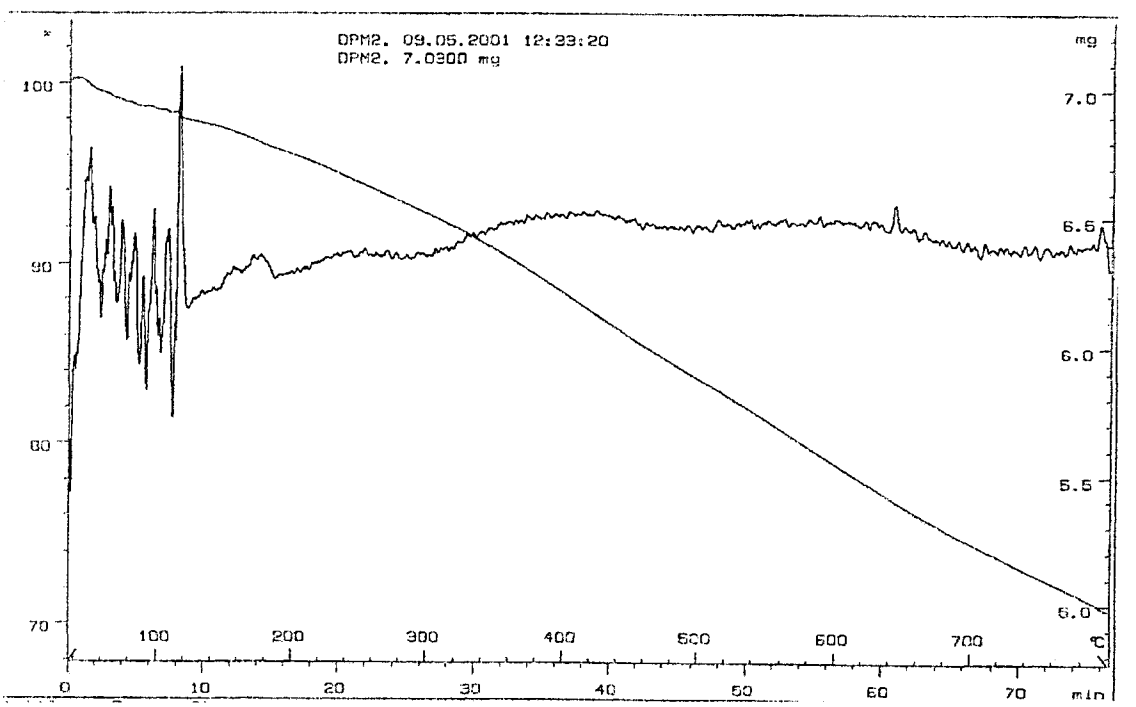

Figure 4.3.1: TGA and DTG traces for DPM heated to 800°C

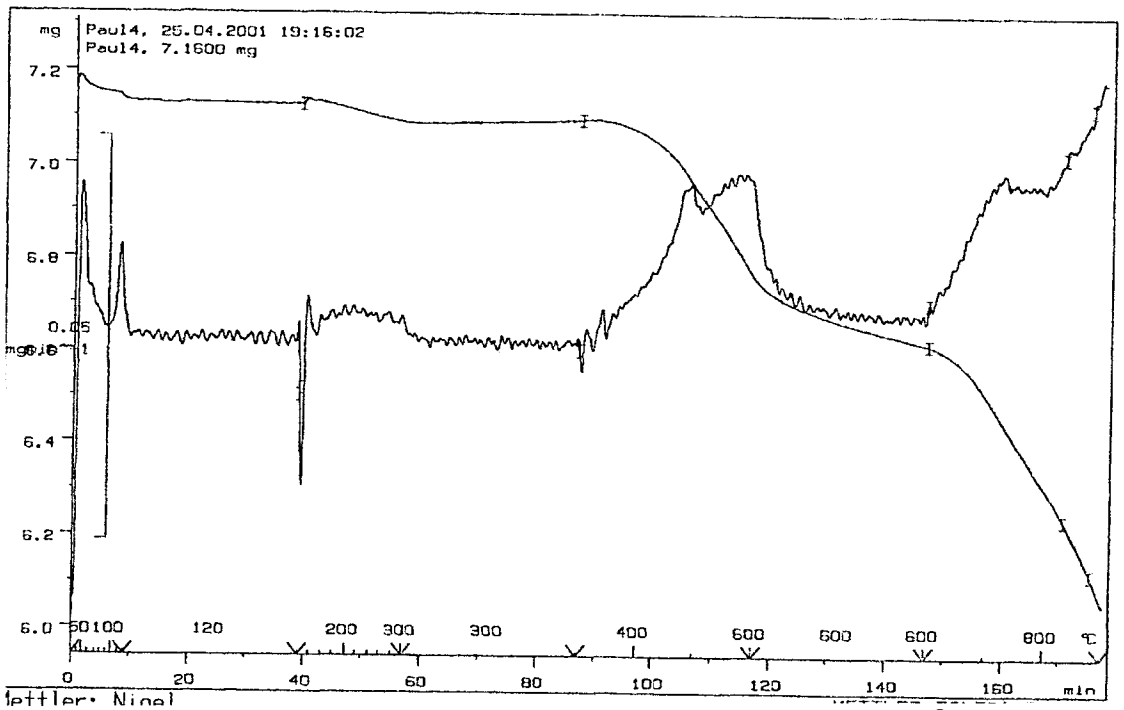

Figure 4.3.2: TGA and DTG traces for coal dust heated to 800°C

The TGA trace for the coal shows three general stages of weight loss.
These stages have been previously observed for TGA studies of coal [18-21] and can be summarised as follows:

1) Below 200°C – loss of the interlayer water from minerals and other physical changes such as softening and molecular rearrangement associated with the release of gases.
2) 200 – 600°C majority of the extractable organic content is evolved. (devolatisation)
3) Above 600°C – less volatile organic compounds and some inorganic compounds are evolved; for example the decomposition of carbonate compounds (perhaps calcite and dolomite)

Coal dust had a weight loss of approximately 17% and the DPM of approximately 30%, when heated to 800°C, showing that the DPM has a much greater organic content than the coal dust. A large amount of weight loss for the DPM occurred between 200 and 600°C showing that there are a lot more volatile organic compounds present in the DPM than the coal dust.

4.4 X-Ray Fluorescence (XRF) Spectrometry

4.4.1 Introduction

In this section XRF is used to determine the quantity of elemental oxides present in a coal dust sample. Kyotani and Iwatsuki[22] have presented XRF work on DPM samples as small as 20-30μg but recommend using at least 300μg of sample for reliable results. However, their work involved a lengthy and difficult sample preparation and their technique is beyond the capabilities of the XRF equipment used here. If we were to perform XRF on DPM, using our instrument, we would require a sample in the order of 1g, which would take several days to collect. Therefore, it was decided not to perform an XRF analysis on a DPM sample.

4.4.2 Experimental

1g of coal dust was made up to 11g by mixing it with lithium-tetraborate ($Li_2B_4O_7$). The mixture was fused together by placing it in a platinum plate and heating it to 1250°C for 10 minutes. This fusion method improves the determination of minor and major elements because mineral species are dissolved and dispersed in the diffusion glass.[23] The sample was analysed using a wavelength dispersive Phillips PW 2440 XRF spectrometer, with a 4kW Rh tube as a source and sequential detection.

4.4.3 Results and discussion

O, Mg, Al, Si, P, K, Ca, Fe, Sr, and Ba. S were detected in the coal dust from the XPS analysis. However, no S was detected here. This may be due to the sulphur compounds being heated off during the fusion process as pyretic sulphur is know to evolve at around 550°C.[17] The detected elements have previously been detected in coal by XRF.[23-25] The presence of Mg may be due to smectite and chlorite. Al and Si are primarily attributed to kaolinite although illite and phosphate minerals make significant contributions to Al in some cases and quartz can contribute to the Si content. P can be attributed to the presence

of apatite or other phosphorous minerals. Illite can also contributed to the K present. Ca can be contributed to by calcite and apatite. Fe is mainly controlled by pyrite. However, carbonate minerals can also contribute to Fe in coals. Ba and Sr are associated with phosphorous minerals.

The atomic percentage calculated for the oxides present in the coal, as estimated by the Phillips oxide program, is given in table 4.4.1.

Compound	Concentration (at. %)
MgO	0.09
Al_2O_3	1.35
SiO_2	1.64
P_2O_5	0.02
K_2O	0.13
CaO	0.41
Fe_2O_3	0.64
SrO	0.02
BaO	0.06
Total	**4.36**

Table 4.4.1: Oxide content (atm. %) of coal dust from XRF analysis

The total atomic percentage of the oxide compounds was 4.36% which indicates that the coal dust contains over 95.5% elemental carbon. The carbon content of the coal dust as calculated by XPS in section 4.1 was 87%. However, XPS is a surface method whereas XRF measures the bulk of the sample. This indicates that the bulk of the coal dust has a different composition than the surface layer. Also, the coal dust sample was heated to 1250°C during the XRF fusion process. This would have removed any volatile organics present in the coal dust. Therefore, the percentage of carbon in the original coal dust sample (before being heated) would have been less than the 95.5% estimated here.

4.5 Scanning Electron Microscopy (SEM)

4.5.1 Introduction

In this section SEM images were obtained of mixture coal dust and DPM samples on quartz fibre filter substrates to investigate the distribution of the samples which were to be analysed by Raman microscopy.

4.5.2 Experimental

A sample with a mixture of 160μg DPM and 235μg coal dust, collected on a quartz fibre filter, was gold coated to promote conduction of electrons as both the sample and substrate were know to be insulators.[26] The coated sample was mounted onto a sample holder and placed in the sample chamber of a JEOL JXA-840A SEM instrument. SEM images were taken of the sample using 15KV acceleration voltage, $3x10^{-9}$I probe current and a secondary electron detection system.

4.5.3 Results and discussion

SEM images of a mixture 160μg DPM and 235μg coal dust sample on a quartz fibre filter are shown in figures 4.5.1 through 4.5.4.

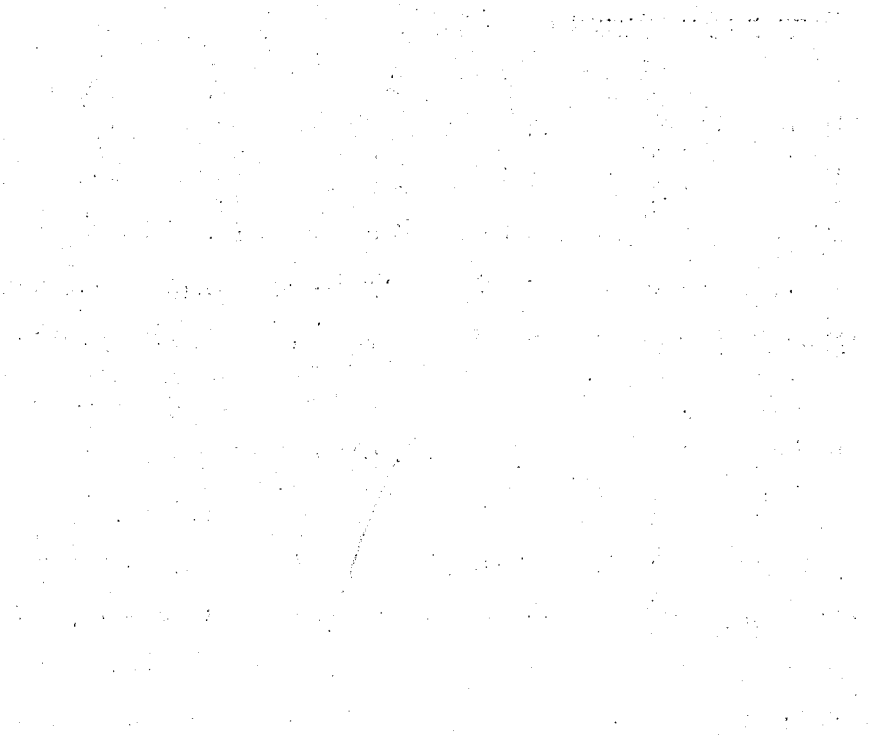

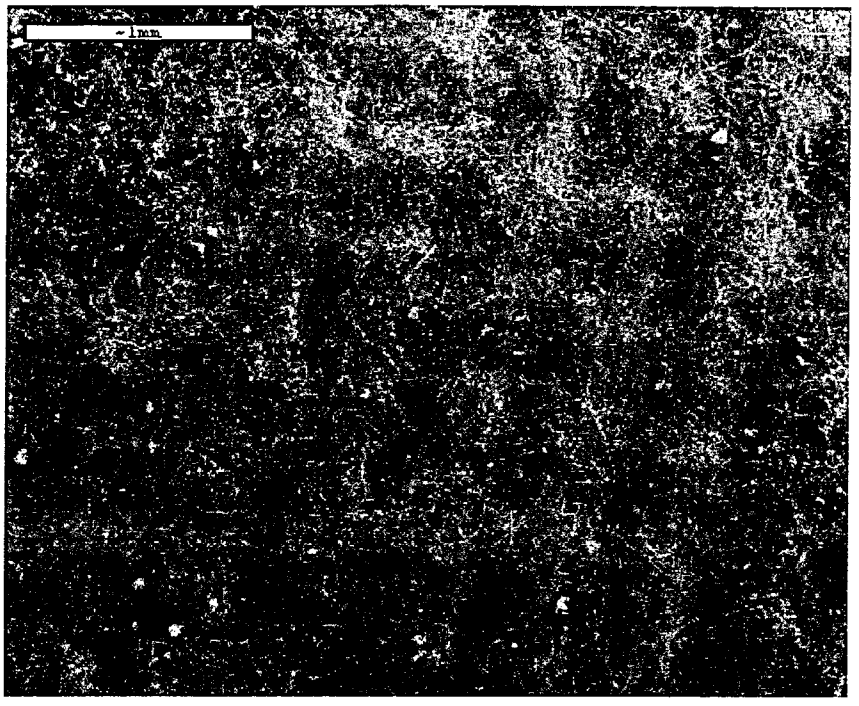

Fig 4.5.1: SEM image of coal dust(235μg) and DPM(160μg) on a quartz fibre filter

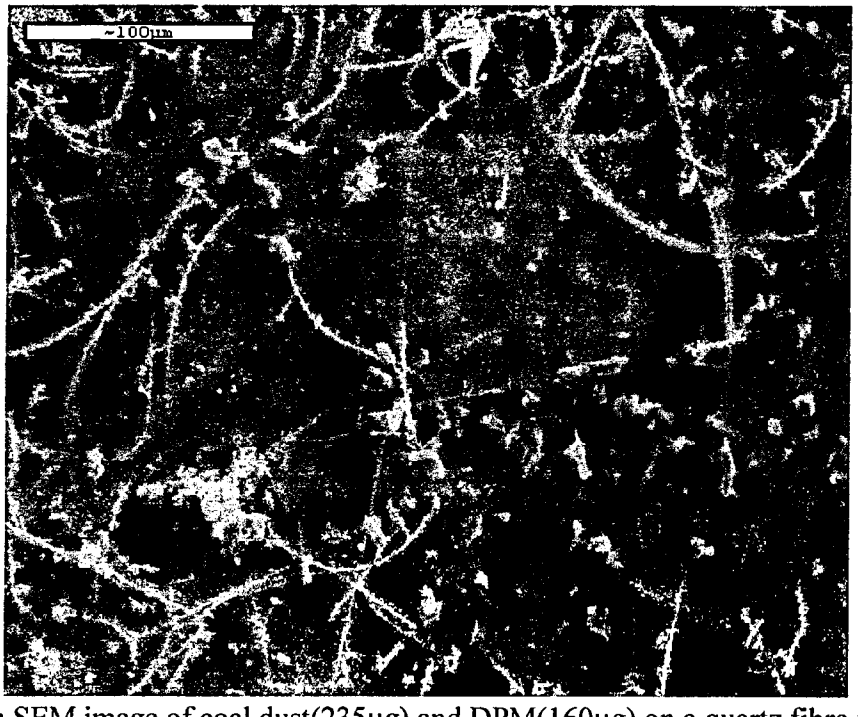

Fig 4.5.2: SEM image of coal dust(235μg) and DPM(160μg) on a quartz fibre filter

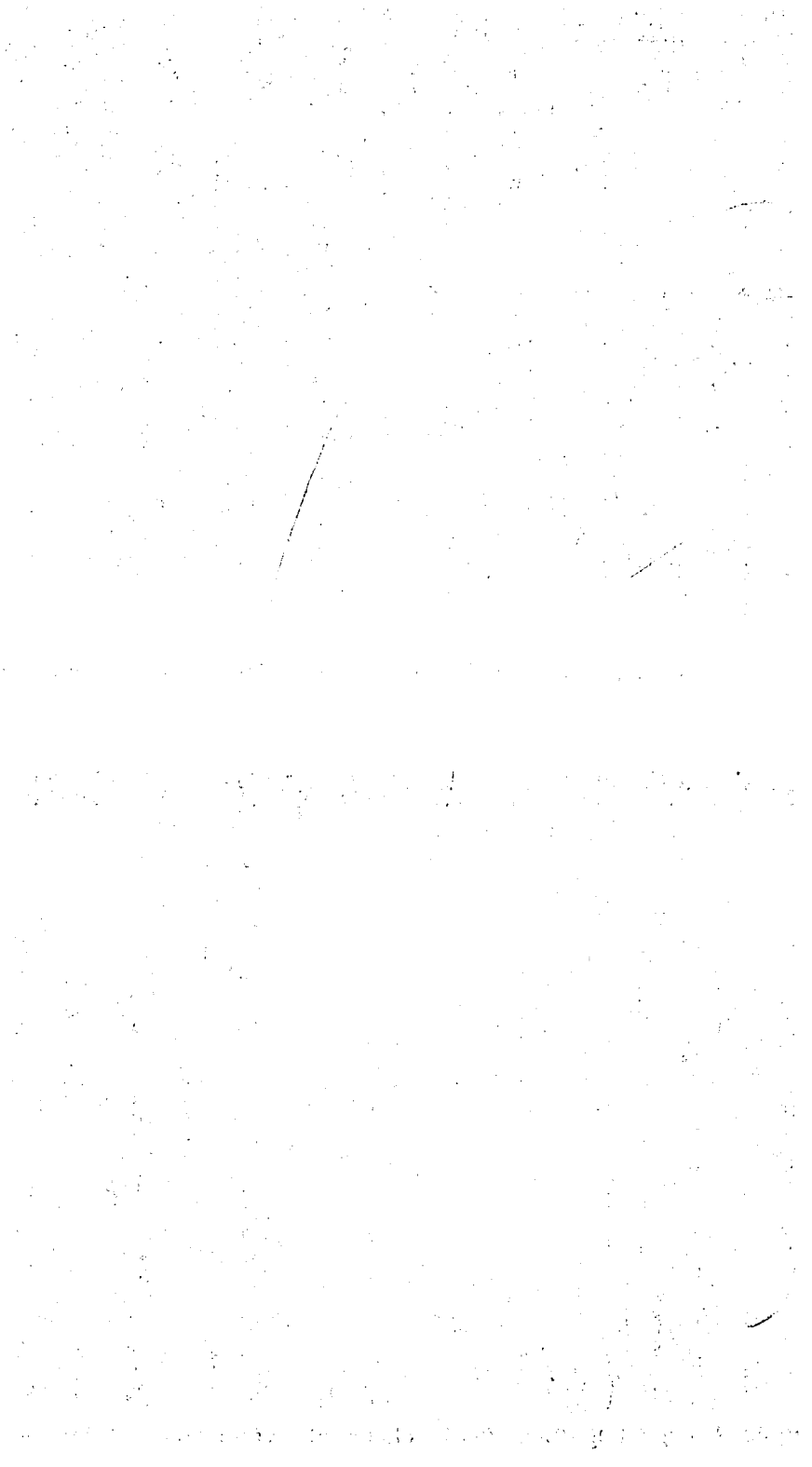

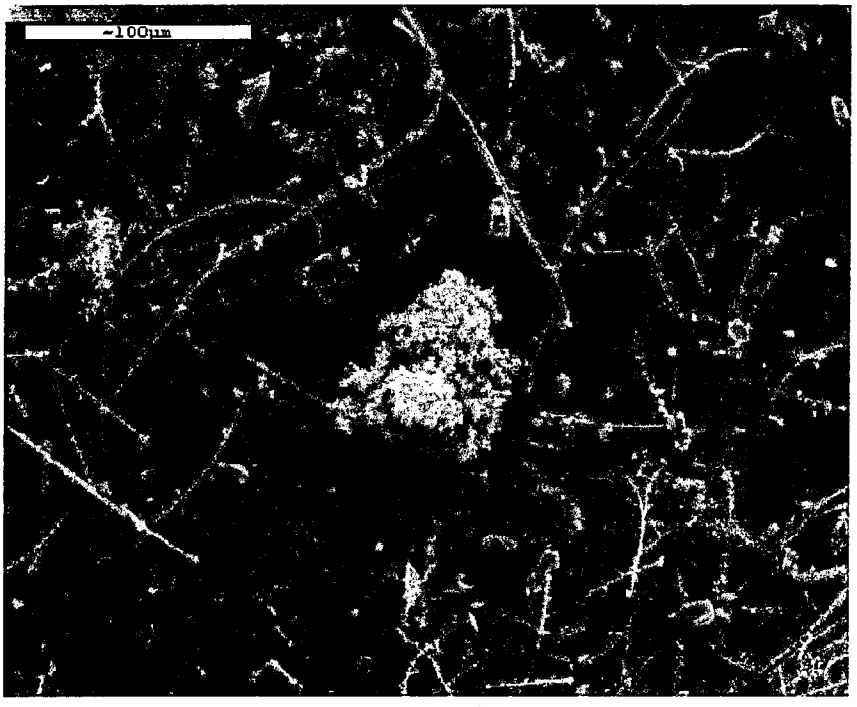

Fig 4.5.3:SEM image of coal dust(235µg) and DPM(160µg) on a quartz fibre filter

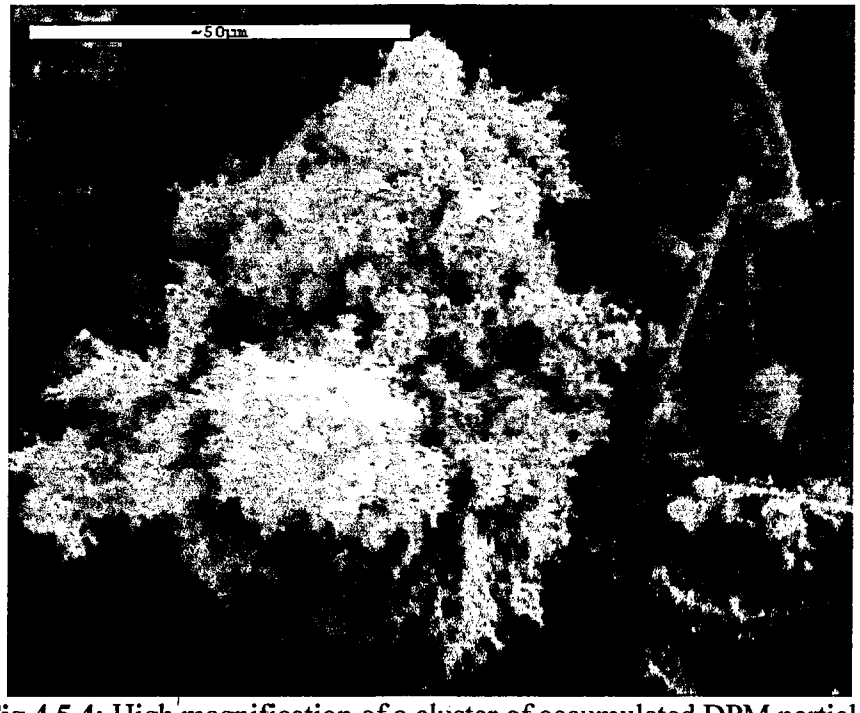

Fig 4.5.4: High magnification of a cluster of accumulated DPM particle

From the SEM images we can see that the mixture samples are highly heterogeneous. The white 'fluffy' particles correspond to the DPM and the darker more structural particles correspond to the coal dust. The quartz fibre filters are also visible, which shows that the substrate is not completely covered. In image 4.5.1 we can see that the substrate is not flat and the woven structure of the quartz fibres is clearly visible. As Raman is a surface technique this affects the spectra collected on different areas of the sample. Although the majority of individual DPM particles are known to be in the nanometer range[27] accumulated DPM particles of the order of 50μm were observed here. It is possible that the accumulated DPM particles shown in figure 4.5.4 may be surrounding a coal dust particle. The coal dust particles themselves appear to range in size from a few μm to around 25-30μm. Both the DPM and coal dust appear to be unevenly distributed on the filter. However, in figures 5.4.2 and 5.4.3 there are certain areas between the coal dust particles and the large agglomerates of DPM where the substrate appears to be covered. These areas are likely to be taken up by very fine DPM particles, which shows, apart from the large agglomerates, that the DPM is more evenly distributed on the filter, than the coal dust. When performing a Raman analysis of the samples on these filters the sample area can range from 1μm to 30μm. Therefore, it could prove very difficult to collect reproducible spectra if sampling different points on the filter. This heterogeneity has profound implications for the analysis of DPM and coal dust mixtures using Raman microscopy.

References

1) Y. Taki, O. Takai, Thin Solid Films, **316**, 1998, 45
2) B. Hutton, D. Williams, The Analyst, **125**, 2000, 1703
3) H. Klein, E. Lox, K. Seibold, G. Prescher, Physical Chemistry Chemical Physics, **2**, 2000, 1051
4) M. Kleeman, J. Schauer, G. Cass, Environmental Science & Technology 34,7,2000 1132
5) D. Kittelson, Journal of Aerosol Science 29, **5-6**, 1998, 575
6) V. Kerminen, T. Makela, C. Ojanen, R. Hillamo, J. Vilhunen, L. Rantanen, N. Harvers, A. Von Bohlen, D. Klockow, Environmental Science & Technology, **31**, 7, 1997, 1883
7) A. Buckley, M. Kelly, P. Nelson, K. Riley, Fuel Processing Technology, **43**, 1995, 47
8) D. Cagniant, R. Gruber, J. Boudou, C. Bilem, J. Bimer, P. Salbut, Energy & Fuels, **12**, 1998, 672
9) C. Weitzsacker, J. Gardella, Energy & Fuels, **10**, 1996, 141
10) T. Leung, W. Man, P. Lim, W. Chan, F. Gaspari, S. Zukotynski, Journal of Non-Crystalline Solids, **254**, 1999, 156
11) L. Perry, A. Grint, Fuel, **62**, 1983, 1024
12) C. Alciaturi, M. Escobar, R. Vallejo, Fuel, **75**, 1996, 491
13) S. Mominuzzaman, T. Soga, T. Jimbo, M. Umeno, Thin Solid Films, **376**, 2000, 1
14) J. Thomasson, C. Coin, H. Kahraman, P. Fredericks, Fuel, **79**, 2000, 685
15) I. Nosyrev, R. Gruber, D. Cagniant, A, Krzton, J. Pajak, M. Stefanova, S. Grishchuk, Fuel, **77**, 1996, 1549
16) M. Mastalerz, R. Bustin, Fuel, **74**, 1995, 536
17) N. Oztas, Y. Yurum, Fuel, **79**, 2000, 1221
18) D. Zoller, M. Johnston, Energy & Fuels 1999,**13**,1097
19) I. Pitkanen, J. Huttunen, H. Halttunen, R. Vesterinen, Journal of Thermal Analysis and Calorimetry, **56**, 1999, 1253
20) J. Podder, T. Hossain, M. Mannan, Thermochimica Acta, **255**, 1995, 221
21) J. Jaber, S. Probert, Fuel Processing Technology, **63**, 2000, 57
22) T. Kyotani, M. Iwatsuki, Analyst, **123**, 1998, 1813
23) G. Suarez-Fernandez, J. Vega, A. Fuertes, A. Garcia, M. Martinez-Tarazona Fuel, **80**, 2001, 255
24) D. Spears, L. Manzanares-Papayanopoulos, C. Booth, Fuel, **78**, 1999, 1671
25) D. Spears, Y. Zheng, International Journal of Coal Geology, **38**, 1999, 161
26) Personal communication with Mr. Graham Revell at the Health and Safety Laboratory, Broad Lane, Sheffield, UK
27) D. Kittelson, Journal of Aerosol Science, **29**, 1998, 575

Chapter 5

Multivariate Analysis of Carbon Particles from DPM and Coal Dust

5. Multivariate Analysis of Carbon Particles from DPM and Coal Dust

5.1 Introduction

The principal aim of the present work is the development of a Raman spectroscopy-based method to analyse carbon particulates in mixtures produced from DPM and coal dust. The Raman spectra of separate DPM and coal dust samples are very similar and it is expected that features due to each constituent the mixture samples will strongly overlap. This makes it very difficult to determine the amount of each component in an unknown mixture sample. Partial Least Squares (PLS) is a quantitative method, which predicts the amount of each constituent by taking advantage of the correlation relationship that already exists between the spectral data and the constituent concentrations. A range of mixture samples with different amounts of DPM and coal dust will be produced and a PLS model constructed using Raman spectra of these known mixture samples. This model can then be used to predict the amount of DPM and coal dust present, from the spectra, of unknown mixture samples.

A data set of Raman spectra with highly reproducible spectral shapes and intensities is essential to produce a PLS model that can reliably predict the amount of DPM and coal dust in a mixture sample. Optimisation of instrumental parameters is inherent to collecting the most reproducible spectra possible. The important instrumental parameters here being laser power, microscope objective and scan time. Investigation of the effects of sample treatments, such as heating, is also important. The development of a PLS model involves the production and analysis of a range of mixture samples with known amounts of DPM and coal dust. Production of the mixture samples for the present work was a non-trivial process and is discussed later in this chapter. Hence, the use of individual PLS models to investigate the effect of each parameter change or sample treatment would involve a considerable amount of effort. Therefore, it was desirable to use a less complicated method, where possible, for investigating the effects of parameter changes. Principle component analysis (PCA) is a qualitative chemometric method for which spectral areas are usually normalised to avoid any influence on the analysis. From

the PCA scores plots of replicate spectra of the same sample it is possible to determine how similar the replicate spectra shapes are. Essentially, the closer the scores are clustered together the more similar the spectra are. This method can be used to directly compare the reproducibility of spectral data before and after the application of the parameter change or sample treatment and does not, unlike PLS, require a range of samples with know concentrations. PCA has been used throughout the present study to do exactly this. It has been used for mixture DPM and coal dust samples but also for individual constituent samples, which avoided the necessity to produce extra mixture samples for the investigation of the effects of destructive sample treatments such as heating. The investigation of individual DPM and coal dust samples was also useful to determine if the parameter changes and sample treatments had similar or different effects on each constituent. PCA calculations are performed without considering intensity data. So, independent measurements of integrated spectral areas of replicate spectra can be used to determine the reproducibility of their spectral intensities. It follows that if both the spectral shapes and intensities have high reproducibility (determined respectively by PCA and integrated spectral areas) that spectra of mixture samples collected under the same conditions should give reliable results, when used for a PLS model.

5.2 Multivariate analysis

Here it is attempted to give a brief introduction to multivariate analysis, what it is, what it is used for and how it works. For a more comprehensive treatment of multivariate/chemometric principals and techniques the reader is referred to Otto[1].

Loosely translated chemometrics is commonly understood as the use of linear algebraic methods to make qualitative and quantitative measurements of chemical data such as spectra. The application of this method is best understood if we consider the data output from the Raman instrument to be a variety of profiles. A measurement of a property or 'variate' (i.e. cm^{-1}) a single specimen experiment is called an observation. A single experimental observation (i.e. a Raman spectrum) is comprised of a large number of discrete data values. A complete experiment generally comprises observations that are

multivariate (i.e. multiple frequencies 200-4000cm^{-1}). Sometimes, different constituents result in very similar spectra, and there may only be subtle differences between their measurements. It is not possible to directly apply many of the traditional methods of statistical analysis to data of this kind. However, there are chemometric approaches that are especially useful for dealing with such data. These are known as data compression/projection techniques. The main goal of data compression/projection is to transform a data set comprising a large number of inter-correlated variates into a new uncorrelated (or nearly so) and ordered data set, which contains most of the significant information that was spread across the original variates (frequencies).[2-3]

One such data projection method is Principal Component Analysis (PCA). PCA decomposes a set of data into separate signal a noise parts. The data is presented as a matrix, with one row for each object (eg. a sample, an experiment or a state) and one column for each variate (measurement). The resulting model describes the structure in the data in terms of sample patterns and variate relationships. PCA is used for data exploration and classification. Partial Least Squares (PLS) is an alternative regression method, which decomposes the X (variates) matrix guided by the structure in Y (Raman intensity), and thus focuses very hard on prediction modelling of Y. PLS can be used for exploration, classification, regression and prediction. Common for both methods is that systematic variations in the data are found through projection and modelling of variance and covariance structure of the data matrices.

The direction of the largest variations in the multidimensional data space is found and a new coordinate axis in this direction (the first principal component (PC)) is determined. Then the direction of the second largest variations in the multidimentional data space is found and a new, second coordinate (the second PC) orthogonal to the first PC, is determined. Further PCs are found in a similar way, until all systematic variation has been described. The PCs may be seen as a transformed coordinate system consisting of fewer dimensions than the original variable system. Often two or three PCs are enough to describe the main variations in the data. For PLS principal components are usually called PLS-factors.

The projections of the samples onto the PC are defined as scores, which display the sample patterns in the data. The relationships between the original variates and the new PCs are expressed by loadings. Loadings display variate correlations. Scores are simply the sample coordinates in the new coordinate system, while loadings are the directions of the new axes relative to the original coordinate system. The residuals are the differences between the real sample positions in the old system and the projected positions. The scores/factors are ordered so that the first few contain most of the variance that was shared amongst the original variates and reduces the data set to a more manageable number of variates. Because the data are now uncorrelated, patterns or groups of observations may be revealed which were not apparent from the original data.

One of the most difficult tasks in using PLS is determining the correct number of factors to use for the model.[2] As more and more factors are calculated, they are ordered by the degree of importance to the model. Eventually, the factors will begin to model the system noise. The earlier factors in the model are most likely to be related to the constituents of interest. Later factors generally have less useful information for predicting concentration. In fact, if these factors are included in the model, the predictions can actually be worse than if they were ignored altogether. Models that include more factors than are really necessary to predict the constituent concentrations are called over fitted models. Models that do not use enough factors are known as under fitted models. There are many methods for determining the correct amount of factors but there is only one method used in this current work. This is called cross-validation. Simply explained cross-validation involves removing a spectrum (or a group of spectra) from the training data set and using the remaining data in the training set to predict its concentration. The predicted spectrum is then returned to the training data and the next spectrum (group) is predicted. This is repeated until all the data has been predicted. Using the difference between the predicted value and the known value, for each spectrum, a Predicted Residual Error Sum of Squares (PRESS) value is calculated for each factor. Usually the number of factors that results in the smallest PRESS value is determined to be number of factors to be used for the model.

5.3 Raman Microscopic Analysis of Carbon Particles from Coal Dust and DPM

5.3.1 Single Component Calibration Plots Using Integrated Spectral Areas

5.3.1.1 Introduction

The exposure limits for elemental carbon (EC) from DPM in coal mines was discussed in chapter 1. There is no legal limit in the UK due to there being no reliable method for determining the difference between EC from DPM and coal dust. However, the German occupational exposure limit of 0.1mg/m^3 (100μg/m^3) is used as a guideline. The development of a method for monitoring occupational exposure requires the capability of measuring down to five times lower and up to two times higher than the exposure limit. So, in this case, it is required to develop a method that can determine EC, from DPM, in the range of 20 to 200μg. In this section separate samples with a range of different loadings of DPM and coal dust are analysed using Raman microscopy to determine the linear range of the technique. The samples used in this thesis were collected on quartz fibre filters of 2.5cm in diameter. As stated earlier, these samples appear to be highly heterogeneous. The reproducibility of integrated areas of spectra taken at different points on the 2.5cm filters is also investigated.

5.3.1.2 Experimental

Separate DPM and coal dust samples were collected on quartz fibre filters using a multi-port air-sampling device know as a "Sputnik". A schematic diagram of the sampling rig is shown in figure 5.3.1. This system has previously been used to collect dust samples with very high accuracy and precision.[4]

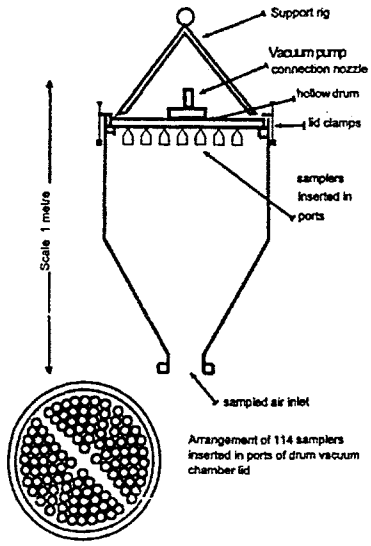

Fig 5.3.1: Schematic cross-section of Sputnik multi-port sampler[4]

The amount of material on the filter is known as the loading. This term will be used throughout the present report. It was decided, to get a reasonable estimation of the reproducibility of measurements on a sample, that a minimum of 10 "replicate" spectra of each sample was required. The word "replicate" warrants a precise definition to avoid confusion as its exact meaning depends on the different types of experiments carried out throughout this thesis. In this section 10 different spectra (each one taken at a different point on the filter) were taken of a sample, using the same instrument parameters for each spectrum. Each spectrum is considered to be a "replicate" analysis of the sample.
The filters were 2.5cm in diameter and the laser spot size ranged from 1-30μm. Therefore, 10 different scans analyse a very small proportion of the whole sample. However, it was necessary to systematically analyse the samples so that the 10 different scans gave the best possible representation of the whole sample. This was achieved by firstly imagining the filter to be in four quarters. These four quarters were then separated into inner, middle and outer sections. 2 spectra were taken in the inner section and 1 spectrum is taken in a middle and outer section of each quarter. These add up to 10 replicate spectra, per sample, in total. The areas from which each spectrum was taken on the filter is shown in figure 5.3.2. Some of the experiments to follow will use the same sampling criteria and the term replicate will be similar to here. Other experiments will

investigate the effects of other methods of sample analysis, which will change the manner that each replicate spectrum is collected. However, this will be clearly explained in the experimental section of each particular experiment.

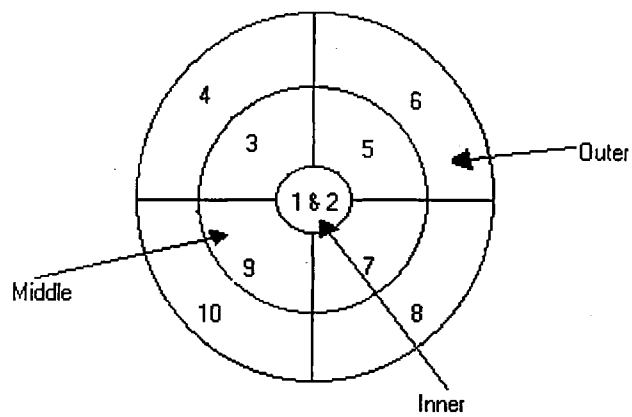

Figure 5.3.2: 10 different sample areas on the filters

Raman microscopic analysis was performed on a collection of filters with a range of separate coal dust and DPM loadings. The loadings for the samples analysed are shown in tables 5.3.1 and 5.3.2. Ideally samples with similar loadings of coal and DPM should have been analysed. However, the samples were prepared by a third party before the project started. So, the available samples were analysed. The parameters used for all the samples were 250 seconds scan time, x50 objective and the 25mW 633nm laser at 10% power, using the $900cm^{-1}$ to $1900cm^{-1}$ spectral range. These parameters were chosen because the 250s scan time resulted in an approximately 15 minute acquisition time, the x50 objective has a low refractive index, resulting in a large proportion of the scattered light being collected back up the microscope. 10% laser power was used to help prevent sample heating due to the laser being focused onto approximately a 2μm spot with the x50 objective.

Filter	Coal Loading (µg)
1	109
2	318
3	486
4	702
5	1010
6	1314

Table 5.3.1: Coal Loadings

Filter	DPM Loading (µg)
1	39
2	73
3	211
4	313
5	405
6	511

Table 5.3.2: DPM Loadings

5.3.1.3 Results and Discussion

Example spectra of pure coal dust (318µg loading) and DPM(313µg loading) are shown in spectra 5.3.1 and 5.3.2 respectively.

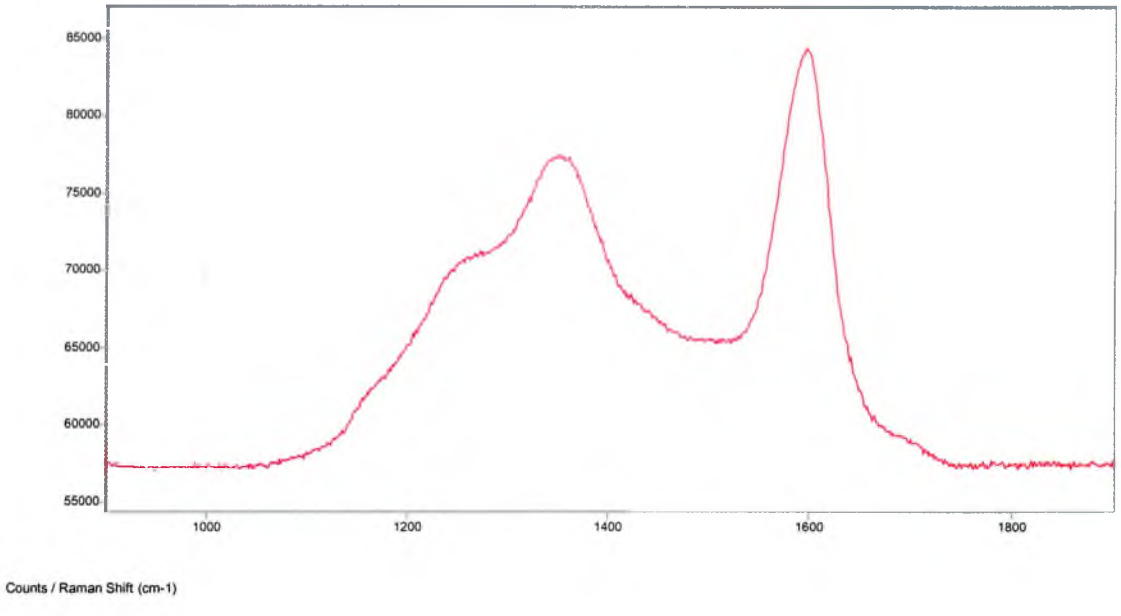

Spectrum 5.3.1: 318µg coal dust, 250s scan time, x50obj, 25mW 663nm laser at 10%

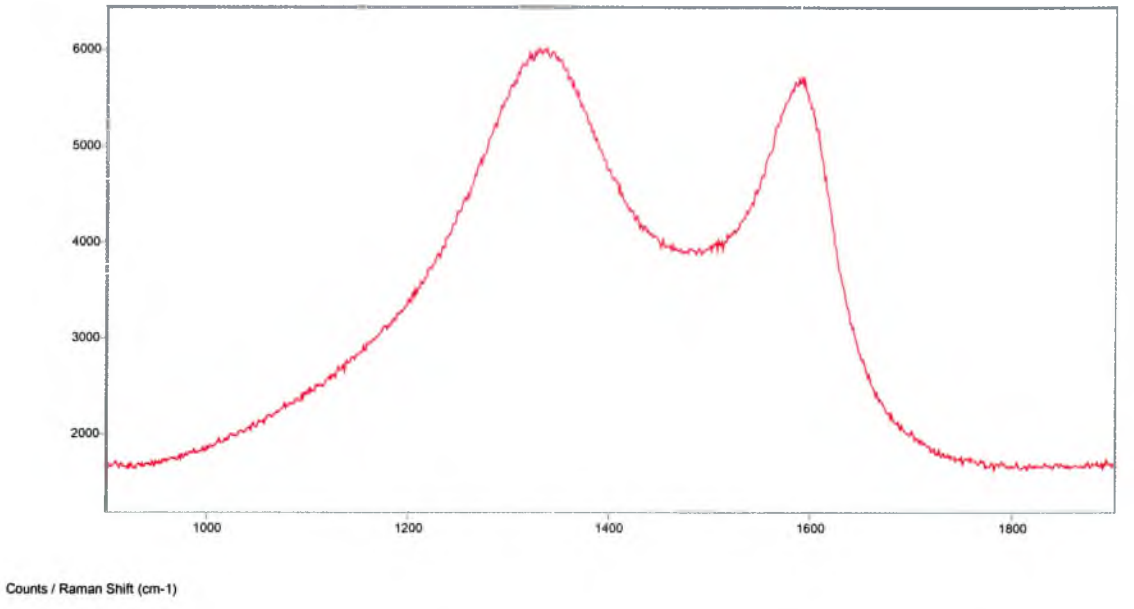

Spectrum 5.3.2: 313μg DPM, 250s scan time, x50obj, 25mW 663nm laser at 10%

The average integrated spectral areas and the standard deviation for 10 replicate spectra of each DPM and coal sample are shown in tables 5.3.3 and 5.3.4 respectively. The plots of the integrated spectral areas for each replicate spectrum versus the sample loadings of the DPM and coal dust are respectively shown in graphs 5.3.1 and 5.3.2.

Filter	DPM Loading (μ)	Average Integrated Area	Standard Deviation (%)
1	39	639084	41.6
2	73	807332	37.3
3	211	1150258	22.4
4	313	1496049	19.7
5	405	1263335	14.6
6	511	1604689	16.8

Table 5.3.3: average integrated spectral areas and standard deviation for DPM spectra

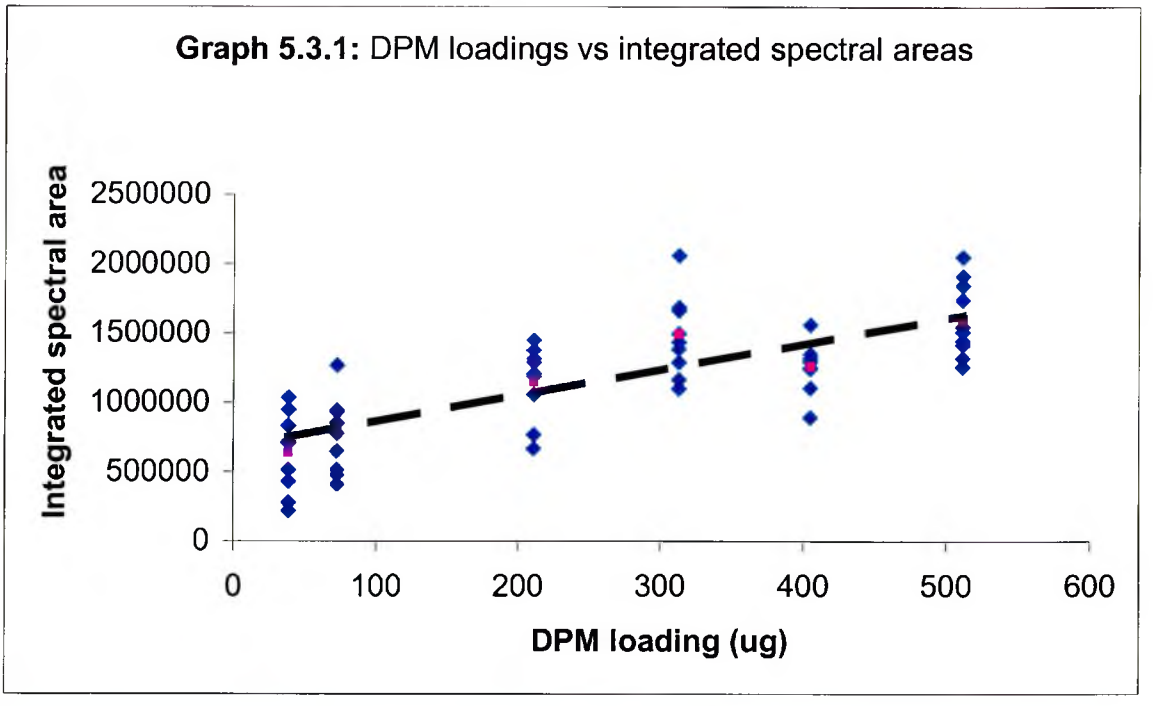

Filter	Coal Loading (μ)	Average Integrated Area	Standard Deviation (%)
1	109	5134183	39.9
2	318	7968761	13.1
3	486	8981387	10.7
4	702	8912654	24.3
5	1010	8531121	18.1
6	1314	7426244	18.1

Table 5.3.4: average integrated spectral areas and standard deviation for coal dust spectra

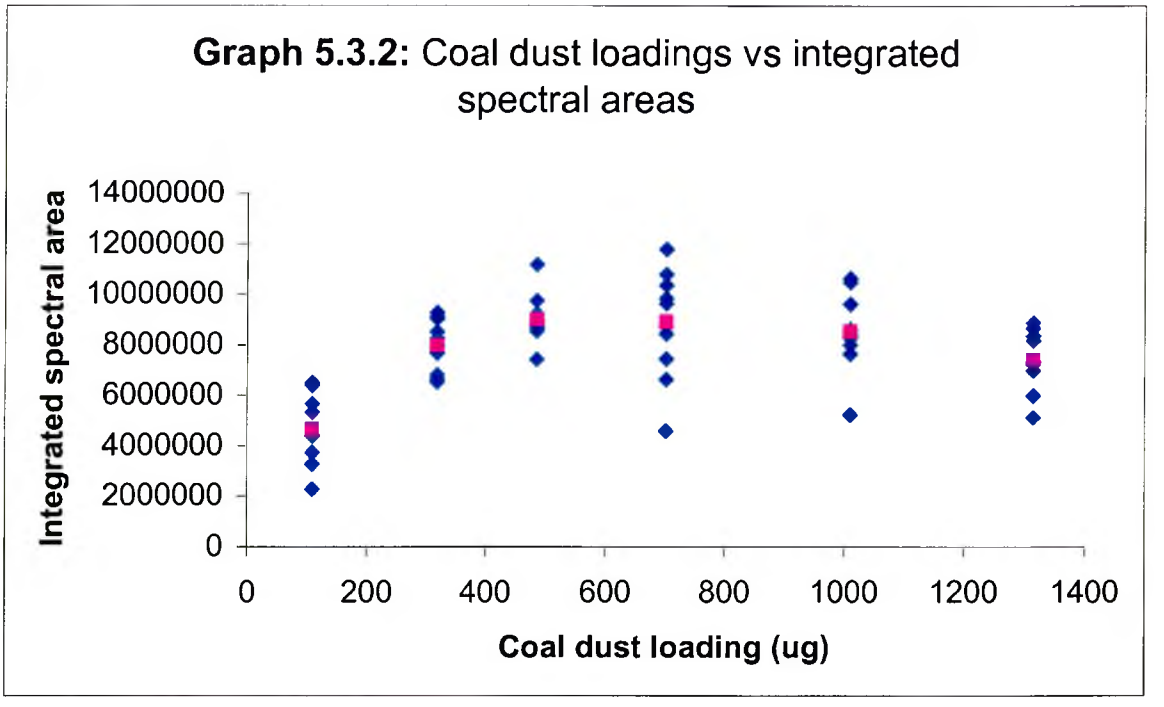

From the DPM loading versus integrated spectral areas plot (graph 5.3.1) we can see that there are large differences in the integrated spectral areas for the 10 replicate spectra of each sample. In fact, the standard deviation of spectral areas ranges from 41.6% for the 39μg sample to 14.6% for the 405μg sample. There appears to be a linear relationship between the sample loading and the spectral areas, in the 39μg to 511μg total DPM loading range. The proportion of EC in the DPM was unknown at this stage but a typical DPM sample has between 40 and 60% EC.[5] Therefore, the 39μg sample would have an expected EC content of between 15.6 and 23.4μg and the 511μg sample would contain 204.4 to 306.6μg EC. This indicates that the technique has the potential to determine EC from DPM in the required range of 20 to 200μm. However, if a reliable PLS model was to be produced an improvement in the reproducibility of the integrated spectral areas would be required.

The coal dust plot reaches a plateau at around 500μg. This indicates at loadings above this level we are just piling layers of coal dust on top of each other and the filter has effectively become saturated. As a result of this, loadings of greater than 500μg are outside the linear range of the technique. Therefore, when producing mixture standards

for a PLS model it will be necessary to keep the total sample weight to less than 500μg to avoid this problem. Also, this technique can not be used for determining DPM in the presence of high loadings of coal (>500μg) even if the DPM loading is within the 20 to 200μg range.

5.3.2 Principle Component Analysis (PCA) of separate cold dust and DPM spectra from section 5.3.1.

5.3.2.1 Introduction

In this section a PCA analysis is performed on a selection of the coal dust and DPM spectra collected in the previous section. This analysis can be used to firstly investigate if it is possible to distinguish (or discriminate) between the similar carbon spectra of coal and DPM, by chemometric means. In figure 5.2.4 (section 5.2) an example plot of PC scores is shown. In the example given the observations for each group are spread far apart. However, in a real situation the observations can be very close or even in the same position. Generally, the closer together the observations the more similar the corresponding spectral shapes are for the observations. So, the PC scores plot can give useful information on the reproducibility of spectral shapes, independent of concentration. To perform a PCA discriminate analysis it is necessary to divide the set of data into two different groups. The first group is used to develop the best parameters for the model. This is called the training set. When the best possible model has been developed (using the training set) a second group of spectra of known samples are applied to the model to test its predictive accuracy. Hence, this is called the test set. Ideally, the training set should contain two thirds of the data and the test set should contain the remaining third.

5.3.2.2 Experimental

40 spectra in total were chosen for the PCA analysis. These comprised of 20 DPM spectra, which were 10 replicates each of the 405μm and 511μm samples, analysed in the

previous section. The remaining spectra were 20 coal dust spectra, which were 10 replicates each of the 109μm and 318μm samples. 13 DPM and 13 coal dust spectra (26 in total) were used for the training set and the remaining 14 spectra (7 DPM and 7 coal) were reserved for the test set. All the spectra were normalised. A model was developed using the training set and this model was used to predict which group (coal or DPM) each spectrum of the test set belongs to. The accuracy of the model was checked by comparing the predicted group for each test spectrum with its know grouping.

5.3.2.3 Results and discussion

Table 5.3.3 shows the percentage variance for each PC. Almost 100% of the variance is contained in the 1st PC. Therefore, if this variance is due to spectral true spectral differences, it is only necessary to use the first component when applying the analysis to an unknown. Using a greater number of components would result in a data being overfitted.. However, before discussing the results of the test set it is first necessary to discuss the training set results in more detail.

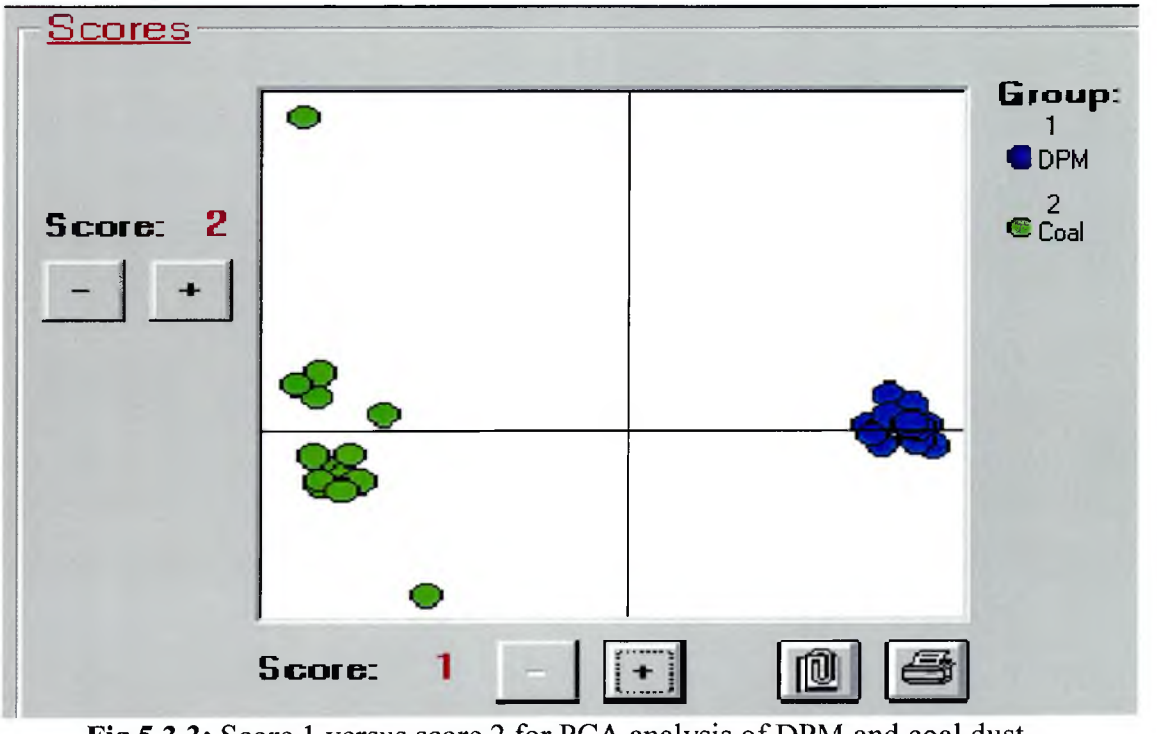

Fig 5.3.3: Score 1 versus score 2 for PCA analysis of DPM and coal dust

PC score	1	2	3	4	5
%Variance	99.71	0.14	0.04	0.02	0.01

Table 5.3.6: Variance of each PC for PCA analysis of DPM and coal dust

The PC scores plot for the 1st versus the 2nd score is shown in figure 5.3.3. The observations for the coal dust and DPM spectra are clearly separated into two different groups, which shows that PCA is capable of easily distinguishing between carbon spectra from coal dust and DPM. The DPM observations are bunched together in a very closely spaced group. This indicates that their corresponding spectra have very similar shapes. However, the coal dust spectra are not bunched as closely together as the DPM spectra, which indicates that their spectral shapes are not very similar, compared with those of the DPM. This large distribution (or spread) in observations is not a major concern for this particular analysis because the DPM and coal spectra are separated into two distinct individual groups. However, if the analysis involved trying to distinguish between more than two carbon types some of the coal dust observations may become confused with these other carbon types, due to their wide distribution. Another concern is that PLS calculates the concentrations of different components by using a combination of reference spectral shapes and concentrations. If there is a difference in spectral shapes for mixture standards, with the same concentrations of components, it would undermine the ability of a PLS model to predict the concentrations of these different components.

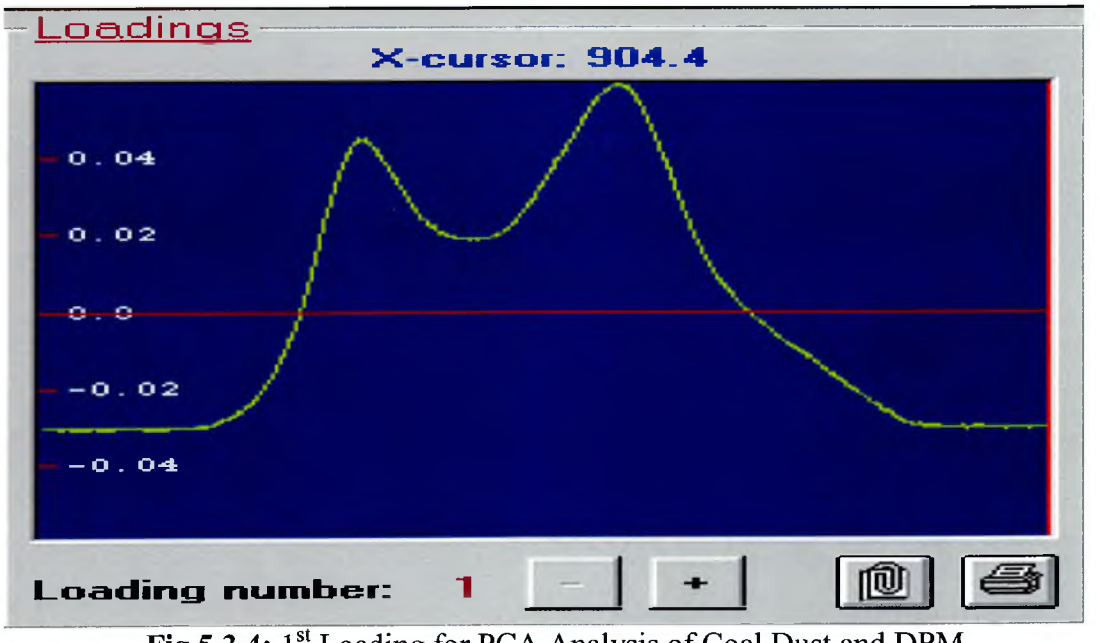

Fig 5.3.4: 1st Loading for PCA Analysis of Coal Dust and DPM

The 1st loading for the PCA analysis, which corresponds to the 1st PC, is shown in figure 5.3.4. The loading basically shows where the variance between the observations for each group occurs. Where the loading is at a maximum the variance between the groups is at its largest. Variance between different groups need not necessarily be due to real spectral differences. There can be differences in the spectra due to different methods of processing, such as baseline corrections or smoothing, or perhaps differences due to interference from water vapour, in IR spectra. PCA recognises the variance between the spectra and assigns the variances sequentially to each PC. So, there is the distinct possibility for the 1st PC to contain variances from differences other than true spectral features. Unfortunately there was no option in the software to display values on the x-axis. However, it will correspond to the same scale as the inputted Raman spectra. In this case the range is 900-1900cm-1, going from right to left. Therefore the two major peaks in the variance correspond to 1350cm^{-1} and 1585cm-1, which are due to differences in the Raman carbon D and G bands respectively, for each component. There is also a distinct shoulder at around 1250cm^{-1}, which corresponds to the Raman feature, due to an sp^3-bonded carbon phase, observed in the Raman spectra of the coal dust but not in the DPM spectra. The positions of the variance peaks confirm that the variance between the coal dust and DPM spectra was definitely due to differences in their spectra for the first PC.

Using the developed model group predictions were made for a test set of 14 spectra (7 DPM and 7 coal dust). The model correctly assigned all 7 DPM test spectra to group 1 and all 7 coal dust test spectra to group 2. This showed that the developed model was capable of distinguishing between separate coal dust and DPM carbon spectra.

5.3.3 Investigation of Effect of Changing Objective on Reproducibility of Integrated Spectral Areas

5.3.3.1 Introduction

Changing the objective used for the analysis from X50 to X5 increases the laser spot size from around 2μm to approximately 30μm. Sampling a larger area may help improve the reproducibility of the spectra. Figure 5.3.5 illustrates the possible difference in sample areas for different laser spot sizes focused onto heterogeneous carbon particles. We can see from this figure that the larger laser spot samples a much more representable sample area than the smaller spot size. Therefore, if the larger area spot was moved to a different region of the sample it is much more likely, than the smaller spot size, to be focused on a region similar to the previous region. This in turn, should result in more reproducible spectra. In this section we will investigate the effects of increasing the laser spot size, by using a lower magnification objective, on the reproducibility of integrated spectral areas of DPM and coal dust.

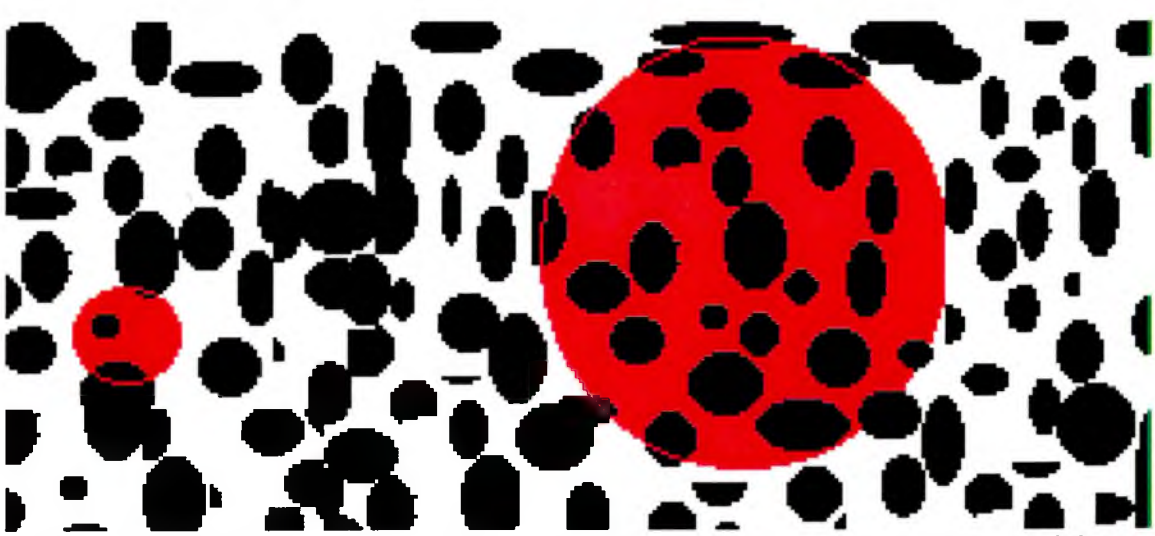

Figure 5.3.5: Different laser spot sizes focused onto heterogeneous carbon particles

5.3.2.2 Experimental

In section 5.3.1, samples with a range of loadings were analysed using 250s scan time, X50 objective and 10% laser power. The work in this section involves the use of the X5 objective. Due to the difference in the aperture of the X5 objective much less of the scattered light is collected back up through the microscope, greatly reducing the signal reaching the detector. The laser spot size is approximately 30μm for an X5 objective, compared to about 3μm for an X50 objective. This has the effect of spreading the laser power over a larger area. So, it is possible to increase the incident laser power from 10% to 100% without increased risk of heating the sample. The increase in laser power will go some way to compensate for the loss of signal due to the use of the X5 objective but it was also necessary to increase the scan time to improve the signal further. The new parameters used were 400s scan time, X5 objective and 100% laser power.

Three coal dust samples with 109, 218 and 486μg loadings were analysed using these new parameters and the sampling criteria outlined in section 5.3.1.2 (10 replicate spectra taken at different points on the filter). A DPM sample with a 405μg loading was also analysed using these parameters.

5.3.2.3 Results and discussion

Table 5.3.7 shows the percentage standard deviation for the integrated spectral areas of 10 replicate spectra taken for three different coal dust samples using the two different parameters. A dramatic improvement in the reproducibility of the spectral areas for the spectra taken of the coal dust with the X5 objective was observed. The 109μg sample standard deviation improved from almost 40% to less than 20%, the 318μg sample improved from 13% to almost 7% and the 486μg sample improved from almost 11% to less than 6%. A large improvement was also observed for the 405μg DPM sample with the standard deviation decreasing from 14.6 to 9.5%.

Filter	Coal Dust Loading (μg)	Error (±%) 1st Parameters*	Error (±%) 2nd Parameters**
1	109	39.9	18.6
2	318	13.1	7.2
3	486	10.7	5.6

Table 5.3.7: Comparison of variation of integrated spectral areas for different parameters
*x50obj,250s,10% power laser **x5obj,400s,100% laser power

5.3.4 Mixture Sample Production

5.3.4.1 Introduction

The production of standards containing a mixture of coal dust and diesel particular matter is not a trivial process. When sampling air in a coal mine it is filtered through quartz fibre filters which are connected to sample pumps with a know flow rate (usually 2l/min). When making synthetic standards, it is imperative to create a sampling system that results in the collected samples being deposited onto the filters in a similar manner as in a coal mine. Therefore, it is essential to sample both the DPM and coal dust simultaneously. When sampling both particle types it is essential to know the rate of deposition of each component. Therefore, each component was first sampled separately. This allowed the characterisation of each component's deposition rate, so the concentration each component present in mixture samples, collected under similar conditions, could be estimated.

5.3.4.2 Experimental

A sampling apparatus was set up, which was similar to the system shown in figure 5.3.6. The system contains a sample chamber positioned in the centre of a sealed box. A hole was cut at one end of the box, so an exhaust pipe from a diesel-powered van could be inserted. There were also several holes punched in the opposite end of the box to assist the airflow. The chamber consisted of a steel cylinder with a removable cone-shaped lid with holes in it to allow air to enter the chamber. Four pumps, calibrated to 2L/min, were connected to valves at the bottom of the chamber, from the outside. These were used to

draw air from the surrounding atmosphere, of the box, into the sampling chamber. Filter holders, with paper filters, were connected to these valves inside the chamber, to prevent dust being sucked into the pumps. Two more pumps, positioned outside the box, were calibrated to approximately 2L/min. These pumps were connected to samplers containing clean pre-weighed quartz fibre filters. The samplers were placed into the centre of the chamber to sample air from the chamber's atmosphere.

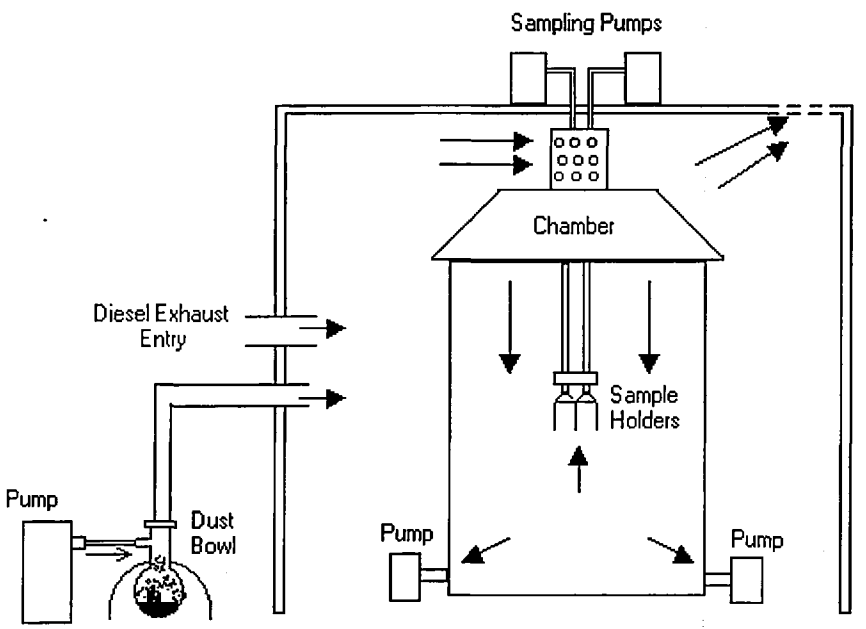

Fig 5.3.6: Schematic diagram of the mixture standard sampling system

Before the sampling took place, the diesel van engine was warmed up, to give consistent emissions, by running it on idle for 1 hour. The exhaust was connected to the sampling apparatus and the pumps at the base of the chamber turned on. This allowed the box to fill and a state of equilibrium to be achieved in the box and chamber's atmospheres. The sampling pumps were turned on and the exhaust fume drawn into the chamber was sampled for 10 minutes. When the sampling was complete, all the pumps were turned off and the exhaust disconnected from the sampling apparatus. The procedure was repeated using different sample times of 2.5,10,15 and 20 minutes. The filters were weighed and the amount of particulate collected on each was calculated by subtracting the original weight of the filter from the loaded filter. There was only one filter with a loading for 20

minutes because one of the pumps failed during sample collection. The total weight of DPM for each sample was normalised according to the flow rate of the pump used to collect the sample. The EC content of the DPM was estimated for **6** of the 9 samples, using a coulometric technique similar to that described in chapter 1 (section 1.2.5). The sample weights, corresponding sampling times and flow rates for the samples are shown in table 5.3.8. The sample weights were normalised according to the sample pump's flow rate (approx. 2L/min). The normalised weights were plotted against their sampling times and a linear plot resulted with an R^2 value of 0.98 for the total DPM weights and 0.99 for the EC weights, as can be seen in graph 5.3.3. This process provided a calibration to predict the rate of DPM collection.

Filter	Sample time (min)	Pump Flow Rate (L/min)	Total DPM Weight (g)	Estimated Elemental Carbon (µg)	Elemental Carbon (%)
1	2.5	2.03	68	-	-
2	2.5	2.02	44	14	32
3	5	1.96	85	49	58
4	5	2.04	118	77	65
5	10	1.97	214	-	-
6	10	1.91	209	164	78
7	15	2.02	286	-	-
8	15	2.03	295	230	78
9	20	2.067	374	307	82

Table 5.3.8: DPM weights for different sample times

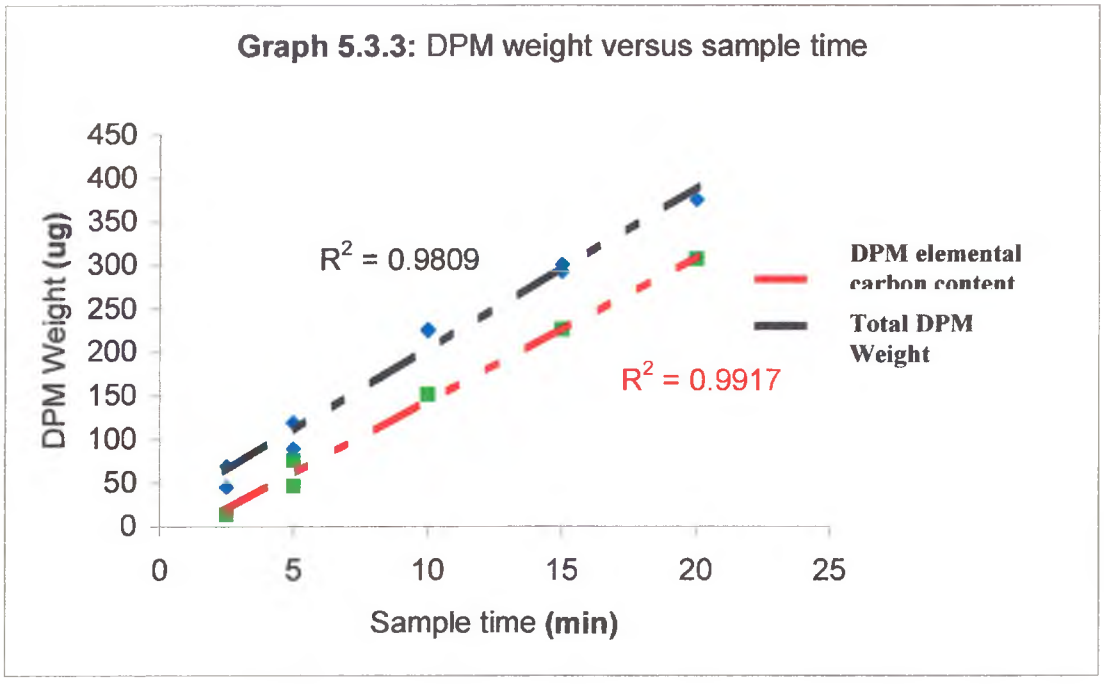

The proportion of EC in the DPM samples appeared to increase as the sampling time increased. It is not fully clear why this occurs. As stated earlier the engine was run on idle for 1 hour to give it time to warm up and give constant emissions. The 10 minute samples were collected first. If the elemental carbon content of the emissions was unstable when the sampling started the 2.5 and 5 minute samples would be expected to have a higher EC proportion than the 10 minute samples. However, this was not the case. A possible explanation for the higher loading samples having a higher proportion of EC (or a lower proportion of organic carbon) is that the quartz fibre filters readily adsorb CO_2 from the athmosphere. For short sample times a small proportion of the filter was covered by DPM and there were a large number of fibres available to adsorb CO_2. The DPM particles themselves readily adsorb organic material but this would occur in the engine. So, as the sample time increases more of the filter becomes covered with the DPM and there are less fibres for the organic material in the emissions to be adsorbed onto, therefore decreasing the organic carbon content of the higher loading samples.

For later work in this thesis we used the total DPM weight for our PLS models and then useed graph 5.3.3 to estimate the EC content.

After the deposition rate of the DPM had been established it was necessary to repeat the procedure for the coal dust. This was firstly attempted by using an instrument called a dust bed flow chamber, which was designed to give a constant flow of fine dust particles. This instrument was filled with coal dust in one compartment and a chain-like mechanism carried the dust into another compartment that was essentially a pressurised dustbowl with a constant airflow. The instrument was connected to the box containing the sample chamber and the system was allowed to fill for 10 minutes. The dust was then collected in the same manner as the diesel fumes. However, very little dust was collected on the sample filters. Various combinations of increasing the dust bowl pressure, increasing the fill time and adding extra coal dust to the first chamber were attempted. However, the flow rate for the coal dust could not be increased sufficiently. This meant that if the coal dust and the diesel fume were collected simultaneously there would be a few orders of magnitude more DPM present. It was desirable to produce standards that had loadings of similar magnitudes, of both constituents. Hence, this method could not be used for supplying coal dust to the system.

The next attempt at preparing samples with coal dust was to use a dust bowl connected to an air pump. After a several trials it was observed that using 4g of coal dust and applying 6L/min air pressure resulted in an appropriate amount of coal dust being deposited onto the sample filters. However, the rate of sample deposition was non-linear. The main reason for this was a large amount of coal dust was flowing from the dust bowl at the start of the experiment. As the experiment continued there was less dust present in the bowl. Therefore, less and less was dust entering the box as the experiment continued. Another problem was that the procedure was not reproducible. When the experiment was repeated again, different sample rates were observed for similar sample times. The principal reason for this was that the distribution of coal dust in the sampling system was highly dependent on positioning of the tubing connecting the dust bowl to the sampling system. It was always inserted into the box through the same hole but it appeared that the slightest difference in direction of entry resulted in a different deposition rate due to a change in sample distribution in the chamber. An attempt was made to tape the tube into position but when the tubing had to be removed from the dust bowl to put more sample in

its position was changed again. Considerable time and effort was spent on trying to set up an arrangement which gave reproducible results. However, this was unsuccessful. Hence, it was decided when collecting the mixture samples it would be necessary to measure the total deposited particulate weight and to calculate the weight of the coal dust by subtracting the predicted DPM deposit.

The system was set up as shown in fig 5.3.7 and various sampling times were used to get mixtures of coal dust and DPM on the filters. The sampling parameters and resultant weights are shown in table 5.3.9. The fill time corresponds to the amount of time the coal and diesel was allowed to circulate around the system before the sample pumps were turned on. The sample time corresponds to how long the sampling pumps were turned on. 4g of coal dust were added to the dust bowl when necessary.

Sample Collection Number	Sample Number	Pump Flow Rate (L/min)	Fill Time (min) Coal|DPM		Sample Time (min)	Total Weight (μg)
1	1(a)	2.03	3	10	5	538
(4g dust)	1(b)	1.998	3	10	5	506
2	2(a)	1.975	3	10	10	344
	2(b)	1.972	3	10	10	368
3	3(a)	2.05	3	10	15	182
	3(b)	2.06	3	10	15	420
4	4(a)	2.08	10	10	7.5	295
(4g dust)	4(b)	1.998	10	10	7.5	275
5	5(a)	2.07	3	10	12.5	381
	5(b)	2.064	3	10	12.5	329
6	6(a)	2.05	4.5	10	7.5	393
(4g dust)	6(b)	2.03	4.5	10	7.5	395

Table 5.3.9: Sampling parameters and total weights for each sample

Using graph 5.3.3 it was possible to estimate the amount of DPM present for each sample. The amount of coal dust present was calculated by subtracting the estimated DPM weight from the total weight. The calculated DPM and coal dust weights for each sample are shown in table 5.3.10.

Sample Number	Total Weight (μg)	Total DPM Weight (μg)	Normalised DPM Weight (μg)	Coal Dust Weight (μg)
1(a)	538	64	65	473
1(b)	506	64	66	440
2(a)	344	204	214	140
2(b)	368	204	214	154
3(b)	420	297	299	123
4(a)	295	157	156	139
4(b)	275	157	162	118
5(a)	381	251	251	130
5(b)	329	251	251	78
6(a)	393	157	159	234
6(b)	395	157	160	235

Table 5.3.10: Calculated weights of DPM and coal dust for each sample

5.3.5 Analysis of mixture carbon standards

5.3.5.1 Introduction

Mixture samples with a range of know coal dust and DPM loadings were now available. These samples could now be analysed and their spectra ultimately be used for a PLS calibration model.

5.3.5.2 Experimental

6 of the samples with various mixtures, as shown in table 5.3.11, were analysed using an x5 objective, 400s scan time and 633nm 25mW laser at 100% power. 10 replicate spectra were taken of each sample, using the same criteria as in sections 5.3.1 and 5.3.4, with each scan taken at a different point on the filter.

The response of the Raman instrument can vary considerably from day to day and it was not possible to collect all 60 spectra in one day. Therefore, if these spectra were to be used for a PLS model, it was necessary to calibrate the instrument at the start and at the end of each day, to account for the different response of the instrument. The instrument

was calibrated by collecting a 1 second scan of a clean piece of flat crystalline silicon, using the X50 objective and 100% laser power. This was repeated three times at the start and end of each day. The integrated spectral areas of the resultant spectra were measured and the average values for each day were compared.

One spectrum of each sample was curve fitted using the fitting application of the Grams32 software. When performing the curve fit of each sample, it would have been ideal to include all the bands determined for each component (7 for coal and 4 for DPM), in section chapter 3 (section 3.5). Then the change in relative intensities for each peak could be monitored for each sample. However, this process would be beyond the capabilities of the curve fitting software. Especially since some the bands are very broad (over 170cm^{-1}) and appear in similar positions for both the coal and DPM, resulting in them being strongly overlapped. Therefore, it was decided to keep the fitting process relatively simple by only including 4 Gaussian bands. These bands being the D and G bands and bands at around 1250cm^{-1} and 1500cm^{-1}. The D and G band ratios and positions were used to quantitatively show changes in the spectra for each mixture sample.

Sample	Total Weight (μg)	DPM Weight (μg)	Coal Dust Weight (μg)
1	506	66	440
2	344	214	140
3	420	299	123
4	275	162	118
5	329	251	78
6	393	159	234

Table 5.3.11: Calculated coal and DPM weights for each sample analysed

5.3.5.3 Results and discussion

An example spectrum of a mixture sample shown in spectrum 5.3.3 and its curvefit is shown in figure 5.3.7. Peak positions, heights, widths and areas for the curvefits of each sample are shown in tables 5.3.12 through 5.3.17. The D/G

band ratios and the standard deviation for 10 replicates spectra of each sample are shown in table 5.3.18.

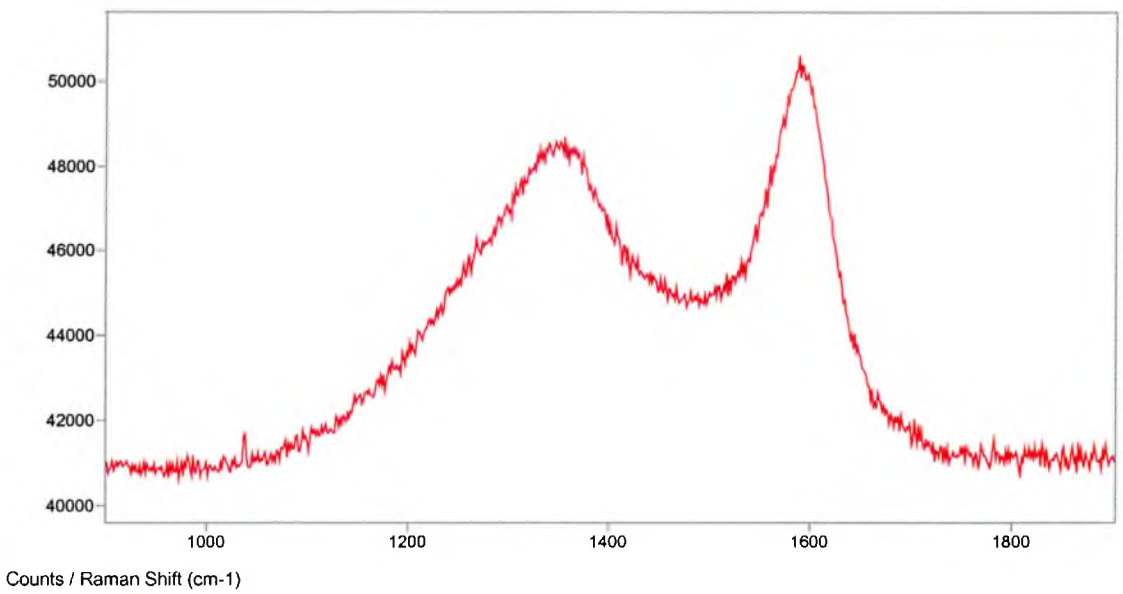

Spectrum 5.3.3: 66mg DPM and 440mg Coal Dust, x5obj, 400s, 633nm laser at 100%

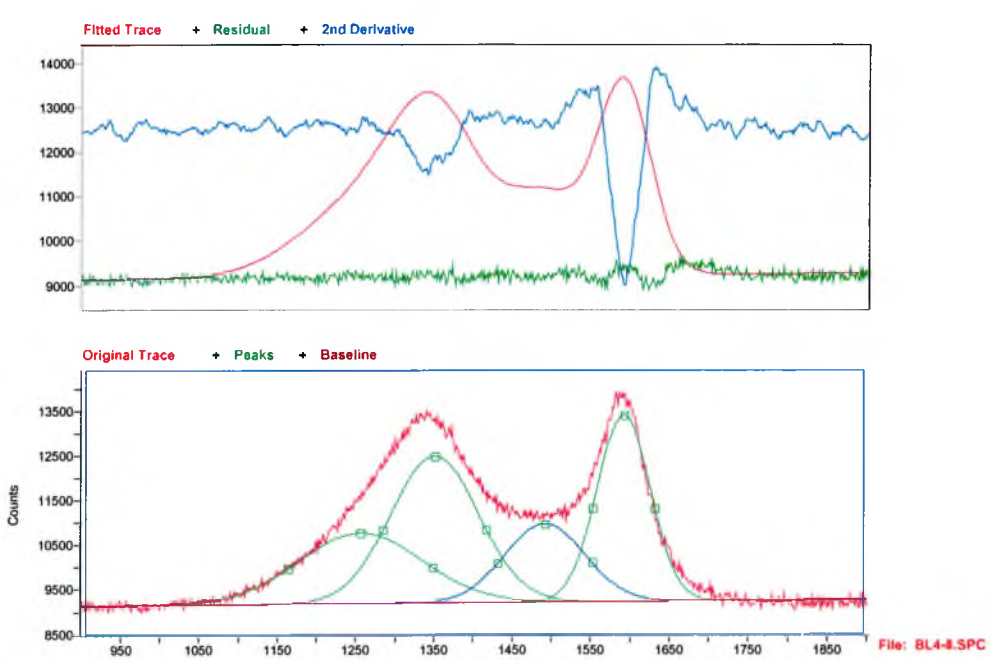

Figure 5.3.7: Curve fit of a 66µg DPM and 440µg coal dust mixture sample spectrum

Peak	Position (cm^{-1})	Height (a.u.)	Width (cm^{-1})	Integrated Area
1	1257	1577	185	311392
2	1351	3283	133	463473
3	1492	1751	119	222881
4	1593	4173	79	353550

Table 5.3.12: Fitted peak positions, heights, widths and areas of a 66μg DPM and 440μg coal dust mixture sample spectrum

Peak	Position (cm^{-1})	Height (a.u.)	Width (cm^{-1})	Integrated Area
1	1225	545	184	107143
2	1339	2401	144	368410
3	1488	1057	122	138114
4	1591	2276	89	214868

Table 5.3.13: Fitted peak positions, heights, widths and areas of a 214mg DPM and 140μg coal dust mixture sample spectrum

Peak	Position (cm^{-1})	Height (a.u.)	Width (cm^{-1})	Integrated Area
1	1244	1403	175	261916
2	1349	3548	137	518803
3	1493	1725	115	211680
4	1593	4202	80	357069

Table 5.3.14: Fitted peak positions, heights, widths and areas of a 299mg DPM and 123μg coal dust mixture sample spectrum

Peak	Position (cm^{-1})	Height (a.u.)	Width (cm^{-1})	Integrated Area
1	1220	879	168	157594
2	1344	3655	151	587165
3	1487	1492	99	156545
4	1590	3743	91	365053

Table 5.3.15: Fitted peak positions, heights, widths and areas of a 162mg DPM and 118μg coal dust mixture sample spectrum

Peak	Position (cm^{-1})	Height (a.u.)	Width (cm^{-1})	Integrated Area
1	1231	1224	165	214791
2	1348	3774	143	574431
3	1494	1689	111	198949
4	1592	4232	80	360766

Table 5.3.16: Fitted peak positions, heights, widths and areas of a 251mg DPM and 78μg coal dust mixture sample spectrum

Peak	Position (cm^{-1})	Height (a.u.)	Width (cm^{-1})	Integrated Area
1	1260	514	147	80948
2	1353	713	104	79704
3	1475	362	129	49839
4	1592	959	80	82187

Table 5.3.17: Fitted peak positions, heights, widths and areas of a 159μg DPM and 234μg coal dust mixture sample spectrum

Sample	Total Weight (μg)	DPM Weight (μg)	Coal Dust Weight (μg)	D/G Integrated Area Ratio	Standard deviation (%) of Integrated spectral areas
1	506	66	440	1.3	21.8
2	344	214	140	1.7	21.1
3	420	299	123	2.4	4.9
4	275	162	118	1.5	14.1
5	329	251	78	1.6	13.3
6	393	159	234	1.0	21.8

Table 5.3.18: Coal and DPM weights and D/G ratios for an example spectrum of each sample and integrated spectral areas standard deviation

When comparing the D and G peak height ratios with DPM and coal dust loadings, no obvious trend was observed. A plot of DPM/coal dust loading ratios versus D/G band ratios is shown in graph 5.3.4. From this plot it is evident that the D/G band ratios increase systematically with increasing DPM/coal dust ratios. However, two exceptions to this trend are the samples with 0.15 and 3.2 DPM/coal dust ratios. These samples respectively have 6.6 times more coal dust than DPM and 3.2 times more DPM than coal dust. So, perhaps the much higher amount of one component compared to the other, for both these samples, explains why they do not conform to a monatomic trend. A plot of the DPM/coal dust loading ratios versus D/G band ratios, omitting these two samples, is shown in graph 5.3.5. A linear trendline with an R^2 of 0.997 was fitted to these points. This is an acceptable R^2 value. However, this study only involved 4 points and the two samples omitted from study, in graph 5.3.5, had similar total loadings and D/G band ratios compared to the other samples. Therefore, it would not be possible to use this method alone for determining the amount of DPM and coal dust in unknowns.

Graph 5.3.4: DPM/Coal Dust Ratios vs D/G band Ratios

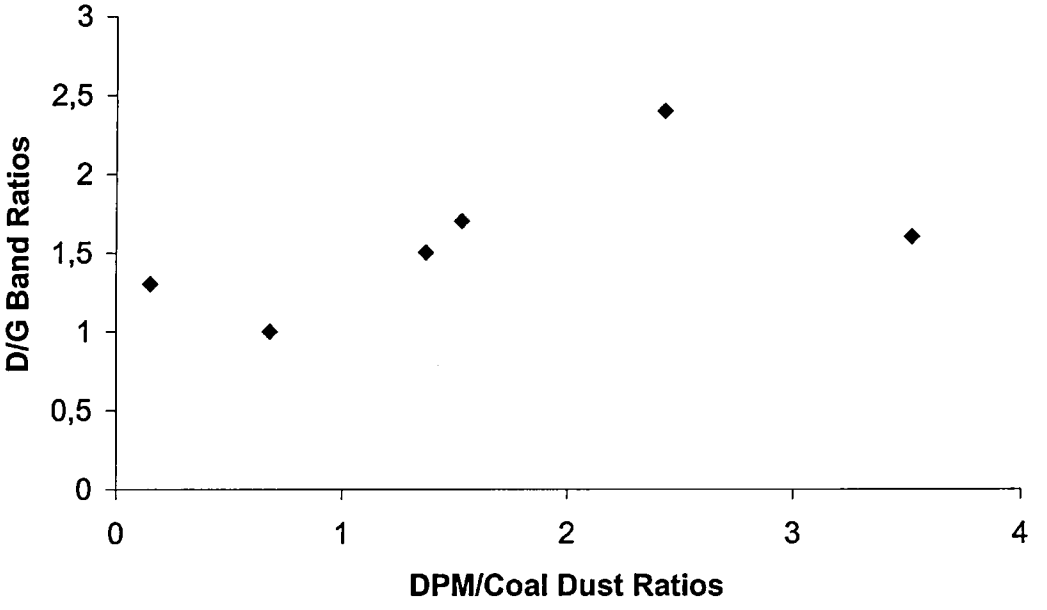

Graph 5.3.5: DPM/Coal Dust Ratios vs D/G band Ratios

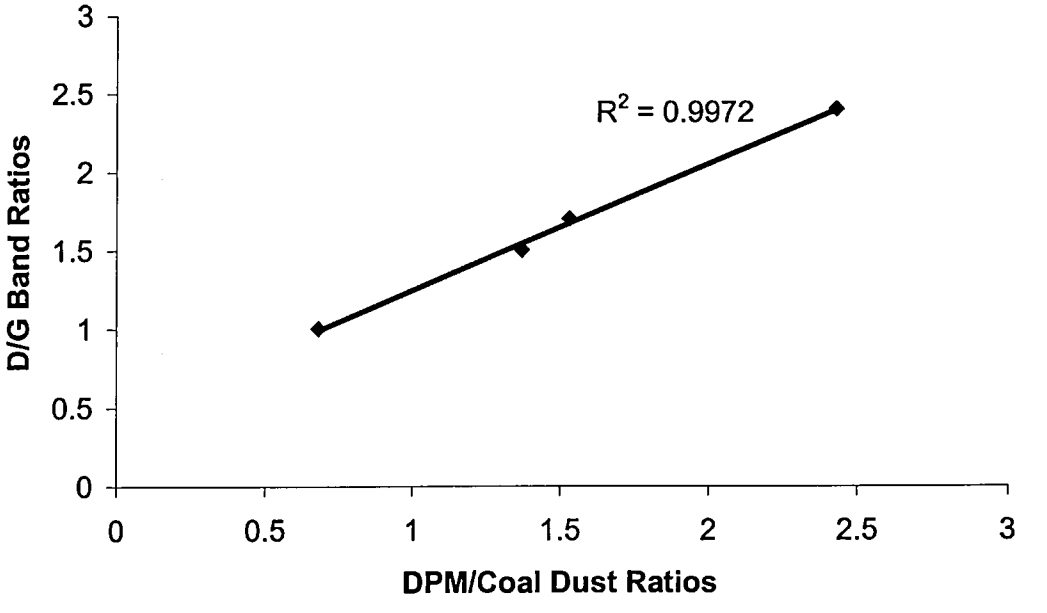

The curvefit performed on the mixture samples was somewhat simplified and known bands were omitted from the fit. This would result in different results from the curve fits on the mixture samples compared to the separate samples (studied in chapter 3 section 3.5). However, it is still important to compare the G and D band positions and widths of the mixture samples with the original separate samples. This gives information on idea of how the spectra of the mixture standards change according to their contents.

The G band positions for the separate coal and DPM spectra were 1596cm^{-1} and 1595cm^{-1} with bandwidths of 63cm^{-1} and 79cm^{-1} respectively.

The G band positions and widths change very little across the range of mixture samples, lying in the range of 1590-1593cm^{-1} and 79-91cm^{-1} respectively. The broader G bands of 89cm^{-1} and 91cm^{-1} occurred for samples with a greater DPM content, compared to coal dust. However, some samples with a greater DPM content had G bandwidths of around 80cm^{-1}, which is comparable with samples that had a greater coal dust content. The omission of certain bands from the curvefit, may explain the shift of the G band position from around 1595cm^{-1}, in the separate samples, to around 1590cm^{-1}, in the mixture samples. The separate coal dust and DPM samples had D band positions at 1353cm^{-1} and 1335cm^{-1} with widths of 118cm^{-1} and 154cm^{-1} respectively. The D band position for the mixture standards studied here varied from 1339cm^{-1} to 1353cm^{-1}. With the exception of the sample with 214μg DPM and 140μg coal dust, which had a D band position of 1339cm^{-1}. All samples appear to have D band positions closer to that of a coal dust sample rather than a DPM sample. This may be due to the fact the coal dust spectra are more intense than DPM spectra (as discussed in section 3.5.4). The D bandwidths of mixture samples varied from 104-151cm^{-1}.

5.3.6. The first PLS calibration model calibration of mixture coal dust and DPM samples

5.3.6.1 Introduction

The availability of mixed standard samples, with known amounts of DPM and coal dust, made it possible to produce a set of spectra to be used for a PLS model.

In the previous section, the standard deviation of spectral areas of 10 replicates for mixture samples was determined to be as large as almost 22%. Also, a wide distribution in the PCA observations for coal dust spectra had been observed. These results suggested that using the current parameters (X5 objective, 400s scan time and 100% laser power) would result in a PLS model with poor predictive accuracy. However, although time consuming, it was useful at this stage to analyse the mixture standards to determine if similar results, to the separate samples, were obtained. The use of the mixture samples' spectra for a PLS model gave valuable experience at performing PLS calibrations. This also helped us become familiar with the operation of the Grams PLS-PlusIQ chemometic software. This software had the capability of outputting a plethora of information pertaining to a developed model. This information included spectral/concentration residuals, t-tests, f-tests etc. However, for the initial PLS models we were only interested in using the PRESS plot to determine the number of factors to be used for the model and the actual versus predicted concentration plots to investigate the predictive accuracy of the model. When the actual versus predicted concentration plots indicated that a model with adequate predictive capability had been developed we investigated the additional information available from the software. We also waited until this final model had been developed before testing its predictive accuracy with a mixture sample(s) with known loadings, which were not used in the development of the model.

5.3.6.2 Experimental

PLS models were constructed using all the replicate spectra for each mixture sample listed in table 5.3.19. 60 spectra in total were used for the model. The concentrations for each sample were normalised according to the response on the day they were analysed, using the calibration method outlined in section 5.3.5.2 (using the 520cm^{-1} band of crystalline silicon). A PLS model was constructed using the Grams32 PLSplus/IQ software. The spectra were baseline corrected, mean centred, the whole spectral range was used, 10 factors were calculated and cross-validation was applied.

5.3.6.3 Results and discussions

The DPM and coal dust loadings for each mixture were normalised, according to the average integrated area of the 520cm^{-1} Si peak, for the particular day each sample was analysed. The component concentrations input into the data set for each mixture sample is shown in table 5.3.19.

Sample	DPM Weight (μg)	Normalised DPM Weight (μg)	Coal Dust Weight (μg)	Normalised Coal Dust Weight (μg)
1	66	91	440	608
2	214	338	140	211
3	299	299	123	123
4	162	231	118	168
5	251	335	78	104
6	159	212	234	312

Table 5.3.19: Mixture standards DPM and coal dust loadings and their normalised values used for the PLS model

From the PRESS plots, in figures 5.3.8 and 5.3.10, 3 factors were chosen for the DPM analysis and 2 factors for the coal dust spectra. The actual versus predicted concentration plots for the PLS model are shown in figures 5.3.9 and 5.3.11. The R^2 values for DPM and coal dust were 0.865 and 0.7625 respectively.

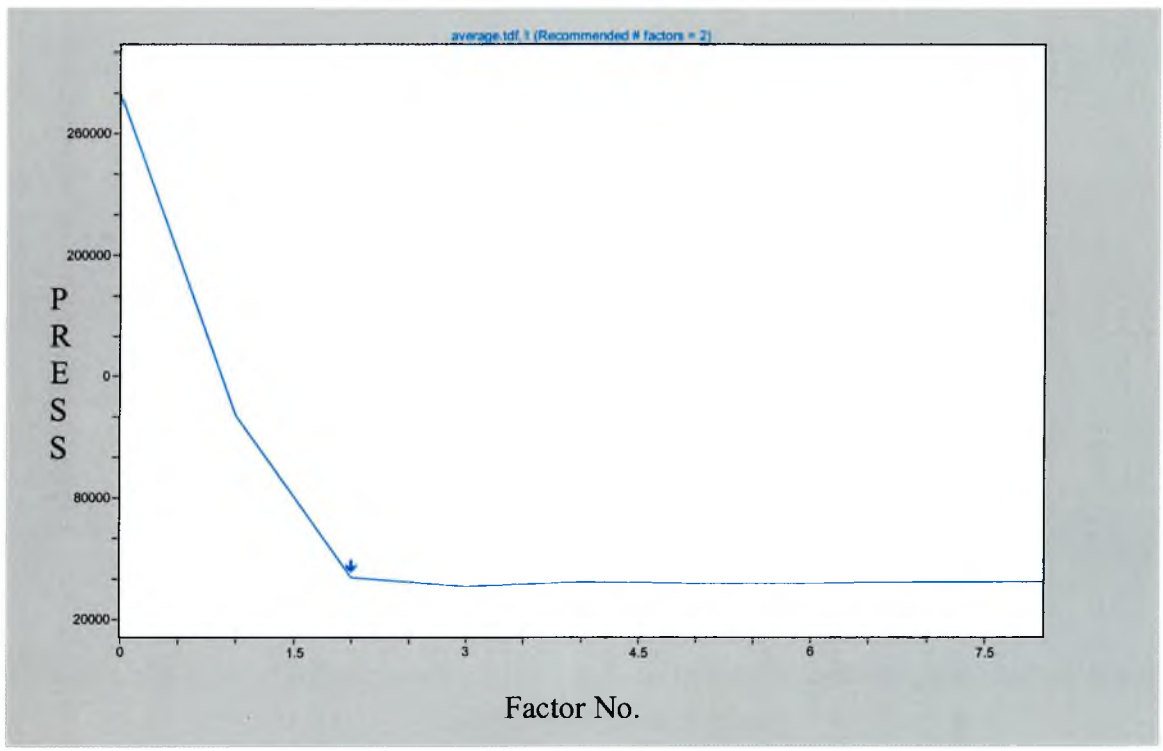

Figure 5.3.8: PLS PRESS plot for the DPM component

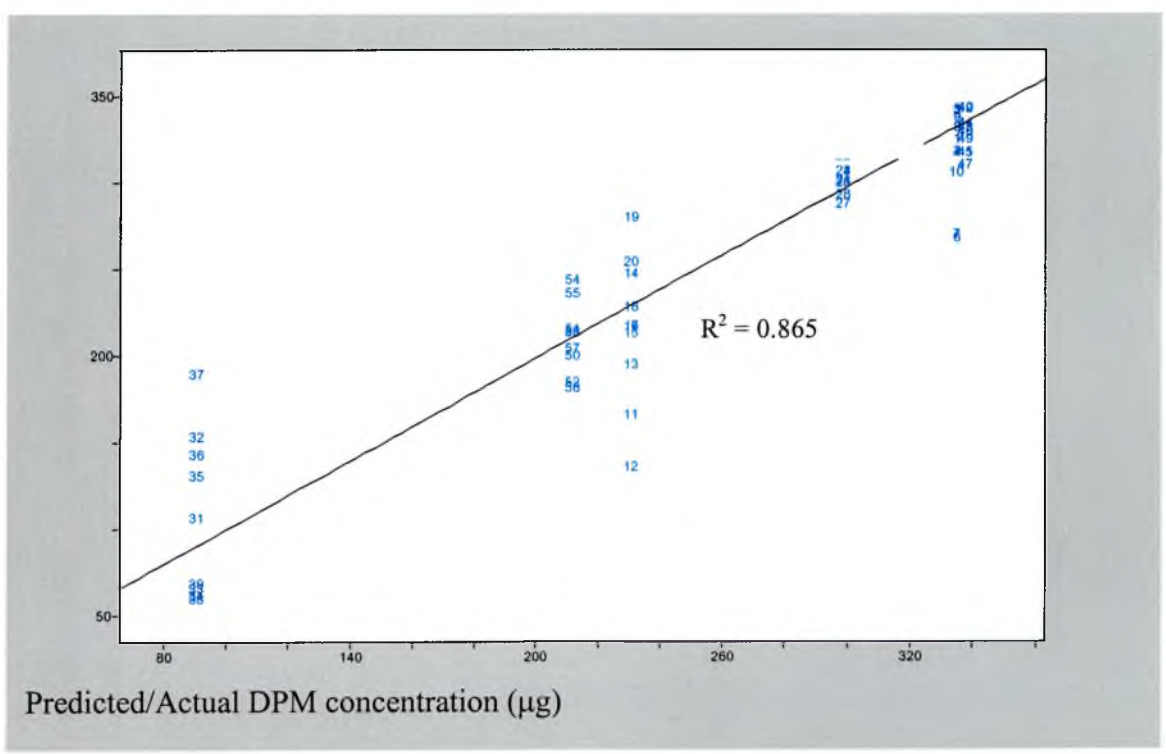

Figure 5.3.9: Actual vs Predicted Concentration Plot for DPM

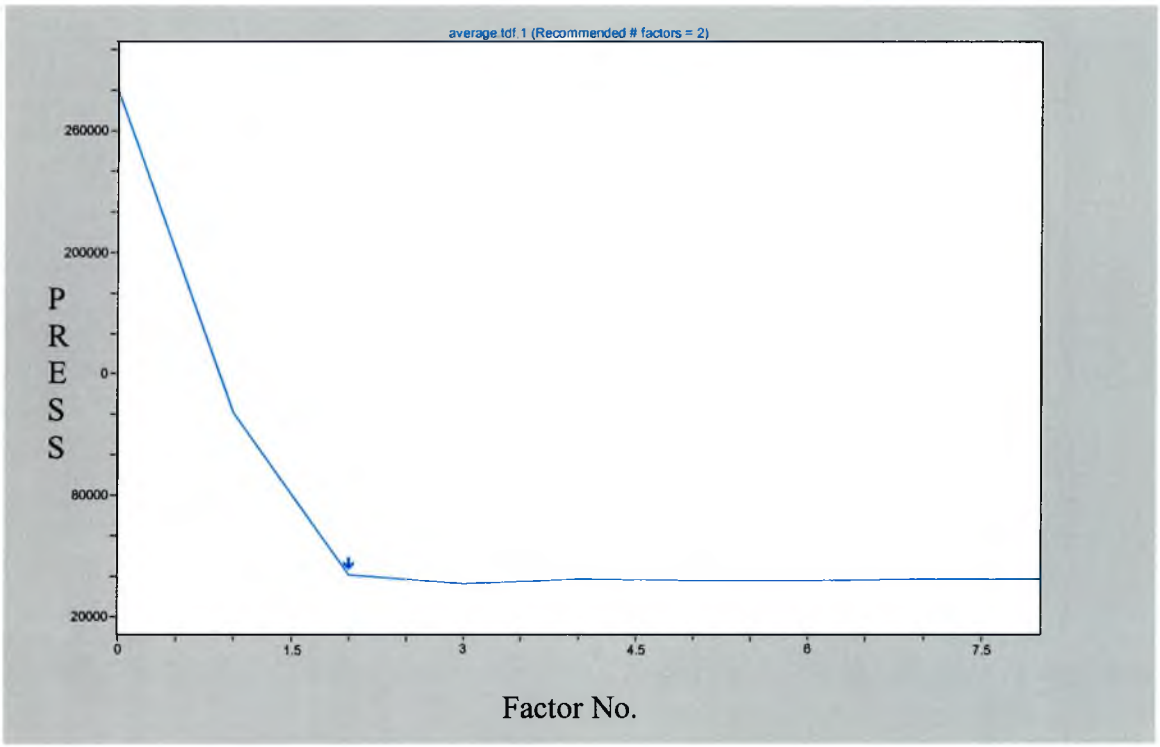

Figure 5.3.10: PLS PRESS plot for the coal dust component

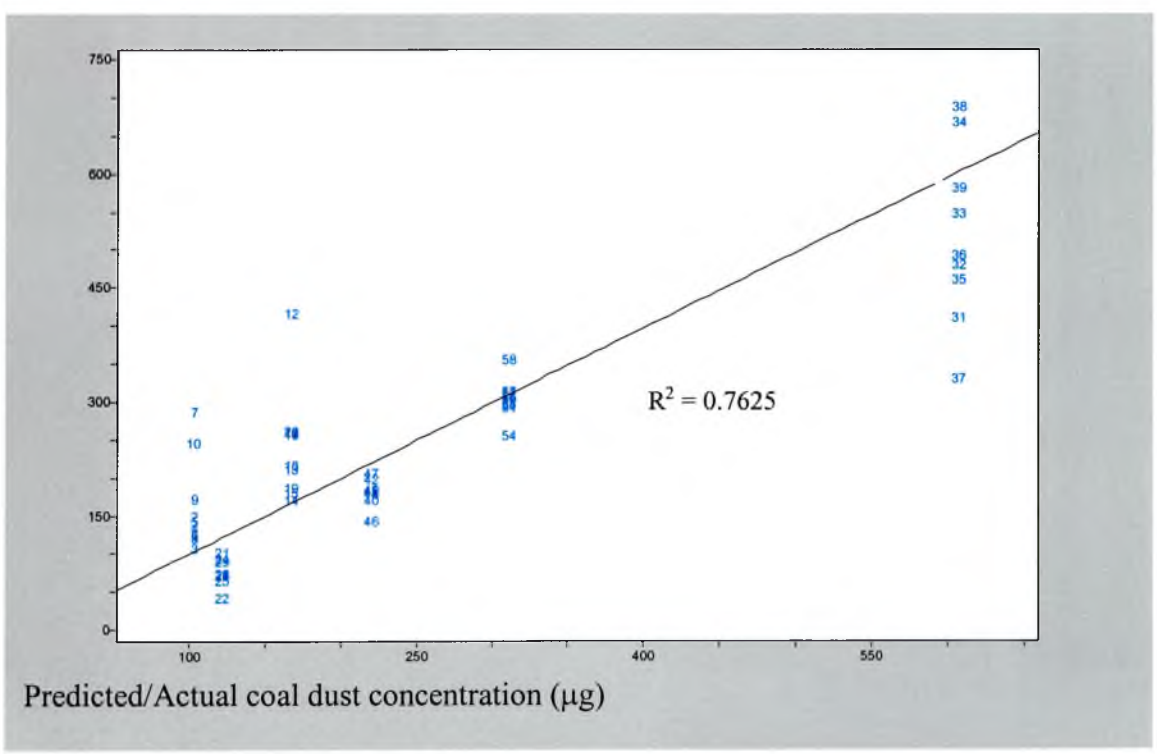

Figure 5.3.11: Actual vs Predicted Concentration Plot for Coal Dust

The R^2 values for both the DPM and coal concentration plots show that the current PLS plot is not accurate enough for predicting their concentrations. This low R^2 is largely due to the large distances between the observations. This large separation between the observations could be due to poor reproducibility of either the spectral shapes or integrated areas. If a reliable model were to be developed it would be necessary to improve the reproducibility of both.

5.3.7 Investigation of the effect of sample rotation on integrated spectral area reproducibility

From the high standard deviation of the mixture samples integrated spectral areas and the large scatter of the points in the actual versus predicted plot from the PLS model, in the previous section, it was evident that a new strategy was required to improve the reproducibility of the spectra collected, if a reliable model was to be developed.

In section 5.3.3 the reproducibility of the integrated spectral areas was dramatically improved by increasing the laser spot size from approximately 2μm, with the X50 objective, to about 30μm, with the X5 objective. This work indicated that increasing the area sampled even more would improve the reproducibility of the integrated spectral areas, even further. Unfortunately, the X5 objective was the lowest magnification, with the largest laser spot size, available. One method that would increase the area sampled was rotating the sample during analysis. So, the next stage of the project was to investigate if rotating the sample during analysis would improve the integrated spectral areas for the mixture samples.

5.3.7.2 Experimental

A rotating stage was designed to fit directly under the Raman microscope, which had a level sample holder large enough to accommodate a 2.5cm quartz fibre filter. A 9v motor revolving at 12rpm powered this apparatus. Each of the mixture samples analysed in section 5.3.5 (see table 5.3.11) were reanalysed using the same parameters (X5 objective,

400s scan time and 100% laser power) but the sample was rotated during analysis. 10 replicate spectra were again taken of each sample. Each spectrum was taken at a different point on the filter using the same sampling procedure as in section 5.3.1.2. The integrated spectral areas of the resultant spectra were measured and their standard deviations compared to the standard deviation of the spectra in section 5.3.5, where the samples were not rotated.

5.3.7.3 Results and discussion

Sample No.*	Standard deviation of Integrated area (%) Stationary Analysis	Standard deviation of Integrated area (%) Rotating Analysis
1	21.8	12.1
2	21.1	19.2
3	4.9	15.9
4	14.1	10.1
5	13.3	21.9
6	21.8	10.1

Table 5.3.20: Comparison of variance of integrated areas for stationary and rotating analysis

*See table 5.3.11 for sample loadings

The standard deviation of integrated spectral areas for both the samples analysed in a stationary position and samples analysed while rotating, are shown in table 5.3.20. The standard deviation decreased for some samples when rotated but it also increased for other samples. So, no significant improvement in the reproducibility of integrated spectral areas was observed, when rotating the samples. However, this failure to improve the reproducibility by rotating the sample may have been due to poor design of the rotating stage. The laser spot from the microscope was focused almost exactly on the centre of the stage, which resulted in a very small area being analysed on the filter. The diameter of the circle covered was in the order of about 50μm. It was not possible to adjust the stage to cover a larger area of the sample. Using the formula for the circumference of a circle ($2\pi r$) and a spot size of around $30\mu m^2$, the estimated sample area was approximately $4700\mu m^2$. This was an improvement of the original $30\mu m^2$ sample area, for the stationary analysis. However, from the results it is obvious that the increase in the area was not significant enough to improve the reproducibility of the

spectral areas. Therefore, it was necessary to modify the rotating stage to increase the sample area further and investigate if this increased sample area would have the desired effect of improving the spectral area reproducibility.

5.3.8 Further investigations into the effect of sample rotation on integrated spectral area reproducibility

5.3.8.1 Introduction

In the previous section it was suggested the small increase in the sampled area, when using the current rotating stage, may have been the reason for the failure to improve the reproducibility of spectral areas, when rotating the sample. This section involves work carried out when rotating the sample using a modified version of the original rotating stage, which could be adjusted to give a larger circle area.

5.3.8.2 Experimental

The spinning stage was set up so that its centre was approximately 0.75cm from the centre of the microscope centre. This resulted in a circle with a radius of 0.75cm being sampled on the filter. 5 mixture samples, which had been previously analysed in sections 5.3.6 and 5.3.7 (see table 5.3.11), were reanalysed using the same instrument parameters (X5 objective, 400s scan time and 100% laser power) and the new stage set up. The circumference of the sampled area was 470,000μm and the laser spot size was approximately 30μm. Therefore, the sampled area was approximately 1,400,000μm^2, which was a vast increase on the original 30μm^2 sample area, when no rotating stage was employed. This time the 10 'replicate' or repeat spectra were taken at the same position on the filter, unlike the previous work where each spectrum was taken at a different point on the filter. This allowed the automatic collection of each spectrum because it was not necessary to move the filter and refocus the laser after each scan. The standard deviations of the spectral areas for the 10 spectra of each sample were calculated and compared to the standard deviation of spectra taken without rotating the sample.

5.3.8.3 Results and discussion

As stated in the experimental section, the spectral software was set up to collect and save 10 spectra of each sample automatically. This process took approximately 5 hours per sample. So, the operator was free to perform other tasks, in between each sample analysis, while the instrument collected spectra. The 10 spectra were saved as one large file with the last spectrum taken present in the viewing area, when the operator returned to change the sample. These types of files are called multi files. They can be split or separated into the individual spectra when necessary. When the multi files in the present study were split into individual spectra, it was observed that the first 1 or 2 spectra of the 10 replicate spectra, of some samples, had unusual baseline anomalies. These baseline anomalies were attributed to changes in the fluorescence levels during analysis. A possible explanation for a change in the fluorescence levels is the burn off of adsorbed organic material because of sample heating, due to laser heating during the analysis. This may not have been observed previously because the samples were initially analysed when stationary and the organic material would have been burned off almost instantaneously. Also, the first analysis using the rotating stage covered a very small area (approx 4,500μm^2) compared to the area sampled for this work (1,400,000μm^2). So, the organic material would have been burned off much quicker. Example raw/unprocessed spectra of a mixture sample with 159μg DPM and 234μg coal dust are shown in spectrum 5.3.4. The blue spectrum is a spectrum with the described baseline anomalies. The red spectrum is a typical unprocessed spectrum collected after the adsorbed organic material had been burned off due to several hours exposure to the laser beam.

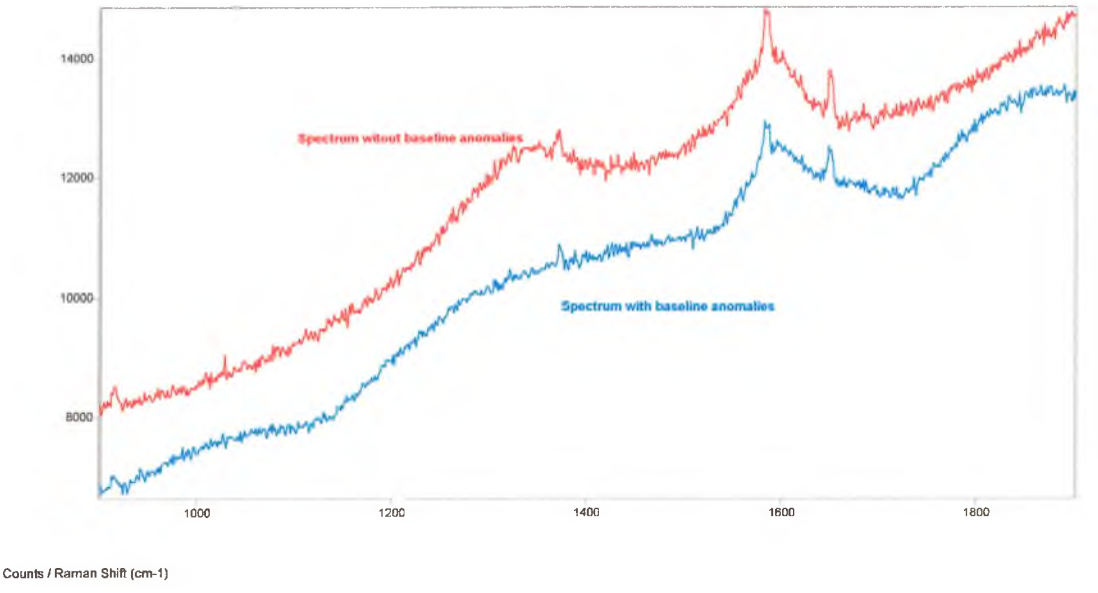

Spectrum 5.3.4: Spectra of 159µg DPM and 234µg coal dust mixture with and without baseline anomalies

Another observation of spectra taken using the modified rotating stage is the presence of bands from the laser plasma lines (as discussed in chapter 3 section 3.5.3). When the analysis was performed without the use of a rotating stage, the laser was focused onto one area of the filter and remained in focus there throughout the analysis. However, when analysing the samples using a rotating stage it is inevitable that the sample will move in and out of focus during the analysis, especially since the substrate is not extremely flat. This would result in, the laser being focused onto the quartz fibre filters at certain times during the analysis, resulting in an increase in the laser light being reflected back up the microscope and also an increase in the laser plasma line signal reaching the detector.

It was not possible to use all of the spectra, collected in this study, for calculating the standard deviation of the spectral areas of each sample because of the baseline anomalies discussed earlier. In total the integrated spectral areas of 43 out of the 50 spectra were measured. The sample compositions, number of measured spectra for each sample and the standard deviation of their integrated areas are shown in table 5.3.21.

Sample	DPM (μg)	Coal Dust (μg)	Number of Spectra	Standard Deviation (%)
1	214	154	5	10
2	299	123	9	4.7
3	156	139	9	4.4
4	251	78	10	1.9
5	159	234	10	1.7

Table 5.3.21: DPM and coal dust mixture sample loadings, number of spectra and the standard deviation of their integrated spectral areas

A comparison of the standard deviation of the integrated spectral areas for the mixture coal and DPM samples for the stationary analysis and the analysis using the modified rotating stage is shown in table 5.3.22.

Sample No.*	Standard deviation of Integrated area (%) Stationary Analysis	Standard deviation of Integrated area (%) Rotating Analysis
1	21.1	10.0
2	4.9	4.7
3	14.1	4.4
4	13.3	1.9
5	21.8	3.7

Table 5.3.22: Comparison of variance of integrated areas for stationary and rotating analysis*

***See table 5.3.18 for sample loadings**

Increasing the sample area, with the modified rotating stage, resulted in a marked improvement in the standard deviation of the integrated spectral areas of all samples. In fact, all had values of 10% or less. It must be noted that the replicate spectra here were taken at the same point on the filter. Undoubtedly, repeat sampling of the same area for each spectrum will have also helped improve the reproducibility of the spectral areas. Only 5 spectra of sample 1 were measured because the other 5 of the 10 replicate spectra suffered from the aforementioned baseline anomalies. The standard deviation of these spectra was 10%. In all probability, if 10 spectra were available for this sample they too might have had a standard deviation of less than 5%, like the rest of the samples. A set of spectra with adequate reproducibility in integrated spectral areas was now available for constructing a PLS model.

5.3.9 PLS model using spectra collected from mixture coal and DPM samples using the modified rotating stage

5.3.9.1 Introduction

In the previous section the standard deviation of the spectral areas of mixture samples was reduced from a range of 4.9 to 21.8% down to between 1.9 to 10%, by employing the use of a rotating stage. We now explore whether an improvement in the precision of observations in a PLS model coincides with this significant improvement in spectral area reproducibility. If there is no marked improvement, it indicates that the variation of the spectral areas was not solely responsible for the large spread in the observations but that there were also differences between spectra due to their shapes.

5.3.9.2 Experimental

The sample concentrations were normalised using the integrated spectral areas of the $520cm^{-1}$ band of a clean, flat piece of crystalline silicon, as described in section 5.3.5. The spectra collected in the previous section were entered into the chemometric software and a PLS model constructed. The spectra were baseline corrected, mean centred, the whole spectral range was used, 10 factors were calculated and cross-validation was applied.

5.3.9.3 Results and discussion

The DPM and coal dust loadings for each mixture were normalised, according to the average integrated area of the $520cm^{-1}$ Si peak, for the particular day each sample was analysed. The component concentrations input into the data set for each mixture sample is shown in table 5.3.23. From the PRESS plots, in figures 5.3.12 and 5.3.14, 3 factors were chosen for the DPM analysis and 3 factors for the coal dust spectra. The actual versus predicted plots for the PLS model are shown in graphs 5.3.13 and 5.3.15. The R^2 values for DPM and coal dust were 0.67 and 0.817 respectively.

Sample	DPM Weight (μg)	Normalised DPM Weight (μg)	Coal Dust Weight (μg)	Normalised Coal Dust Weight (μ)
1	214	210	154	151
2	299	271	123	111
3	162	210	118	151
4	251	225	78	70
5	159	159	234	234

Table 5.3.23: Mixture standards' DPM and coal dust loadings and their normalised values used for the PLS model

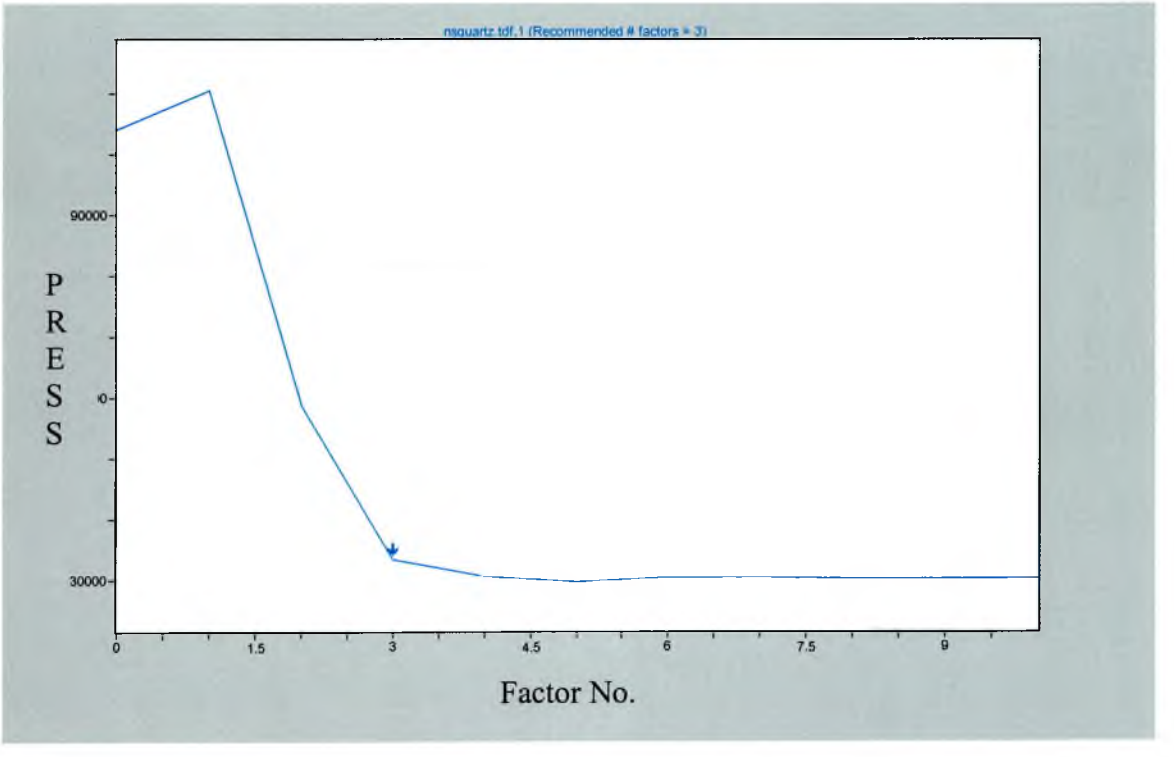

Figure 5.3.12: PLS PRESS plot for the DPM component

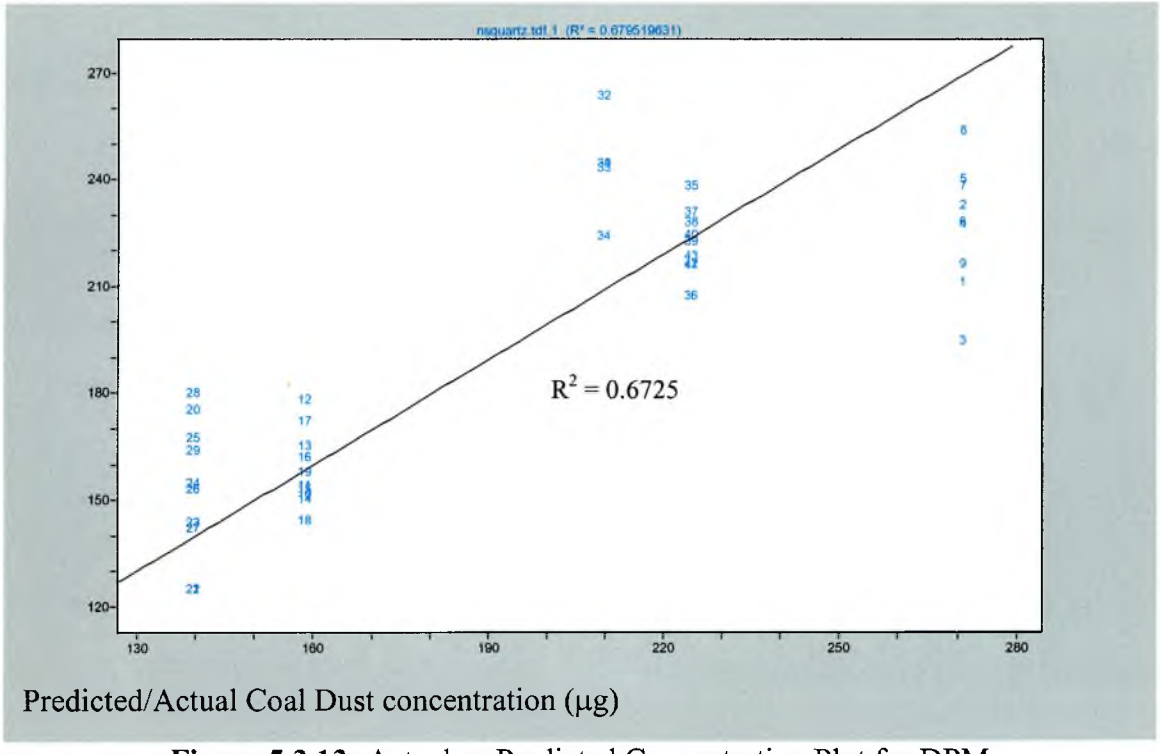

Figure 5.3.13: Actual vs Predicted Concentration Plot for DPM

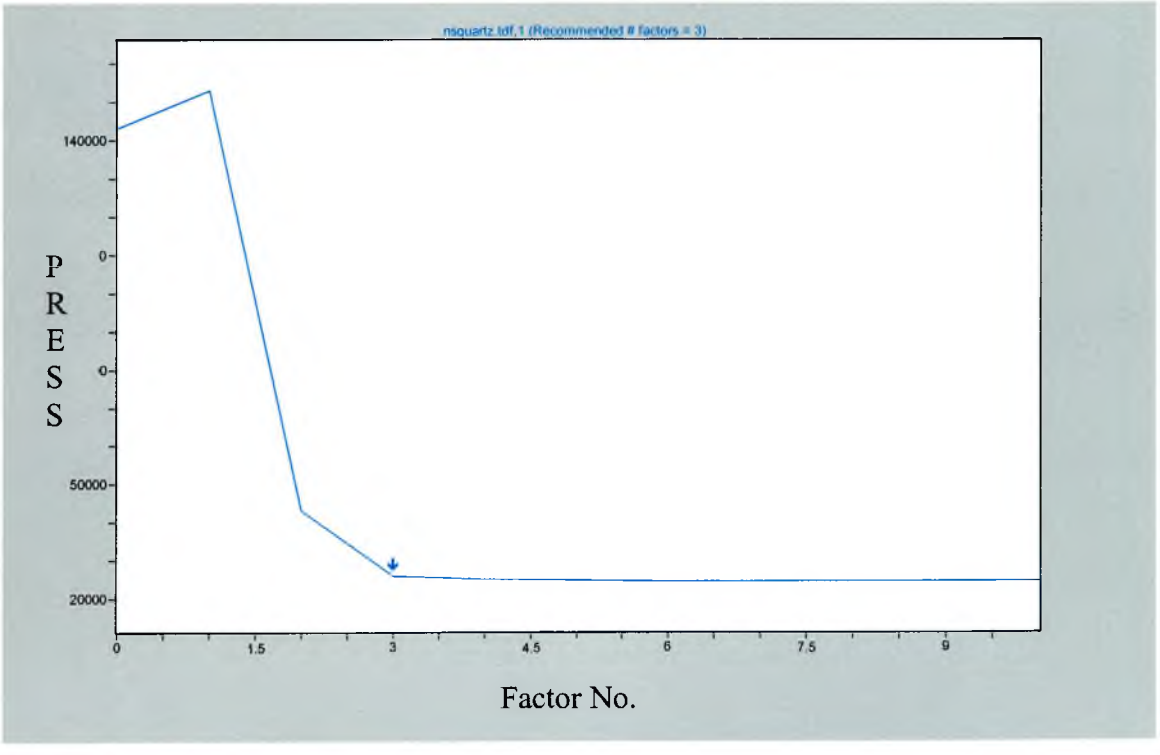

Figure 5.3.14: PLS PRESS plot for the DPM component

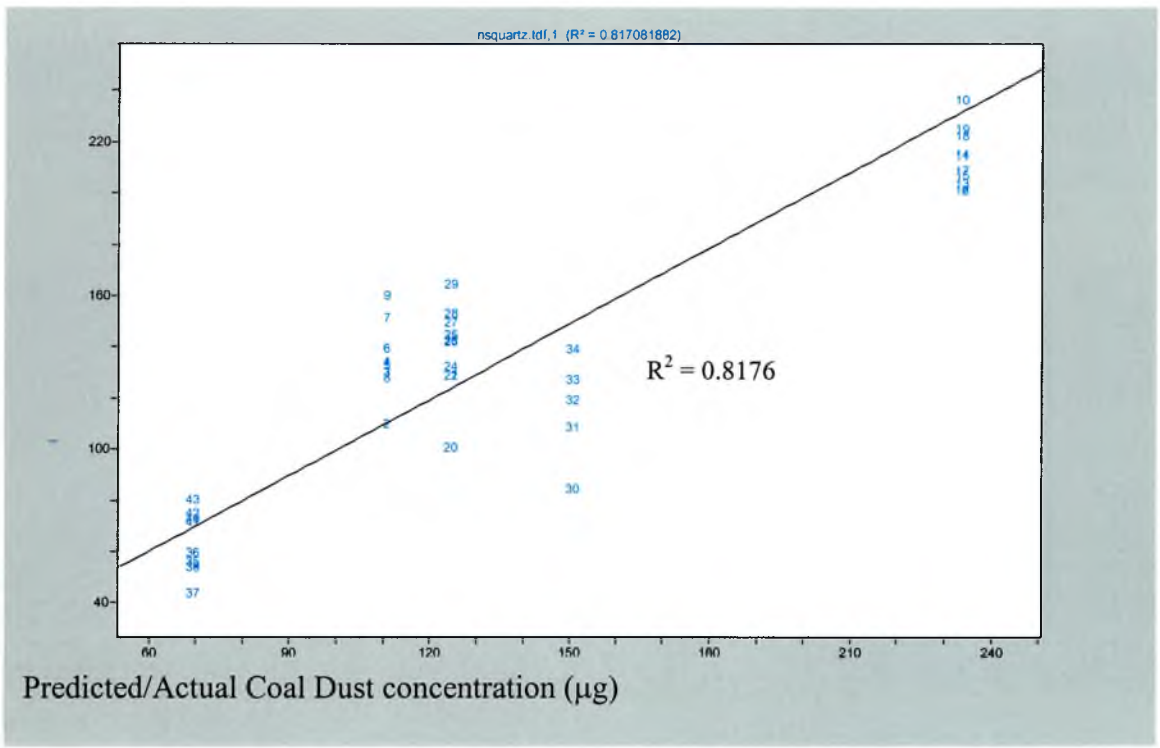

Figure 5.3.15: Coal dust actual concentration versus predicted concentration plot

The large variation in the actual concentration versus predicted concentration observations does not correlate well with the low standard deviations of between 1.9 to 10% for the integrated spectral areas. This indicates that the shapes of the spectra are very different (in PLS terms) for each replicate of a sample. If a reliable PLS model was to be developed it was necessary to improve the reproducibility of the spectral shapes. The work in the next two sections concentrates on this challenge.

5.3.10 Investigations into improving the reproducibility of coal dust and DPM spectral shapes

From the work carried out in sections 5.3.8 and 5.3.9 it was concluded that the shapes of different spectra of the same sample are significantly different. Some of the spectra were subject to baseline anomalies, which was possibly due to changes in the fluorescence levels because of burn off of adsorbed organic material. This may have been due to the laser heating the sample during analysis. For some of the samples the first few spectra had to be discarded due to these baseline anomalies. The effect of the changing

fluorescence levels decreased with each spectrum, as the laser gradually burned off the adsorbed organics, until eventually the spectra appeared to be unaffected. The point at which the spectra appear unaffected is decided by comparing them to spectra collected without the use of a rotating stage. For which, the adsorbed organics were burned off almost immediately. Therefore, this point is decided by comparing the spectra by using the so-called "spectroscopist eye". However, chemometrics is the technique being used here to distinguish between different components and to determine the amount of each present. The reasoning for using chemometrics for this project was for its superior ability to distinguish between very similar spectra, compared to traditional spectroscopic comparisons. Therefore, it is possible that at the point where the spectra appear, to the spectoscopist, to be unaffected by the burn off of organics, that they are still changing sufficiently for chemometric methods to detect a difference in their shape.

The aim in this section is to develop a method of collecting spectra that do not change sufficiently in shape for PLS to detect a difference. One possible method is to continue collecting spectra until all the organic material has been burned off. However, this may take a long time. Also, the difference in spectral shapes because of the gradual burn off of organic is only one possible explanation and using such a method may not be useful for confirming or refuting this postulation. Another method that was considered was using a slower rotation speed than the current 9rpm. This would result in the laser being focused on a particular area for a longer time and could possible increase the temperature of the sample sufficiently to burn off the organics more quickly. Yet another possibility was to heat the samples to a temperature that could not possibly be reached due to heating from the laser. After such a heat-treatment the laser heat should have no effect on the sample and the spectra would not change due the burn off of organic material. If this method worked it would confirm that the continuing burn off of organic material is responsible for the different spectral shapes.

It was decided to investigate how the latter two suggested methods affect the reproducibility of spectral shapes. For these studies we reverted to using PCA analysis on individual coal and diesel samples. There are several reasons for following this strategy.

The first reason being that the heat-treatment process is destructive and we did not wish to needlessly destroy the mixture samples without first investigating if the method was successful. Also, PCA is less complex and less time consuming than PLS, as it requires fewer samples. Investigating the effects on the individual coal and DPM samples will determine if one component is affected more by the treatments than the other. Finally, we are just interested in the effects of the treatments on the spectral shapes and PCA is capable of determining this.

5.3.10.2 Experimental

A variable resistor was fitted to the rotating stage, which was capable of reducing the voltage reaching the motor from 12V to 4V. The speed of the motor could then be reduced from 9rpm to 3rpm. All the analyses in this section were performed using a rotating stage with its centre 0.75cm from the laser spot resulting in a circle of 0.75cm circumference being sampled. 10 replicate spectra were collected of each sample. These 10 replicate spectra were taken at the same position on the filter, as in section 5.3.8. The instrument parameters were the same as the previous 5 sections (X5 objective, 400s scan time and 100% laser power). The first experiment involved the analysis of a quartz fibre filter loaded with 175μg DPM using the spinning stage rotating at 9rpm. This same filter was reanalysed using the spinning stage rotated at 3rpm. Finally, the same filter was heat-treated in an oven with an oxygen free inert N_2 atmosphere. The oven was controlled to increase in temperature at 10°C per minute until it reached 625°C. It was held at this temperature for 15 minutes and then allowed to cool to room temperature. The whole process took several hours. The heat-treated filter was analysed while rotating at 9rpm. The spectra from each experiment were incorporated in a PCA analysis and the distances between their observations compared to investigate if the 3rpm rotation and/or performing the heat-treatment improved the reproducibility of their spectral shapes. The process was repeated for a sample loaded with 270μg of coal dust. The effects of the heat treatment on the spectra were investigated by comparing curve fits of spectra of the heat-treated DPM and coal dust samples with curve fits of spectra of untreated samples.

5.3.10 Results and discussion

Example spectra of untreated 175µg DPM on a quartz fibre filter rotating at 9 and 3rpm are shown in spectrum 5.3.5 and 5.3.6 respectively. An example spectrum of 245µg DPM on a quartz fibre filter heat-treated to 625°C in a nitrogen atmosphere is shown spectrum 5.3.7.

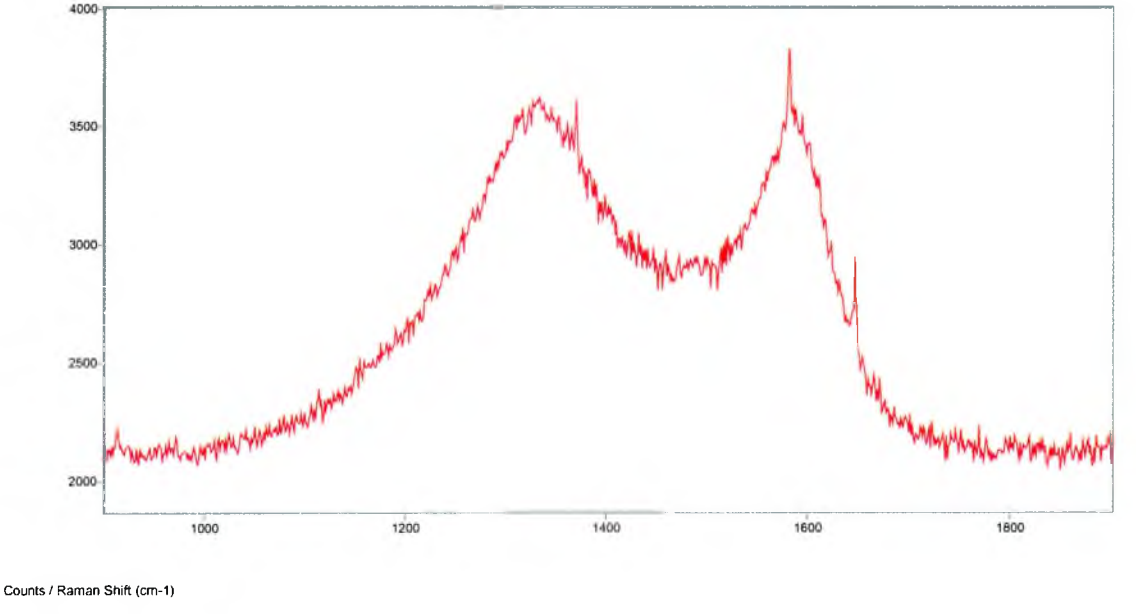

Spectrum 5.3.5: 175µg DPM on a quartz fibre filter, 400s, x5obj, 100% laser power, no heat treatment, rotating at 9rpm

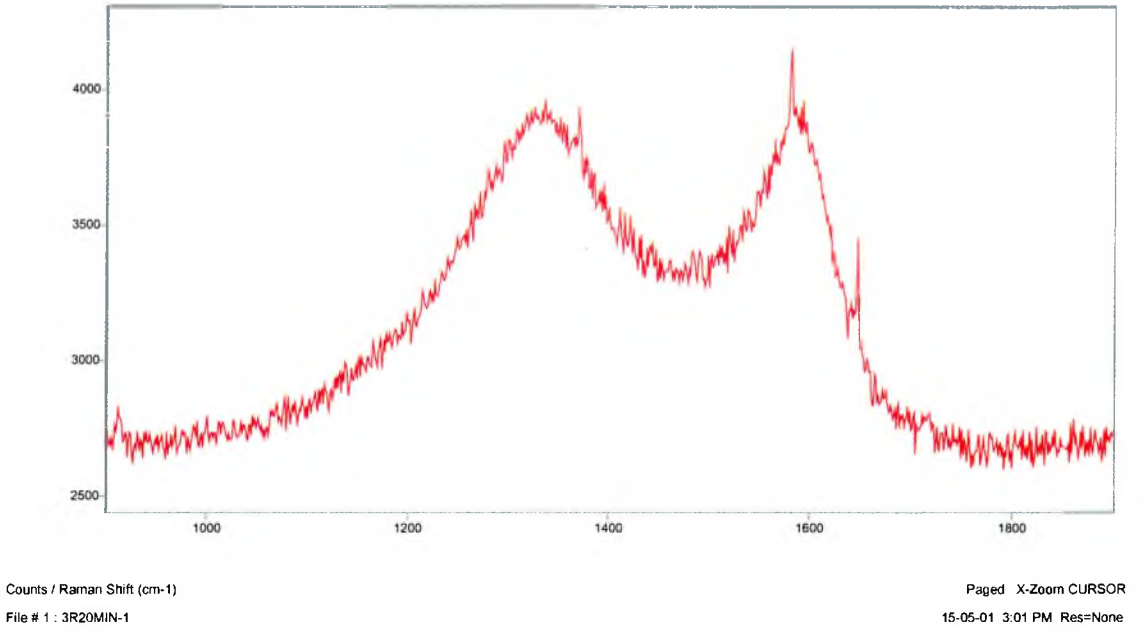

Spectrum 5.3.6: 175µg DPM dust on a quartz fibre filter, 400s, x5obj, 100% laser power, no heat treatment, rotating at 3rpm

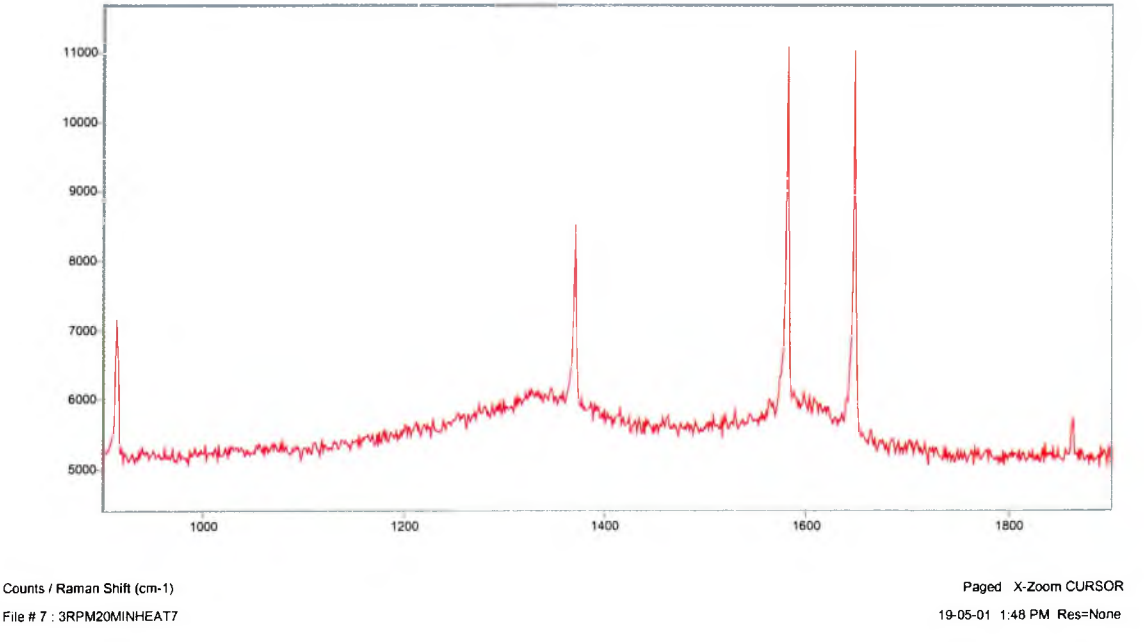

Spectrum 5.3.7: 175µg DPM on a quartz fibre filter, 400s, x5obj, 100% laser power, heat-treated to 625°C in a N_2 atmosphere, rotating at 9rpm

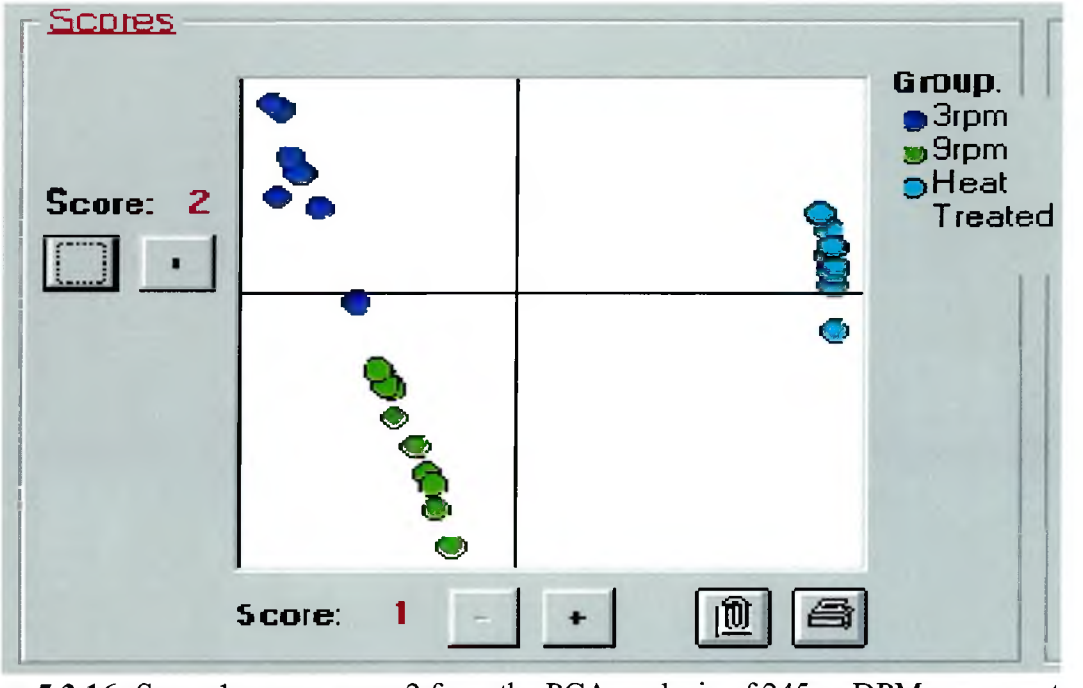

Figure 5.3.16: Score 1 versus score 2 from the PCA analysis of 245μg DPM on a quartz fibre filter, rotating the sample at 3rpm and 9rpm without heat-treatment and spinning at 9rpm after heat treatment to 625°C in a N_2 atmosphere

From the score plot in figure 5.3.16 it is evident that reducing the sample rotation speed from 9rpm to 3rpm does not significantly change the spacing between the observations for the 10 replicate spectra. So, reducing the sample rotation speed did not improve the reproducibility of the spectral shapes. However, when the sample was subjected to heat-treatment the separation between the observations is reduced significantly. In fact all but 1 of the observations are bunched almost on top of each other. This shows that the heat-treatment process resulted in a marked change in the reproducibility of spectral shapes.

The spectra of a 270μg coal dust sample rotated at 9rpm and 3rpm are shown in spectra 5.3.8 and 5.3.9 respectively. It was attempted to heat treat this sample but the nitrogen supply to the oven ran out during the process. This resulted in air getting into the oven and the coal on the filter become volatised due to the presence of oxygen. So, the PCA analysis for this sample could only be used for a comparison of spectra for the sample analysed rotating at 9rpm and 3rpm.

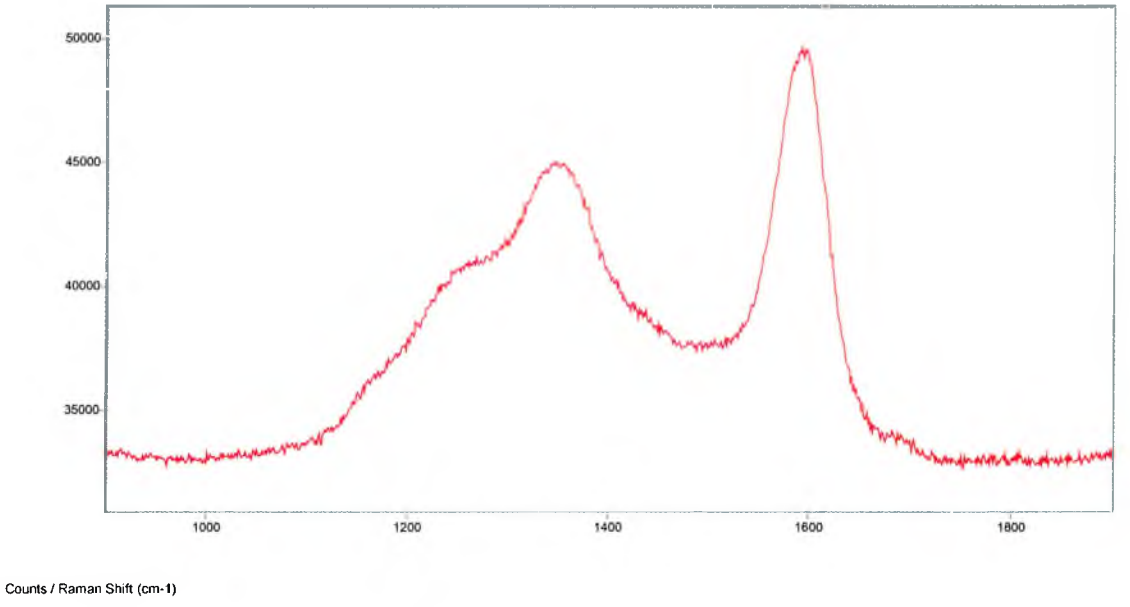

Spectrum 5.3.8: 270µg coal dust on a quartz fibre filter, 400s, x5obj, 100% laser power, no heat treatment, rotating at 9rpm

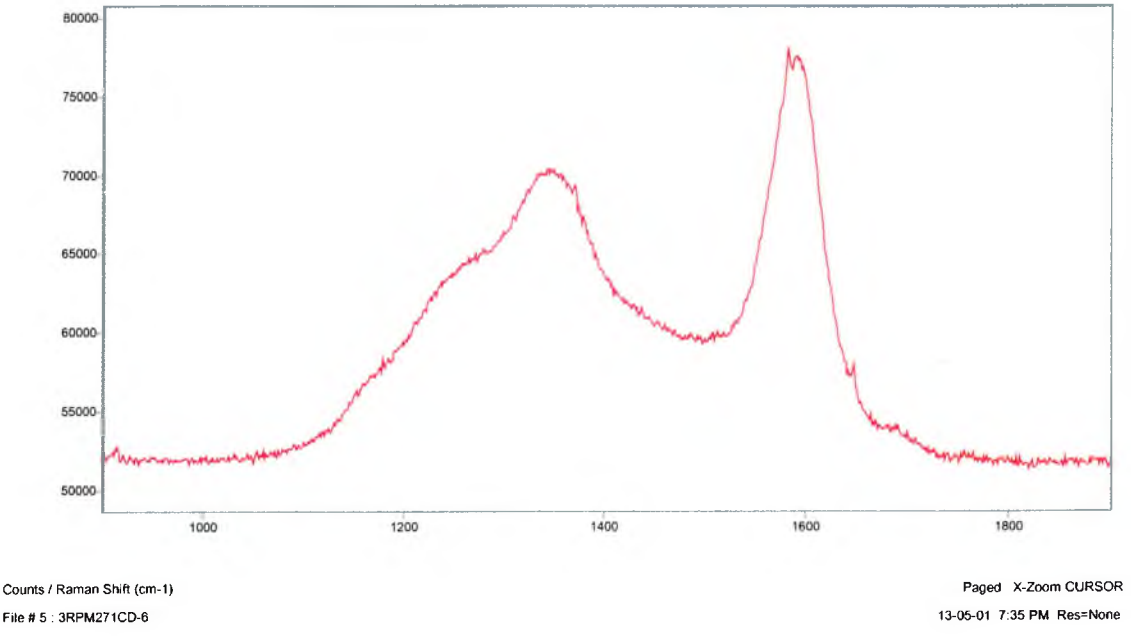

Spectrum 5.3.9: 270µg coal dust on a quartz fibre filter, 400s, x5obj, 100% laser power, no heat treatment, rotating at 3rpm

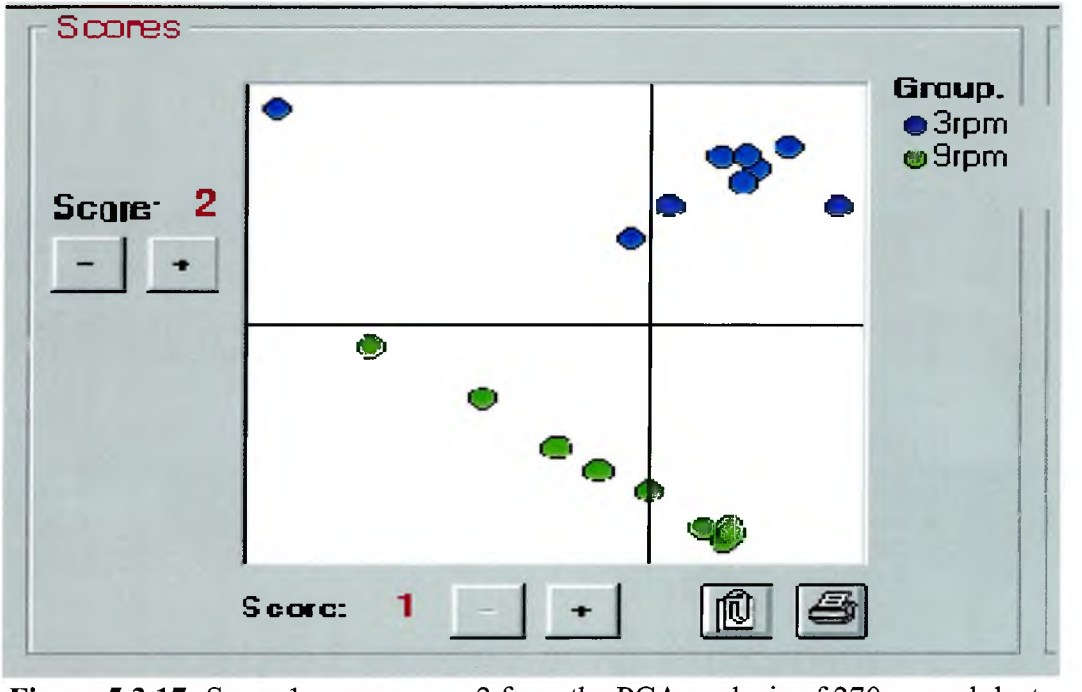

Figure 5.3.17: Score 1 versus score 2 from the PCA analysis of 270µg coal dust on a quartz fibre filter, rotating the sample at 3rpm and 9rpm, without heat-treatment

The 1st score versus the 2nd score plot of the PCA analysis of coal dust sample analysed while rotating at 3 and 9rpm is shown in figure 5.3.17. The spacing between the observations for the sample analysed while rotating at 3rpm has changed from the 9rpm analysis. However, it does not appear to have changed sufficiently enough to indicate a significant improvement in the reproducibility of spectral shapes.

As the sample used for the PCA analysis comparing the effect of changing the rotating speed from 9 to 3rpm was destroyed it was necessary to perform the heat-treatment process on a new sample. A sample with 150µg coal dust was chosen. This sample was firstly analysed, rotating at 9rpm, before heat-treatment. The sample was then analysed after being heat-treated to 625°C for 15 minutes in a N_2 atmosphere. Example spectra for the sample before and after heat-treatment are shown in spectra 5.3.10 and 5.3.11.

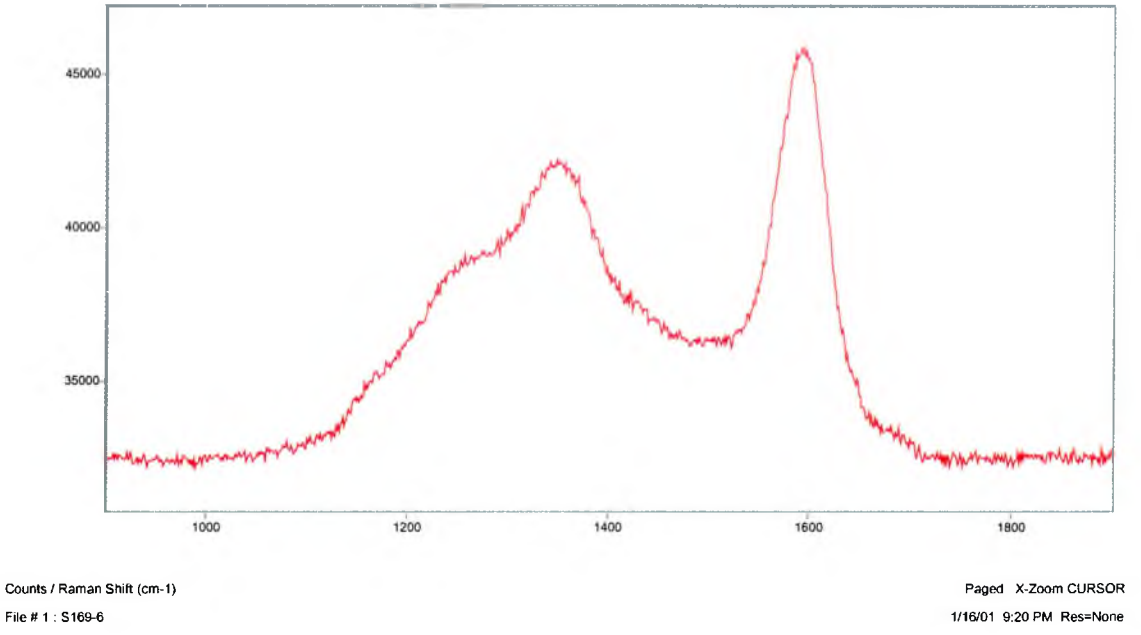

Spectrum 5.3.10: 150µg coal dust on a quartz fibre filter, not heat treated, rotated at 9rpm, 400s scan time, x5obj, 633nm laser at 100% power

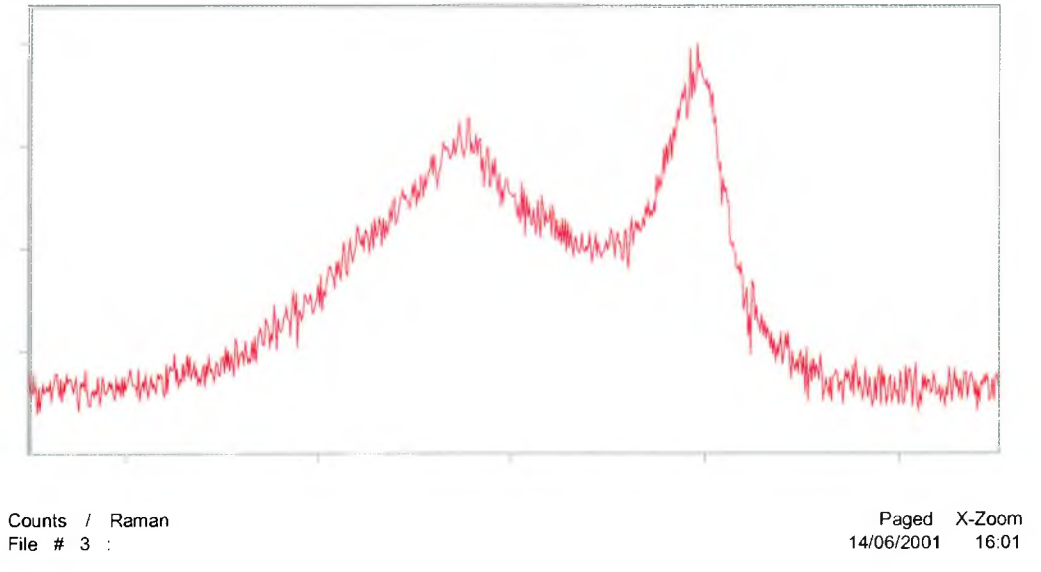

Spectrum 5.3.11: 150µg coal dust on a quartz fibre filter, x5obj, 400s scan time, 633nm laser at 100% power, heat-treated to 625°C, rotating at 9rpm

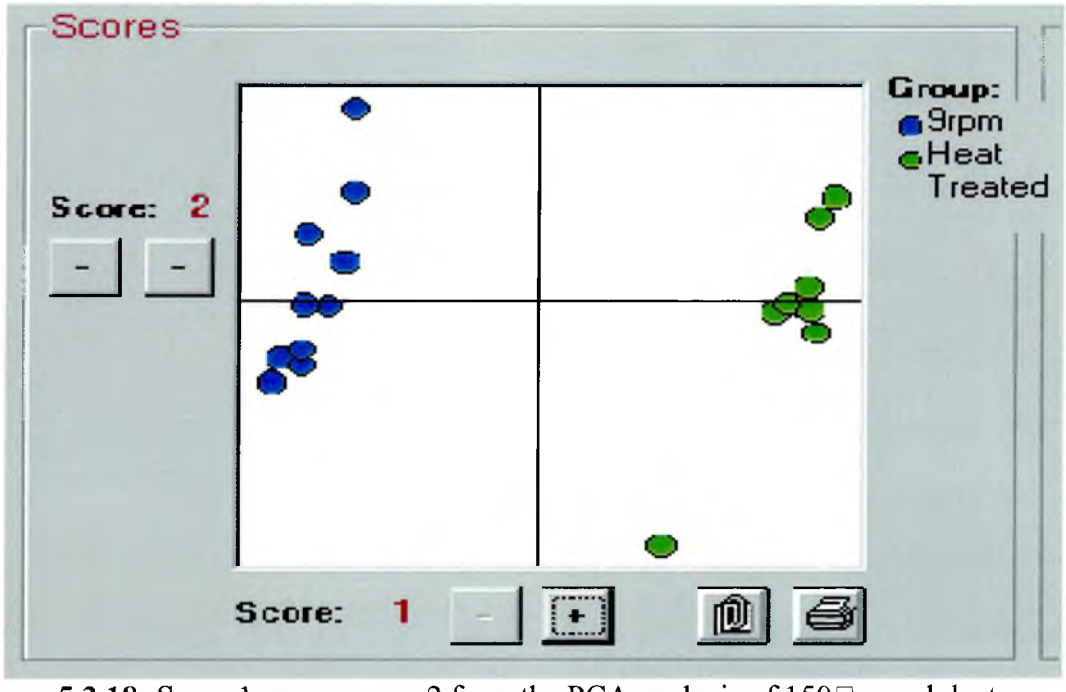

Figure 5.3.18: Score 1 versus score 2 from the PCA analysis of 150□g coal dust on a quartz fibre filter, rotating the sample at 9rpm without heat-treatment and spinning at 9rpm after heat treatment to 625°C in a N_2 atmosphere

The 1st score versus the 2nd score plot of the PCA analysis of coal dust sample analysed while rotating the sample at 9rpm without heat-treatment and spinning at 9rpm after heat-treatment is shown in figure 5.3.18. The heat-treatment process appears to have improved the spectral reproducibility somewhat. However, there is still a large distance between certain observations. Comparing this PCA score plot to the corresponding plot for the DPM (figure 5.3.16) the reproducibility of the spectral shapes of the coal dust has not been improved as significantly as the reproducibility of the DPM spectral shapes. This is not surprising as the DPM has a much higher organic content than the coal dust. So, heating off the organic material should affect its spectra more. In the PCA score plots of heat-treated DPM and coal dust one observation in particular, for each plot, appears to be located much further from the others. On further investigation it was discovered that this observation corresponded to the first spectrum of the 10 replicate spectra taken of each sample. This indicated that the first spectrum was still affected by the burn off of adsorbed organic material, even after the heat-treatment process. So, some organic impurities may have adsorbed onto the samples from the air, after heat-treatment. If the

heat-treatment process was to be used for mixture samples it would be recommended to collect 11 or perhaps 12 replicate spectra of each sample and to discard the first 1 or 2 spectra, when developing a PLS model. However, this trend was not recognised at first and in the next PLS model, which used spectra from heat-treated mixture samples, only 10 spectra were taken of each mixture. In fact, it was the results from the next PLS model (section 5.3.13) which prompted us to return to the PCA results in this section to investigate if it was the first spectrum of the 10 replicates that corresponded to observation that was located far from the other observations.

5.3.11 Comparison of the curve fitted spectra for untreated and heat-treated coal dust and DPM samples

5.3.11.1 Introduction

A general observation of the heat-treated coal dust and DPM is that their spectra appear less intense than before they were treated. This can be attributed to the fact that when the adsorbed organic material had been heated off a larger proportion of the quartz fibre filter was exposed. This is especially the case for the DPM and is evident by the fact that after heat-treatment the laser plasma lines are much more intense after the heat-treatment because a large proportion of the light is reflected from the newly exposed quartz fibres. From an initial look the spectra of heat-treated samples it is apparent that the shoulder between 1100cm^{-1} and 1300cm^{-1} is less prominent for the heat-treated coal dust than for the untreated sample. The effect of the heat-treatment on the coal and DPM spectra can be quantified by comparing the curve fits of spectra for untreated samples to the curve fits of spectra for heat-treated samples.

5.3.11.2 Experimental

Spectra of untreated samples with separate loadings of 150μg coal dust and 175μg DPM were curve fitted. The peak positions, heights, widths and areas were compared to the peaks from curve fits of spectra taken of the samples after heat-treatment.

5.3.11.3 Results and discussion

The spectra of an untreated and heat-treated 150μg coal dust sample are shown in spectra 5.3.12 and 5.3.13 respectively. A curve fit of each spectrum is shown in figures 5.3.19 and 5.3.20 respectively. The curve fitting application automatically performs a 2nd derivative of a spectrum. However, due to the low signal to noise of the heat-treated sample the automatic 2nd derivative did not use enough points. So it was necessary to perform an individual 2nd derivative on this spectrum. A Savitsky-Golay 2nd derivative with 85 points was used and the resultant second derivative curve is shown in figure 5.3.21. The peak positions, heights, widths and areas from an untreated coal spectrum and a heat-treated coal spectrum are shown in tables 5.3.24 and 5.3.25 respectively.

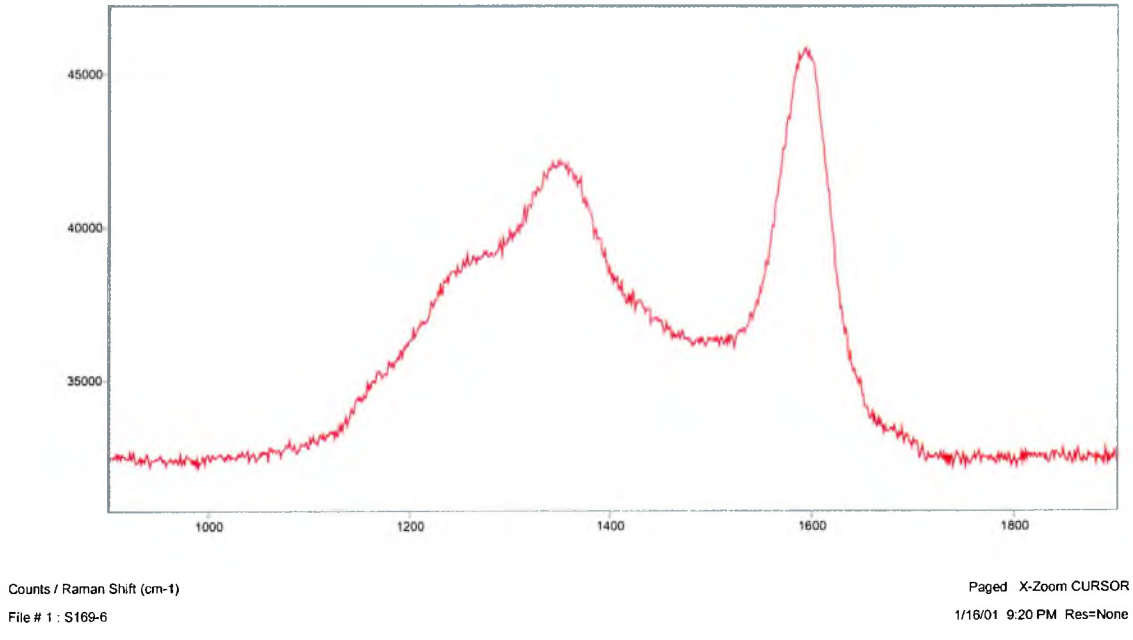

Spectrum 5.3.12: 150μg coal dust on a quartz fibre filter, untreated, rotated at 9rpm, 400s scan time, x5obj, 633nm laser at 100% power

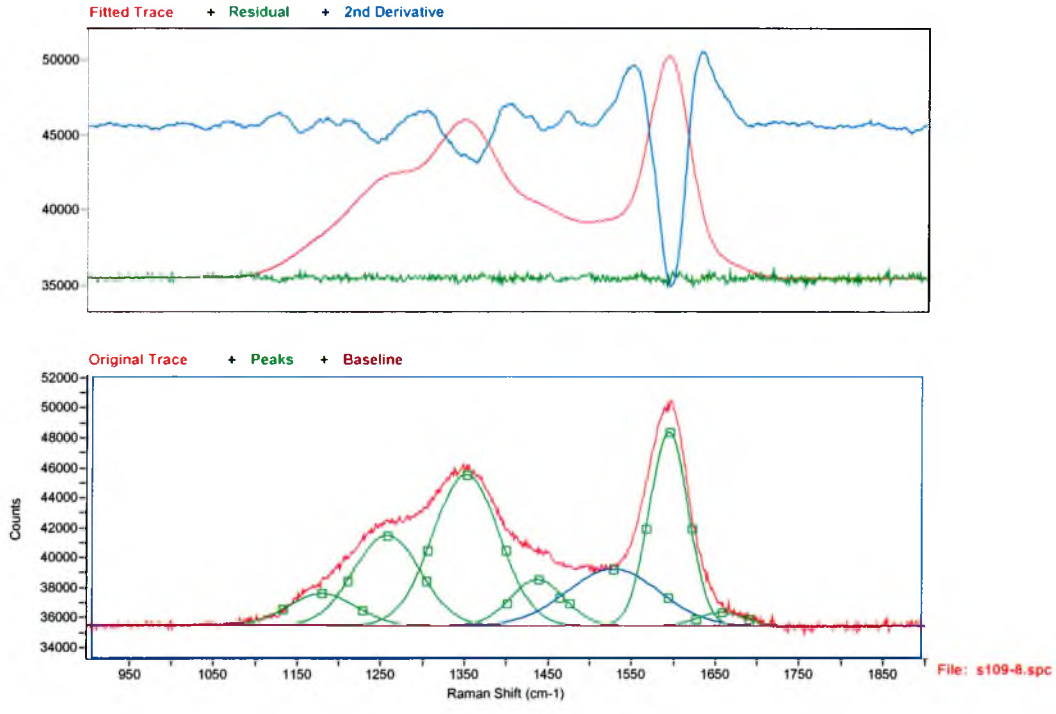

Figure 5.3.19: Curve fit of an untreated 150µg DPM sample spectrum

Peak Number	Position (cm^{-1})	Height	Width (cm^{-1})	Integrated Area
1	1180	2111	95	212687
2	1258	6012	94	600522
3	1352	10086	93	1000136
4	1438	3048	75	244314
5	1529	3781	129	520623
6	1595	12946	54	75417
7	1659	899	64	61276

Table 5.3.24: Peak positions, heights, widths and areas from an untreated coal spectrum curve fit

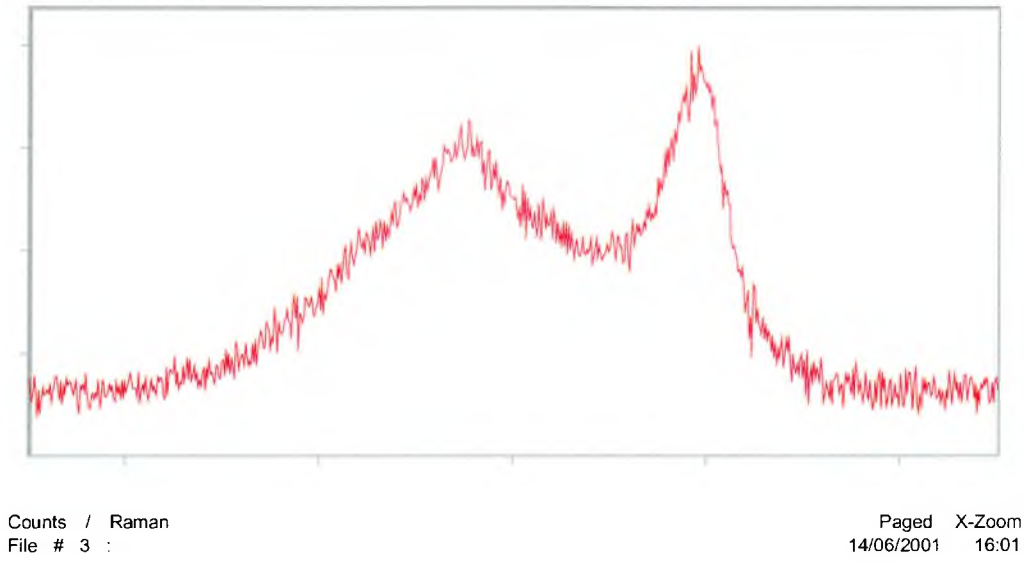

Spectrum 5.3.13: 150µg coal dust on a quartz fibre filter, x5obj, 400s scan time, 633nm laser at 100% power, heat-treated to 625°C, rotating at 9rpm

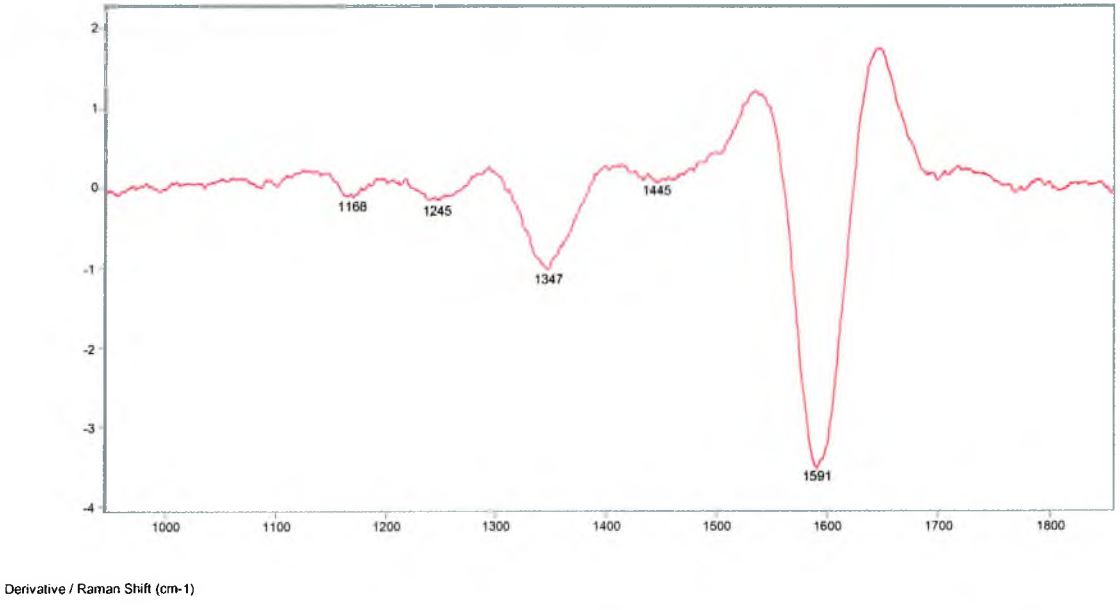

Figure 5.3.20: 2nd derivative curve of a heat-treated 150µg coal dust sample spectrum

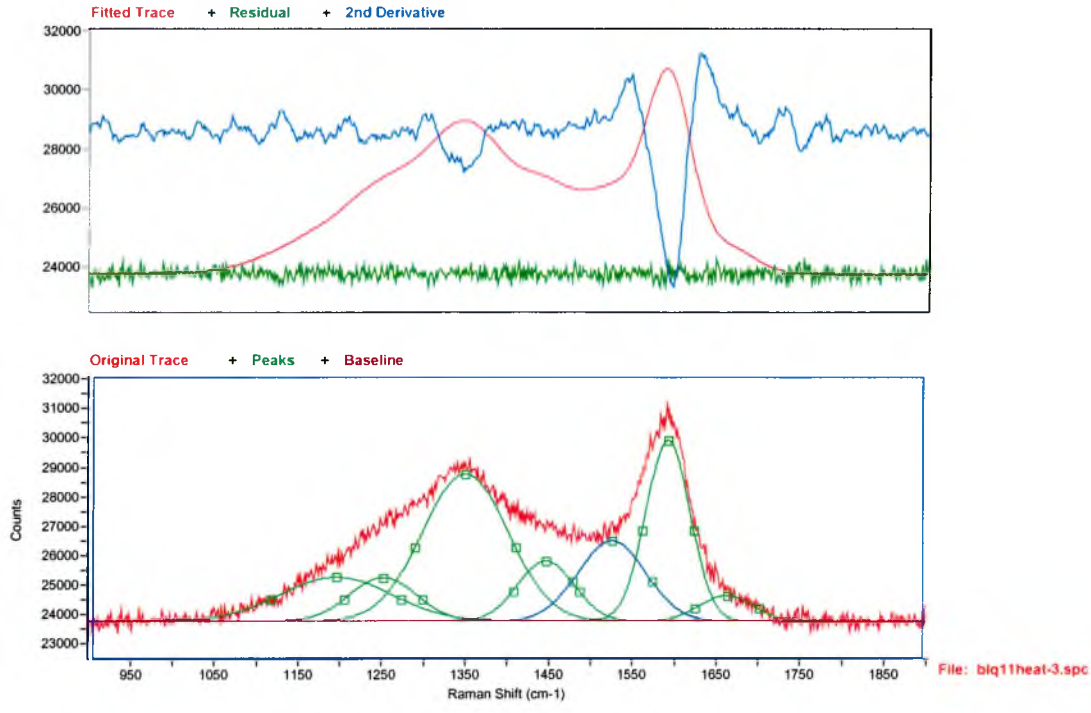

Figure 5.3.21: Curve fit of a heat-treated 150µg coal dust sample spectrum

Peak Number	Position (cm^{-1})	Height	Width (cm^{-1})	Integrated Area
1	1196	1487	155	245568
2	1252	1476	92	146038
3	1350	4990	120	639952
4	1447	2034	78	170751
5	1526	2715	95	274835
6	1593	6144	62	405884
7	1663	869	74	69880

Table 5.3.25: Peak positions, heights, widths and areas from a heat-treated coal spectrum curve fit

The spectra of an untreated and heat-treated 175µg coal dust sample are respectively shown in spectra 5.3.14 and 5.3.15. A curve fit of each spectrum is shown in figures 5.3.22 and 5.3.24 respectively. Again, it was necessary to perform an individual 2nd derivative on this spectrum. A Savitsky-Golay 2nd derivative with 100 points was used and the resultant second derivative curve is shown in figure 5.3.23.

The peak positions, heights, widths and areas from an untreated coal spectrum and a heat-treated coal spectrum are shown in tables 5.3.26 and 5.3.27 respectively.

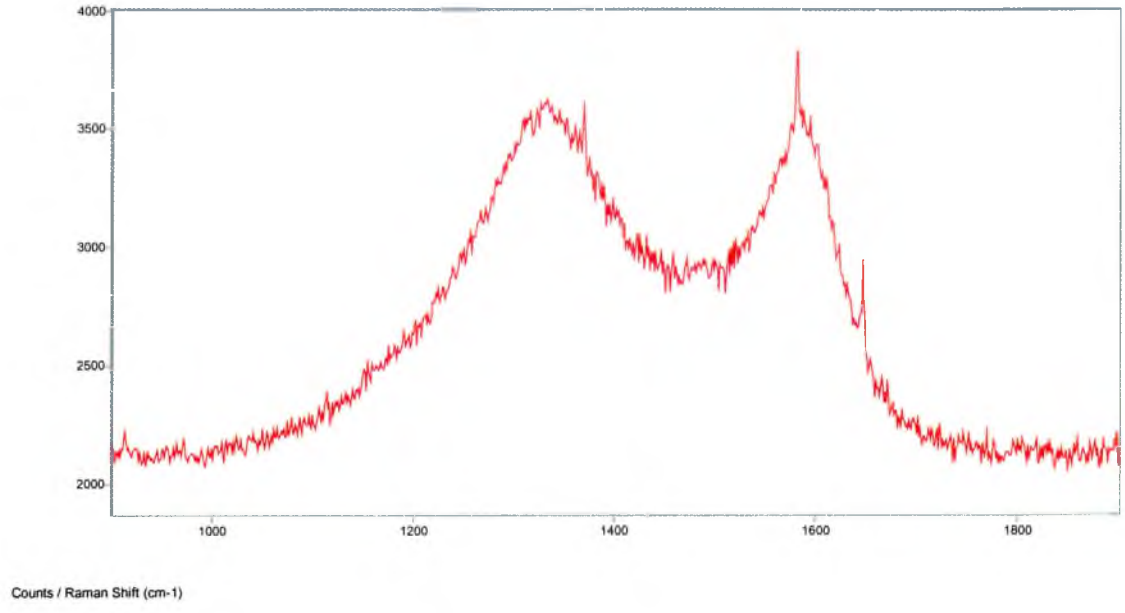

Spectrum 5.3.14: 175µg DPM on a quartz fibre filter, 400s, x5obj, 100% laser power, no heat treatment, rotating at 9rpm

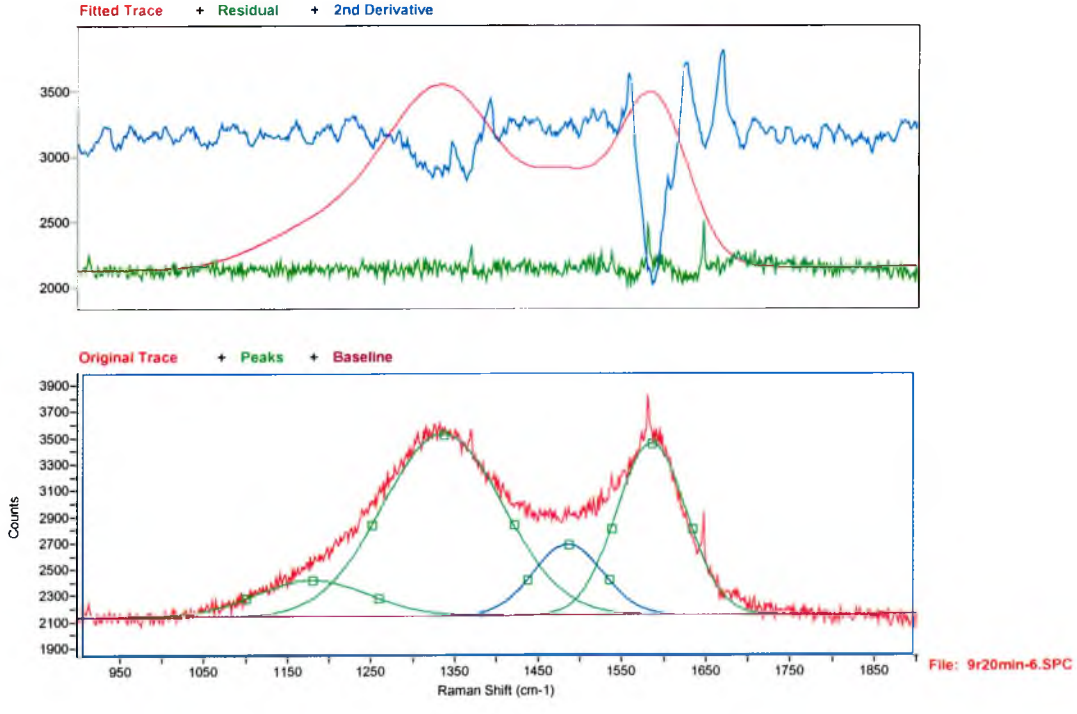

Figure 5.3.22: Curve fit of an untreated 175µg DPM sample spectrum

Peak Number	Position (cm^{-1})	Height	Width (cm^{-1})	Integrated Area
1	1180	274	157	45805
2	1336	1385	170	249904
3	1486	535	98	55805
4	1586	1305	97	135374

Table 5.3.26: Peak positions, heights, widths and areas from an untreated coal spectrum peak fit

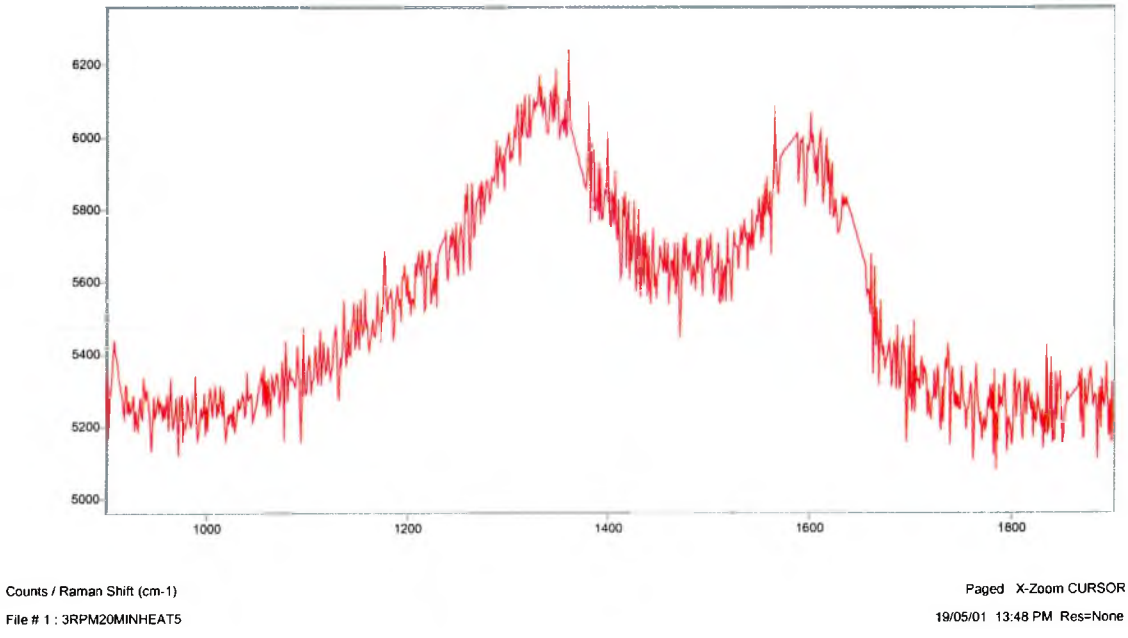

Spectrum 5.3.15: 150µg coal dust on a quartz fibre filter, x5obj, 400s scan time, 633nm laser at 100% power, heat-treated to 625°C, rotating at 9rpm (quartz bands zapped)

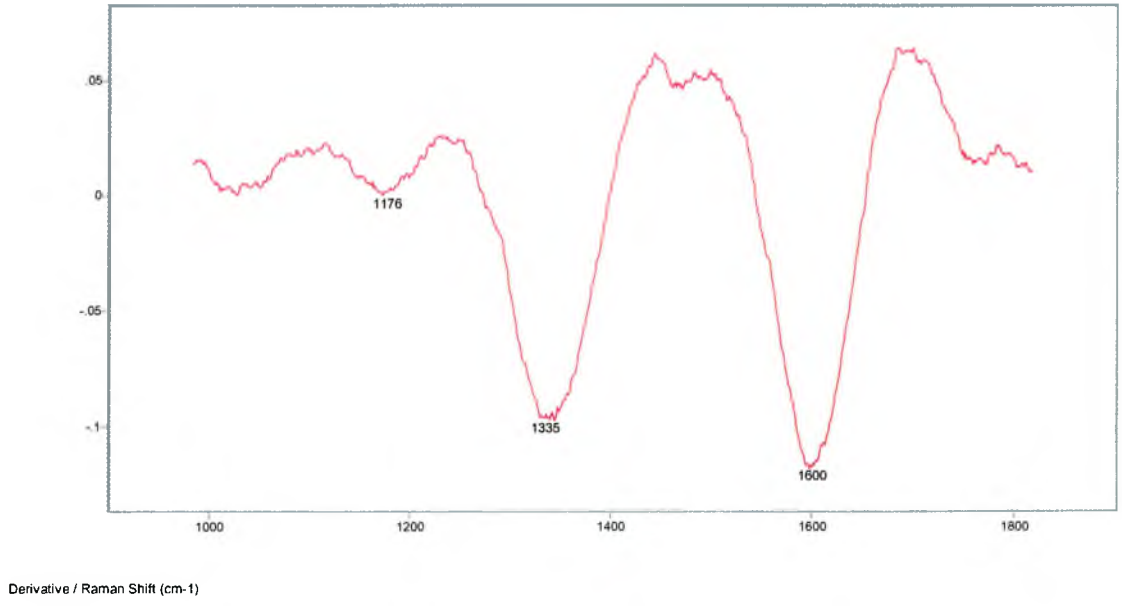

Figure 5.3.23: 2nd derivative curve of a heat-treated 175µg DPM sample spectrum

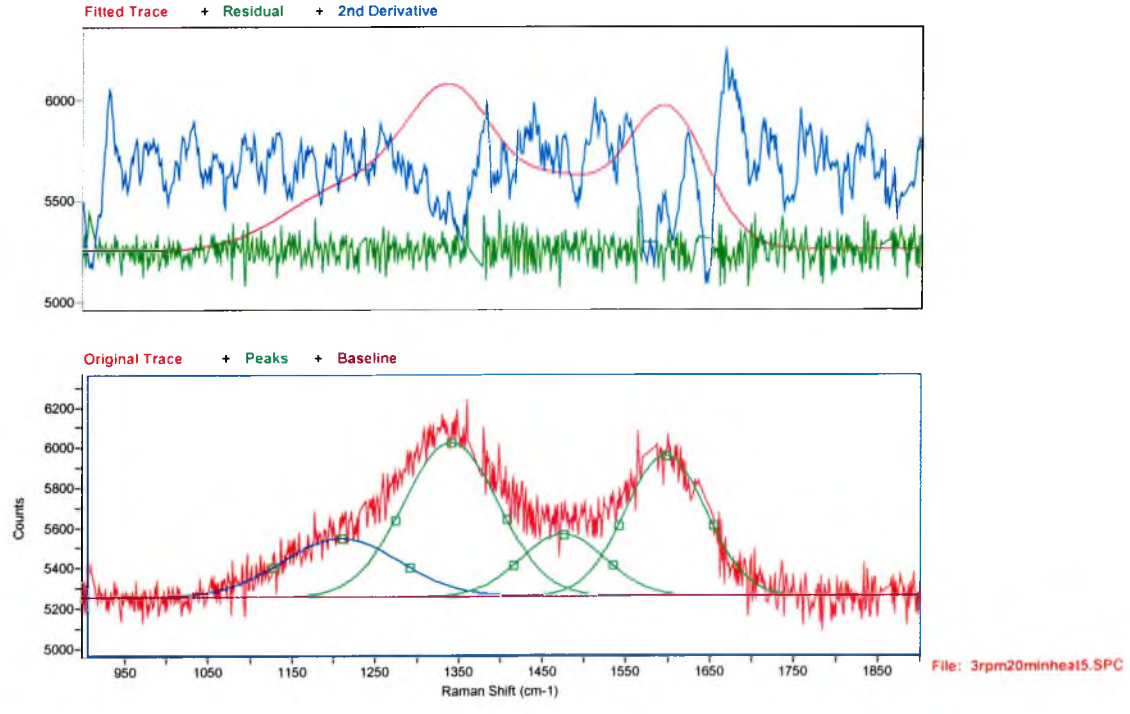

Figure 5.3.24: Curve fit of a heat-treated 175µg DPM sample spectrum

Peak	Position (cm^{-1})	Height	Width (cm^{-1})	Integrated Area
1	1209	289	164	50692
2	1341	765	134	109087
3	1475	307	118	38716
4	1598	699	112	83975

Table 5.3.27: Fitted peak positions, heights, widths and areas of a heat-treated 175μg sample spectrum

The peak ratios for untreated and heat-treated coal dust and DPM are shown in tables 5.3.28 and 5.3.29 respectively.

Sample	1190cm^{-1}/G	1255cm^{-1}/G	D/G	1440cm^{-1}/G
Untreated Coal	0.28	0.80	1.33	0.33
Heat-treated Coal	0.34	0.36	1.57	0.42

Table 5.3.28: Peak ratios for untreated and heat-treated coal dust

Sample	1190cm^{-1}/G	D/G
Untreated DPM	0.34	1.85
Heat-treated DPM	0.60	1.30

Table 5.3.29: Peak ratios for untreated and heat-treated DPM

On comparing the curve fit results for the untreated coal dust with the heat-treated coal dust some unexpected results were obtained. (It may be useful, at this stage, to look back over sections 3.4.4 and 3.4.6 in chapter 3 to understand the following hypothesis) The most surprising result was that both the D and G bands for the spectrum of heat-treated sample were broader than the untreated sample. The D and G bands being 93cm^{-1} and 54cm^{-1} respectively for the untreated sample and 120cm^{-1} and 62cm^{-1} for the treated sample. Another unexpected result was that the D/G band ratio was greater for the heat-treated (1.57) than the untreated sample (1.35). The most noticeable change in the peak ratios was the decrease of the 1250cm^{-1}/G ratio from 0.8, for the untreated sample, to 0.35 for the heat-treated sample. This band at around 1250cm^{-1} has been assigned to a feature in the vibrational density of states (VDOS) of diamond-like, sp^3-bonded, carbon.[6] As sp^3-bonds are less thermally stable than sp^2 bonds [7] it is expected that the heat-treatment would convert some of the bonding of the sp^3-bonded carbon, responsible for the 1250cm^{-1} band, to sp^2-bonded carbon. This would explain the reduction in intensity of this band, after heat-treatment. This hypothesis may also help explain why the D/G band

ratio increases rather than decreases after heat-treatment. The sample was heat-treated using a HTT of 625°C, which is probably high enough to convert some sp^3-bonded carbons into sp^2-bonded carbons. However, the HTT of 625°C is probably only high enough to convert sp^3-bonded carbon into amorphous/disordered sp^2-bonded carbon as the formation of 2-D graphene sheets of carbon (polymerisation) typically occurs between 600-1200°C.[8] The formation of disordered graphitic carbon, from diamond-like carbon, would result in an increase in the D band intensity and in turn an increase in the D/G band ratio. It could be argued that the heat-treatment should also result in increased ordering of the original (before heat-treatment) disordered sp^2-bonded carbon and reduce the intensity and width of the D band. However, from comparing the peak fits, the contribution to the spectrum from the 1250cm^{-1} band, after heat-treatment, is greatly reduced. Taking into account that sp^3-bonded carbon's scattering cross-section can be 50-100 less than that of sp^2-bonded carbon, using visible excitation[9]. This large decrease in the 1250cm^{-1} band would correspond to a large number of sp^3-bonded sites being converted to sp^2-bonded sites. The fact that the D/G band ratio increases with the heat-treatment indicates that the carbon bonding converted from sp^3-bonded carbon to amorphous sp^2-bonded carbon prevails over effects of the ordering of the disordered sp^2-bonded carbon, at this HTT. The D and G band positions were almost unchanged due to heat-treatment.

The D bandwidth for the DPM sample decreased from 170cm^{-1} to 134cm^{-1} and its position shifted upwards from 1336cm^{-1} to 1341cm^{-1} after heat-treatment, which corresponds to ordering of the disordered carbon. The G band was expected to narrow and shift downwards after heat-treatment as the carbon structure becomes more ordered and its position approaches that of graphite. However, the G bandwidth unexpectedly increased from 97cm^{-1} to 112cm^{-1} and is shifted from 1586cm-1 to 1598cm^{-1}. The G/D band ratio decreased from 1.85 to 1.3, which indicates increased ordering after the heat-treatment.

5.3.12 Analysis of heat-treated mixture samples

5.3.12.1 Introduction

From the PCA analysis of DPM and coal dust samples it was observed that the reproducibility of their spectral shapes was significantly improved by heat-treatment. Therefore, it should follow that the spectral reproducibility of mixture coal dust and DPM samples should also be improved by heat-treatment. In this section the samples used for previous PLS models are heat-treated and a new data set for a PLS model is produced.

5.3.12.2 Experimental

The 6 mixture coal dust and DPM samples, used for the previous PLS models, were heat-treated in an oven with an oxygen free inert N_2 atmosphere. The oven was controlled to increase in temperature at a rate of 10°C per minute, until it reached 625°C. It was held at this temperature for 15 minutes and then allowed to cool to room temperature. These samples were analysed using the same parameters as the spectra collected for the previous PLS models (X5 objective, 400s scan time, 100% laser power) with the sample rotating at 3rpm. 10 replicate spectra were taken of each sample at the same position on the filter. An example spectrum for each spectrum was curve fitted and the band positions, widths, heights, areas and ratios determined. The curve fitting procedure was again simplified by only including 4 bands. This allowed us to compare the curve fits of the untreated mixture samples in section 5.3.5 with the heat-treated samples in this section.

5.12.3 Results and discussion

An example spectrum of the heat-treated sample containing 66μg DPM and 440μg coal dust is shown spectrum 5.3.16. A peak fits of this spectrum is shown in figure 5.3.25. The positions, widths, heights and areas of the fitted bands for each sample are shown in tables 5.3.30 through 5.3.35. The coal and DPM loadings, D/G ratios for an example spectrum and integrated spectral areas standard deviation of the 10 spectra of each sample are shown in table 5.3.36.

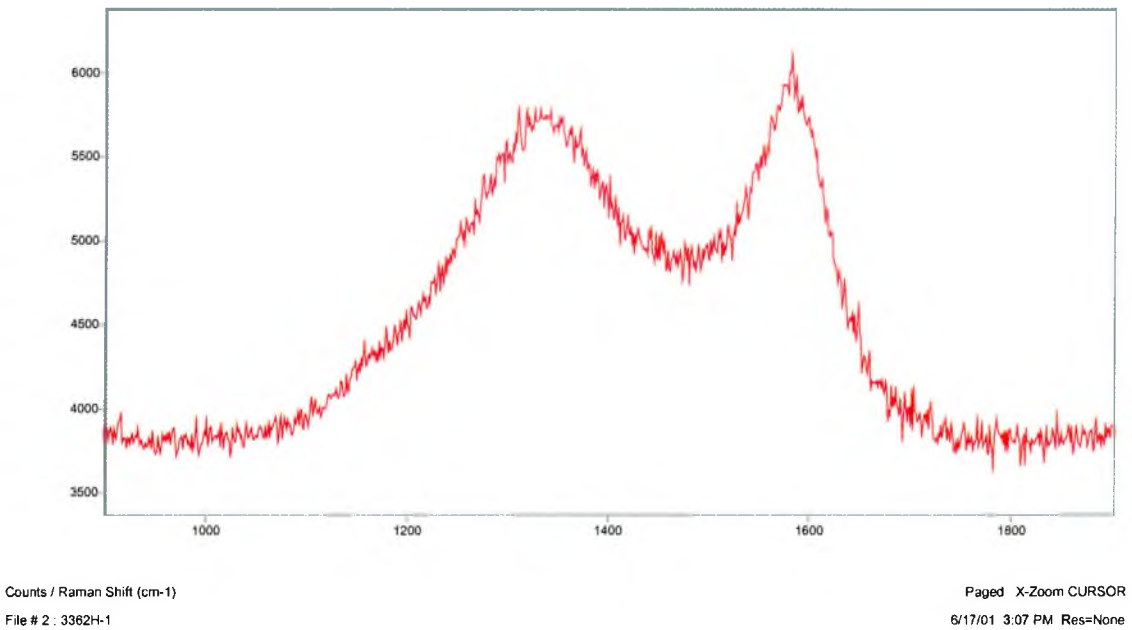

Spectrum 5.3.16: 66µg DPM and 440µg coal dust on a quartz fibre filter, 400s scan time, x5obj, 633nm laser at 100% power, heated-treated, rotating at 3rpm

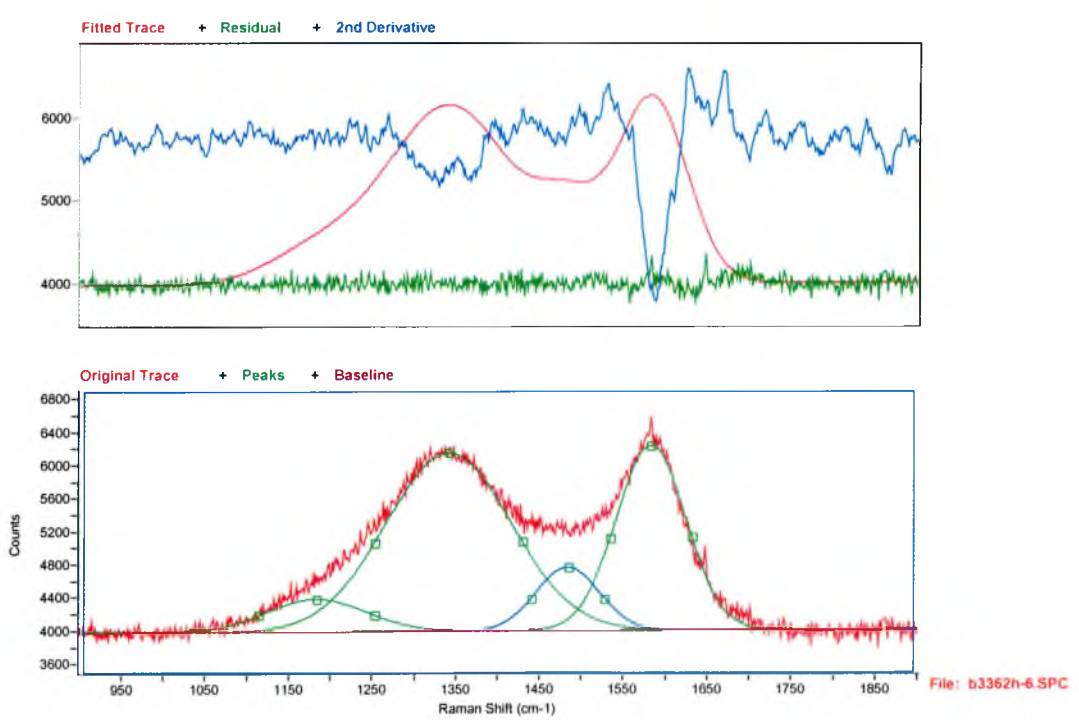

Figure 5.3.25: Curve fit of a heat-treated 66µg DPM and 440µg coal dust mixture sample spectrum

Peak	Position (cm^{-1})	Height (a.u.)	Width (cm^{-1})	Integrated Area
1	1184	392	138	57841
2	1342	2148	176	404289
3	1485	760	89	71642
4	1584	2228	98	232007

Table 5.3.30: Fitted peak positions, heights, widths and areas of a heat-treated 66μg DPM and 440μg coal dust mixture sample spectrum

Peak	Position (cm^{-1})	Height (a.u.)	Width (cm^{-1})	Integrated Area
1	1195	238	147	37221
2	1338	1415	161	242579
3	1480	549	99	58061
4	1585	1307	103	143917

Table 5.3.31: Fitted peak positions, heights, widths and areas of a heat-treated 214μg DPM and 140μg coal dust mixture sample spectrum

Peak	Position (cm^{-1})	Height (a.u.)	Width (cm^{-1})	Integrated Area
1	1198	237	143	36168
2	1335	1277	150	204732
3	1484	552	115	64140
4	1585	1151	91	110906

Table 5.3.32: Fitted peak positions, heights, widths and areas of a heat-treated 299μg DPM and 123μg coal dust mixture sample spectrum

Peak	Position (cm^{-1})	Height (a.u.)	Width (cm^{-1})	Integrated Area
1	1202	373	140	55915
2	1340	1771	159	300881
3	1480	662	90	63808
4	1584	1694	98	178521

Table 5.3.33: Fitted peak positions, heights, widths and areas of a heat-treated 162μg DPM and 118μg coal dust mixture sample spectrum

Peak	Position (cm^{-1})	Height (a.u.)	Width (cm^{-1})	Integrated Area
1	1186	202	106	22932
2	1330	3283	150	220640
3	1498	1751	138	85848
4	1589	4173	83	100389

Table 5.3.34: Fitted peak positions, heights, widths and areas of a heat-treated 251μg DPM and 78μg coal dust mixture sample spectrum

Peak	Position (cm^{-1})	Height (a.u.)	Width (cm^{-1})	Integrated Area
1	1176	256	129	35574
2	1338	1633	175	305731
3	1481	564	89	53581
4	1583	1543	106	174418

Table 5.3.35: Fitted peak positions, heights, widths and areas of a heat-treated 159μg DPM and 234μg coal dust mixture sample spectrum

Sample	Total Weight (μg)	DPM Weight (μg)	Coal Dust Weight (μg)	D/G Integrated Area Ratio	Standard deviation (%) of Integrated spectral areas
1	506	66	440	1.7	3.2
2	344	214	140	1.7	1.9
3	420	299	123	1.9	6.0
4	275	162	118	1.7	2.9
5	329	251	78	1.7	5.9
6	393	159	234	1.8	2.3

Table 5.3.36: Coal and DPM weights and D/G ratios for an example spectrum of each sample and integrated spectral areas standard deviation

Comparing the curve fit for the spectra of the heated samples in this section with the untreated samples in section 5.3.5 the affect of the heat-treatment on the spectra can be investigated. Like the separate coal and DPM samples the spectra of the heat-treated mixture samples appear to generally have broader D and G bands than the untreated samples. This could possibly be due to the production of disordered sp^2-bonded carbon from sp^3-bonded carbon. No general trend was observed for a change in the D/G band ratios, due to the heat-treatment. The value decreased for some samples, increased for others and remained virtually unchanged for other samples. However, it is interesting to note that the range of the value across the samples decreased significantly from between 1.0 to 2.4 for the untreated samples to only a range of 1.7 to 1.9 for the heat-treated samples. This in itself might indicate some kind of ordering of the samples due to heat-treatment. However, it would be necessary to subject the samples to a range of different HTTs to investigate this further. The G band position varied from $1583cm^{-1}$ to $1589cm^{-1}$ for the heat-treated samples, compared to $1590cm^{-1}$ to $1593cm^{-1}$ for the untreated mixture samples. This downward shift may be as a result of ordering of the carbon structure. The

D band position varied from 1330cm^{-1} to 1340cm^{-1} for the heat-treated samples, compared to 1339cm^{-1} to 1353cm^{-1} for the untreated samples which is an indication of the sample becoming more ordered with heat treatment. The standard deviation of the integrated spectral areas for the replicate measurements of each of the heat-treated samples ranged from 1.9 to 6%. The standard deviation of the integrated spectral areas for the replicate measurements of each of the untreated samples, analysed in section 5.3.8, ranged from 1.9 to 10%. However, only 5 spectra of the sample with a standard deviation of 10% were measured. If a greater number of spectra were integrated the standard deviation would be expected to be less. The other untreated samples all had standard deviations of less than 5%. Therefore, the heat-treatment did not significantly change the reproducibility of integrated spectral areas.

Even after heat-treatment a large difference was observed in shape and intensity of the first 2 spectra, of each sample, compared to the last 8 spectra. Therefore, the standard deviation of the spectral areas of the heat-treated samples was calculated while omitting the first two spectra of the 10 replicates taken of each sample. Spectrum 5.3.17 compares the 1st spectrum with the 5th spectrum taken of a heat-treated 299μg DPM and 123μg DPM mixture. The first spectrum appears to have much higher fluorescence levels than the 5th spectrum. After heat-treatment the adsorbed organic matter will have been heated off. This results in the sample readily adsorbing organic material from the air after it is removed from the oven. It is likely that the high fluorescence observed for the first spectrum is due to the presence of these organic impurities adsorbed onto the surface of the carbon particles. After being analysed for approximately an hour these adsorbed organics are heated off by the laser resulting in a reduction in the fluorescence levels.

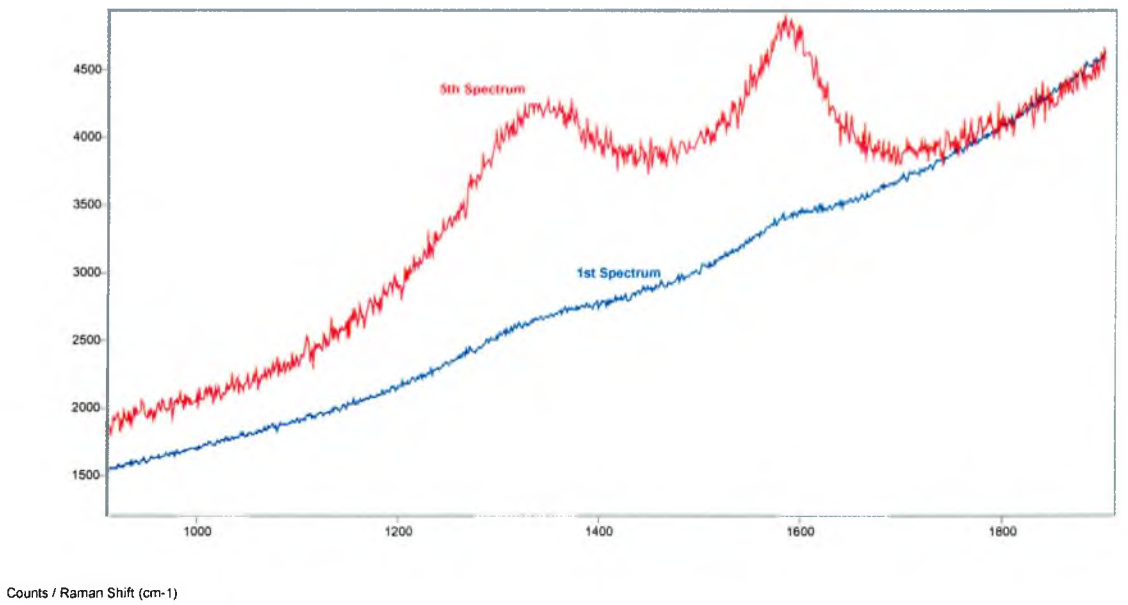

Spectrum 5.2.17: 299μg DPM and 123μg DPM heat-treated mixture, X5 obj, 400s scan time, 100% laser power, rotating at 3rpm, 1st and 5th spectrum.

5.3.13 PLS model from spectra of heat-treated coal dust and DPM mixtures

5.3.13.1 Introduction

In this section a PLS model from the spectra of heat-treated mixture coal dust and DPM samples is produced to investigate the effect of the heat-treatment.

5.3.13.2 Experimental

The sample concentrations were normalised using the integrated spectral areas of the 520cm^{-1} band of a clean, flat piece of crystalline silicon, as described in section 5.3.5. A PLS model was constructed using the spectra from the heat-treated samples. The spectra were baseline corrected, mean centred, the whole spectral range was used, 10 factors were calculated and cross-validation was applied.

5.3.13.3 Results and discussion

The real and the normalised concentrations input into the data set for each mixture sample are shown in table 5.3.37. The best PLS calibration model was found to be using PLS-1 compression, cross validation and using the whole spectrum (900-1900cm^{-1}). Using second derivative curves, rather than original spectra, did not improve the model results. From the PRESS plots, in figures 5.3.26 and 5.3.28, 3 factors were chosen to model the DPM component and 3 factors for the coal dust component. The actual versus predicted plots for the PLS model are shown in figures 5.3.27 and 5.3.29. The R^2 values for DPM and coal dust were 0.932 and 0.826 respectively.

Sample	DPM Weight (µg)	Normalised DPM Weight (µg)	Coal Dust Weight (µg)	Normalised Coal Dust Weight (µ)
1	60	91	398	608
2	214	214	140	140
3	299	282	116	123
4	162	162	118	118
5	251	225	70	104
6	159	156	234	229

Table 5.3.37: Mixture standards DPM and coal dust loadings and their normalised values used for the PLS model

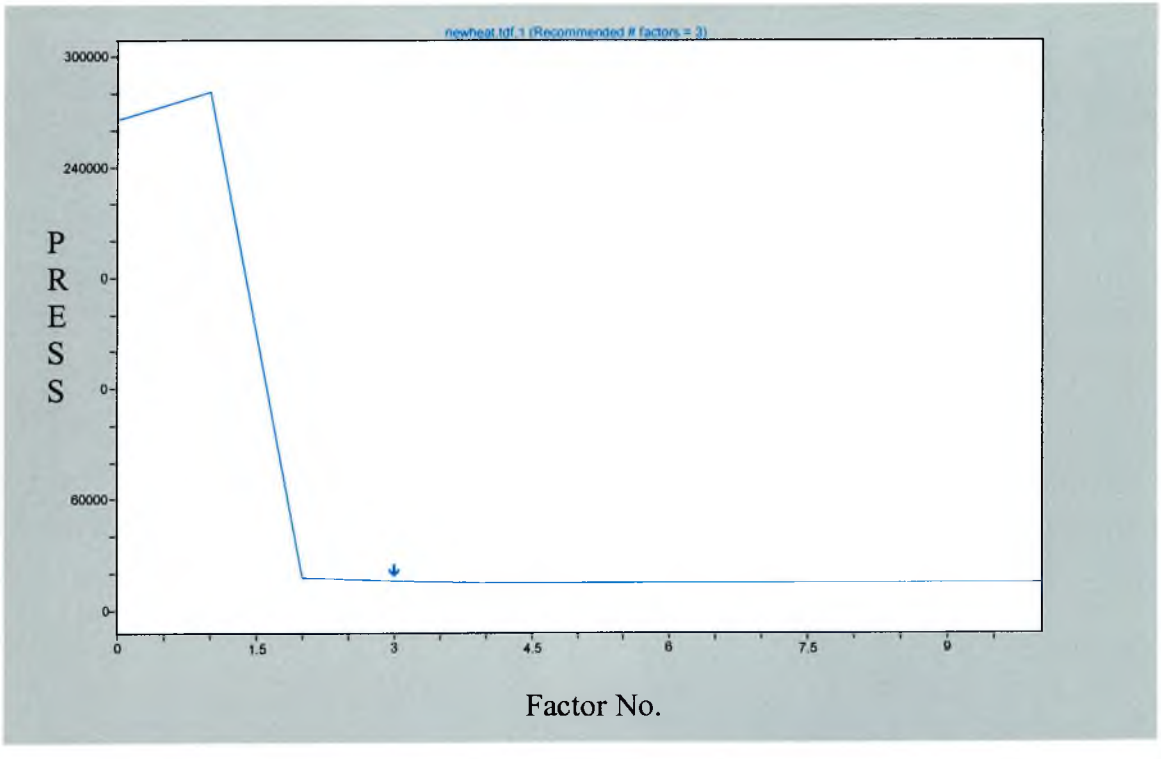

Figure 3.5.26: PRESS plot for the DPM component of a heat-treated mixture sample

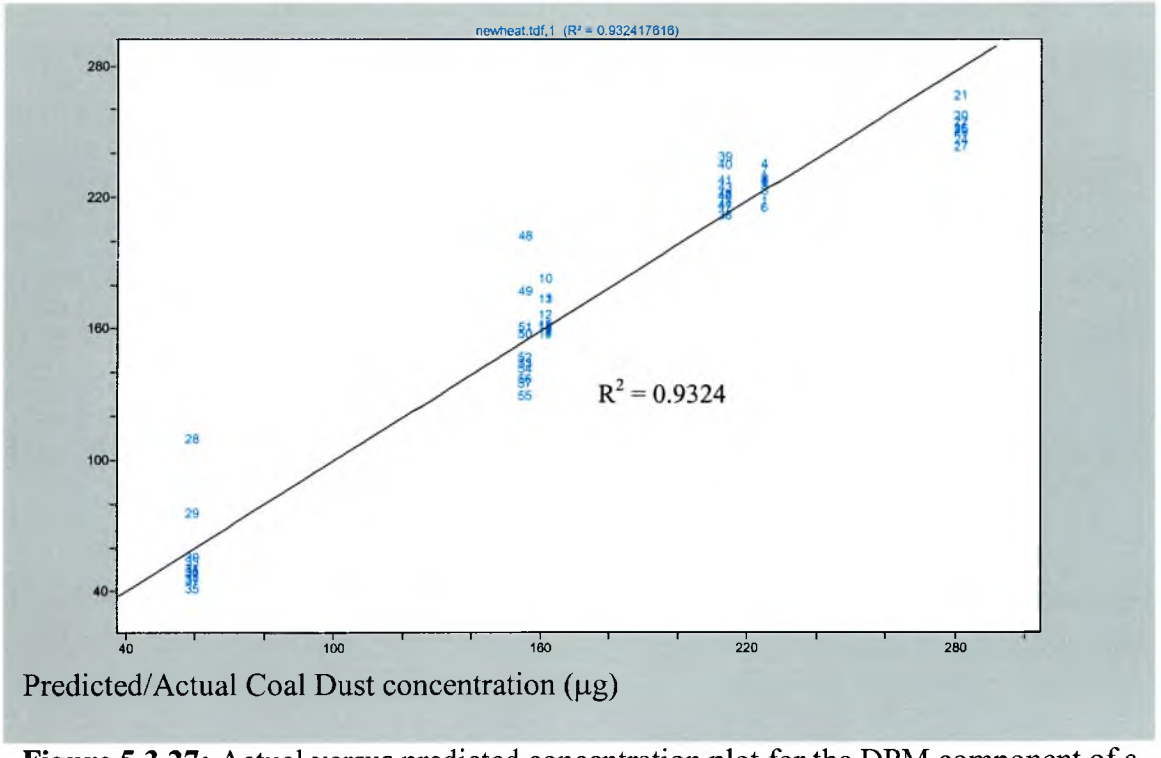

Figure 5.3.27: Actual versus predicted concentration plot for the DPM component of a heat-treated mixture sample, using 2 factors

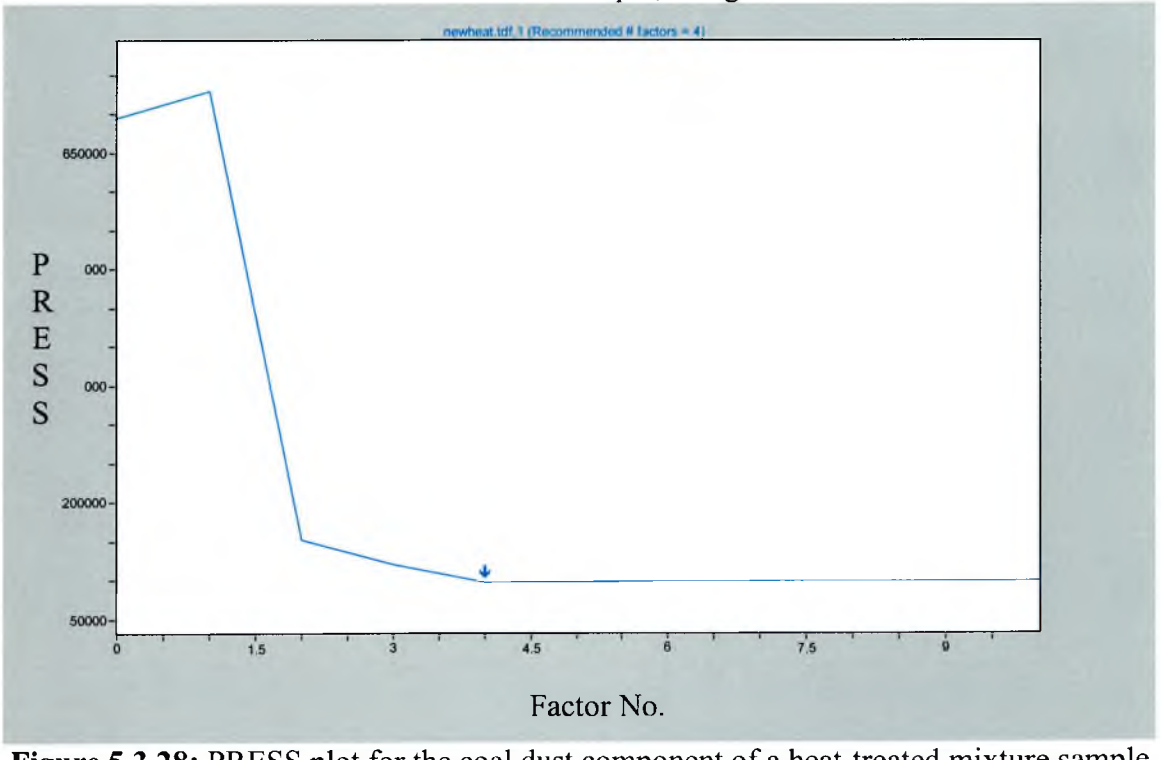

Figure 5.3.28: PRESS plot for the coal dust component of a heat-treated mixture sample

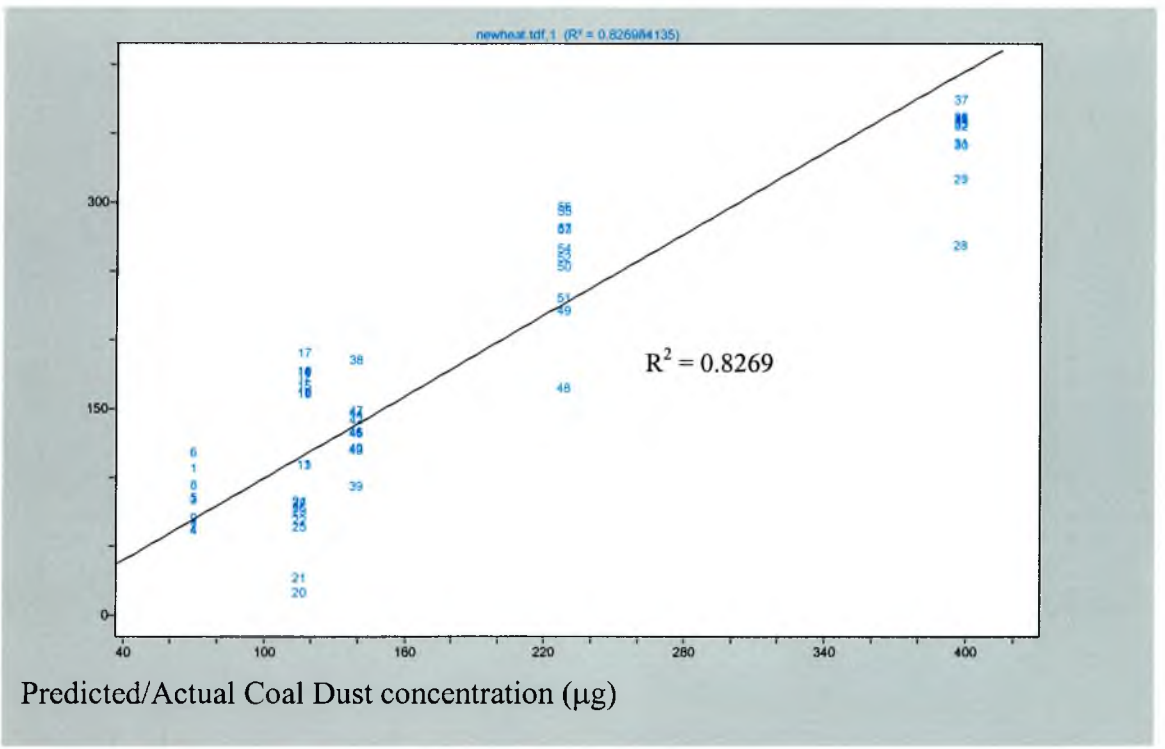

Figure 5.3.29: Actual versus predicted concentration plot for the coal component of a heat-treated mixture sample, using 3 factors

The observations for the DPM actual versus predicted concentration plot in figure 5.3.27 are much more closely spaced for the heat-treated mixture samples than untreated samples in section 5.3.9 (figure 5.3.13). This is reflected in the improvement of the R^2 value from 0.671 to 0.932. The heat-treatment appeared to have little if any effect on the coal dust component with the R^2 only improving from 0.817 to 0.826.

Fortunately, we only have 2 components here. So, if we can develop a model that can only successfully determine the amount of DPM we can still calculate the amount of coal dust by subtracting the estimated DPM loading from the total weight. However, a correlation of 0.932 was not considered to be accurate enough. Therefore, it was desirable to improve the correlation even further. As discussed in the section 5.3.12 some of the spectra had high fluorescence levels due to adsorbed organic impurities. These impurities appeared to be heated off after the first spectrum or 2. The spectra that were obviously subjected to high fluorescence levels were omitted from the PLS model. However, some of the observations for the DPM actual versus predicted concentration plot are still located far from the group centre. This is especially so for the samples with a 60µg and a

156μg DPM loading. In fact, the observations located far from the group centre, for each of these samples, correspond to their first two spectra. In future it would be recommended to take 12 spectra of a heat-treated sample and discard the first 2 spectra to avoid their shape influencing the model. It was decided to re-run the PLS model, omitting the first 2 spectra for each sample, to see if this strategy helped improve the correlation of the actual versus predicted concentration plots.

From the PRESS plots, in figures 5.3.30 and 5.3.32, 2 factors were chosen to model the DPM component and 3 factors for the coal dust component. The actual versus predicted plots for the PLS model are shown in figures 5.3.31 and 5.3.33. The R^2 values for DPM and coal dust were 0.961 and 0.874 respectively. Omitting the first 2 spectra for each sample from the model improved the R^2 value from 0.932 to 0.961 for the DPM and from 0.826 to 0.874 for the coal dust.

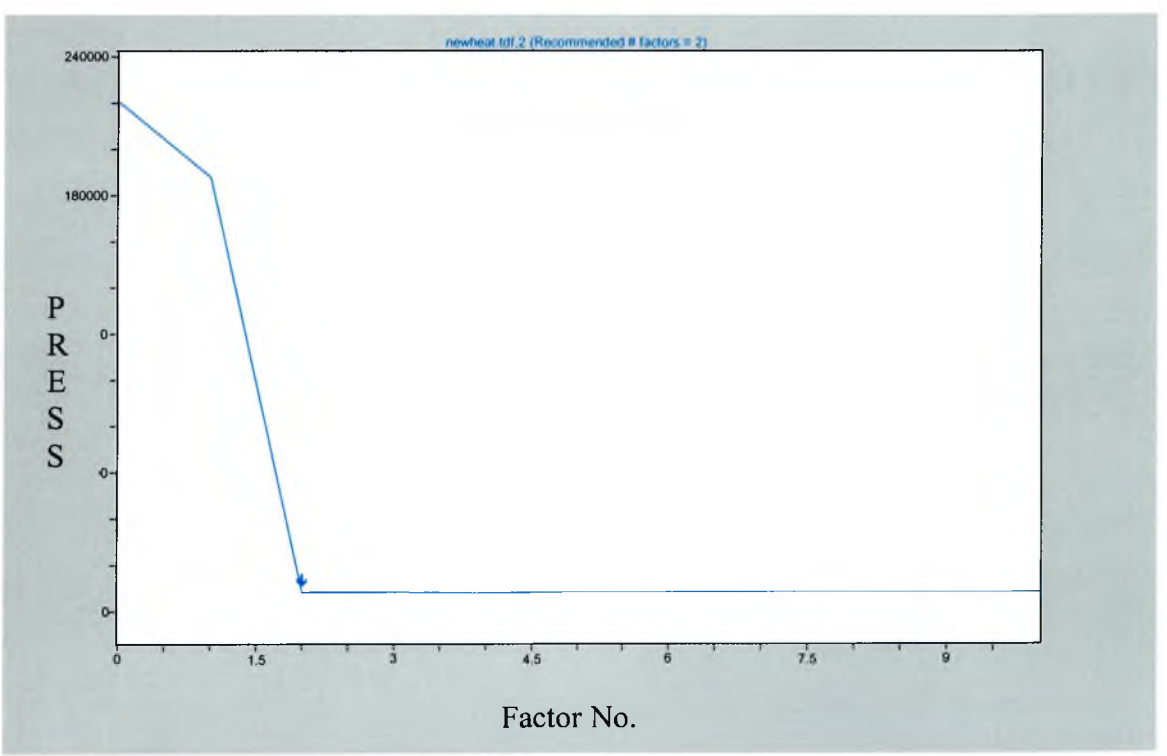

Figure 5.3.30: PRESS plot for the DPM component of a heat-treated mixture sample

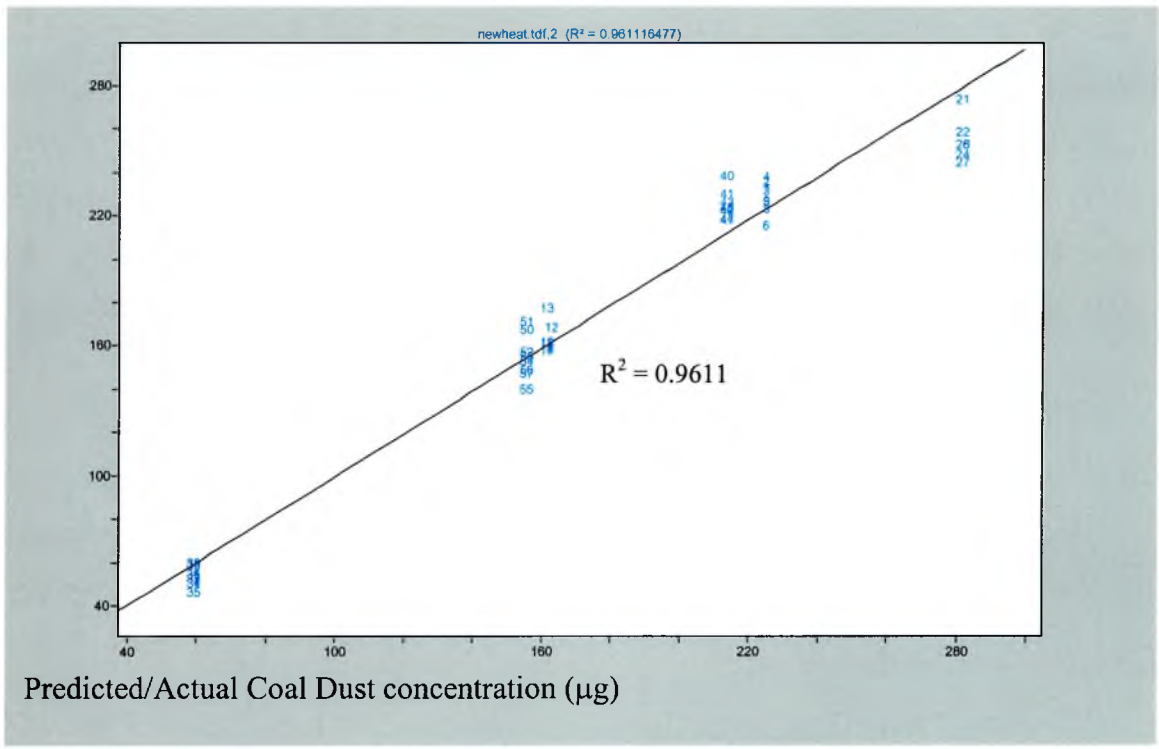

Figure 5.3.31: Actual versus predicted concentration plot for the DPM component of a heat-treated mixture sample, using 2 factors

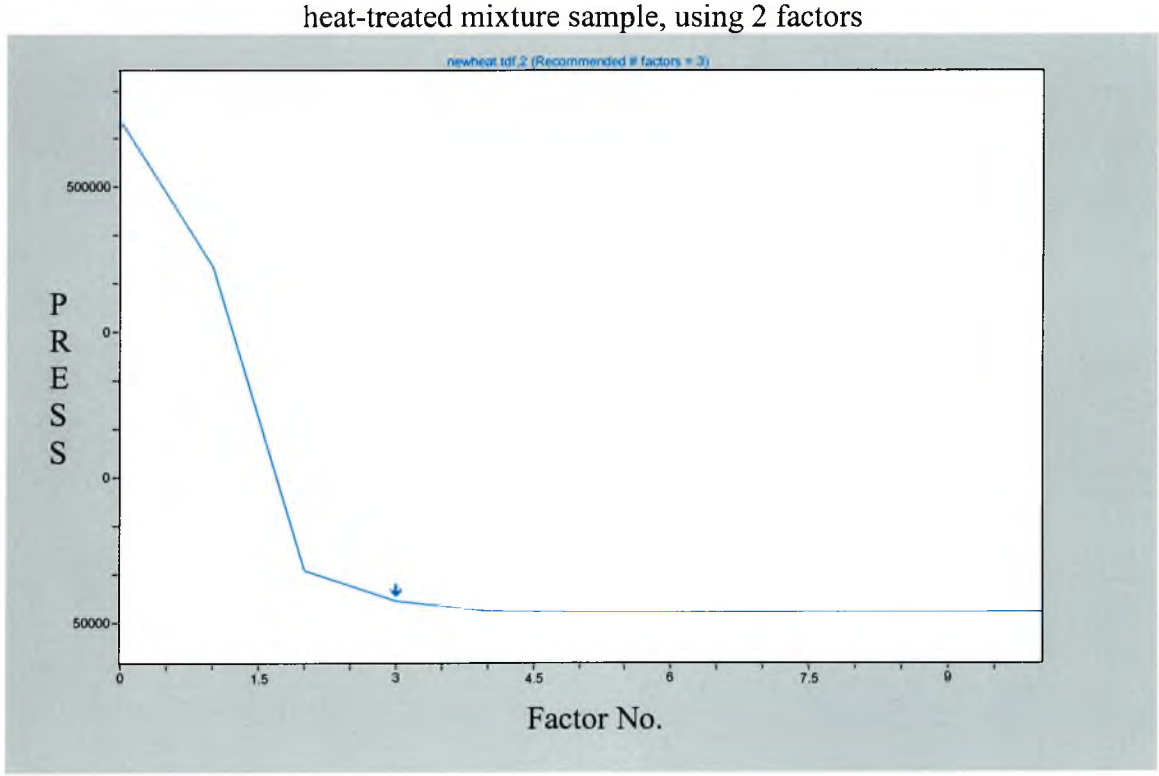

Figure 3.5.32: PRESS plot for the coal dust component of a heat-treated mixture samples

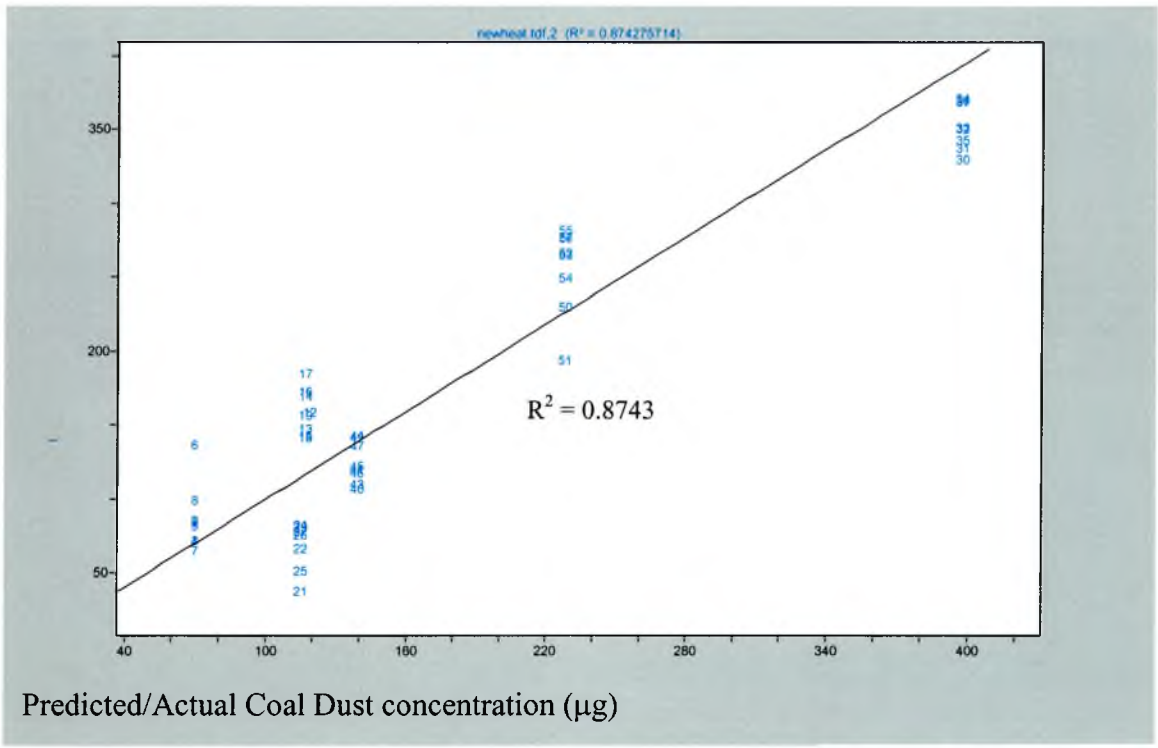

Figure 5.3.33: Actual versus predicted concentration plot for the coal dust component of a heat-treated mixture sample, using 3 factors

From the actual versus predicted plot for DPM (figure 5.3.32) we can see that although we have 6 mixture samples some of these samples had similar loadings. So, we have in effect analysed mixtures with 4 different DPM loadings. It is necessary to produce additional mixture samples with loadings dissimilar to the 6 samples already analysed. In the next section the affect of adding these additional samples is investigated.

5.3.14. Investigation of the affect of adding spectra from additional heat-treated samples to the PLS model

5.3.14.1 Introduction

In the last section we produced a PLS model, from the spectra of heat-treated mixture samples, which resulted in a DPM actual versus predicted concentration plot with an R^2 of 0.962. Although this is a acceptable value it was obviously desirable to get the value as close as possible to 1. From the DPM actual versus predicted concentration plot in figure 5.3.42 we can see that there is no sample with a DPM loading in the range of 70 to

150μg. So, it was necessary to produce additional samples in this range, to make the model more reliable. Also, the current PLS model only predicted down to about 70μg DPM. The addition of sample(s) with DPM loadings of less than 70μg will make the model more reliable and improve the limit of detection too. In this section we attempted to produce additional mixture samples with the necessary loadings. These additional samples were heat-treated and their resultant spectra added to the PLS model to investigate if there was an improvement in the R^2 value for the DPM actual versus predicted concentration plot.

5.3.14.2 Experimental

A new sampling system was set up which was similar to the one used to collect the mixture samples that had been analysed so far (see figure 5.3.6 for a schematic diagram). The only major difference between the new and old sampling systems was that a slightly larger box was used for the new system. DPM alone was collected on quartz fibre filters using this new sampling system to investigate if it had a similar collection rate to the previous system. An attempt was made to produce mixture DPM and coal dust samples using a similar sampling procedure to the one described in section 5.3.4. Coal dust was blown into the system via a tube connected to a dustbowl positioned outside the box and the DPM entered the box via a tube connected to a diesel van exhaust. Four pumps, calibrated to 2L/min, were connected to valves at the bottom of the chamber, from the outside. These were used to draw air from the surrounding atmosphere, of the box, into the sampling chamber. Filter holders, with paper filters, were connected to these valves inside the chamber, to prevent dust being sucked into the pumps. Two more pumps, positioned outside the box, were calibrated to approximately 2L/min. These pumps were connected to samplers containing clean pre-weighed quartz fibre filters. The samplers were placed into the centre of the chamber to sample air from the chamber's atmosphere.

When collecting the DPM alone the new sample system had a similar collection rate as collected previously. However, it proved difficult to produce reliable mixture samples. In the majority of cases it appeared that little or no coal dust had been collected onto the

sample filters. This was known because the weights of the collected samples were similar to the expected weights of DPM collected on its own, according to graph 5.3.3. After many failed attempts to produce mixture samples with the required DPM loadings it was decided to try a new strategy.

In the previous attempts the coal dust was blow into the box from a dustbowl outside and then drawn into the sample chamber using pumps. However, an insufficient amount of coal dust was present in the chamber using this method. The new strategy involved weighing 0.5g of coal dust in a weighing boat and then adhering this weighing boat to the bottom of the sample chamber. An air hose was connected to the sample chamber and its nozzle directed towards the coal dust sample. The air was turned on and maintained at rate of 25 l/min for 5 to 10 seconds. This resulted in the coal dust sample being distributed in the sample chamber. The dust was allowed to settle for 10 minutes, before collecting a sample, so that all the large particles would fall out of the air, leaving the respirable particles to be sampled. The sample collection rate was not reproducible but it ensured that there was coal dust present in the chamber for each sampling period.
To make mixture DPM and coal dust samples using this method it was necessary to re-characterise the DPM collection rate. This was necessary because the DPM collection rate was previously characterised when there were 4 pumps, running at 2 l/min, drawing the diesel emissions into the chamber. Whereas, this new method did not involved the use of these pumps because they would have sucked the coal dust out of the chamber when the larger particles were allowed to settle. The lowest DPM loading for the previous mixtures was estimated to be 66μg, using a 2.5minute collection time. So, to improve the limit of detection it was necessary to produce a mixture sample with a DPM loading of less than this. It was decided that a collection time of 1 minute would be appropriate. The exhaust pipe of a diesel van was connected to the sampling system, after been run on idle for 30 minutes to get consistent emissions. The system was allowed to fill for 10 minutes. The air in the chamber was sampled for 1 minute using a pump running at 2 l/min. This was repeated 3 times and the sample loadings were 27, 32 and 31μg respectively. Therefore, the average DPM loading when collecting for 1 minute was 30μg. It was then necessary to produce a DPM sample with a loading in the range of 70

to 150μg. This was attempted using collection times ranging from 3.5 to 5 minutes. However, no reproducible results were obtained for these collection times. Therefore it was only possible to try to produce an additional mixture sample with a DPM loading of around 30μg.

To produce the mixture sample 0.5g of coal dust was placed in a weighing boat in the centre of the sampling chamber. The dust was blasted with air running at 25 l/min for around 5 seconds and allowed to settle for 10 minutes. Meanwhile, the diesel exhaust was connected to the box and was allowed to fill the sampling system for 10 minutes, while the coal dust settled. After the 10 minutes and sampling pump was turned on for 1 minute. The total weight of the sample was 327μg. From the characterisation of the DPM collection rate it was known that the DPM loading for 1 min was 30μg. Therefore the coal dust loading was 297μg. This sample was heat-treated to 625°C in N_2 for 15 minutes. 12 spectra of the sample were taken using the same parameters as the previous heat-treated mixture sample. The first 2 spectra were discarded due to high fluorescence levels, as discussed in section 5.3.12. An example spectrum of the sample is shown in spectrum 5.3.18.

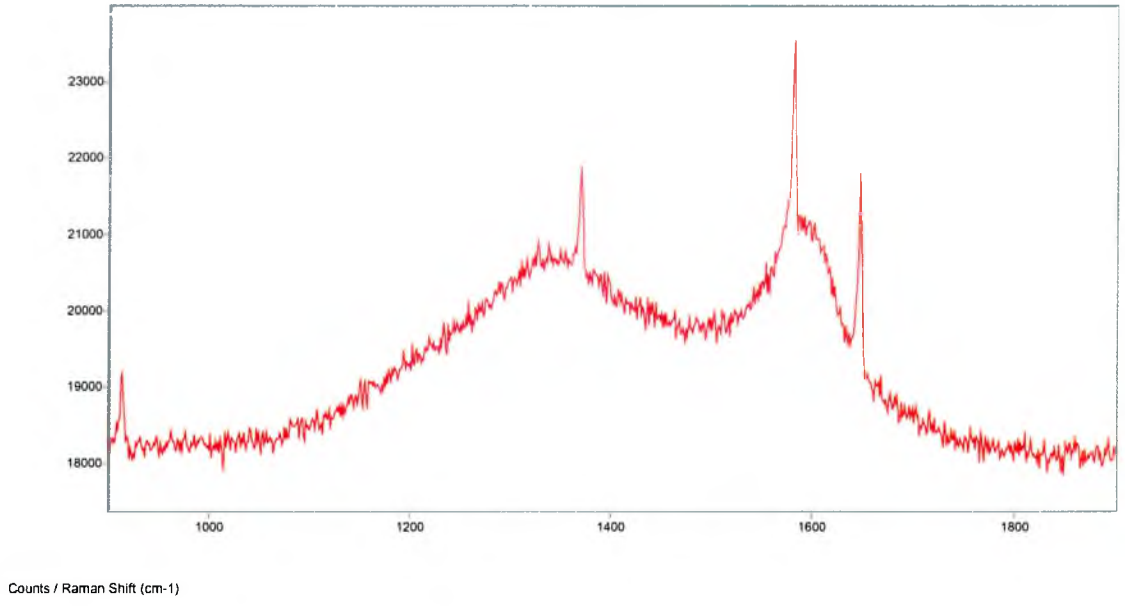

Spectrum 5.3.18: 30μg DPM and 297μg coal dust on a quartz fibre filter, 400s, x5obj, 633nm laser at 100% power, heat-treated to 625°C, rotating at 3rpm

5.3.15 PLS model using an additional mixture sample

5.3.15.1 Introduction

In this section we investigate the effect of using the additional 30μg DPM and 297μg coal dust mixture sample for our PLS model

5.3.15.2 Experimental

The 10 replicate spectra of the 30μg DPM and 297μg coal dust mixture sample were added to the PLS data set used in section 5.3.13 and a new model was constructed. The concentration values for the DPM and coal dust were normalised according to area of the 520cm^{-1} silicon peak for the day of analysis. These values being 35μg and 347μg respectively.

5.3.15.3 Results and discussion

The DPM and coal dust PRESS and actual versus predicted plots are shown in figures 5.3.34 through 5.3.37.

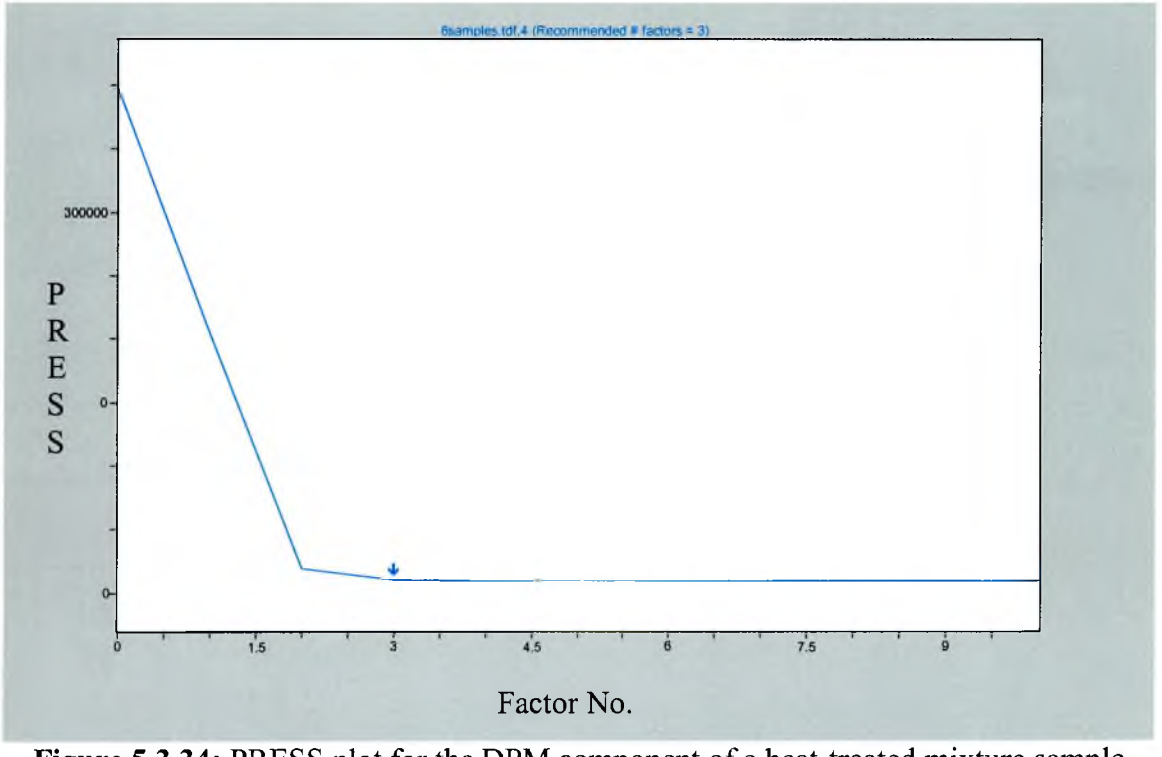

Figure 5.3.34: PRESS plot for the DPM component of a heat-treated mixture sample

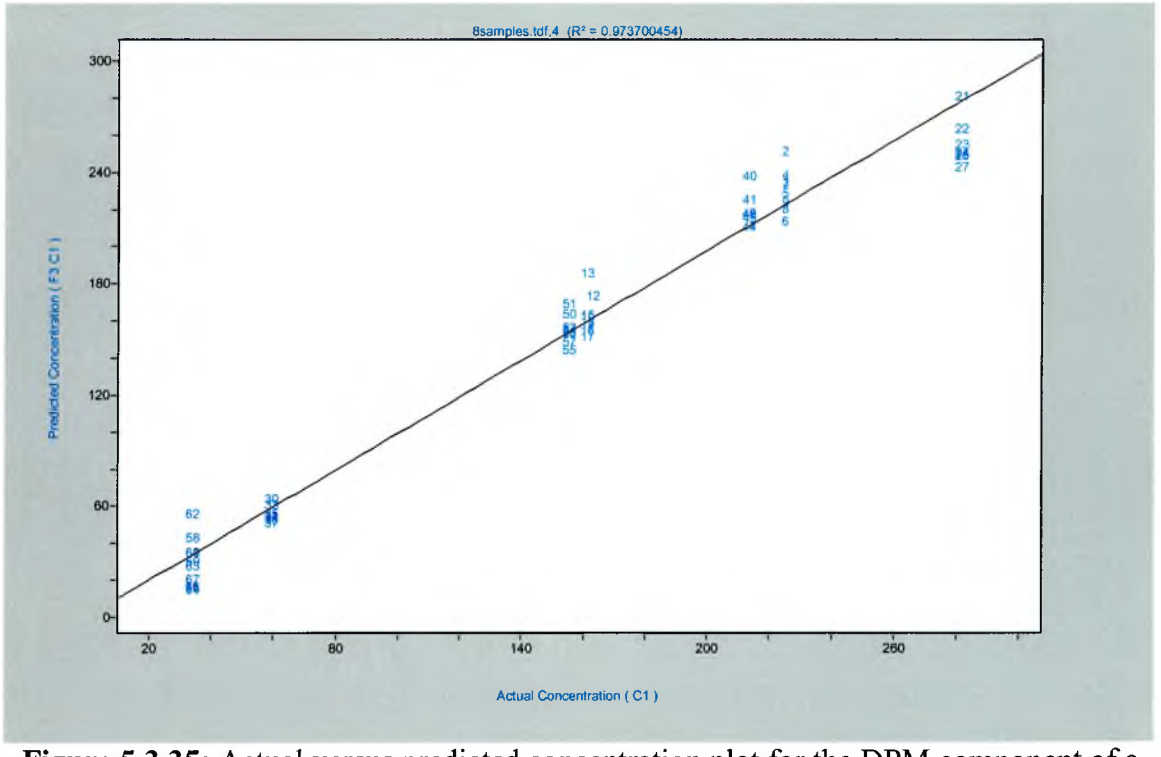

Figure 5.3.35: Actual versus predicted concentration plot for the DPM component of a heat-treated mixture sample, using 3 factors

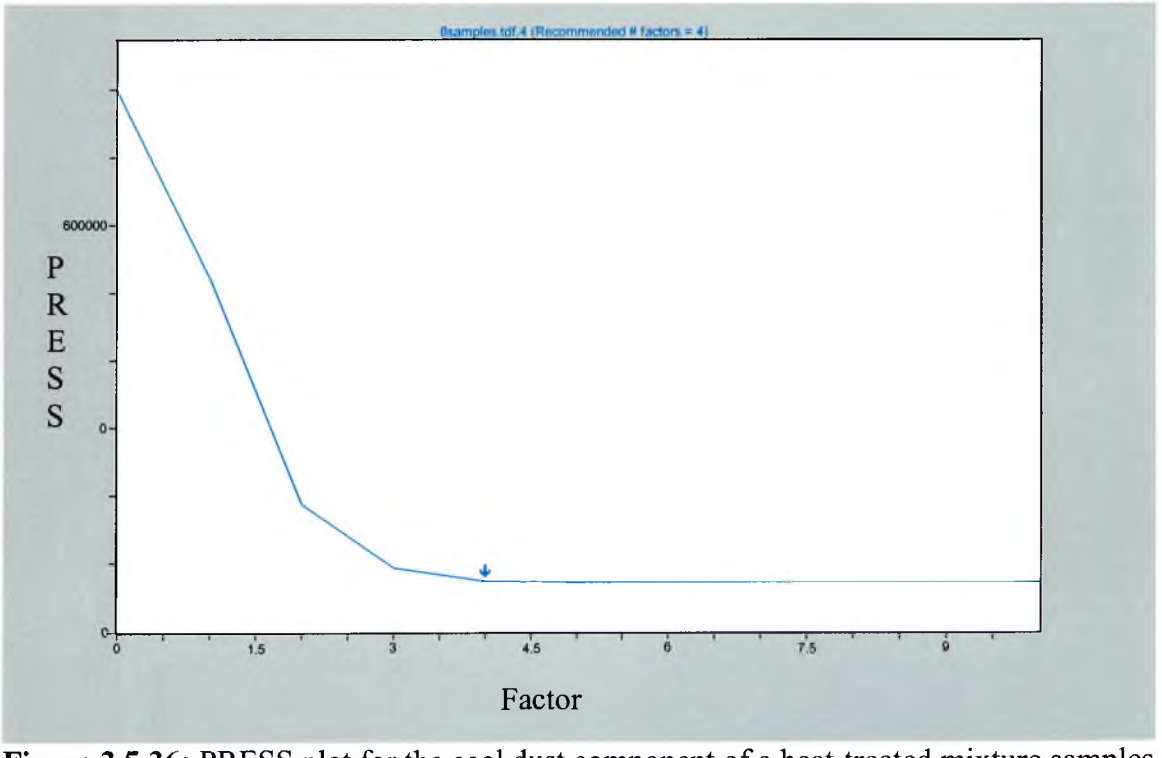

Figure 3.5.36: PRESS plot for the coal dust component of a heat-treated mixture samples

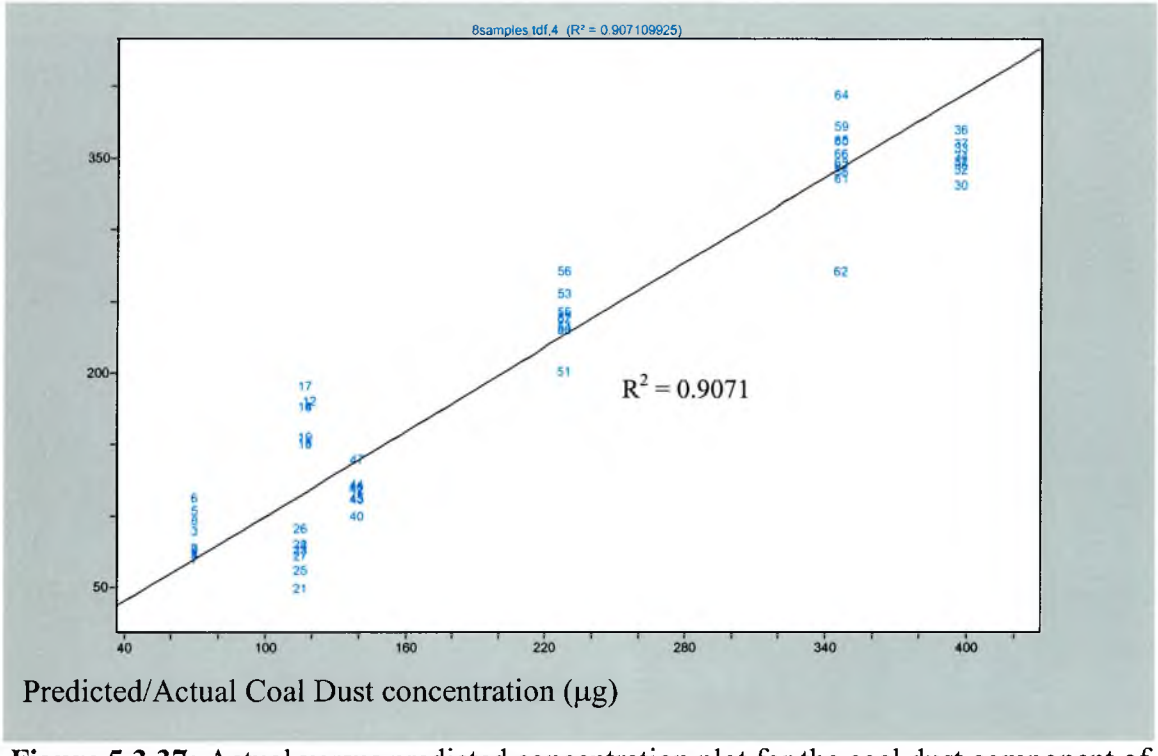

Figure 5.3.37: Actual versus predicted concentration plot for the coal dust component of a heat-treated mixture sample, using 4 factors

The addition of the 30µg DPM and 297µg coal dust mixture sample to the PLS model improved the R^2 value from 0.961 to 0.974 for the DPM actual versus predicted plot and from 0.874 to 0.907 for the coal dust actual versus predicted plot.
A high R^2 value of 0.974 the DPM plot had been achieved. This was an indication that the model may be reliable enough to accurately predict the concentration of DPM and coal dust in an unknown sample.

A reconstructed spectrum for a sample can be produced from a model by combining the scores and loadings. The reconstructed spectrum can then be subtracted from the original spectrum to investigate how well the model fits the data. Typical reconstructed spectra for the DPM component are shown in figure 5.3.38. The red spectrum is the original spectrum, the blue spectrum is the reconstructed spectrum and the blue line at the bottom is the difference between the original and reconstructed spectrum (the residual). Figure 5.3.38 compares the reconstructed spectra when using 1 factor (left figure) and 3 factors

(right figure). When using just 1 factor the model fails to fully account for all the variation in the spectra and there is a large difference between the original spectrum and the reconstructed spectrum. Whereas, when using 3 factors the model adequately accounts for the variation and there is very little difference between the original and the reconstructed spectra

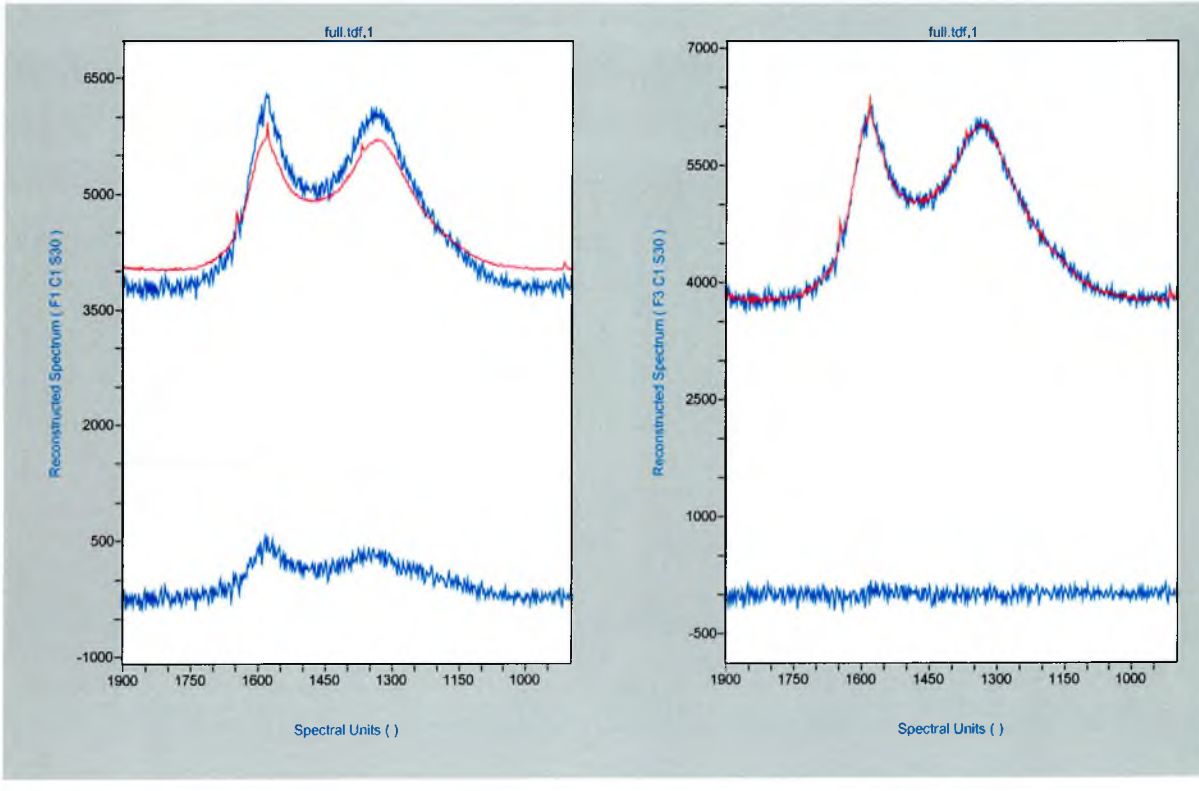

Figure 5.3.38: Comparison of a reconstructed DPM spectrum using 1 factor (left) and 3 factors (right)

In the next section we use the model developed in this section to predict the composition of a test DPM and coal dust mixture sample.

5.3.15 Prediction of an unknown sample using the final PLS model

5.3.15.1 Introduction

When collecting DPM and coal dust mixture samples two samples were collected simultaneously. Therefore, for each sample used in the PLS model we have another sample that was collected at the same time, which should have a similar loading. In this section we treat one of these additional samples as an unknown and use the PLS model to predict the amount of DPM and coal dust present. As we know the true composition of the sample we can determine the accuracy of the prediction.

5.3.15.2 Experimental

The compositions of the mixture samples were determined as described in section 5.3.4. These values are given in table 5.3.10. The sample which consisted of 156μg DPM and 139μg coal dust (sample 4(a) in table 5.3.10) was subjected to a similar heat-treatment process as the samples used for the PLS model. The response of the Raman instrument for the particular day was checked using the peak area of the 520cm^{-1} peak of crystalline silicon. 12 Raman spectra were taken of this sample using the same parameters as the samples used for the PLS model. The first 2 spectra were discarded. Using the remaining 10 spectra, the final PLS model was used to predict the composition of the sample.

5.3.15.3 Results and discussion

An example spectrum of the 156μg DPM and 139μg coal dust mixture sample is given in spectrum 5.3.19.

The average value and the standard deviation of the predicted concentration of the 10 spectra of the mixture DPM and coal dust sample is given in table 5.3.38

	DPM	Coal Dust
Average predicted concentration (µg)	222	91
Standard deviation	6.8	16.5
% Standard deviation	3.1	18.1

Table 5.3.38: Average predicted concentration of 10 spectra of a mixture DPM and coal dust sample

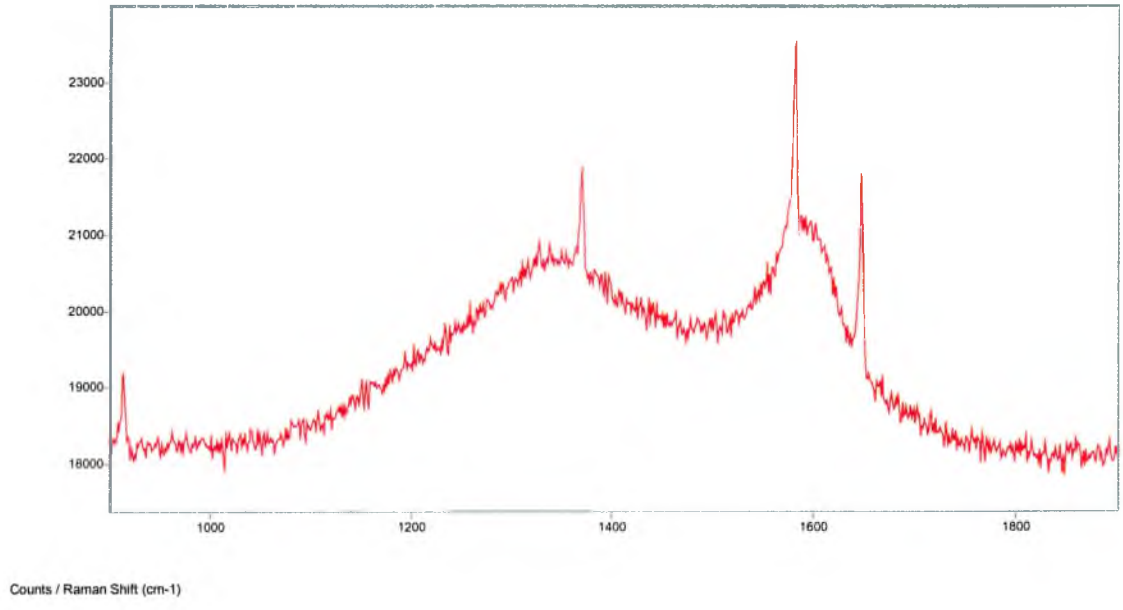

Spectrum 5.3.19: 30µg DPM and 297µg coal dust on a quartz fibre filter, 400s, x5obj, 633nm laser at 100% power, heat-treated to 625°C, rotating at 3rpm

The true composition of the sample was 156µg DPM and 139µg coal dust. However, as mentioned earlier the concentration values of the spectra used in the PLS model were normalised according to the response of the instrument on the day of analysis. The 520cm^{-1} silicon peak area used to normalise the spectra was 15756. The silicon peak area on the day of the analysis of the so-called "unknown" sample analysed in this section was 21024. So, the predicted concentrations needed to be normalised by multiplying the value by 0.749 (15756/21024). The predicted DPM and coal dust concentrations of the unknown sample after normalisation is given in table 5.3.39.

	DPM	Coal Dust
Mean predicted concentration (μg)	166	68
Standard deviation	5.1	12.4
% Standard deviation	3.1	18.1

Table 5.3.39: Average predicted concentration of 10 spectra of a mixture DPM and coal dust sample, after normalisation

To access the accuracy of the prediction is it necessary to develop confidence intervals for the 10 estimates. We will use 95% confidence intervals here. The general format of a confidence interval is the estimate ± the margin of error. The margin of error can be calculated from the standard error on the mean (SEM), which is calculated as in equation 5.3.1. Where n = the number of samples used for the estimate.

$$\text{SEM} = \text{SD of the estimate} / \sqrt{n} \qquad \textbf{(5.3.1)}$$

The SEM for DPM and coal dust were respectively calculated to be 1.6 and 3.9.
The margin of error is 2 times the SEM giving a margin of error for the DPM and coal dust of 3.2 and 7.8 respectively. Therefore the 95% confidence interval for the estimated mean was:

162.1 to 169.9μg (166 ± 3.9μg) for the DPM
60.2 to 75.8μg (68 ± 7.8μg)for the coal dust.

The true composition of the sample was 156μg DPM and 139μg coal dust. The PLS model slightly overestimated the amount of DPM present in the sample but gave a large underestimation of the coal dust content. There are several possible explanations for the inaccurate estimations. The procedure for producing the samples and the estimation of each constituent in the samples is outlined earlier in this chapter (section 5.3.4). DPM and coal dust were simultaneously collected on quartz fibre filters and the total weight of the deposited sample was determined by subtracting the weight of a filter before the collection from the weight after the sample collection. The deposition rate of the DPM had been accurately characterised. So, the amount of DPM on the filter was known for a

given time. The amount of coal dust was then determined by simply subtracting the expected weight of DPM from the total sample weight. It is possible that the sample by which the PLS model was tested may not have contained the expected amount of each constituent. The fact that the DPM was overestimated and the coal dust was underestimated may be an indication that there was more DPM and less coal dust on the filter than expected. If this was the only explanation for the inaccurate estimates the overestimation for the DPM and the underestimation of the coal dust should be similar. However, the over estimation for the DPM was 3.8 to 8.9% more and the underestimation of the coal dust was 45.5 to 56.7% less than the known values, indicating that there were additional explanations for the poor estimates. Another possibility is that the primary data used to construct the PLS model was inaccurate. A high R^2 value of over 0.97 was obtained for the DPM actual versus predicted plot and an R^2 of 0.91 for the coal dust. This may explain why the DPM estimation was more accurate than the coal dust estimation. Nevertheless, it is not sufficient to rely solely on the R^2 value to validate the accuracy of the model. Another valuable calculation for evaluating the accuracy of the model is the standard error of prediction (SEP) this involves comparing the difference between the actual concentration values (Y_{act}) and the predicted concentrations (Y_{pre}) of the spectra used to construct the model. The current model was validated using cross-validation (as explained in section 5.2). So, this value is called the standard error of cross-validation (SEVC) rather than SEP. The calculation is shown in equation 5.3.2 below:

$$\text{SEVC} = \sqrt{\frac{Y_{act} - Y_{pre}}{n}} \qquad \textbf{(5.3.2)}$$

The SEVC values for DPM and coal dust using the current model were calculated to be 13.5μg and 36.1μg respectively. This implies that a test sample with concentrations of 156μg DPM and 139μg coal dust could be predicted to contain 142.5 to 169.5μg DPM and 102.9 to 139μg coal dust, using this model. The average estimated value for the DPM was 166μg and this indeed falls within the expected prediction range for the test sample. However, the average coal dust estimation of 68μg is still considerably lower than the SEVC would suggest. Also, it is required that the method can be used to measure DPM

levels down to 20μg. Therefore, a SEVC of 13.5μg for DPM is totally inadequate. Further investigation of the model diagnostics is required to determine why this value is so high. One possibility is the inclusion of outliers in the training set.
When the optimum number of factors for the model has been determined, the predicted concentrations of each training sample with the selected factor model can be used for outlier detection. The difference between the actual and predicted concentrations for a sample is known as the concentration residual.

$$Rc = Corig - Cpred \qquad \textbf{(5.3.3)}$$

The model attempts to account for all the variations in the training data when the calibration calculations are performed. Therefore, the prediction error of most of the samples should be approximately the same. Samples that have significantly larger concentration residuals than the rest of the training set are known as concentration outliers. Similarly, spectral residuals can be used to detect spectral outliers. A reconstructed spectrum is produced and the spectral residual is the difference between this spectrum and the actual prediction spectrum and is calculated using equation 5.3.4.

$$Rs = \sum_{k=1}^{p} \left(Aorig_k - Apred_k \right)^2 \qquad \textbf{(5.3.4)}$$

where p is the number of wavelengths (data points) in the spectrum, Aorig are the original spectrum intensities, and Apred are the model predicted spectrum intensities. The concentration and spectral residual plots of DPM and coal dust for the current model are shown in figures 5.3.39 through 5.3.42

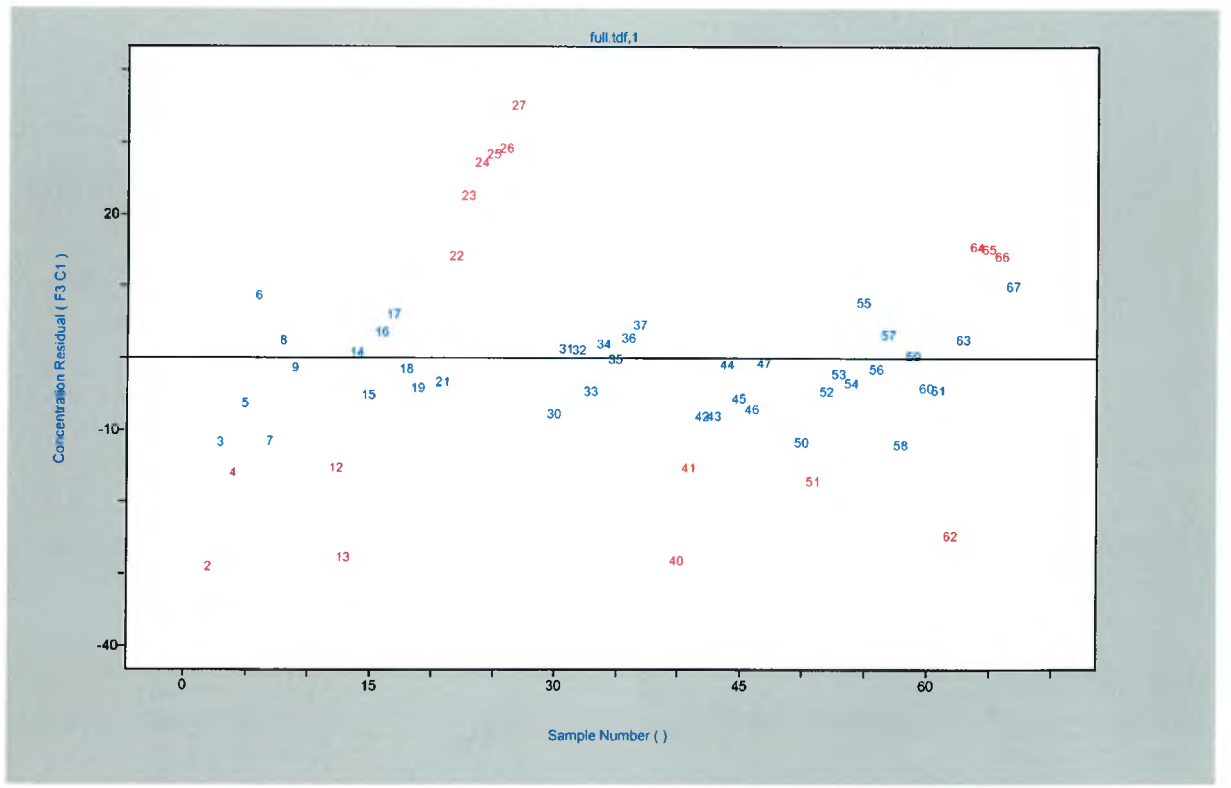

Figure 5.3.39: DPM concentration residuals

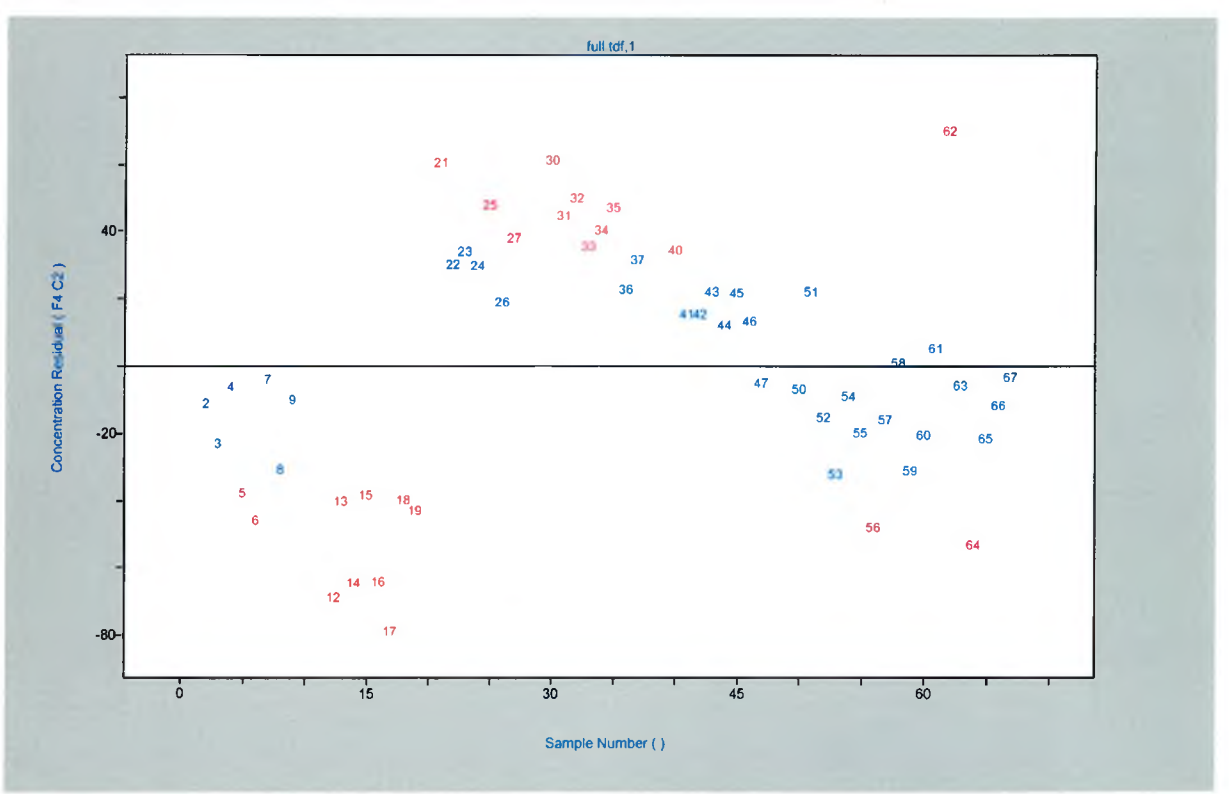

Figure 5.3.40: Coal dust concentration residuals

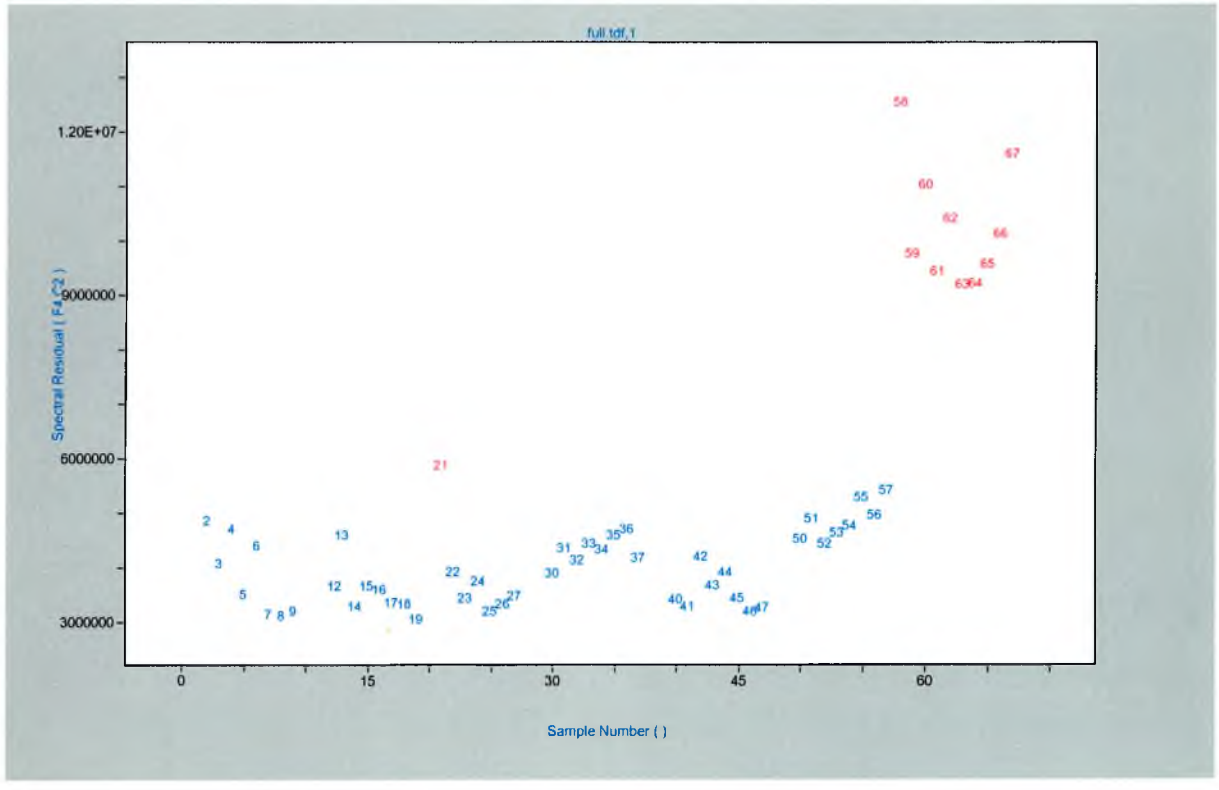

Figure 5.3.41: DPM spectral residuals

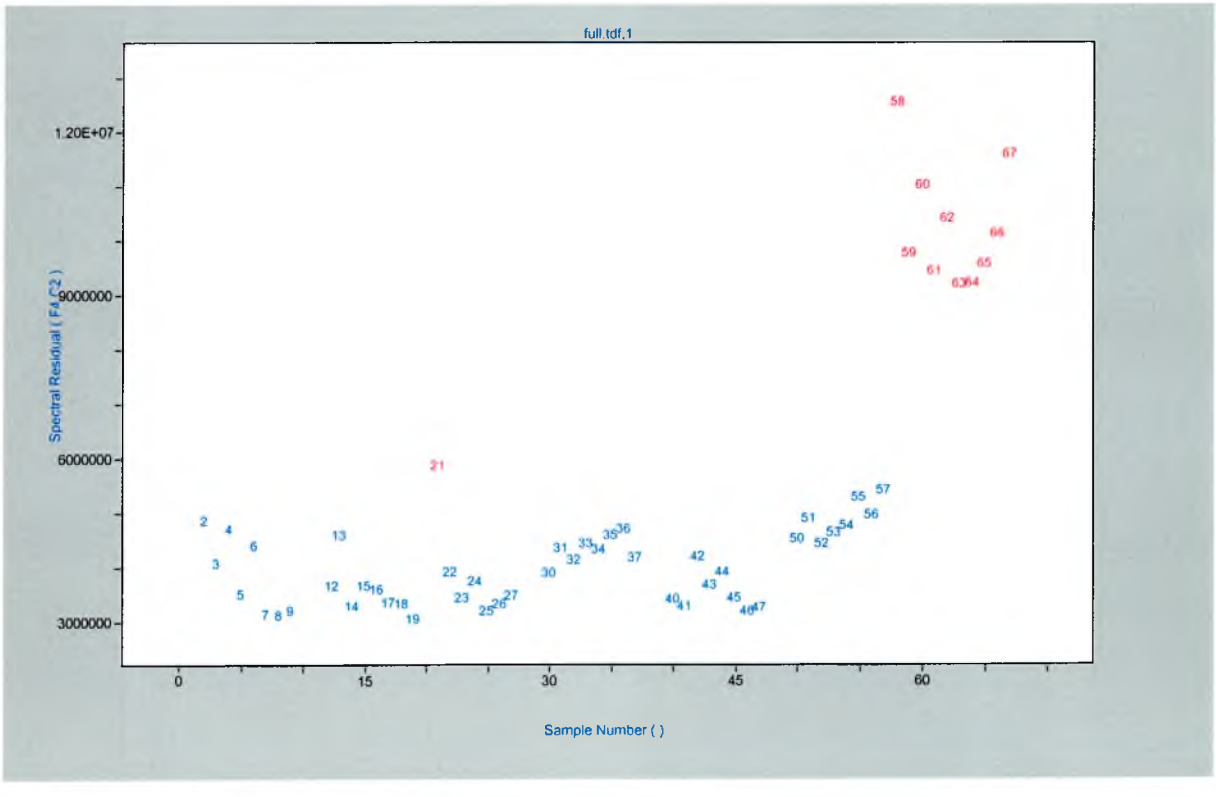

Figure 5.3.42: Coal dust spectral residuals

The concentration residuals for both the DPM and coal dust are spread over a wide range making it difficult to determine the likelihood that a sample is really an outlier. The Grams PLSplus/IQ software used for the current work applies an F-test method for determining the statistical significance of a sample's concentration residual with respect to the rest of the training set. The suspected outliers are marked in red in the residuals plots (fig 5.3.43). A similar method is used for determining the spectral outliers. Although in the present case the spectral outliers are obvious to the naked eye. The suspected spectral outliers marked with the numbers 58-67 correspond to the spectra from the new sample with 30ug DPM and 297ug coal dust. This suggests that the model may be able to predict better without this sample included. However, in the previous section (5.3.13) a PLS model was constructed where this sample was not include and the R^2 values for DPM and coal were 0.961 and 0.874 respectively (figures 5.3.31 and 5.3.33), compared to 0.974 and 0.907 for the current model. Also the SEVC for the model without this sample was 13.6 and 39.1 for the DPM and coal dust respectively, compared to 13.5 and 36.5 for the current model.

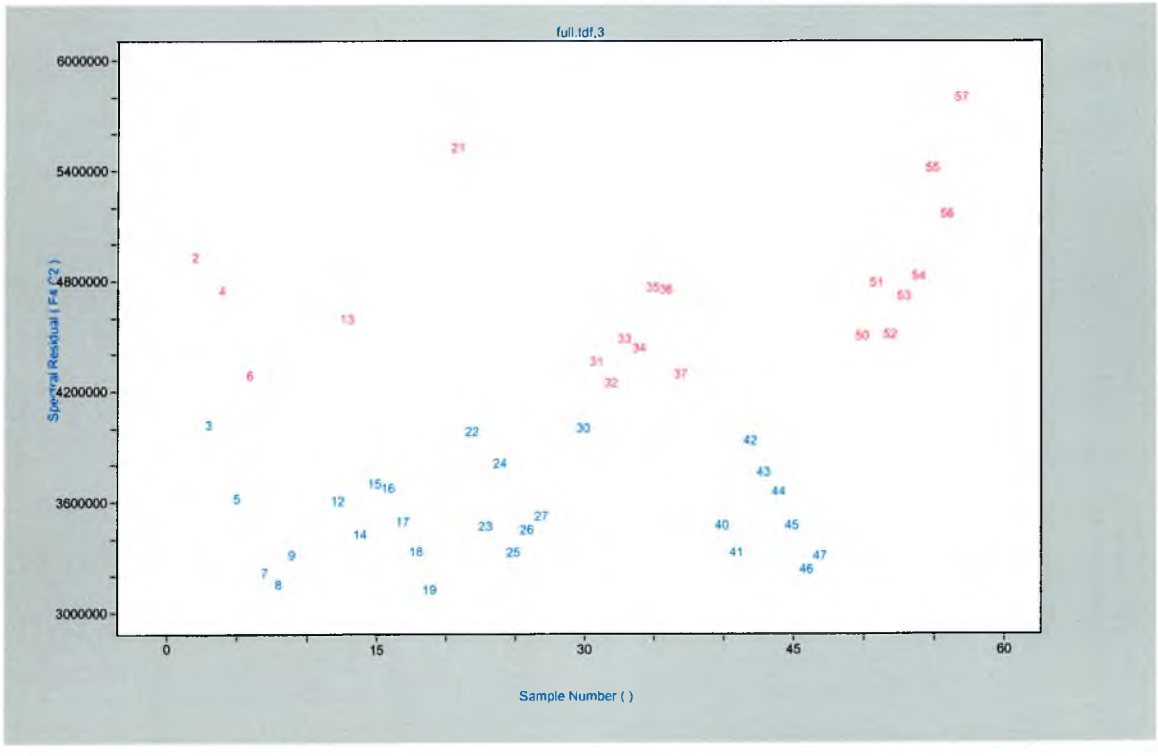

Figure 5.3.43: Spectral outliers for PLS model with only 6 heat-treated samples (from model in section 5.3.12)

The spectral residuals for the model in section 5.3.12 (without the addition of the extra sample) are shown figure 5.3.43. Without the strong influence of the new sample on the F-test outlier detection many of the remaining spectra were predicted to be outliers. Using the F-ratio method has identified many possible concentration and spectral outliers. The next logical step would be to remove these potential outliers from the model and investigate if the R^2 value increases and the RMSV value decreases. However, the outlier detection suggests the removal of a vast number of the spectra. This could possibly undermine the model because only 1 or 2 of the replicate spectra for one sample would be removed and the majority of the spectra for another sample would be removed. Resulting in the model containing 2 or 3 replicate spectra from one sample and up to 10 spectra for another sample. This would result in the model being much more heavily influenced by one sample than another and weaken its predictive accuracy. Also, it is known that the mixture DPM and coal dust samples are highly heterogeneous. So, it is likely that the large number of detected outliers is due to 10 replicate for each sample simply not being adequate enough to account for the possible different spectra for each sample. Therefore, it would probably be better to collected 15 or even 20 spectra of each sample, for future PLS training sets, rather than removing all the suspected outliers from the current model to account for the variance in the spectra for each sample.

Another important diagnostic for chemometric models are the factor loadings. It can be seen from the PLS loadings plots in figures 5.3.44 and 5.3.45 that for DPM 3 factors was sufficient to model the variance as the loading plot for the 4^{th} factor contains little or no variance and using any more than 3 factors would result in incorporating noise into the model. For the same reason 4 factors was considered to be sufficient to model the coal dust variance. The PLS factor loadings can be used to investigate if the modelled variance is actually due to real spectral differences between the constituents. Just like with the PCA loadings for the PCA model in section 5.3.2, where the 1^{st} loading contained variances occurring in similar positions to the D and G bands and was attributed to definite spectral differences. However, it is clear that here the laser plasma lines account for a large amount of the variance for the 1^{st} PLS factor.

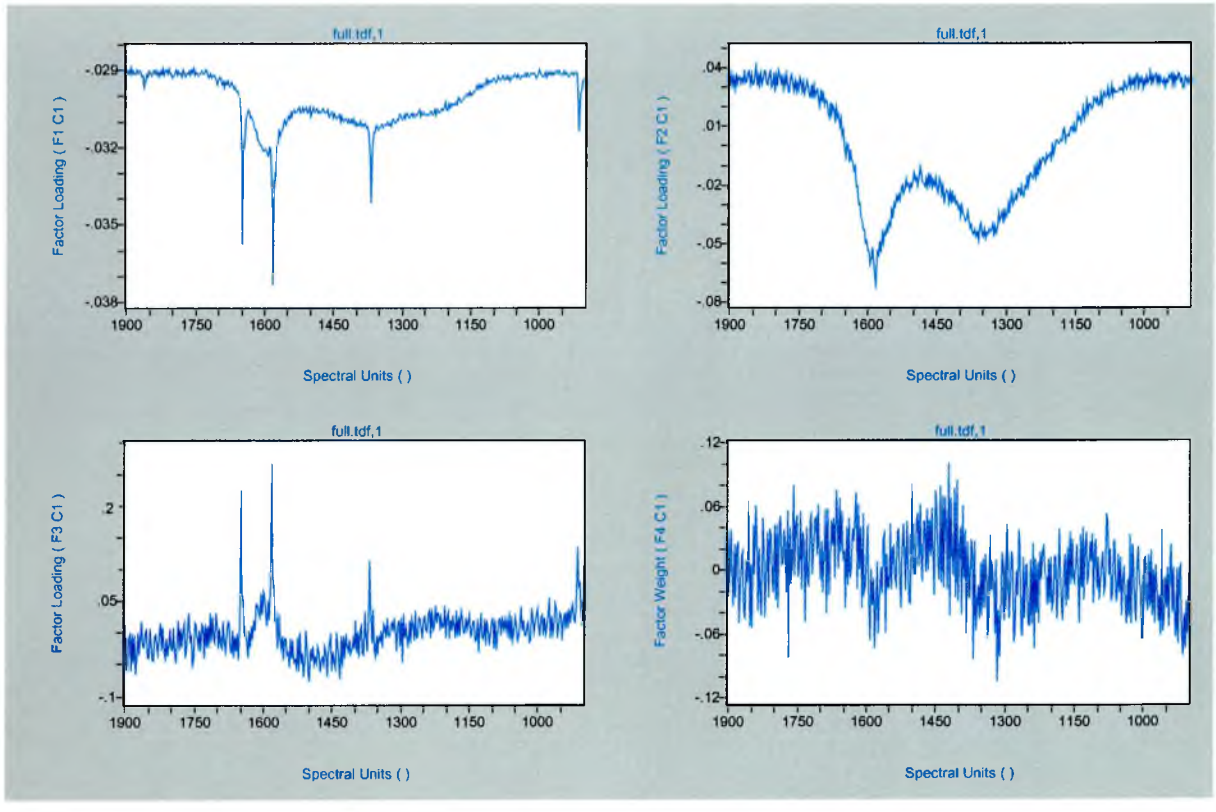

Figure 5.3.44: DPM factor loadings

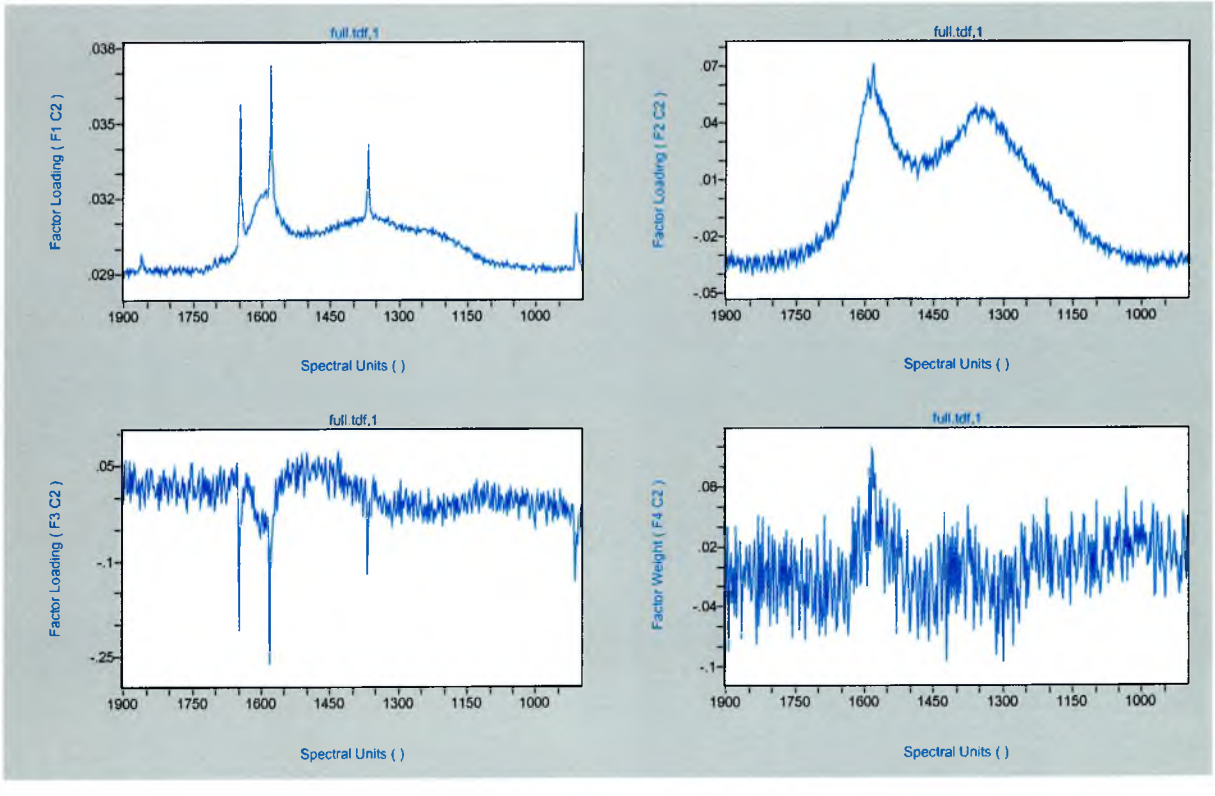

Figure 5.3.45: Coal dust factor loadings

In the second loading the major variance is due to the difference between the D and G bands at ca. 1350cm^{-1} and ca1585cm^{-1} respectively. The fact that the plasma lines have such a large contribution to the variance in the 1st factor signifies that they could influence the predictive accuracy of the current model. It is possible these plasma lines are responsible for the high SEVC and the inaccurate estimates for the test sample. Fortunately, one can remove spurious peak from spectra via spectral processing. Later we will try to remove any obvious plasma lines from the spectra used in the model and then re-run a model with these modified spectra, to investigate if this improves the R^2 and SEVC values. However, in the next section we will first investigate the effect of normalising the areas of the spectra used in the training set and inputting the DPM/coal dust ratios instead of their absolute concentrations.

5.3.16 Investigation of the effect of spectral area normalisation

5.3.16.1 Introduction

Earlier in this work it was mentioned that the signal of a Raman instrument varies from day to day and making it is necessary to calibrate the instrument each day. It is possible to remove variations due to laser power fluctuations, sample alignment etc by normalising the spectra in the training set so that they all have the same total area (integrated intensity). Then instead of inputting the absolute concentrations of the DPM and coal dust one can input the DPM/coal dust concentration ratios. This results in the PLS analysis only using relative intensity changes within a spectrum for the calibration, rather than the absolute intensity. This sometimes gives much better calibrations.

5.3.16.2 Experimental

The spectra used for the PLS model in the previous section were normalised to unit area by dividing each point in the spectrum by its integrated spectral area. These area normalised spectra were then used to construct a new PLS model using the same parameters as the previous model. The spectra were baseline corrected, mean centred, the

whole spectral range was used, 10 factors were calculated and cross-validation was applied.

5.3.16.3 Results and discussion

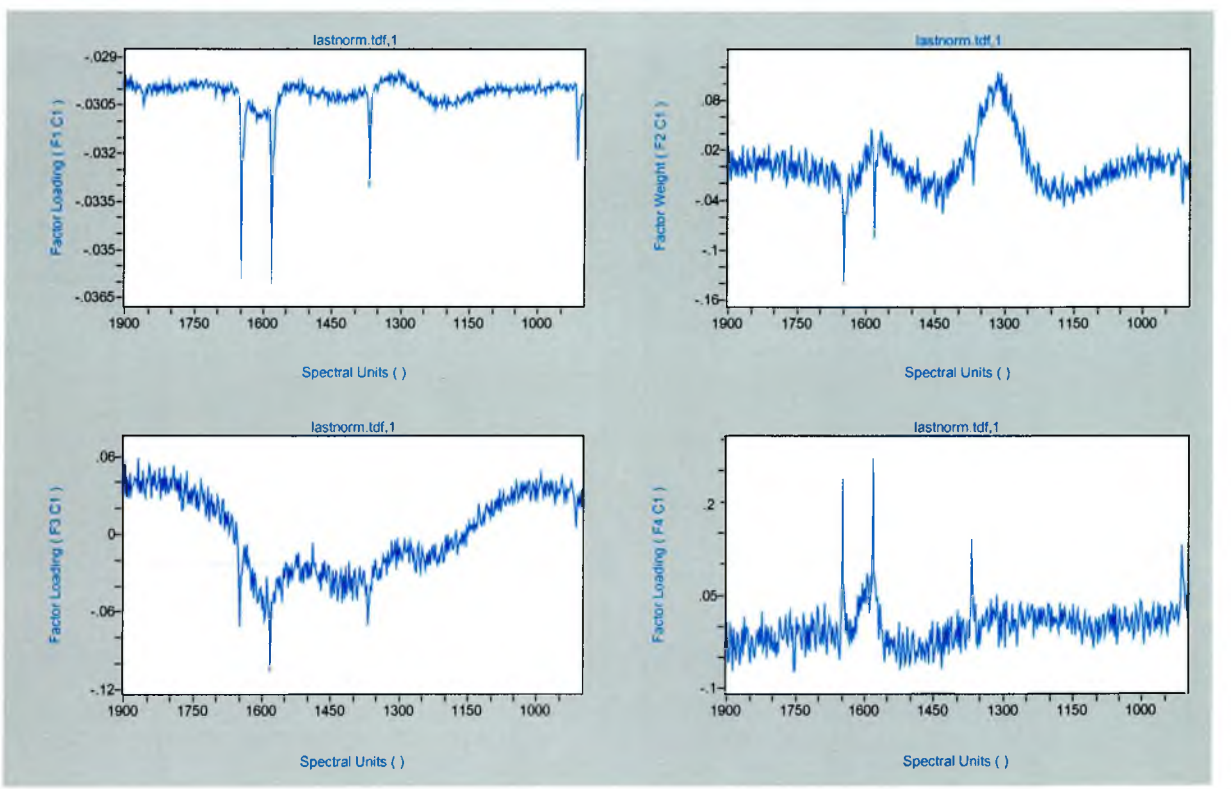

Figure 5.3.46: Factor loadings the normalised spectra

From the factor loadings in figure 5.3.46 it is can be seen that the plasma lines have an even greater contribution to the variance for the model produced with normalised spectra, than for the previous model. This may possibly be due to different coverage of the substrate for each sample. When there is low coverage more light is reflected from the substrate resulting in a larger contribution to the spectra by the plasma lines. When there is a higher level of coverage more of the light is absorbed by the black samples resulting in less contribution from the plasma lines. This can particularly be a problem with a model using the DPM/coal ratios because some samples with similar ratios will have different total weights (substrate coverage) and therefore different contributions from the

plasma lines. The influence of the plasma lines may have contributed to the poor R^2 value of 0.8401 here.

In the next section we will investigate the effect of removing any obvious plasma lines from the spectra before constructing a new PLS model.

5.3.17 Investigation of the effect of removing plasma lines from the training set spectra

5.3.17.1 Introduction

It was determined from the previous PLS factor loadings that laser plasmas line contribute heavily to the variance. It is believed that these lines may affect the predictive accuracy of the model. So, if they were removed from the spectra and a new model produced with the "plasma line free" spectra it is possible that the R^2 and SEVC values would be improved and in turn improve the predictive accuracy of the model.

5.3.17.2 Experimental

Any obvious plasma lines were removed from the spectra to be used for the training set and a new model was produced using these modified spectra. The spectra were baseline corrected, mean centred, the whole spectral range was used, 10 factors were calculated and cross-validation was applied.

5.3.17.3 Results and discussion

The DPM and coal dust actual versus predicted plots are shown in figures 5.3.47 and 5.3.48.

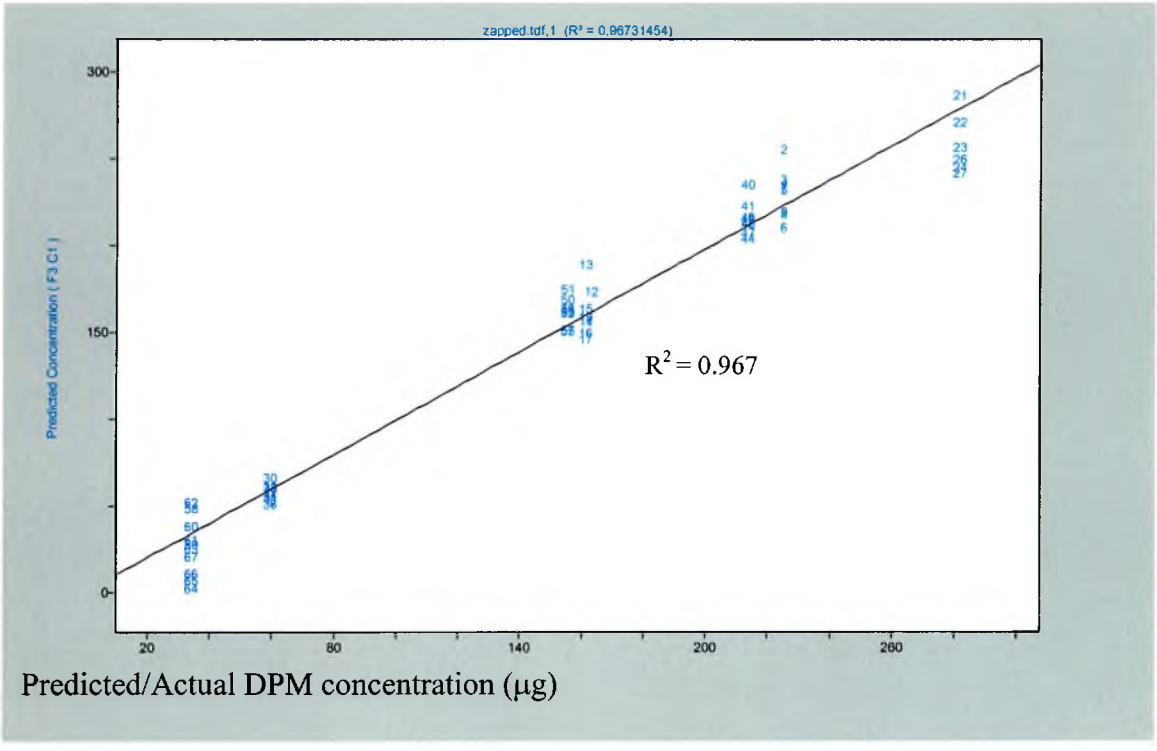

Figure 5.3.47: Actual versus predicted concentration plot for the DPM component using 3 factors

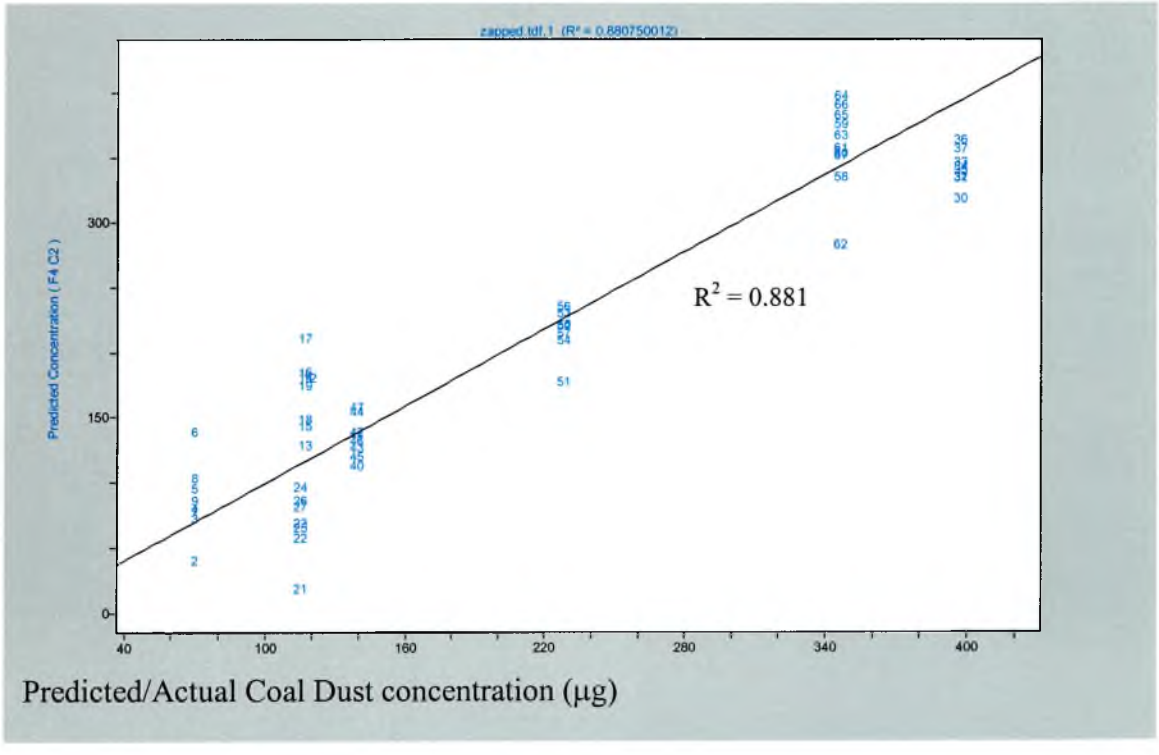

5.3.48: Actual versus predicted concentration plot for the coal dust component, using 4 factors

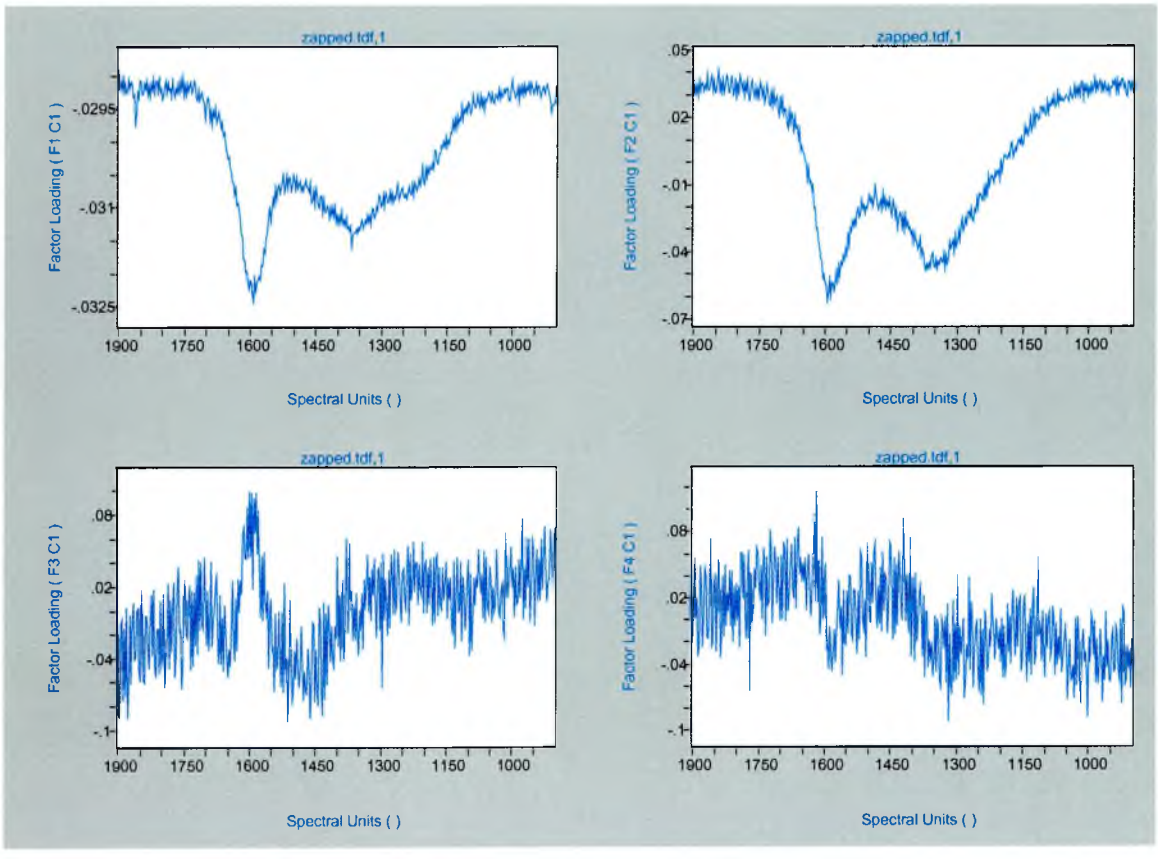

Figure 5.3.49: DPM factor loadings

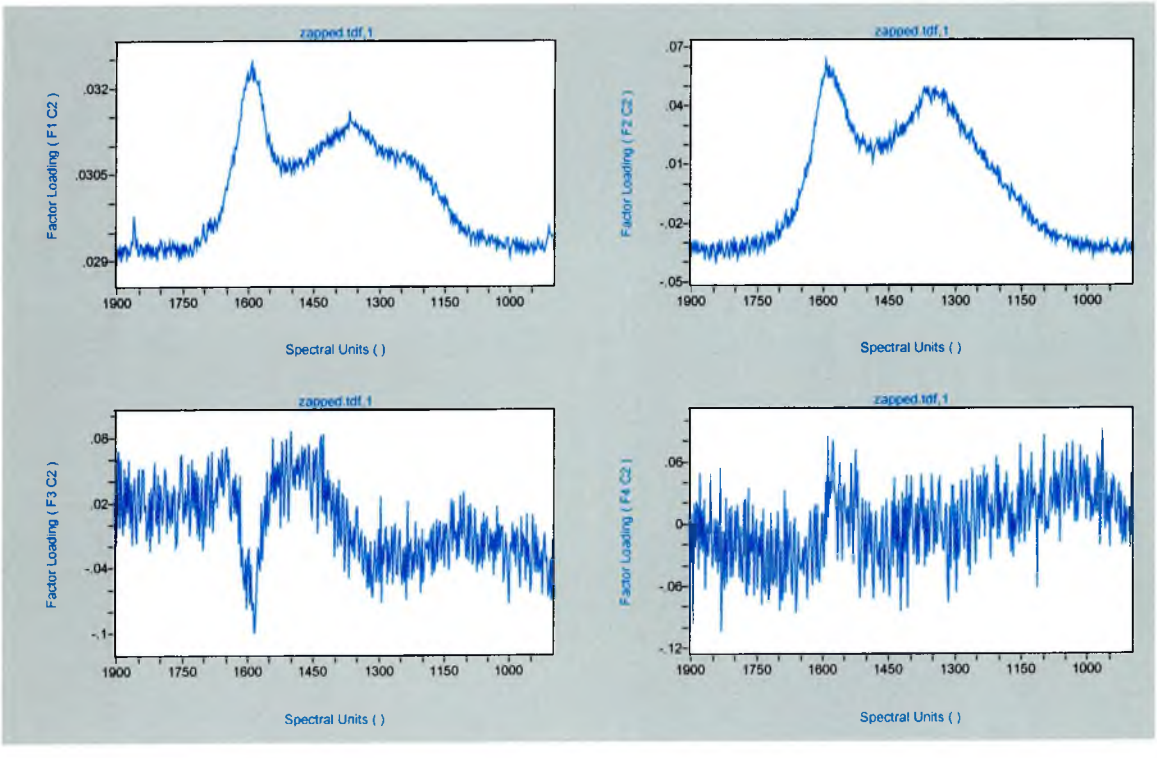

Figure 5.3.50: Coal dust factor loadings

A final attempt to produce a model with improved R^2 and SEVC values is made in the next section. This again involves normalising the spectral areas and inputting the DPM/coal concentration ratios rather than their absolute concentrations but using the spectra with the removed plasma lines.

5.3.18: PLS model of spectra with the plasma lines removed after area normalisation

5.3.18.1 Introduction

Now that the plasma lines had been almost completely removed from the spectra a model using area normalised spectra might work better than the previous attempt where the variance due to the plasma lines dominated the factor loadings. Even though the removal of the plasma lines had no significant effect on the R^2 and SEVC values on the previous model, using absolute concentrations, it is still possible that a model using area normalised spectra would be improved.

5.3.18.2 Results and discussions

The actual versus predicted plot for the DPM/coal dust ratios is shown in figure 5.3.51. The R^2 has decreased to 0.835 for this model from 0.848 from the model using area normalised spectra without the removal of the plasma lines. This indicates that the removal of the plasma lines results in slightly reducing the predictive accuracy of the model. It is possible that the plasma lines themselves offer some useful information or because the modification of the spectra after the removal of the plasma lines introduces some variance into the model.

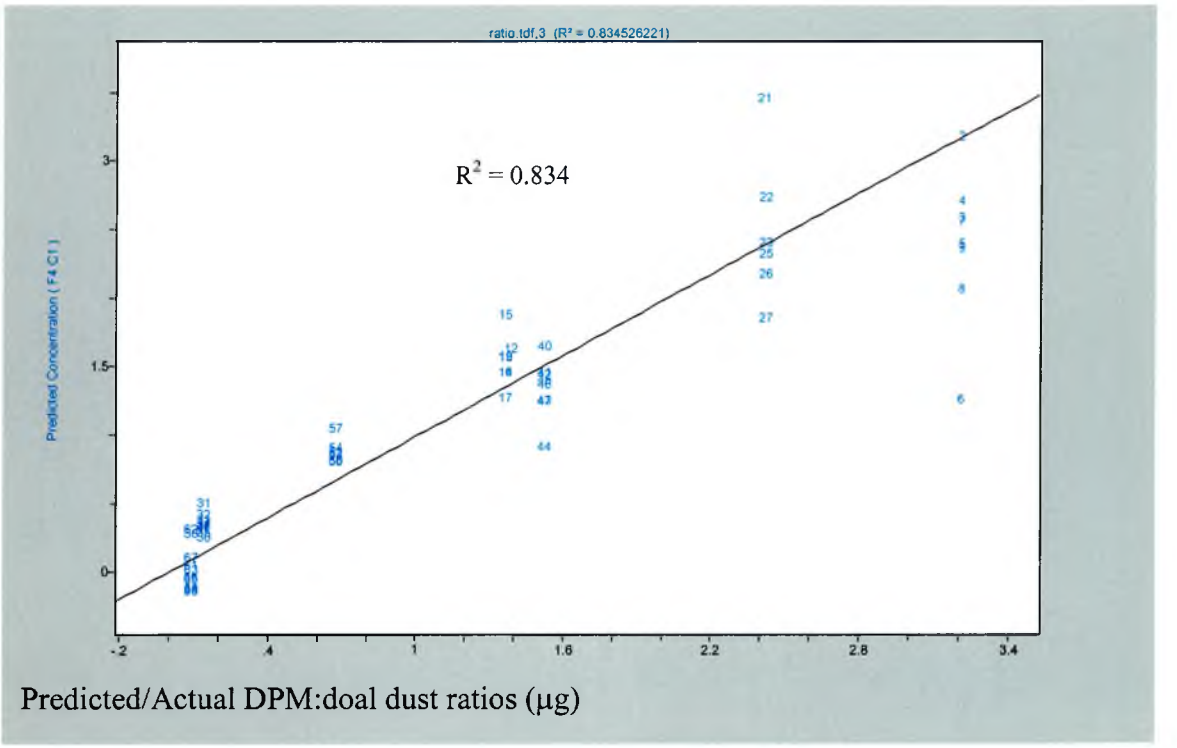

Figure 5.3.51: Actual versus predicted plot for the DPM/coal dust ratios, using 3 factors

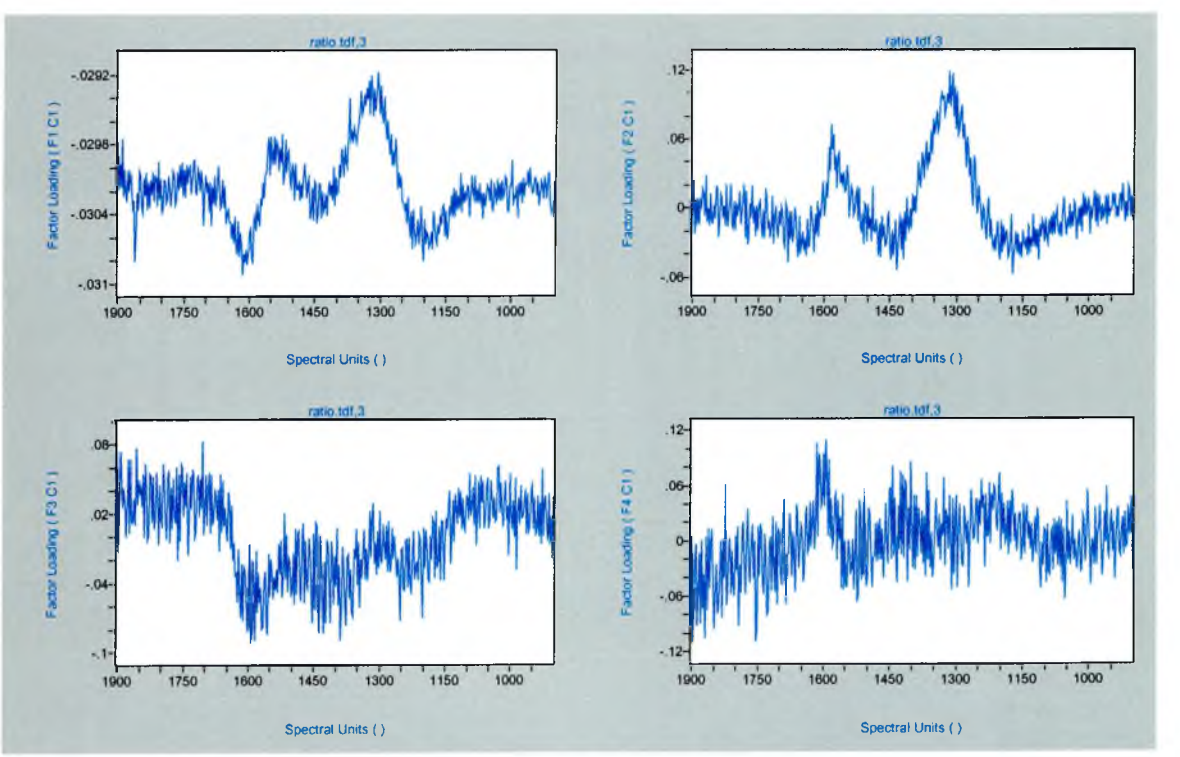

Figure 5.3.52: DPM/coal dust ratio factor loadings

The factor loadings for this particular model are shown in figure 5.3.52. The variance due to the plasma lines was almost completely removed. The loading for the first factor is difficult to interpret. It is a negative loading so the peaks for the variance occur at around $1600cm^{-1}$, which corresponds to the G band. There is also a peak at around $1450cm^{-1}$ which is could be due to a disordered sp^3-bonded carbon phase present in the coal dust but not in the DPM. We would also expect a peak at around $1350cm^{-1}$ due to difference in the D band. However there was a trough observed in this region for an unknown reason.

After investigating the various model types, it was concluded that the best possible model, using the data collected during the present work, was with the spectra without removing the laser plasma lines and inputting the absolute concentrations for the constituents rather than area normalising the spectra and inputting their constituent ratios. The parameters for the final model involved mean centring the data, validation with cross-validation sequentially removing 1 sample, using 3 factors for the DPM prediction plot and 4 factors for the coal dust plot. This resulted in R^2 values of 0.974 and 0.907 with SECV values of 13.5μg and 36.1μg respectively.

In the next section a general discussion on the findings from the current work and recommendations for further work which may possibly improve the current model, are given.

References

1) M. Otto, Chemometrics Statistics and Computer Application in Analytical Chemistry, Wiley, VHC, 1999
2) Galactic Industries Corp, Grams32 PLS/Plus-IQ software and chemometric manual, Galactic Industries Corp, Salem, USA, 2000
3) K. Kemsley, Win-das^{TM} chemometric software user manual, "Introduction to WIN-DAS", Wiley Scientific, Chichester, UK, 1998
5) H. Hotelling, Journal of Educational Psychology, 24, 1998, 498
6) D. Kittelson, Journal of Aerosol Science, **29**, 1998, 575
7) E. Rzepka, A. Lusson, C. Levy-Clement, M. Kumar, K. Mukhopadhyay, M. Sharon Diamond and Related Materials, **8**, 1999, 481
8) M. Paterson, Diamond and Related Materials, **5**, 1996, 1407
9) J. Dennison, M. Holtz, G. Swain, Spectroscopy, **11**, 1996, 38

Chapter 6

Discussion

6 Discussion

6.1.1 The initial Raman study of separate DPM and coal dust

The initial Raman study of separate DPM and coal dust samples documented some distinct differences between their spectra. The DPM spectra had broader bands, were less intense and contained a saddled shaped feature between 200-900cm^{-1}. These facts indicated that the carbon from the DPM was much more "amorphous" than the carbon from the coal dust. The presence of additional bands at 1173cm^{-1}, 1252cm^{-1} and 1440cm^{-1} in the coal dust spectra indicated that a large proportion of the carbon was sp^3-bonded.

6.1.2 XPS analysis of DPM and coal dust

From the XPS analysis of the DPM and coal dust it was observed that they respectively contained 69% and 87% carbon. The second most abundant element for both samples was oxygen, being 29% for DPM and 12% for the coal dust. Trace amounts of Fe, S and Si were detected in the DPM and trace amounts of Fe, S, Si and Al were detected in the coal dust. From the curvefit of the XPS C1s peaks of DPM and coal dust it was estimated that the DPM carbon was 71% sp^2-bonded and 12% sp^3-bonded. The carbon from the coal dust was estimated to be 29% sp^2-bonded and 41% sp^3-bonded. These values correlated well with the Raman spectra, which indicted that the coal dust had a much higher sp^3-bonded carbon content than the DPM.

6.2.3 DRIFTS of coal dust and DPM

The DRIFTS spectrum of the coal dust sample contained aromatic and aliphatic bands, which confirmed the presence of organic material that was not detected in the Raman spectra of the coal dust. There were also bands present which were possibly due to carbonate and silicate minerals. No DRIFTS spectrum was obtained of a DPM sample because it was deep black in colour and strongly absorbed the infrared radiation. This

was even observed for dilute samples. Sp^2-bonded carbon materials are less transparent than sp^3-bonded carbons and therefore more readily absorb radiation. The fact that carbon in the DPM was 71% sp^2-bonded (calculated from XPS spectra) compared to only 29% for the coal dust may explain why it was possible to get a DRIFTS spectrum of coal dust but not of the DPM.

6.1.4 TGA analysis of coal dust and DPM

From the TGA analysis of coal dust and DPM samples it was observed that the coal dust had a weight loss of approximately 17% and the DPM of approximately 30%, when heated to 800°C, showing that the DPM has a much greater organic content than the coal dust. The majority of the weight loss for the DPM occurred between 200 and 600°C showing that there was a larger volatile organic fraction present in the DPM than the coal dust.

6.1.5 XRF analysis of coal dust

O, Mg, Al, Si, P, K, Ca, Fe, Sr, and Ba were detected in the coal dust from the XRF analysis. These elements were attributed to the presence of different minerals such as illite, kaolinite, smectite, apatite and other phosphorous minerals. The carbon content of the coal dust was estimated to be over 95%. This was a large difference from the XPS results, which estimated the carbon content of the coal to be 87%. However, the XPS value only represented a very small surface layer (10-50Å) of the coal dust and the XRF measured the bulk of the sample. Also, the coal dust sample was heated to 1250°C during the XRF fusion process. This would have removed any volatile organics present in the coal dust. Therefore, the percentage of carbon in the original coal dust sample (before being heated) would have been less than the estimated 95%.

6.1.5 SEM images of mixture DPM and coal dust samples

From the SEM images of mixture DPM and coal dust it was observed that the samples were highly heterogeneous. The quartz fibre filter substrate was not flat and the fibres were not completely covered by the sample. Although the majority of individual DPM particles are known to be in the nanometer range, accumulated DPM particles of the order of 50μm were observed here. It was possible that the accumulated DPM particles may have surrounded the larger coal dust particles. The coal dust particles themselves ranged in size from a few micrometers to around 25-30μm. Both the DPM and coal dust were unevenly distributed on the filter. However, there were certain areas between the coal dust particles and the large agglomerates of DPM where the substrate was covered. These areas were likely to be taken up by very fine DPM particles, which indicated, apart from the large agglomerates, that the DPM was more evenly distributed on the filter, than the coal dust. This heterogeneity has profound implications for the analysis of mixture samples using Raman microscopy.

6.1.6 Calibration plots of separate DPM and coal dust samples

The separate DPM and coal dust calibration plots in section 5.3.1 showed that there was a linear response between the Raman spectral areas and sample concentration. However, at coal dust concentrations of greater that 500μg the plot reached a plateau. This indicated that at loadings above this level layers of coal dust were being piled on top of each other and the filter had effectively become saturated. As a result of this, loadings of greater than 500μg were outside the linear range of the technique. Therefore, when producing mixture standards for a PLS model it was necessary to keep the total sample weight to less than 500μg to avoid this problem.

6.1.7 PCA of separate DPM and coal dust spectra

In the PCA analysis of separate DPM and coal dust samples 99% of the variance occurred in the first principal component and the observations for the coal dust and DPM

spectra were clearly separable into two different groups. This showed that PCA was capable of easily distinguishing between carbon spectra from coal dust and DPM. The DPM observations were bunched together in a very closely spaced group. This indicated that their corresponding spectra had very similar shapes. However, the coal dust spectra were not bunched as closely together as the DPM spectra, which indicated that their spectral shapes were not very similar (in chemometric terms), compared with those of the DPM. The loading for the 1st component looked similar to a Raman spectrum of carbon, with large variances occurring in similar positions to the D and G bands. There is was a distinct shoulder at around 1250cm^{-1}, which corresponds to the Raman feature, due to an sp^3-bonded carbon phase, observed in the Raman spectra of the coal dust but not in the DPM spectra. The positions of the variance peaks confirm that the variance between the coal dust and DPM spectra was definitely due to differences in their spectra for the first PC.

Using the model developed, group predictions were made for a test set of 14 spectra (7 DPM and 7 coal dust). The model correctly assigned all 7 DPM test spectra to group 1 and all 7 coal dust test spectra to group 2. This showed that the model developed was capable of distinguishing between separate coal dust and DPM carbon spectra.

6.1.8 Development of the sample analysis criteria for quantitative multivariate Raman analysis of mixture DPM and coal dust samples

The initial investigation into the reproducibility of spectral areas involved using X50 objective, 250s scan time and 10% laser power. 10 replicate spectra were measured for a range of samples. Their standard deviations of their integrated areas ranged from 13 to over 40%. It was believed the large errors were due to the heterogeneity of the samples. So, it was investigated if increasing the laser spot size was from 2-3μm, using the X50 objective, to 30μm with an X5 objective and sampling a more representable area would improve the reproducibility. Using the X5 objective standard deviations of integrated spectral areas of the mixture samples were in the range of 4.9 to 21.8%. The improvement in the reproducibility of the spectral areas, due to the increase in the sample

area, indicated that a further increase in the sample area would improve the reproducibility even more. This was achieved by using a rotating stage resulted in a sample area of 1,400,000μm^2. A vast increase on the original 30μm^2 sample area, when no rotating stage was employed. Using the rotation stage the standard deviation of the spectral areas of mixture samples was reduced from a range of 4.9 to 21.8% down to between 1.9 to 10%. A PLS model was constructed using the spectra from the mixture standards that had been analysed when rotating. The R^2 values for the DPM and coal dust actual versus predicted concentration plots were 0.673 and 0.818 respectively. The large variation in the actual concentration versus predicted concentration observations, for replicate spectra, did not correlate well with the low standard deviations of between 1.9 to 10%, for the integrated spectral areas. This indicated that the spectral shapes were very different (in PLS terms) for each replicate spectrum of a sample. It was concluded that one of the major reason for the differences in the shapes of replicate spectra was the differential burn-off of organic material due to the laser heating of the sample. Therefore it was decided to heat-treat the sample to 625°C in a N_2 atmosphere. After such a heat-treatment the laser heat should have no effect on the sample and the spectra would not change due the burn off of organic material.

A PLS model was constructed with spectra from the heat-treated mixture samples and the R^2 values for DPM and coal dust actual versus predicted concentration plots improved from 0.673 and 0.818 to 0.932 and 0.826 respectively. Therefore, the heat-treatment reduced the effect of the differential burn-off of organic material due to laser heating. This work was performed by collecting 10 replicate spectra of each sample and it was observed that the first one or two spectra of the 10 replicates, for each sample, had higher fluorescence levels. On a closer look at the PLS actual versus predicted plots it was observed that the observation corresponding these spectra could be possible outliers. The difference for the first one or two spectra of each sample was attributed to them being still affected by the burn off of organic material, even after the heat-treatment process. This may have been due to organic material from the atmosphere adsorbing onto the surface of the sample after the heat-treatment. Therefore, the PLS model using the heat-treated mixture sample was re-calculated omitting the first 2 spectra, of the 10 replicates,

for each sample. The R^2 values for DPM and coal dust actual versus predicted concentration plots improved from 0.932 and 0.826 to 0.961 and 0.874 respectively. It was decided that future analysis should involve collecting 12 replicate spectra of each sample and the first 2 spectra omitted for any calculations/predictions. At this stage it became apparent that the model would be much more reliable for the prediction of DPM concentrations compared to coal dust concentrations. However, we were fortunate that there were only two components. So, once the DPM concentration has been calculated we can predict the coal dust concentration by subtracting the estimated DPM weight from the total weight of the sample. It is also worth noting that the standard deviation of the integrated spectral areas of the spectra now ranged from 1.9 to 6.0% compared to 1.9 to 10% for the non-heat-treated mixture samples.

Using the step-by-step investigations detailed above the analysis criteria for mixture DPM and coal dust samples was developed. The final criteria involved firstly heat-treating the sample to 625°C in a Nitrogen atmosphere for 15 minutes. Then collecting the Raman spectrum using the optimal parameters of X5 objective, 400 second scan time and 100% laser power, while rotating the sample at 3rpm and sampling an area with a radius of 0.75cm. Also 12 replicate spectra should be taken of each sample and the first 2 discarded due to fluorescence from adsorbed organic material.

6.1.8 PLS models using the final data set

6.1.8.1 PLS model with the original spectra from the heat-treated mixture samples

The final data set involved the addition of an extra sample containing 30μg DPM and 297μg coal dust. The sample was analysed using the developed criteria and the 10 resulting spectra added to the data set. A new PLS model was constructed and R^2 values of 0.974 and 0.907 were obtained for the DPM and coal dust actual versus predicted plots respectively.

This model was tested by using it to predict the weights of DPM and coal dust in a mixture known to contain 156μg DPM and 139μg coal dust. Using the predicted values

from 10 spectra of the test sample, the 95% confidence interval for the estimated mean was 162.1μg to 169.9μg (166 ± 3.9μg) for DPM and 60.2μg to 75.8μg (68 ± 7.8μg) for coal dust. Therefore the model slightly overestimated the DPM content but gave a large underestimation for the coal dust.

There were several possible explanations for the poor estimations. Firstly the test sample may not have contained the expected amount of each constituent. Also the higher R^2 value of 0.974 for the DPM compared to 0.907 for the coal dust may explain why the prediction was more accurate for the DPM. The SEVC values for DPM and coal dust 13.5μg and 36.1μg respectively. This implied that a test sample with concentrations of 156μg DPM and 139μg coal dust could have been predicted to contain 142.5 to 169.5μg DPM and 102.9 to 139μg coal dust. The average estimated value for the DPM was 166μg and this indeed did lie within the expected prediction range for the test sample. However, the average coal dust estimation of 68μg is still considerably lower than the SEVC would suggest. A large variation in the both concentration and spectral residuals which indication there was a variation in the spectra due to both the spectral intensities and shapes. This was not a major surprise due and would mainly have been due to the samples being highly heterogeneous. Perhaps 10 replicate spectra of each sample were not enough to effectively model the variance. Another possible source of error was identified from the factor loadings where it was observed that the laser plasma lines contributed heavily to the variance.

6.1.8.2 PLS model with area-normalised spectra

A model was constructed by normalising the areas of the spectra and inputting the DPM/coal ratios rather than their absolute concentrations. This was performed to eliminate the effect of laser fluctuations and different sample alignments. However, the R^2 for this model was 0.84. Also, from looking at the factor loadings it was observed that the laser plasma lines contributed even more to the variance in this model and than for the previous model. This was because with a model using the DPM/coal ratios some samples

with similar ratios will have different total weights (substrate coverage) and therefore different contributions from the plasma lines.

6.1.8.3 PLS models using spectra with the laser plasma lines removed

It was decided to return to using absolute concentration and non-normalised spectra. However, this time any obvious laser plasma lines were removed from the spectra. No major difference was observed for the model with the DPM and coal dust actual versus predicted R^2 values being 0.967 and 0.881 respectively compared to 0.974 and 0.907 the earlier model. From the factor loadings plots it was observed that the variance due to the laser plasma lines was almost completely removed. This indicated that if these spectra could be used in model similar to the previous one where the spectra were area normalised and the DPM/coal ratios rather inputted than their absolute concentrations. That is exactly what was performed for the final model. The R^2 was observed to be 0.835 which was even lower than the R^2 of 0.848 for the on the earlier model using normalised spectra without removing the plasma lines.

Finally it was concluded that the best possible model using the available data was using the data collected during the present work, was with the spectra without removing the laser plasma lines and inputting the absolute concentrations for the constituents rather than area normalising the spectra and inputting their constituent ratios. The parameters for the final model involved mean centring the data, validation with cross-validation sequentially removing 1 sample, using 3 factors for the DPM prediction plot and 4 factors for the coal dust plot. This resulted in R^2 values of 0.974 and 0.901 with SECV values of 13.5μg and 36.1μg respectively.

6.1.9 Relevance of the current work to occupational environments other than coal mines

The major difficulty in achieving the current aim of determining the amount of DPM and coal dust in a mixture sample is undoubtedly due to the complexity of the samples.

However, an R^2 value of 0.974 was still achieved for the DPM. In another occupational setting where there is expected to be high levels of DPM but no major interference from another carbon source, it is conceivable that this method could be quite effective. Several examples would be other mining industries such as salt mines or garages for fleets of vans or buses are which use the same fuel source. There are currently methods available for the analysis of DPM alone (as discussed in chapter 1). However, once an effective calibration plot had been developed it would be much simpler and quicker to perform a Raman analysis.

6.2 Future Work

6.2.1 SEM images of separate DPM and coal dust samples

The SEM work presented in the present study included images of mixture DPM and coal dust samples. Accumulated DPM particles of the order of 50μm were observed. It was suggested that these large agglomerates might have been coal dust particles surrounded by DPM. SEM images of DPM on its own would help establish if these large agglomerates were pure DPM or not. SEM images of separate DPM and coal dust samples could be compared to the images of mixture samples to see to what extent collecting the DPM and coal dust simultaneously affects the distribution of the DPM on the quartz fibre substrate.

6.2.2 XPS of heat-treated coal dust

From the comparison of the Raman spectra of an un-treated coal dust sample and a sample heat-treated to 625°C it was observed that the D bandwidth and the D/G band ratio increased for the heat-treated sample. These observations indicted that the heat-treated sample structure was more disordered. This was surprising because it is known that heat-treatment induces ordering of carbonaceous materials. From the XPS analysis of the carbon C1s peak of coal dust it was estimated that its carbon content was 41% sp^3-bonded. This correlated well with the Raman spectrum, which had a large band at around

1240cm^{-1} that is known to be due to an sp^3-bonded carbon phase. The contribution of the band at 1240cm^{-1} to the Raman spectrum of the heat-treated coal dust spectrum was greatly reduced compared to the untreated sample. This indicated that the heat-treatment might have converted some sp^3-bonded carbon to sp^2-bonded carbon. However a HTT of 625°C might only have been high enough to convert the sp^3-bonded carbon to disordered sp^2-bonded carbon. This would explain why the Raman spectrum of the coal dust indicated that the heat-treated sample was more disordered than the untreated sample.

The validity of this hypothesis could be investigated by performing an XPS analysis on a heat-treated coal dust sample to determine if and how much of the sp^3-bonded carbon had been converted to sp^2-bonded carbon, after heat-treatment. It may also be useful to heat-treat the coal dust using a range of HTTs. The change in sp^2/sp^3 hybridisation could be determined for each temperature and compared to a change in the Raman spectrum of the sample.

6.2.3 The addition of more samples to the PLS model

Originally 6 mixture samples were used for the PLS model. The best R^2 value of the actual versus predicted concentration plots using 6 samples was 0.961 for the DPM and 0.874 for the coal dust. An additional sample was added in an attempt improve these values. The addition of a 7th sample improved the R^2 value from 0.961 to 0.974 for the DPM actual versus predicted plot and from 0.874 to 0.907 for the coal dust actual versus. This indicates that the addition of extra mixture samples would further improve the model.

The current data set does not include any samples with DPM loadings between 70 and 150µg. Therefore if new samples were to be added to the model it would be desirable for them to have DPM loadings in this range.

6.2.4 Increase the number of spectra taken for each sample

Large variations were observed for both concentration and spectral residuals and many of the samples were identified at outliers using an F-ratio test. It was presumed this was due to the heterogeneity of the samples and it was possible that 10 replicate spectra of each sample was not enough to effectively model all the possible variations for the spectra of each sample. It is recommended that further work should involve collecting 15 or possibly even 20 spectra for each sample to investigate if this helps improve the model's capability to account for the variations in the spectra.

6.2.5 Test the model with more samples

The final model produced here was tested with a mixture sample with a known amount of DPM and coal dust, which was not used to develop the model. The model slightly overestimated the DPM concentration but gave a large underestimation for the coal dust sample. However, this was the result of just one test sample. To effectively test the current model or future models it will be necessary to use a number of test samples with a wide variety of different DPM and coal dust weights, ranging from low to high concentrations. Testing the model in such a way would identify if the outcome for the sample tested here (large underestimation for the coal and an overestimation for the DPM) was a general trend, specific to a particular concentration range or just specific to this sample.

6.2.6 Predict the composition of real unknown (field) samples

The PLS model has been tested with a mixture DPM and coal dust sample that was synthesised in the laboratory. The model should be tested further by using it to predict the composition of real mixture DPM and coal dust samples collected in a coal mine. The model developed here used a specific type of coal dust and DPM source. If a Raman spectroscopy-based method to analyse carbon particulates in mixtures produced from DPM and coal dust in a coal mine was to be successful it may be necessary to produce

mixture samples using the type of coal and DPM source used in the coal mine of interest. Using the analysis criteria developed in the present work a new PLS model could then be constructed form the spectra of these samples, producing a calibration which would be specific to the particular coal mine.

6.2.7 Calibration plots of separate DPM samples using the final analysis criteria

Calibration plots of concentration versus integrated Raman spectral areas of separate DPM and coal dust samples were presented in chapter 5. However, these samples were not analysed using the analysis criteria developed later in this work. The production of a calibration plot for DPM alone, using the optimised parameters, sample rotation and heat-treatment may be useful for monitoring DPM exposure in occupational environments other than coal mines. The fact that a high R^2 of 0.974 was achieved for DPM in a mixture indicates the use of a calibration using DPM alone has the potential to be very accurate method.

Conclusions

The principal aim of the current work was to develop a Raman-spectroscopy based method to analyse carbon-based particulates in mixtures produced from DPM and coal dust and determine the amount of each constituent in unknown samples from coal mines. The heterogeneity of the samples and the similarity of the Raman spectra of DPM and coal dust presented a very difficult challenge. This resulted in the present work only progressing to the laboratory stage, where synthesised samples were analysed rather than real samples from a coal mine. However, the work carried out with the synthesised samples provided some encouraging results. The criteria for the Raman analysis of mixture samples have been systematically developed. This involved determining the optimum instrumental parameters, rotating the sample during analysis and heat-treatment of the samples before analysis. The overall result being that errors in the reproducibility of the Raman integrated spectral areas of a collection of mixture samples were reduced from a range of 4.9 to 21.8% down to a range of 1.9 to 6%. The best PLS model developed here had R^2 values of 0.974 and 0.901 for the DPM and coal dust actual versus predicted models and SECV values of 13.5μg and 31.6μg respectively. This model was tested with a sample known to contain 156μg DPM and 139μg coal dust. From the estimate of 10 replicate spectra of this sample the 95% confidence interval for the estimated mean was 166 ± 3.9μg (162.1 to 169.9μg) for the DPM and 68 ± 7.8μg (60.2 to 75.8μg) for the coal dust. The inaccurate estimates were attributed to the test sample possibly not containing the expected amount of each component, high SECV values due to large variations in the spectra or interference from laser plasma lines. The final model would not be accurate enough to apply to unknown samples from a coal mine. However, there was only a slight overestimation of the DPM and if the recommendations for further work were carried out there is a strong possibility that a model capable of more accurately estimating. DPM in mixtures sample can be developed.

The recommended further work included:

- Use additional samples for the PLS model to help model the possible sample variations over the whole analysis range.
- Increase the number of spectra of each sample to improve the model's capability to account for the possible variations in the spectra.
- Test the future models with more samples to further investigate their predictive accuracy.
- Take extra care to prevent laser plasma lines entering the Raman spectrometer during the analysis.